



Provided by the author(s) and NUI Galway in accordance with publisher policies. Please cite the published version when available.

Title	Magnetotelluric research of the Rathlin Basin
Author(s)	Delhaye, Robert
Publication Date	2018-12-24
Publisher	NUI Galway
Item record	http://hdl.handle.net/10379/15015

Downloaded 2019-03-19T11:54:25Z

Some rights reserved. For more information, please see the item record link above.



MAGNETOTELLURIC RESEARCH OF THE RATHLIN BASIN

ROBERT DELHAYE

BSc, University of Auckland, 2008
MSc (Hons), University of Auckland, 2011
NUIG Student Number: 12233096

The thesis is submitted to the Faculty of Science,
National University of Ireland, Galway,
in fulfilment of the requirements for the degree of
DOCTOR OF PHILOSOPHY



NUI Galway
OÉ Gaillimh

School of Natural Sciences, Faculty of Science,
National University of Ireland, Galway
Galway, Ireland

SUPERVISED BY:

Prof. Colin Brown, *NUI Galway, Galway, Ireland*
Dr. Volker Rath, *Dublin Institute for Advanced Studies, Dublin, Ireland*

May 2018

Robert Delhaye: *Magnetotelluric Research of the Rathlin Basin*,
© May 2018

CONTENTS

Table of Contents	v
List of Figures	viii
List of Tables	ix
List of Symbols	x
List of Acronyms	xii
Preface	xiv
Declaration	xv
Acknowledgements	xvi
Dedication	xvii
1 INTRODUCTION	1
1.1 The Rathlin Basin	2
1.2 Magnetotellurics and the Static Shift Effect	7
1.2.1 Introduction to Magnetotellurics	7
1.2.2 MT Data Acquisition	9
1.2.3 Static-Shift Distortion of MT Data	10
1.3 Research Questions	12
1.4 Thesis Structure	12
1.4.1 Article 1 (Chapter 2): Correcting for Static Shift of Magnetotelluric Data with Airborne Electromagnetic Measurements: A Case Study from Rathlin Basin, Northern Ireland	12
1.4.2 Article 2 (Chapter 3): Quantitative Interpretation of a Magnetotelluric Model of the Rathlin Basin, Northern Ireland	13
1.4.3 Article 3 (Chapter 4): Establishing the Sensitivity of a 3D Magnetotelluric Model of Rathlin Basin, Northern Ireland	14
2 CORRECTING MT STATIC SHIFT WITH AEM, RATHLIN BASIN	16
2.1 Abstract	16
2.2 Introduction	17
2.3 Electromagnetic methods	23
2.3.1 Magnetotelluric method	24
2.3.2 Frequency domain AEM method	26
2.4 Rathlin Basin survey	27
2.4.1 Correction of static shifts	32
2.5 Model evaluation and discussion	36
2.6 Conclusions	48

2.7	Code availability	49
2.8	Data availability	49
2.9	Author Contribution	49
2.10	Acknowledgements	50
2.A	Comparison with Inversion of Non-rotated Data and Mesh	50
3	QUANTITATIVE GEOTHERMAL INTERPRETATION OF THE RATHLIN BASIN	60
3.1	Abstract	60
3.2	Introduction	61
3.3	Tectonic and Geologic Setting	63
3.4	Stratigraphy	63
3.5	Boreholes	64
3.5.1	Port More 1 borehole	65
3.5.1.1	DC resistivity log	66
3.5.1.2	Neutron porosity log	68
3.5.1.3	Laboratory porosity and permeability measurements	68
3.5.2	Ballinlea-1 borehole	69
3.6	Magnetotelluric exploration	71
3.7	Indicated geothermal reserve estimation	75
3.8	Implications and discussion	80
3.9	Conclusions	81
3.10	Acknowledgments	82
3.A	Examination of 1D MT Model Boundary Tolerances	82
4	A MAGNETOTELLURIC SENSITIVITY STUDY OF RATHLIN BASIN, NORTHERN IRELAND	85
4.1	Abstract	85
4.2	Introduction	86
4.2.1	Geological Setting	86
4.3	Methodology and Results	87
4.3.1	Magnetotelluric Theory	87
4.3.2	Magnetotelluric Data Acquisition and Analysis	89
4.3.3	Model Jacobian Sensitivity	90
4.3.4	Examination by Jacobian Sensitivity	93
4.3.5	SVD Truncation of the Jacobian Sensitivity	94
4.4	Discussion	95
4.5	Conclusions	97
4.6	Acknowledgments	97
5	CONCLUSIONS	109
5.1	Revisiting the Research Questions	109

5.1.1	How can regional airborne EM data from the Tellus Project be used in static shift correction of MT data?	109
5.1.2	What can be inferred about the geothermal potential of Rathlin Basin from MT models?	110
5.1.3	What additional value can be added to 3D model interpretation by also considering the sensitivity of model responses?	110
5.2	Recommendations for Further Research	111
5.2.1	Methodological Recommendations	111
5.2.2	Recommendations for the Assessment of the Rathlin Basin	112
5.3	In Conclusion	113
	Bibliography	124
i	APPENDICES	125
A	APPENDIX 1: CHAPTER 2 DATA AND RESPONSES	126
B	APPENDIX 2: CHAPTER 3 DATA AND RESPONSES	145

LIST OF FIGURES

Figure 1.1	Extrapolated geothermal gradient below Ireland at 5000 m depth	2
Figure 1.2	Extrapolated temperature distribution below Ireland at 2500 m depth	3
Figure 1.3	Three-dimensional model of sedimentary basins in north-east Ireland	4
Figure 1.4	Geological cross-section diagram of the Rathlin and Foyle Basins	5
Figure 1.5	Porosity and hydraulic permeabilities of NE Ireland Permian and Triassic sandstones	6
Figure 2.1	Geological map of Rathlin Basin area	18
Figure 2.2	Port More 1 Borehole stratigraphy	20
Figure 2.3	Density model of the Rathlin Basin	21
Figure 2.4	Dimensionality of Rathlin Basin MT data	29
Figure 2.5	Chart of frequencies used in 3D inversion process over Rathlin Basin	30
Figure 2.6	Flowchart of static shift correction methodology	32
Figure 2.7	Map of Rathlin Basin modelled AEM resistivities	35
Figure 2.8	Map of static shift corrective factors over Rathlin Basin	36
Figure 2.9	Distribution of static shift corrective factors over Rathlin Basin	37
Figure 2.10	Bivariate distribution of static-shift corrective factors over Rathlin Basin	38
Figure 2.11	Resistivity and comparison variable depth slices through 3D MT models	39
Figure 2.12	Resistivity and comparison variable profile A through 3D MT models	40
Figure 2.13	Resistivity and comparison variable profile B through 3D MT models	40
Figure 2.14	Resistivity and comparison variable profile C through 3D MT models	41
Figure 2.15	Representative histogram 1D model of static-shift-corrected Rathlin Basin 3D MT model	42
Figure 2.16	Visualisation of static shift-corrected Rathlin Basin 3D MT model misfit	45
Figure 2.17	Comparison of 3D MT models at Port More 1 borehole	47
Figure 2.18	Resistivity and comparison variable depth slices through rotated 3D MT models	52
Figure 2.19	Resistivity and comparison variable depth slices through non-rotated 3D MT models	53
Figure 2.20	Resistivity and comparison variable profile A through rotated 3D MT models	54
Figure 2.21	Resistivity and comparison variable profile A through non-rotated 3D MT models	55

Figure 2.22	Resistivity and comparison variable profile B through rotated 3D MT models	56
Figure 2.23	Resistivity and comparison variable profile B through non-rotated 3D MT models	57
Figure 2.24	Resistivity and comparison variable profile C through rotated 3D MT models	58
Figure 2.25	Resistivity and comparison variable profile C through non-rotated 3D MT models	59
Figure 3.1	Onshore sedimentary basins of Northern Ireland	61
Figure 3.2	Surficial geology of the Rathlin Basin survey area in Northern Ireland	64
Figure 3.3	Formations encountered in the Port More 1 borehole	66
Figure 3.4	Measured wireline resistivity data in Port More 1 borehole	67
Figure 3.5	Measured neutron porosity in Port More 1 borehole	69
Figure 3.6	Laboratory porosity and hydraulic permeability of sandstones from Port More 1 borehole	70
Figure 3.7	Temperature and geothermal gradient data from Ballinlea 1 borehole	71
Figure 3.8	MT model ensemble compared to Port More 1 resistivity data	74
Figure 3.9	MT model ensemble compared to Ballinlea 1 resistivity data	75
Figure 3.10	Depth distribution of interpreted stratigraphic horizons in Rathlin Basin	76
Figure 3.11	Estimated thickness distribution of target sediments within Rathlin Basin	77
Figure 3.12	Thermal energy in place within the Rathlin Basin vs. final reservoir temperature	77
Figure 3.13	Change in Rathlin Basin geothermal reservoir volume vs. final reservoir temperature	79
Figure 3.14	Distribution of density of thermal energy in place	80
Figure 3.15	Tolerance of SSG Boundary Shifts in PM1 Resistivity Model	83
Figure 3.16	Tolerance Distribution vs dh change for Rathlin Basin 1D Models	84
Figure 4.1	Geological map of Rathlin Basin area	87
Figure 4.2	Bulk lithologies encountered in the Port More 1 borehole	88
Figure 4.3	Rathlin Basin resistivity and sensitivity depth slices	98
Figure 4.4	Rathlin Basin Profile A - resistivity and sensitivity	99
Figure 4.5	Rathlin Basin Profile B - resistivity and sensitivity	100
Figure 4.6	Rathlin Basin Profile C - resistivity and sensitivity	100
Figure 4.7	Comparison of Jacobian weightings	101
Figure 4.8	Comparison of impedance and tipper Jacobian elements	102
Figure 4.9	Image of adjusted sensitivity of Rathlin Basin MT model	103
Figure 4.10	Histogram of adjusted sensitivities of Rathlin Basin MT model	104

Figure 4.11	Histogram of integrated sensitivities of Rathlin Basin MT model	105
Figure 4.12	Singular values of SVD-decomposed Rathlin Basin MT model Jacobian . .	106
Figure 4.13	Comparative histograms of truncated-SVD sensitivity	107
Figure 4.14	Comparative histograms of summed truncated-SVD sensitivity	108

LIST OF TABLES

Table 2.1	Statistical measures of static shift corrective factor for Rathlin Basin MT data	35
Table 3.1	Formations of the Rathlin Basin	65

LIST OF SYMBOLS

Following is a list of symbols used in this thesis. Their meanings (and typical units if appropriate) are indicated. Vector quantities are underlined, whereas tensors and matrices are in boldface text. If a symbol is used multiple times, its different meanings are separated by a semicolon.

Symbol	Description (Units)
δ	Electromagnetic skin depth (m)
δ_{Ei}	Static shift corrective factor for electric field E_i
Δ	Logarithmic resistivity difference (i.e. $\Delta = \log_{10} \rho_1 - \log_{10} \rho_2$), for resistivity model comparison.
ϵ	Electric permittivity (Fm^{-1})
κ	Thermal conductivity ($\text{Wm}^{-1}\text{K}^{-1}$); hydraulic permeability (D)
μ	Magnetic permeability (Hm^{-1})
μ_0	Magnetic permeability of free space ($4\pi \times 10^{-7} \text{ Hm}^{-1}$)
ρ	Resistivity (Ωm); density (kgm^{-3})
ρ_a	Apparent resistivity, i.e. equivalent half-space resistivity for specific signal frequency (Ωm)
ϕ	Magnetotelluric phase (°, or radians)
Φ	Porosity (fraction or %)
ω	Angular frequency (rad.s^{-1})
C	Specific heat capacity ($\text{Jkg}^{-1}\text{K}^{-1}$)
\underline{E}	Electric field (Vm^{-1})
E_x, E_y, E_z	Cartesian components of \underline{E} , (Vm^{-1})
e_i	Error associated with datum Z_i
f	Frequency (Hz)
\underline{H}	Magnetic field intensity (Am^{-1})
H_x, H_y, H_z	Cartesian components of \underline{H} , (Am^{-1})
\mathbf{J}	Jacobian matrix describing relationship between model and response

continued on next page

continued from previous page

Symbol	Description (units)
J_{ij}	Element of Jacobian describing partial derivative of response Z_i with respect to model element m_j
J_{eV}	Jacobian matrix, penalised by data error e_i and model element volume V_j
$\Sigma J_{eV}(m_j)$	Integrated sensitivity of model element m_j , found by summation of J_{eV} over m_j
ΣJ_{nS}	Reconstituted integrated sensitivity, computed from first n singular values
k	Complex wave number (m^{-1})
m	Cementation factor for Archie's Law
m_j	Element of model (typically resistivity Ωm)
Ma	Million years ago, i.e. 10^6 years
Q_{th}	Thermal energy in place (J)
s	MT model sensitivity, defined as summation over data of a model's Jacobian matrix
T	Period (s); temperature ($^\circ\text{C}$)
\mathbf{T}	Complex vertical magnetic transfer function
$\begin{pmatrix} T_{zx} \\ T_{zy} \end{pmatrix}$	Elements of vertical magnetic transfer function
USV^T	Constituent parts of a singular value decomposition of a matrix
V	Volume (m^3)
V_j	Volume of model element m_j (m^3)
\mathbf{Z}	Complex magnetotelluric impedance tensor (Ω)
$\begin{pmatrix} Z_{xx} & Z_{xy} \\ Z_{yx} & Z_{yy} \end{pmatrix}$	Elements of magnetotelluric impedance tensor (Ω)

LIST OF ACRONYMS AND ABBREVIATIONS

Following is a list of acronyms and abbreviations used in this thesis. Their definition and explanations are indicated, as well as references where required.

Acronym	Description (Units)
1D	1-Dimensional
2D	2-Dimensional
3D	3-Dimensional
AEM	Airborne electromagnetic method/data (as appropriate). Generally herein refers to frequency-domain AEM.
ALG	Paleogene Antrim Lava Group
AMT	Audiomagnetotelluric method/data (i.e. frequencies from 10000 Hz to 10 Hz)
B1	Ballinlea 1 borehole
BBMT	Broadband magnetotelluric method/data (i.e. frequencies from 100 Hz to 0.001 Hz)
BG	Permian Belfast Group of sandstones
EG	Permian Enler Group of sandstones
EM	Electromagnetic
FDEM	Frequency-domain electromagnetic method/data
IGR	Indicated Geothermal Resource (Lawless, 2010)
LLG	Jurassic Lower Lias Group mudstones
MCMC	Markov chain Monte Carlo modelling scheme
MMG	Triassic Mercia Mudstone Group
MT	Magnetotelluric method/data
NCG	Normalised cross-gradient product (Gallardo and Meju, 2003 ; Rosenkjaer et al., 2015 ; Schnaidt and Heinson, 2015)

continued on next page

continued from previous page

Acronym	Description (units)
NLCG	Non-linear conjugate gradient method for inversion (Rodi and Mackie, 2001; Baba et al., 2006)
nRMS	Normalised RMS
PM1	Port More 1 borehole
rjMCMC	Reversible jump MCMC modelling scheme
RMS	Root-mean-square, usually with respect to misfit
SSG	Triassic Sherwood Sandstone Group
SVD	Singular value decomposition of a matrix
TD	True depth of borehole (m)
TDEM	Time-domain electromagnetic method/data
TVF	Tow Valley Fault
UWLF	Cretaceous Ulster White Limestone Formation

PREFACE

This thesis is based upon results of the IREtherm Project, and includes two journal articles written in collaboration with *Volker Rath, Alan G. Jones, Mark R. Muller, Derek Reay at Dublin Institute for Advanced Studies*. The contents of these articles were unaltered to conform with Journal copyrights.

The results presented were generated using a range of geophysical modelling programs, including *strike* (McNeice and Jones, 2001), WinGLink, the OCCAM1D 1D MT inversion code Constable et al. (1987), the 2D MT inversion code of R. Mackie (Rodi and Mackie, 2001), the 3D MT inversion code ModEM (Egbert and Kelbert, 2012; Kelbert et al., 2014), and the 1D reversible-jump, Markov chain Monte Carlo modelling code of R. Brodie (Brodie and Jiang, 2018). Additionally, modelling of the airborne EM data used the Airbeo code of Raiche et al. (1985), as implemented by the Geological Survey of Ireland-funded project "Spatially constrained Bayesian inversion of frequency- and time-domain airborne electromagnetic data from the Tellus projects". Further minor tools and utilities were implemented in Matlab and shell-scripts.

Figures were produced predominantly with the Generic Mapping Tools (GMT; Wessel et al., 2013), with minor use of ArcGIS and QGIS. Note that where possible, every effort has been made to use colour maps that can be easily understood by readers with colour vision deficiency.

DECLARATION

I hereby certify that all of the work contained herein is my own work, and has not been used as the basis for the pursuit of a degree at NUI Galway nor any other institute. To the best of my knowledge, the material within this thesis has not been previously published or written by another person, except where due reference is made in the thesis itself.

Robert Delhaye
Dublin, Ireland,
May 2018

ACKNOWLEDGEMENTS

The research presented in this study is part of the IREtherm Project (www.iretherm.ie), funded by Science Foundation Ireland under grant number 10/IN.1/I3022. The author is grateful to the project for supporting him financially throughout, and for funding the travel and fieldwork required. Additionally, Providence Resources are also gratefully thanked for funding the pilot magnetotelluric study on Rathlin Island.

I wish to thank Prof. Alan Jones, Dr. Mark Muller, and Dr. Volker Rath for their guidance and suggestions throughout my doctoral studies. I greatly appreciate being a part of the IREtherm research project. I wish to also thank my supervisor at NUIG, Prof. Colin Brown, for taking on an extramural PhD and helping with the logistical side of research.

Thank you to the Geological Survey of Northern Ireland, particularly Derek Reay and Mohammed-nur Desissa Ture, for providing useful data and discussions about the research area. Thank you also to the Geological Survey of Ireland, and particularly Dr. James Hodgson, for both providing and supporting work with data from the Tellus Project and its follow-up projects. Both Providence Resources and Rathlin Energy are thanked for their cooperation and access to data.

It has been a continued source of joy to see my friends and colleagues within the IREtherm Project progress and succeed. Sarah, Thomas, and Colin deserve special mention for many cold muddy mornings retrieving field gear - far too many holes for one man to dig. I wish to also thank Jan, Joan, Sean, Mark, Chris, Miles, Jason and Paul for their assistance in the field. I am eternally grateful to the landowners who allowed us access to their fields for data acquisition. It has always meant a lot to me that we respect not just the land, but also the people that it belongs to. Thank you also to the staff and students at DIAS for the continued interest and support. It is comforting and exhilarating to be surrounded by others breaking new ground in their own fields. Special mentions should be made of poor Andrew, Duygu and Javier, each of whom have had their ears talked off far too many times by myself!

Thank you to Christina, Tom and Annie, without whom I'd have never learnt about magnetotellurics. Following from that, there is a clear string of mentors and teachers that have taught and inspired me about science. To S. Webb, L. Pellerin, P. Malin, D. Robertson, B. Brennan, J. Eccles, J. Cassidy, C. Locke, S. Bradley, G. Austin, B. Mason, J. Wright, G. Milne, I. Scoltock, S. Walker, G. Bardsley, and C. Percy, thank you all so much. It's humbling to realise how much time you invested teaching both myself and the rest of my classmates, occasionally against our immature wills. I am enormously indebted to all of you, and can scarcely think how to thank you.

Finally, every day would be a struggle were it not for the love, encouragement, and support of my family, chief amongst them my wife Charlotte. I know I've not been the easiest to cheer for, but here we are at the summit together.

“Whatungarongaro te tangata,
toitū te whenua.

As man disappears from sight,
the land remains.”

— Maori proverb —

This thesis is dedicated to Charlotte Delhayé,
for her perpetual love and support.

INTRODUCTION

The research presented in this thesis concerns the geophysical exploration and modelling of Rathlin Basin in Co. Antrim, Northern Ireland as a possible geothermal resource. The basin was previously remarked upon by e.g., Goodman et al. (2004); Reay and Kelly (2010); Pasquali et al. (2010); Busby (2014), due to its Permo-Triassic sediment fill, as the units are known to possess reasonable hydraulic properties, and are coincident with elevated thermal conditions within the Earth.

The *Geothermal Resource Map of Ireland* was compiled by Goodman et al. on behalf of the Sustainable Energy Authority of Ireland, in order to assess and categorise Ireland's low- to mid-enthalpy geothermal potential. Alongside the other results of the report, Goodman et al. assembled interpolated temperature and geothermal gradient maps from existing and new borehole measurements of 500 m true depth (TD hereafter) or greater. Two of the maps generated from the borehole dataset are presented in Figure 1.1 and Figure 1.2, showing the geothermal gradient at 5000 m depth and the interpolated temperature at 2500 m, respectively (note that due to the extrapolation from borehole bottom hole temperatures at shallow depths the geothermal gradient is modelled as approximately constant from 500 to 5000 m). Both maps show a distinct trend of elevating geothermal conditions to the north of Ireland, as well as several localised anomalies. In particular, the sedimentary basins in the north-east of Ireland show markedly higher anomalies in both maps due to temperature observations in a number of deep (i.e. TD over 1000 m) boreholes.

Since issue of the *Geothermal Resource Map of Ireland*, deep geophysical exploration of two of the north-eastern basins has taken place; namely, Loewer (2011) presented the results of gravity and magnetotelluric exploration of the Lough Neagh Basin, whereas Sihelník (2011) presented the results of magnetotelluric exploration of the Larne Basin. Both studies successfully recovered conductors associated with the target Permo-Triassic sediments, contemporaneous with the sediments found within the Rathlin Basin. As the sedimentary fills of the three basins are largely similar, with similar electrical and hydraulic properties, the magnetotelluric method was expected to perform well in resolving sediment distribution within the Rathlin Basin.

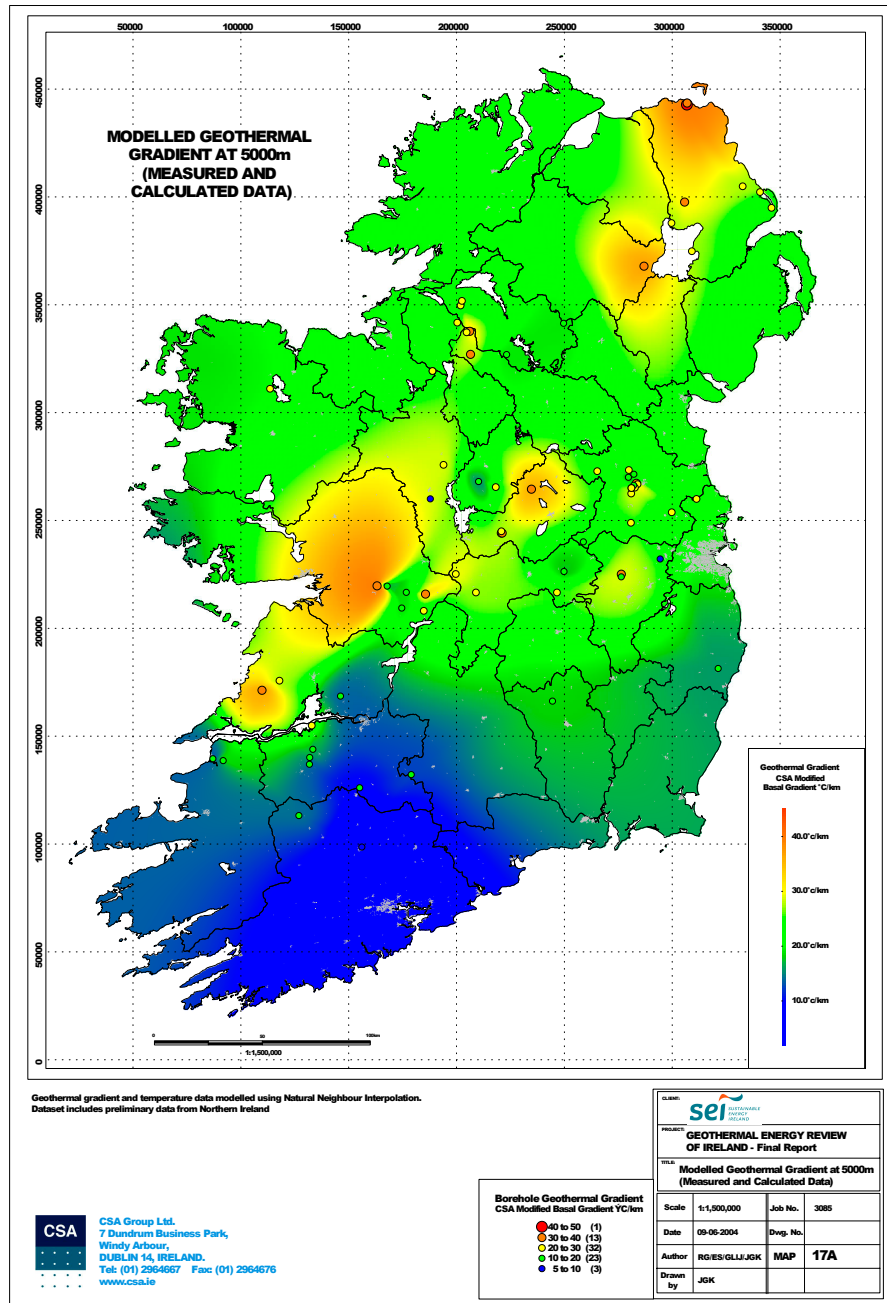


Figure 1.1.: Extrapolated geothermal gradient at 5000 m depth, from Goodman et al. (2004). Note that these geothermal gradient estimates are generally computed from bottom hole temperatures of boreholes of greater than 500 m depth, then interpolated laterally.

1.1 THE RATHLIN BASIN

Like the adjacent Foyle, Larne, and Lough Neagh Basins, the Rathlin Basin formed as a result of the reactivation of NE-SW trending faults during the Caledonian Orogeny (490–390 Ma). The locations of the Rathlin Basin and the adjacent Foyle, Larne, and Lough Neagh Basins are shown in

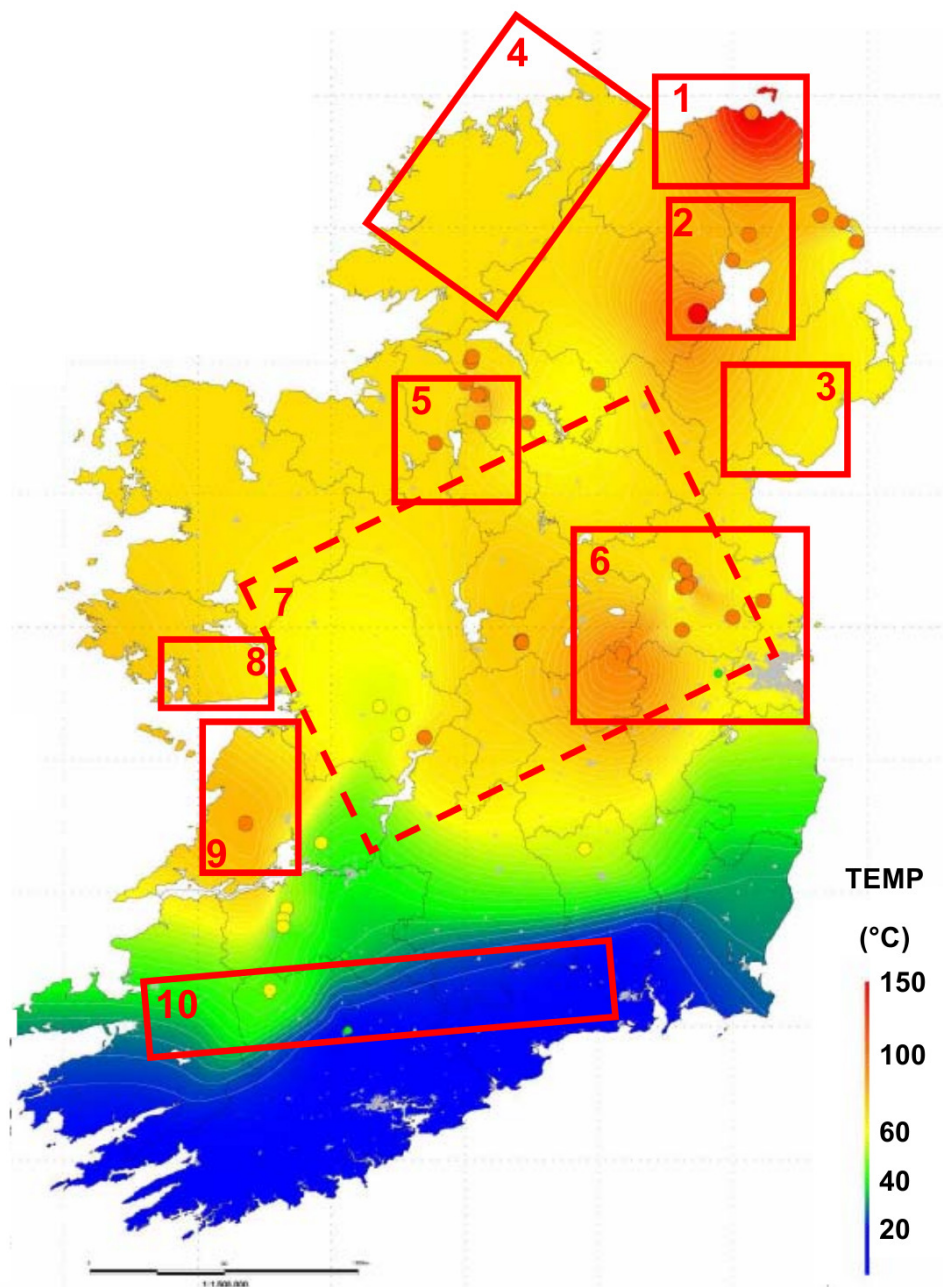


Figure 1.2.: Extrapolated temperature distribution at 2500 m depth, from Goodman et al. (2004). Note that these temperatures are extrapolated from boreholes of greater than 500 m depth to the requisite 2500 m, then interpolated laterally. The red, numbered polygons indicate areas of interest to the IREtherm Project; in particular, areas 1 and 2 are the Rathlin and Lough Neagh Basins.

Figure 1.3, overlain by estimated depths to base of Permo-Triassic sediments from gravity modelling (Naylor and Shannon, 2011). The south-east margin of the Rathlin Basin consists of the major Tow Valley Fault lineament, and the deepest extents of the basin are expected to lie adjacent to this boundary.

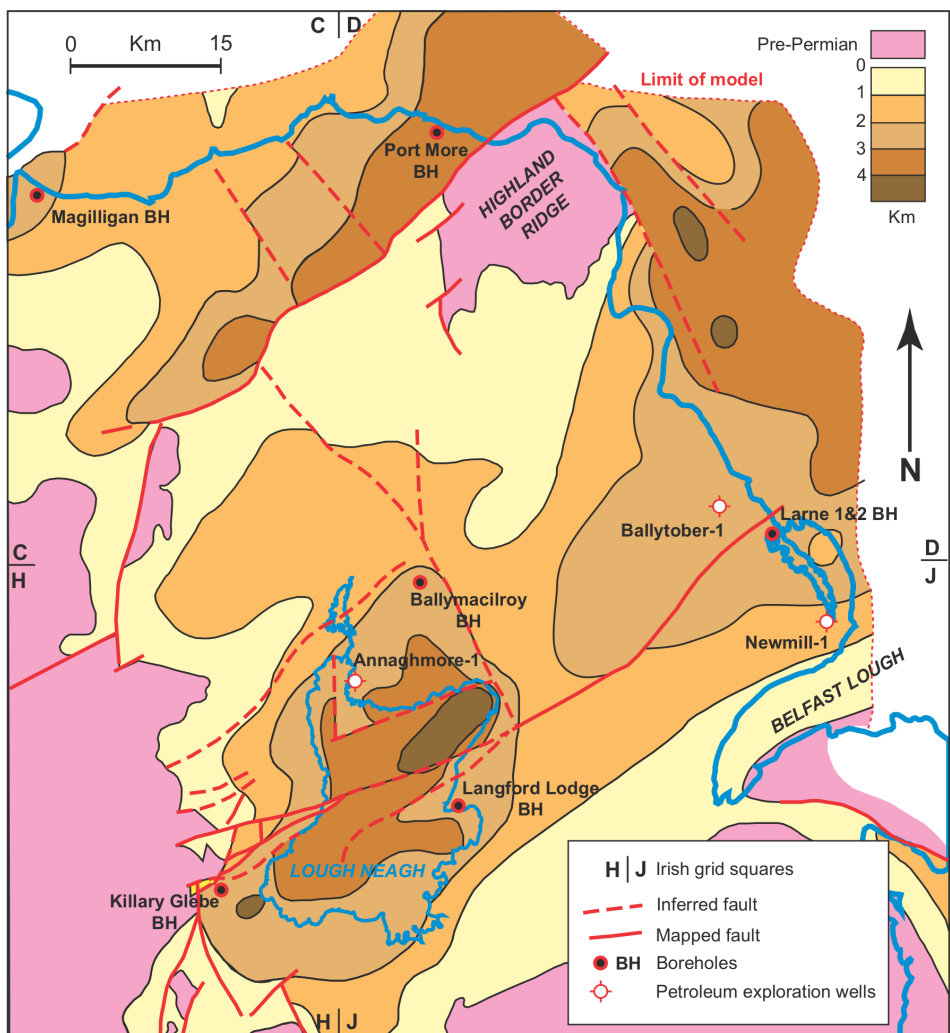
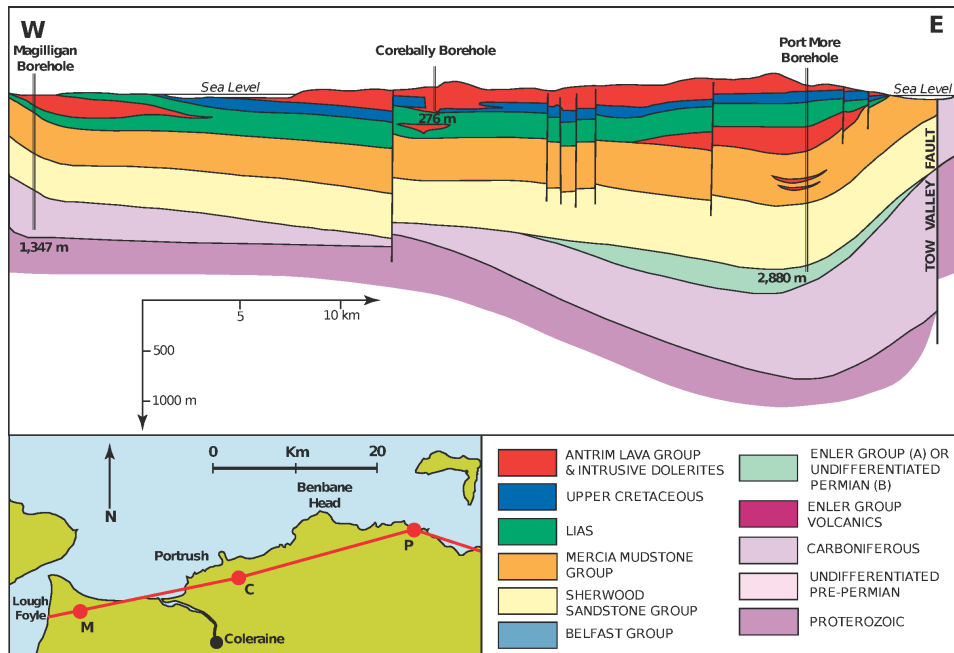


Figure 1.3.: Three-dimensional model of sedimentary basins in north-east Ireland, showing the relative locations of the Rathlin (north), Larne (east) and Lough Neagh (south) basins. Solid contours show a simplification of the modelled depth to Permo-Triassic sediment base from Naylor and Shannon (2011), originally from Mitchell (2004). Location of pertinent deep boreholes, particularly the Port More 1 borehole, also shown.

The Rathlin Basin lies within the Central Highlands Terrane that once formed a portion of Laurentia; this terrane generally comprises mid- to late-Neoproterozoic (1000-635 Ma) metasedimentary rocks classified as the Dalradian supergroup. Specifically, the country rock around and below the basin is assumed to consist of the late-Proterozoic (635-541 Ma) Argyll Group of psammites and semipelites. The basal sediments within the basin are poorly known Carboniferous sediments; only one borehole has so far reached the required depths (the Ballinlea 1 borehole), and information from this drilling is not fully available at this time. The Permian is represented by thick successions of early-Permian Enler (EG) and late-Permian Belfast (BG) sandstone groups; these are followed by the early-Triassic Sherwood Sandstone Group (SSG), late-Triassic Mercia Mudstone Group (MMG), and early-Jurassic (Lias) Waterloo Mudstone Group. The youngest sediments within the

basin belong to the late-Cretaceous Ulster White Limestone Formation. Finally, the basin is almost completely concealed by the Paleogene Antrim Lava Group of flood basalts. Additionally, Paleogene igneous activity is also represented by dolerite sills within the basin; these have been encountered in both deep boreholes. A diagrammatic cross-section of this stratigraphy along the axis of the Rathlin Basin is presented in [Figure 1.4](#); this figure is a simplification from [Naylor and Shannon \(2011\)](#) of the original based from gravity and magnetic modelling in [McCann \(1988\)](#).



[Figure 1.4.](#): Geological cross-section diagram of the Rathlin and Foyle Basins, based on gravity models. Taken from [Naylor and Shannon \(2011\)](#), itself a simplification of the interpreted density model presented in [McCann \(1988\)](#).

As the Rathlin Basin represents a significant volume of Permian and early-Triassic sediments that coincides with elevated geothermal conditions, it may represent an exploitable geothermal resource by hosting warm fluids within reservoir sediments. However, in order to host a sufficient volume of fluid for exploitation, the sediments also require significant porosity and hydraulic permeability. Laboratory measurements of porosity and permeability on Permian and Triassic sandstones from the Larne, Lough Neagh and Rathlin Basins are presented in [Figure 1.5](#), from [Mitchell \(2004\)](#). Measurements of the Permian and Triassic sediments from the Port More 1 borehole within the Rathlin Basin show porosities of 10–25%, and permeabilities generally from 10–1000 mD, suggesting that the sediments have moderate-to-good reservoir potential.

Previous geophysics gathered over the Rathlin Basin include gravity, magnetic, and seismic reflection; however, due to the overlying basalt the seismic reflection data is noted to be of generally poor quality and has not been considered further. Gravity data has been modelled on a regional level (discussed in [Carruthers et al., 1997](#); [Mitchell, 2004](#); [Naylor and Shannon, 2011](#), image from the last), shown in [Figure 1.3](#); from the gravity modelling a maximum depth of up to 4 km to

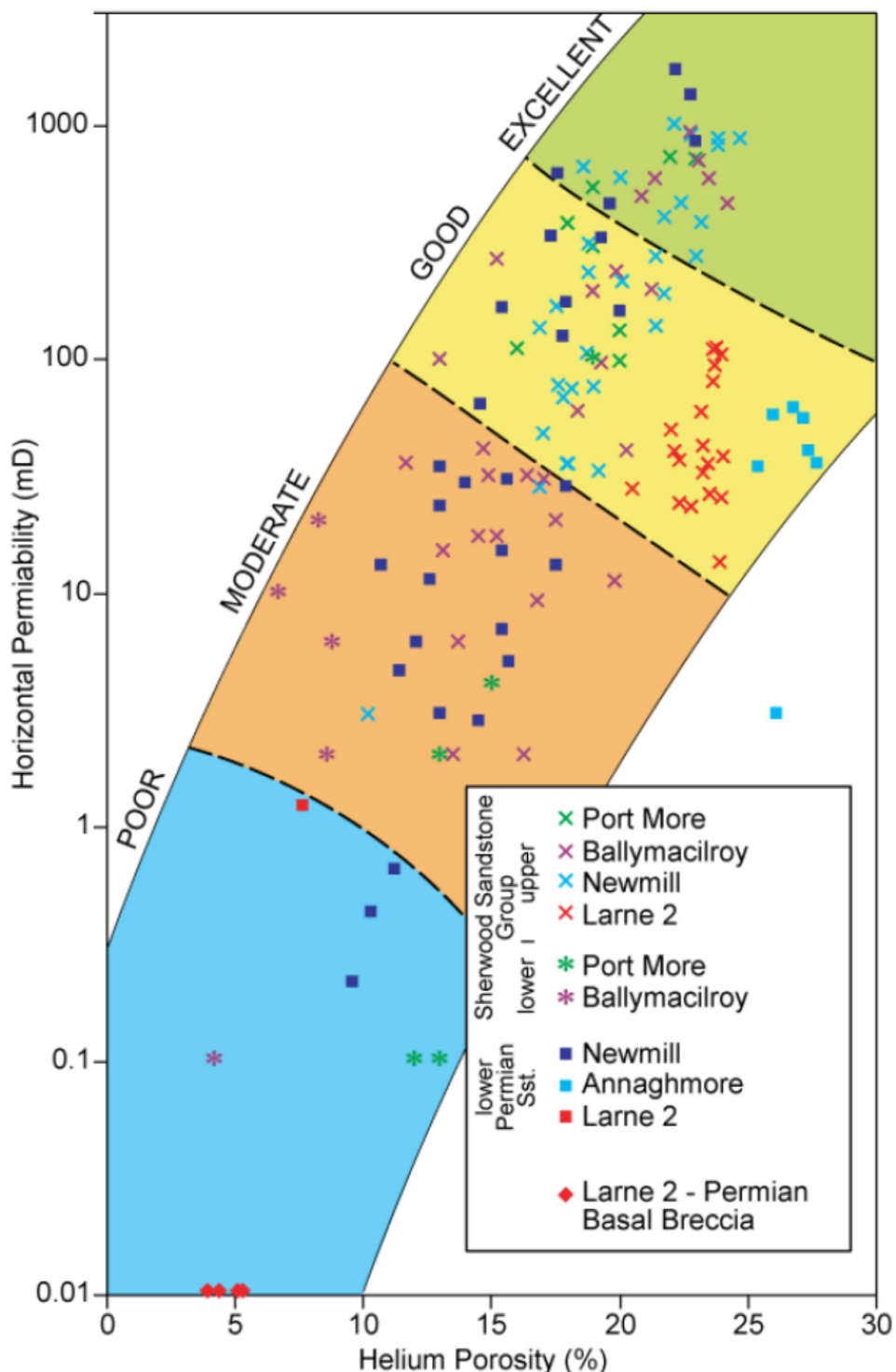


Figure 1.5.: Laboratory measurements of porosity and hydraulic permeabilities of Permian and Triassic sandstone core samples taken from the deep boreholes identified in Figure 1.3. In particular, green asterisks and crosses represent samples from the Port More 1 borehole, in the Rathlin Basin.

the base of the Permo-Triassic sediments is interpreted. The diagrammatic cross-section along the axis of the basin presented in Figure 1.4 was found by modelling both gravity and magnetic data

McCann (1988); although this profile does not intersect the deepest modelled portion of the basin, it shows the general stratigraphic expectation within the region. Further modelling of gravity and magnetic data has also been performed by Gibson (2004), focusing on characterisation of the TVF. Gibson determined that the TVF dips to the north-west at angles between 20 and 50° along its length, and agrees with the thick (2.4 km) estimate of Permo-Triassic sediment thicknesses.

Porous, predominantly water-saturated sediments are expected to have low resistivities due to the conductivity introduced by dissolved solids in the fluid; as the formations that surround the target Permo-Triassic sediments have significantly lower hydraulic properties, higher resistivities are expected. Hence, the target sediments should show strong resistivity contrasts with their surroundings. As part of the IREtherm Project, magnetotelluric exploration of the Rathlin Basin was proposed in order to model the extent and continuity of resistivity (as a proxy for hydraulic properties) of the target sediments in three dimensions. As an electromagnetic method of exploration, the magnetotelluric method should be relatively unobstructed by the overlying basalts, as more resistive materials are more easily penetrated by the MT signal fields.

1.2 MAGNETOTELLURICS AND THE STATIC SHIFT EFFECT

1.2.1 *Introduction to Magnetotellurics*

Magnetotellurics (MT) is an electromagnetic geophysical method that investigates the Earth's resistivity structure by modelling the attenuation of time-varying electromagnetic fields within the Earth (Chave and Jones, 2012; Simpson and Bahr, 2005). The electrical resistivity of the Earth has proven to be an insightful quantity to examine for both practical and insightful reasons; practical, as the natural variation of resistivity over orders of magnitude within the Earth leads to potentially large, easily detectable contrasts, and insightful, as resistivity is sensitive to a number of factors regarding the state of the material. Hence, investigation of subsurface resistivity can be useful for a wide range of geological targets, including mining, environmental, archaeological, and geothermal studies.

In stark contrast to the majority of electromagnetic methods, MT can be applied over an extreme range of depths. Indeed, surveys can be done at the scale of a metre or less for topsoil, up to a scale of hundreds of kilometres for studies of the lower crust and upper mantle. Such a range of application is possible due to the frequency-dependent behaviour of electromagnetic fields within the conductive (relative to vacuum or air) Earth. The electromagnetic fields can be described by Equation 1.1 (full derivation showed in, e.g., Simpson and Bahr, 2005).

$$\nabla^2 \mathbf{F} = -\omega^2 \mu \varepsilon \mathbf{F} - \frac{j\omega \mu}{\rho} \mathbf{F} \quad (1.1)$$

If the field permeates a vacuum, i.e. with infinite resistivity ρ , then the second term vanishes, leaving a wave equation with $c = 1/(\mu \varepsilon)$ that describes the propagation of the wave. However,

for finite resistivity and reduced frequencies the second term remains; in the limiting case of a frequency ω small enough that the first term is insignificant (i.e. $\omega^2 \ll \mu$), the expression can be considered as a Helmholtz equation describing a diffusive process, $\nabla^2 \mathbf{F} + k^2 \mathbf{F} = 0$, with a complex wavenumber k . The real portion of k is a spatial wavelength that describes the attenuation of the wave, equivalently, the inverse of $\text{Re}(k)$ describes a scale length over which the amplitude of \mathbf{F} decays by a factor of $1/e$ ([Equation 1.2](#)). This length is defined as the electromagnetic skin depth δ , and is commonly assumed to be the depth of penetration of an EM field. For MT surveys deeper than the immediate subsurface, and not in the vicinity of significant magnetic minerals, the magnetic permeability μ is taken as invariant, and the skin depth is a function of the resistivity of the Earth, and the frequency of the wave. It should be noted that although the skin depth is a linear measure, the wave is sensitive to a volume of induction.

$$\delta = \sqrt{\frac{2\rho}{\omega\mu}} \quad (1.2)$$

Natural electromagnetic fields for MT come from two sources depending on frequency; high frequency (i.e. > 1 Hz) fields originate from distance lightning strikes, whereas low frequency fields originate from ionospheric interactions with charged solar winds ([Garcia and Jones, 2002](#)). MT signals can also be generated using controlled sources; however, the frequencies of such methods are typically limited to 1 Hz and above due to lower frequencies requiring increased power to generate.

As time-varying electric fields induce magnetic fields (and vice versa), attenuation can be considered in terms of the ratio between correlated electric and magnetic field amplitude. The ratio of an electric field E_i and magnetic field H_j in frequency space is defined as the impedance Z_{ij} ([Equation 1.3](#)), measured in Ohm-metres (Ωm). However, as impedances have an exponential increase in magnitude with respect to frequency; impedances are often recast as apparent resistivities ρ_a and phases ϕ , with more intuitive magnitudes. The apparent resistivity as a function of frequency is the resistivity (Ohm-meters, Ωm) of a half-space (i.e. homogeneous) for a wave of that specific frequency, whereas the phase lead is the angular lead of the electric field over the magnetic field (in radians or degrees). For a uniform half-space, the phase is constant at $\phi = \pi/4$. The conversions from impedances to these quantities are presented in [Equation 1.4](#) and [Equation 1.5](#)

$$Z_{ij}(\omega) = \frac{E_i(\omega)}{H_j(\omega)} \quad (1.3)$$

$$\rho_{a,ij} = \frac{1}{\omega\mu}|Z_{ij}|^2 \quad (1.4)$$

$$\phi = \arg(Z_{ij}) = \tan^{-1} \left(\frac{\text{Im}(Z_{ij})}{\text{Re}(Z_{ij})} \right) \quad (1.5)$$

By considering both orthogonal and parallel pairs of fields with respect to the data acquisition coordinates, an impedance tensor \mathbf{Z} with four components $Z_{xx}, Z_{xy}, Z_{yx}, Z_{yy}$ can be defined ([Equation 1.6](#)).

$$\mathbf{Z} = \begin{pmatrix} Z_{xx} & Z_{xy} \\ Z_{yx} & Z_{yy} \end{pmatrix} \quad (1.6)$$

The relative magnitudes of the impedance tensor components at a specific frequency are dependent on the dimensionality of the resistivity structure within the inductive volume, assuming that the impedances are defined on the same coordinate system as the resistivity. One-dimensional resistivity structures varies solely in one direction (typically depth), two-dimensional resistivity structure varies in one lateral direction and with depth, and three-dimensional resistivity structure varies in both horizontal directions as well as depth. These forms are shown in [Equation 1.7](#).

$$\mathbf{Z}_{1D} = \begin{pmatrix} 0 & Z_{xy} \\ -Z_{yx} & 0 \end{pmatrix}; \mathbf{Z}_{2D} = \begin{pmatrix} 0 & Z_{xy} \\ Z_{yx} & 0 \end{pmatrix}; \mathbf{Z}_{3D} = \begin{pmatrix} Z_{xx} & Z_{xy} \\ Z_{yx} & Z_{yy} \end{pmatrix} \quad (1.7)$$

1.2.2 MT Data Acquisition

The impedances for a given EM wave cannot be directly measured; instruments at the surface of the Earth instead measure time-varying voltages proportional to the electric and magnetic fields. Typically five fields are measured; two horizontal electric fields, two horizontal and one vertical magnetic field. Electric fields are estimated from voltage differences obtained between two non-polarising electrodes over a distance using the straightforward $V = Ed$, whereas magnetic fields are estimated from voltages induced in sealed magnetometer coils by Maxwell's Equations. Having measured electric and magnetic fields as voltages over time, discrete time Fourier transforms are applied to convert to the frequency domain. Robust cross-correlation of fields is performed in order to determine the respective electric and magnetic fields that comprise a single wave, and impedances then computed as above for the various field combinations.

The MT data used in this thesis were collected as part of the IREtherm field acquisition program, using Phoenix Geophysics MT equipment belonging to DIAS. MTU-5A magnetotelluric systems were used to log both audiomagnetotelluric (AMT, 10,000 to 10 Hz) and broadband MT (BBMT, 300 to 0.001 Hz) data. The E_x and E_y electric fields were sampled by Pb-PbCl PE4 non-polarising electrodes with 80 m dipole lengths arranged in a cross configuration, whereas the H_x , H_y and H_z magnetic fields were sampled by either MTC-50 (BBMT) or AMTC-30 (AMT) magnetometers. In some locations where a vertical magnetometer was unable to be installed due to local ground conditions, an AL-100 airloop magnetometer was instead used for both AMT and BBMT. AMT data were recorded overnight at each location, giving time series of at least 12

hours. BBMT data were recorded over three nights for data collected during the 2012 Rathlin Basin survey.

Robust estimates of the frequency domain MT transfer functions were determined from the MT time series using commercial processing software from Phoenix Geophysics that implements the technique described in Jones and Jödicke (1984) and Jones et al. (1989). This approach is based on cascade decimation (Wight and Bostick, 1980), and uses a Least Trimmed Squares algorithm (Rousseeuw, 1984; Rousseeuw and Leroy, 2003) to achieve robustness of the estimate. Whilst a dedicated distant remote reference site was not used, the principle of remote referencing, as described in Gamble (1979) and Gamble et al. (1979), was applied by using the horizontal magnetic field components of each simultaneously acquired site as reference fields, and selecting the best available site as reference (typically five sites were recorded simultaneously). Finally, the AMT and BBMT data at each site were merged into a single response, spanning from 10,000 to 0.001 Hz at most sites.

1.2.3 *Static-Shift Distortion of MT Data*

An issue of some concern to the magnetotelluric research presented here is static-shift-type galvanic distortion, discussed in Chapter [Chapter 2](#). This form of distortion is so named for its effect of displacing the magnitudes of the magnetotelluric impedance functions vertically, independent of frequency. Such distortion is commonly assumed to arise from biased voltage measurements that are then used for electric field estimation. During the computation of the electric field from the voltage measurements, a constant resistivity is assumed for the volume of Earth between the electrodes; however, this assumption may not always be valid. If significant near-surface resistivity anomalies are present in contrast to the bulk resistivity, then the constant resistivity assumed will be incorrect, adding bias to the electric field estimate.

The ramifications of static-shift distortion for modelling of MT data are well-known in simple 1D frameworks (Árnason, 2015), wherein an upwards static-shift bias leads to an increase in the product of resistivity and thickness (i.e. increases in thicknesses and/or resistivity) and vice versa. For modelling in 2- or 3D, the effects are more pronounced, as variations in static-shift at adjacent sites can require spurious resistivity structure between locations in order to reproduce the observed effects.

Several approaches have been proposed over time in order to account for static-shift distortion of observed MT data; brief summaries of these approaches are listed below.

- [Torres-Verdin and Bostick \(1992\)](#) proposes a method called Electromagnetic Array Profiling (EMAP), wherein electric fields are measured over an array of dipoles placed end to end along a profile. As the static-shift effects are assumed to be highly localised (due to small near-surface bodies), using electric field estimates from increasing dipole lengths effectively functions as a low-pass spatial filter on the electric field. The low-pass spatial filter suppresses the influence of the assumed source of static-shift distortion, as shown in the article. However,

the EMAP method is logically complex, requiring the simultaneous observation of electric fields across significant distance. Such large-scale MT site installations are impractical within the IREtherm MT exploration due to the equipment demand, terrain, and permission issues.

- Berdichevsky (1989) extends upon the EMAP method by proposing the spatial filtering of MT data to determine a "regional" near-surface data distribution, amongst other modelling approaches. The regional spatial filtering approach assumes that the near-surface resistivity distribution is sufficiently homogeneous to allow recovery of appropriate values; as the MT data considered in this thesis were generally collected over flood basalts created by discrete flows, this assumption may not be valid and as such has not been attempted.
- Jones (1988) proposes a method of correcting for static-shift effects over sedimentary basins with sub-horizontal layers, similar to the expected structure of the Rathlin Basin. The proposed method requires a parametric layer at depth beneath each MT site, the resistivity of which can be described as a function of distance in some statistically robust form. With the resistivity of this parametric layer defined, the layer's conductance (i.e. thickness/resistivity) can be predicted for each site's data, and the data shifted to match. However, such an approach requires good knowledge of the resistivity variation with distance (preferably from multiple boreholes), and additionally results in some smoothing of the final model resistivity estimates for the parametric layer. Currently resistivity information exist only for one borehole within the Rathlin Basin, and as one aim of MT exploration of this area is to examine the resistivity variation of the sediments at depth, this approach may obscure the desired result.
- Various authors, including Sasaki and Meju (2006); Miensopust (2010); Avdeeva et al. (2015); De Groot-Hedlin (1991); DeGroot-Hedlin (1995), have adapted MT inversion algorithms to solve for distortion parameters in addition to the resistivity structure.
- Various authors, including Sternberg et al. (1988); Pellerin and Hohmann (1990); Árnason (2015); Spitzer (2001), propose the use of complementary geophysical methods (DC resistivity, time domain EM) to determine an appropriate near-surface resistivity model. The near-surface model can then be forward modelled to obtain an MT response that is nominally unaffected by static-shift, and corrections for static-shifts in the observed MT data made by shifting the data to match the synthetic response. This approach is generally performed in a 1D framework, i.e. the near-surface resistivity distribution is assumed to be laterally homogeneous. Additionally, both the MT data and complementary geophysical data must have some common illuminated volume to avoid extrapolation.

All but the last category of approaches to static-shift correction are only dependent on the MT data. As a result, although the corrected MT data are consistent within themselves, we are unable to determine whether any remnant of the static-shift remains when considering real data. However, if static-shifts are corrected by forward MT modelling based on complementary geophysical data, then the complementary data also act as a measure of model verification (alternately, constraint).

It should be stressed that since the definition of static-shift-type distortion in the mid-1970s (Berdichevsky and Dmitriev, 1976), further forms of distortion have been realised; however, these are not considered extensively within this thesis. As a standard part of MT data analysis, all data were subjected to multi-site, multi-frequency decomposition in order to gauge the dimensionality and degree of distortion present. For the majority of MT datasets in both surveys, the highest few decades of MT data (10,000–100 Hz) are 2D at most, and bear only small amounts of distortion.

1.3 RESEARCH QUESTIONS

The research presented in this thesis concerns the magnetotelluric exploration of the Rathlin Basin as part of the IREtherm Project. In order to clarify the results of the research, the goals can be formalised into a set of research questions, namely, (1) how can regional airborne EM data from the Tellus Project be used in static-shift correction of MT data, (2) how much can be inferred about the geothermal prospect of Rathlin Basin from an MT model, and (3) what additional value can be added to 3D model interpretation by also considering the sensitivity of model responses, as determined by the Jacobian matrix of the model. These three questions lead themselves to being answered by a chapter each within the thesis.

1.4 THESIS STRUCTURE

This thesis is presented in the form of three articles, each intended to be coherent when considered independent of the others. Note that as a result there are unavoidable redundancies in the introductory sections of each. In particular, the geological setting and explanation of magnetotelluric theory occur in each article; although redundant in the context of a thesis, they are present in order to retain the independence of each article.

1.4.1 Article 1 ([Chapter 2](#)): *Correcting for Static Shift of Magnetotelluric Data with Airborne Electromagnetic Measurements: A Case Study from Rathlin Basin, Northern Ireland*

Contribution: Lead Author - major role.

Delhaye, R., Rath, V., Jones, A.G., Muller, M.R., Reay, D.

Published in Solid Earth, 22 May 2017, DOI:10.5194/se-8-637-2017.

The modelling of time domain electromagnetic data acquired at MT sites has become accepted as an appropriate method of compensating for static-shift type distortions of magnetotelluric data (Árnason, 2015; Miensopust et al., 2014). The TDEM approach assumes that the near-surface resistivity structure can be reproduced by one dimensional modelling of the TDEM data; the 1D model allows computation of a simple MT response that observed MT data can be shifted to coincide with. The article presented here proposes that the TDEM approach be modified by

modelling regionally-acquired airborne frequency domain EM (AEM) in place of co-located TDEM data.

The article explains the process of correcting static-shift by the FDEM approach, and examines the effect of the process on the onshore Rathlin Basin magnetotelluric data. AEM data are available in the research area, and indeed throughout Northern Ireland, as part of the Tellus Project. Due to the acquisition pattern of the AEM, i.e. sampled at high density along spaced flightlines, inverse 1D modelling of AEM was performed to obtain single-layer resistivity estimates for each sampling point. The single-layer estimates were combined to form a quasi-3D resistivity model that allows forward computation of the MT responses in 3D for both the Z_{xy} and Z_{yx} MT modes. Taking the ratio of the magnitudes of the forward responses and observed data at high frequencies (i.e. above 1000 Hz) gives a pair of correction factors $\delta_{Ex,Ey}$ that compensate for the observed shift in magnitude. Furthermore, if static-shift distortion is assumed to occur solely from the electric field estimates, then the two corrections $\delta_{Ex,Ey}$ can also be applied to the diagonal impedance elements.

In addition to examining the approach of static-shift correction with respect to data, complementary 3D inversions were performed on both the uncorrected and corrected MT data. The two models are compared to one another and to the lithology observed in the deep Port More 1 bore-hole within the basin. Upon inspection the static-shift corrected model shows better recovery of the layered lithology than the uncorrected. Additionally, significant variation in resistivity values and structural extents (predominantly vertical) are observed between the models. As a result of comparing these models, static-shift correction clearly has benefits for 3D inversion, even as an incomplete method of handling distortion. Subsequent projects affiliated with the original Tellus Project have also extended AEM coverage across a significant portion of Ireland, enabled further application of this method if desired by others.

The author was responsible for: the acquisition and analysis of the MT data, development and implementation of the static-shift correction methodology, 3D inversion of both MT data sets, and analysis of results. All tables, figures, and the majority of writing also done by the author.

1.4.2 Article 2 ([Chapter 3](#)): Quantitative Interpretation of a Magnetotelluric Model of the Rathlin Basin, Northern Ireland

Contribution: Lead Author - major role.

Delhaye, R., Rath, V., Jones, A.G., Muller, M.R., Reay, D.

Published in Geothermics, 26 October 2018, DOI:10.1016/j.geothermics.2018.09.012.

This article continues examination of the mainland Rathlin Basin considered in the first article by presenting the results and interpretation of 1D modelling of the static-shift corrected MT data in the context of two deep boreholes. In order to comply with the constraining information available from the boreholes (i.e. observed lithology and normal resistivity log from PM1, equilibrated temperature from B1), interpreted boundaries were defined based upon the vertical derivative of

resistivity within the model. This was first done below MT sites adjacent to the boreholes to verify the approach, then at all sites above the concealed sediments. The recovered models have been interpolated to obtain sub-horizontal layer boundaries consistent with the expected structure.

The interpretations made of the 1D models are used for estimation of the Indicated Geothermal Resource (IGR) represented by the sediments, using the approach described in the Australian Geothermal Lexicon ([Lawless, 2010](#)). This approach estimates the amount of heat energy in place as a function of the final reservoir temperature, predicated upon estimates of the thermal properties of both rock and pore fluid, bulk porosity, and initial reservoir temperature. Initial temperatures for the model segments were computed using the gradient of equilibrated temperature measurements in the Sherwood Sandstone and Belfast sandstone groups from the Ballinlea 1 borehole, in conjunction with estimated porosities from the Port More 1. The geothermal resource is presented as a function of final temperature from 85 to 35 °C, with a further value at 25 °C to allow comparison to the estimated IGR of the adjacent Larne Basin presented in [Pasquali et al. \(2010\)](#). The geothermal model shows that a final reservoir temperature of 40 °C is required in order to fully exploit the reservoir sediments; however, it should be noted that the geothermal model does not account for the clear heterogeneity of porosity and permeability within the basin.

The author was responsible for: the acquisition, analysis, and 3D inversion of the MT data, interpretation of resistivity model to obtain sedimentary structure, and geothermal modelling based upon the model. All tables, figures, and the majority of writing also done by the author.

1.4.3 Article 3 ([Chapter 4](#)): Establishing the Sensitivity of a 3D Magnetotelluric Model of Rathlin Basin, Northern Ireland

Contribution: Lead Author - major role.

Delhaye, R., Rath, V., Jones, A.G., Muller, M.R., Reay, D.

In preparation, journal still to be chosen.

This article discusses further the assessment of the 3D resistivity model resulting from magnetotelluric exploration of the onshore Rathlin Basin. By examining the sensitivity of the model as a proxy for the relevance of model portions to the observed data, some insight into the mechanism of model parameter control is gained, i.e., whether the governing term in the inversion algorithm is the data residual, or the regularisation parameter.

In order to verify the recovered resistivity structure, we considered the distribution of appropriately-scaled, Jacobian-derived sensitivities of the model with respect to model responses. Examining both the resistivity and sensitivity distributions of our model shows that the near-surface basalts and Lower Lias Sandstones are well-recovered. However, at depths beyond 1,000 m the sensitivity distribution becomes laterally inhomogeneous, with variation that contrasts with that observed in the resistivity distribution and suggests resistivity structure that is more determined by regularisation than by data residual. By considering both resistivity and distribution, an interpretation can be reached that correctly takes into account the smoothing effect of the inversion.

The author was responsible for: the acquisition, analysis, 3D inversion of the MT data, interpretation of resistivity model, analysis of the model sensitivities. All tables, figures, and the majority of writing also done by the author.

2

CORRECTING FOR STATIC SHIFT OF MAGNETOTELLURIC DATA WITH AIRBORNE ELECTROMAGNETIC MEASUREMENTS: A CASE STUDY FROM RATHLIN BASIN, NORTHERN IRELAND

2.1 ABSTRACT

Galvanic distortions of magnetotelluric (MT) data, such as the static-shift effect, are a known problem that can lead to incorrect estimation of resistivities and erroneous modelling of geometries with resulting misinterpretation of subsurface electrical resistivity structure. A wide variety of approaches have been proposed to account for these galvanic distortions, some depending on the target area, with varying degrees of success. The natural laboratory for our study is a hydraulically permeable volume of conductive sediment at depth, the internal resistivity structure of which can be used to estimate reservoir viability for geothermal purposes; however, static-shift correction is required in order to ensure robust and precise modelling accuracy.

We present here a possible method to employ frequency-domain electromagnetic data in order to correct static-shift effects, illustrated by a case study from Northern Ireland. In our survey area, airborne frequency domain electromagnetic (FDEM) data are regionally available with high spatial density. The spatial distributions of the derived static-shift corrections are analysed and applied to the uncorrected MT data prior to inversion. Two comparative inversion models are derived, one with and one without static-shift corrections, with instructive results. As expected from the one-dimensional analogy of static-shift correction, at shallow model depths, where the structure is controlled by a single local MT site, the correction of static-shift effects leads to vertical scaling of resistivity-thickness products in the model, with the corrected model showing improved correlation to existing borehole wireline resistivity data. In turn, as these vertical scalings are effectively independent of adjacent sites, lateral resistivity distributions are also affected, with up to half a decade of resistivity variation between the models estimated at depths down to 2000 m. Simple estimation of differences in bulk porosity, derived using Archie's Law, between the two

This chapter has been published as: R. Delhayé, V. Rath, A. G. Jones, M. R. Muller, and D. Reay. Correcting for static shift of magnetotelluric data with airborne electromagnetic measurements: a case study from Rathlin Basin, Northern Ireland. *Solid Earth*, 8(3):637–660, 2017. doi: 10.5194/se-8-637-2017.

models reinforces our conclusion that the suborder of magnitude resistivity contrasts induced by the correction of static shifts correspond to similar contrasts in estimated porosities, and hence, for purposes of reservoir investigation or similar cases requiring accurate absolute resistivity estimates, galvanic distortion correction, especially static-shift correction, is essential.

2.2 INTRODUCTION

The electrical resistivity of a volume of rock is highly sensitive to the presence of laterally and vertically varying amounts of electrically conductive fluids connected via pore spaces or fluid conduits. Due to these potentially strong resistivity contrasts between competent host rock and fluid penetrated rock, electromagnetic (EM) methods, and in particular magnetotellurics (MT), have been used with considerable success to image conductive volumes at depth (Chave and Jones, 2012; Simpson and Bahr, 2005).

As with all EM methods, MT data are highly sensitive to rock fluid content and distribution (i.e. porosity and hydraulic permeability) and can be related to other properties relevant to fluid movement. This has made the method particularly interesting for the exploration of geothermal resources. Indeed, geothermal research was the first commercial application of MT in the late 1950s, though the interpretation of the corresponding conductive structures is not always straightforward (Muñoz, 2014).

The MT data set studied here was acquired in the context of a multidisciplinary geothermal research program (IRETHERM), the overarching aim of which is to identify and evaluate low-enthalpy geothermal resources within Ireland. One such resource (Goodman et al., 2004) is the thick, porous and permeable succession of Permian and Triassic sandstones found within several concealed sedimentary basins in Northern Ireland, with the Rathlin Basin in particular having significantly elevated estimated geothermal gradients in comparison to the remainder of Ireland (Reay and Kelly, 2010).

The island of Ireland was formed during the Caledonian orogeny by the complex accretion of several continental and island arc fragments during the closure of the Iapetus Ocean between the Early Ordovician (485 Ma) and late Silurian (423 Ma), resulting in seven identifiable terranes that comprise the present-day basement across both Ireland and Great Britain (Mitchell, 2004; Hepworth and Sanders, 2009). Our survey area (Figure 2.1) lies within the Central Highlands Terrane of Laurentia, the basement of which comprises mainly mid- to late-Neoproterozoic (1000-635 Ma) metasedimentary rocks classified as the Dalradian supergroup, a metasedimentary and igneous rock succession that was deposited on the eastern margin of Laurentia between late Neoproterozoic (\approx 800 Ma) and early Cambrian (\approx 510 Ma) times. Specifically, the basement across the test area is assumed to consist of the latest-Proterozoic (Ediacaran, 635-541 Ma) Argyll Group of psammites and semipelites.

Regional shear and stress during the subsequent late-Paleozoic (350-250 Ma) Variscan orogeny reactivated the Caledonian (490-390 Ma) Tow Valley Fault (TVF), and the ensuing normal and

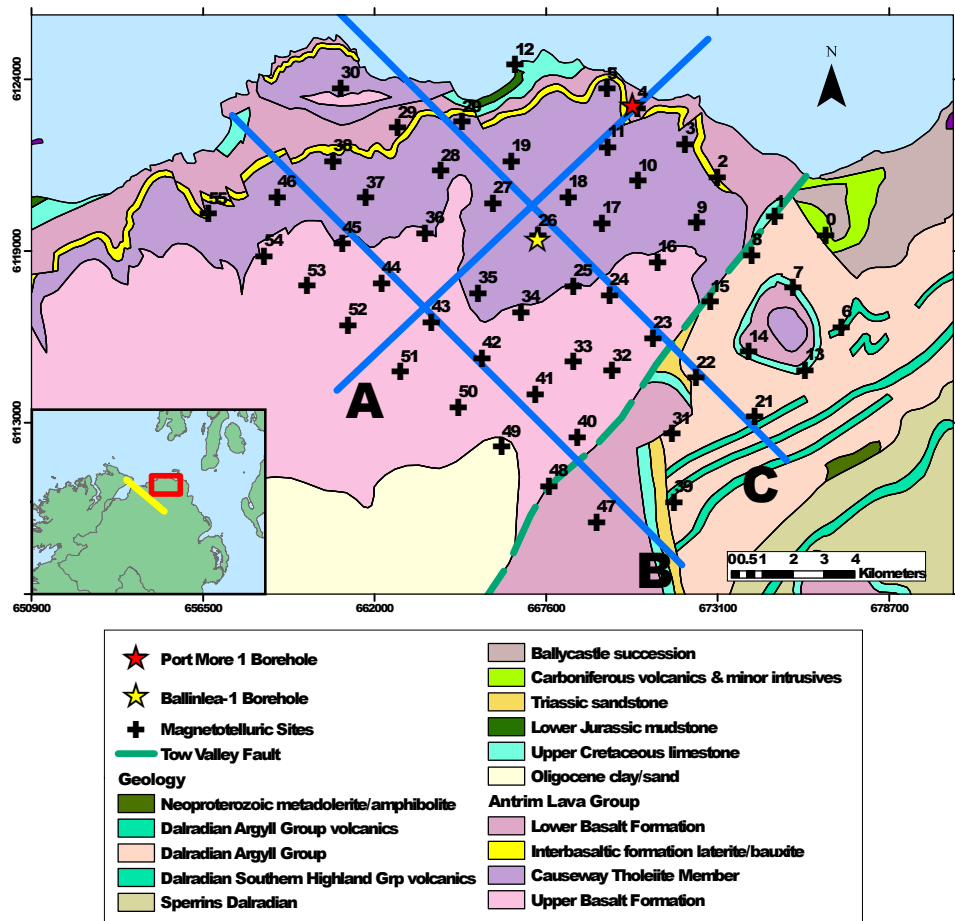


Figure 2.1.: Geological map of Rathlin Basin area, overlain with magnetotelluric acquisition sites numbered and denoted by black crosses. Note the large areal extent of the Antrim Lava Group basalts, with minimal surface expression of the underlying sedimentary basin. Profiles A, B and C denote the locations corresponding to Figure 2.12 – Figure 2.14. Inset map shows the northern half of Ireland, with the location of the magnetotelluric survey area shown by the red rectangle. The yellow line indicates the location of the density profile shown in Figure 2.3.

dextral strike-slip faulting resulted in the formation of a rift basin later filled by a succession of sediments to form the Rathlin Basin. Although drilling in the adjacent Magilligan Basin encountered Carboniferous formations at 1347 m TD, the most basal formations confirmed within the Rathlin Basin are the Permian Enler Group (EG) sandstones and Early-Triassic Sherwood Sandstone Group sandstones (SSG). Both formations are hydrocarbon reservoirs in the Irish Sea to the east (Naylor and Shannon, 2011). The Sherwood Sandstone Group is overlain by the Late-Triassic Mercia Mudstone Group (MMG), which is itself generally overlain by late Jurassic Lower Lias Group (LLG) mudstones. However, in many places significant dolerite and basalt sills (up to approx. 100 m in combined thickness) have been encountered, with poorly known spatial extent. The final and youngest successions in the basin are chalks of the Cretaceous Ulster White Limestone Formation (UWLF), with the Antrim Lava Group (ALG) concealing the basin entirely.

To date, two deep boreholes have been completed onshore in the Rathlin Basin, namely the Port More 1 (PM1) and Ballinlea 1 (B1) boreholes, drilled in 1967 and 2008 respectively; however, only data from the former are available as information from the latter is not yet in the public domain. The PM1 borehole was drilled to a total depth of 1897 m and terminated in the EG sandstones, with wireline log data acquired in two separate sections due to technical difficulties ([Wilson and Manning, 1978](#)). The upper portion of normal resistivity data covers the uppermost 250 m of the hole, including the Antrim Lava Group, Ulster White Limestone Formation and the upper portion of the Lower Lias Group. These data provide relatively consistent resistivity estimates of $\approx 80 \Omega\text{m}$ and $\approx 5 \Omega\text{m}$ for the UWLF and LLG sedimentary formations respectively, whereas estimates for the ALG vary from $\approx 5\text{--}80 \Omega\text{m}$ as it comprises a succession of tuffs and basalts. The lower portion of resistivity data spans the depth interval of $\approx 1050\text{--}1450$ m, covering the boundary between the MMG and SSG at 1320 m, and provides resistivity estimates of $\approx 4 \Omega\text{m}$ and $\approx 6 \Omega\text{m}$ for the respective groups. The estimates within the SSG also show a higher variance, which may be due to the presence of conglomerates and breccias in the upper portion of the group. The stratigraphic column encountered in the PM1 borehole is displayed in [Figure 2.2](#), alongside a plot of the borehole resistivity data.

Modelling of regional gravity and magnetic data has been undertaken, with results presented in [Mitchell \(2004\)](#) and [Gibson \(2004\)](#). The density model of [Mitchell \(2004\)](#) ([Figure 2.3](#)) shows a relatively homogeneous structure along the basin, particularly of the Permo-Triassic section, with a maximum depth to Dalradian basement of approximately 3 km modelled for the Rathlin Basin (located at 33 km distance along profile). This modelling adopts a density of 2.35 Mg/m^3 for the assumed basal Carboniferous rocks; this value comes from borehole samples in the adjacent Foyle Basin, and [Mitchell](#) advises that this value may be insufficiently dense to represent Rathlin Basin conditions. If Carboniferous sediments in the Rathlin Basin are of a higher density, a greater thickness of overlying lighter sediments (i.e. the target Permian and Triassic sandstones) would be required to be consistent with the observed gravity anomaly. Magnetic and gravity modelling by [Gibson \(2004\)](#) suggests that the Tow Valley Fault zone consists of a series of major fault segments with varying dip of $20\text{--}50^\circ$ to the north-west.

Core samples of the EG and SSG sandstones successions gathered from the Port More 1 borehole show promising reservoir properties, with fractional porosities and hydraulic permeabilities ranging from 0.10 to 0.22 and 1 mD–1 000 mD respectively ([Mitchell, 2004](#)). Equilibrated temperatures taken from both the PM1 and B1 boreholes have previously been used to estimate geothermal gradients. A temperature of 35.4°C was observed at 582 m depth in the PM1 borehole, whereas a temperature of 99°C was observed at 2650 m in B1 ([Reay and Kelly, 2010](#)). Assuming a surface temperature of 10°C , simple linear estimation gives calculated geothermal gradients of 43.6 (PM1) and 33.6 K/km (B1), both of which are elevated above the typical estimates of $\approx 20\text{--}30 \text{ K/km}$ measured elsewhere across Ireland ([Goodman et al., 2004](#)). In conjunction with the promising reservoir properties and basin depth expected from gravity modelling, it has been proposed previously ([Goodman et al., 2004; Reay and Kelly, 2010; Pasquali et al., 2010](#)) that the

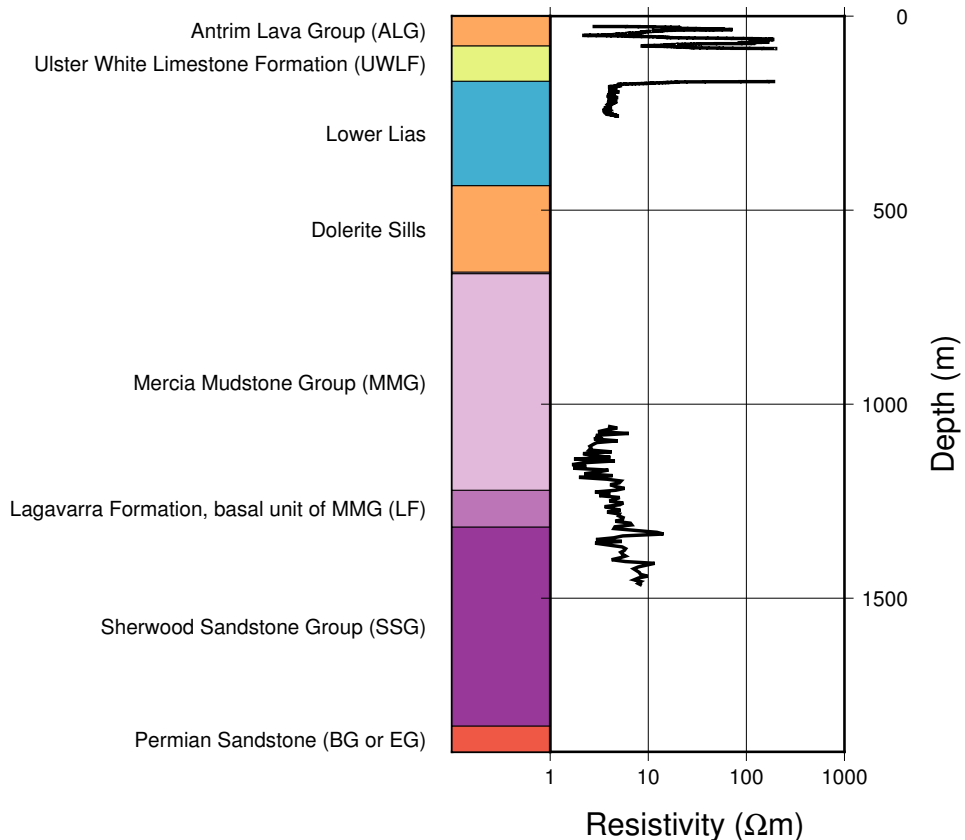


Figure 2.2.: Stratigraphy encountered in the Port More 1 borehole (left), and measured normal resistivity data (right). Stratigraphy encountered includes Paleogene Antrim Lava Group of basalts and tuffs, Cretaceous Ulster White Limestone Formation, Jurassic Lower Lias sandstones, Late-to-Mid-Triassic Mercia Mudstone Group, Early-Triassic Sherwood Sandstone Group, and late-Permian Enler Group sandstones. Due to technical difficulties the resistivity data were acquired in three sections.

Rathlin Basin may be favourable for geothermal exploitation. As the reservoir potential depends strongly on the intra-basin structure, variations in modelled resistivity may be taken as an excellent proxy for images of the presence of fluids, their distribution and interconnection within the basin.

The imaging of sub-basalt structures poses difficulties to other commonly employed geophysical methods, particularly seismics (e.g., Martini et al., 2005; Bean and Martini, 2010) due to the negative acoustic impedance contrast at the base of the basalt, and previous reflection experiments struggled to clearly image the sediments through the overlying ALG (Naylor and Shannon, 2011). As the MT method has been successfully applied in sub-basalt investigations both onshore and offshore (Hautot et al., 2007; Jegen et al., 2009; Colombo et al., 2011; Heincke et al., 2014), the method was proposed to study the three-dimensional electrical resistivity distribution of the sedimentary fill of the onshore portion of the Rathlin Basin.

Due to the expected elevated hydraulic properties and saline pore fluids (both factors that increase conductivity) of the proposed hydrothermal aquifer within the basin, it was expected that MT data could be carefully modelled to image the properties and distribution of the aquifer formations. The

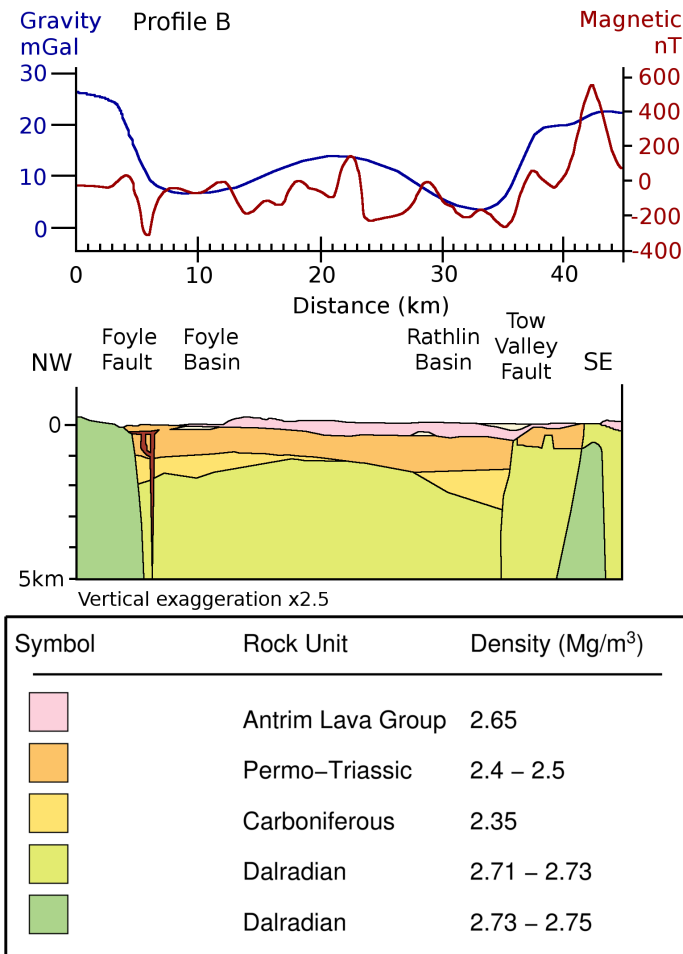


Figure 2.3.: Density model from [Mitchell \(2004\)](#), showing the broad geological structure predicted prior to this study. Density profile locality is shown in [Figure 2.1](#) (inset). Although the profile crosses the Rathlin Basin south-west of the MT survey area, a similar lithological sequence is expected elsewhere in the basin, including the survey area.

increase in resistivity observed in wireline data from the MMG to the underlying target sediments implies that, depending upon the thickness of units beneath the MMG, MT may not be able to accurately estimate the units' resistivities, as MT is primarily sensitive to a layer's conductance (i.e. the ratio of a layer's thickness to resistivity), and thinner or less conductive layers may be shielded by overlying conductors ([Jones, 1992](#)). However, due to the proven thicknesses and similar lithologies of the SSG and EG sandstones, it is still expected that the SSG and EG sediment fill will cause a sufficiently high resistivity contrast against the resistive metasedimentary country bedrock and provide a viable target for MT. The geometry of this interpreted aquifer structure is expected to be compatible with the gravity model presented in [Figure 2.3](#).

The MT method samples the impedance transfer functions that relate the electric and magnetic field components of EM plane waves that propagate into the Earth. As these EM waves attenuate with dependency on the Earth's lateral and vertical resistivity distribution, the observed MT responses can be employed for estimating the underlying 3D resistivity distribution ([Chave and](#)

Jones, 2012). The electric and magnetic field components of these EM source waves are each acquired in (preferentially) orthogonal horizontal directions, allowing the definition of four magnetotelluric transfer functions at the measuring location. These four elements carry information on the value and dimensionality of the subsurface resistivity structure at a range of periods. Many decompositions and analyses have been employed to expose this information (see, e.g., Chave and Jones, 2012, for an overview), with the aim of improving estimation or justifying 1D (i.e. resistivity varying with depth only) or 2D (i.e. resistivity varying with depth and one horizontal dimension only) modelling.

Though sensitive to conductive structures at depth, MT data are prone to distortion, primarily of the electric field, due to the presence of galvanic charges on the boundaries of shallow conductivity structures that are unresolvable at the frequency range of the recorded data. One simple form of this galvanic distortion is often easily identified by vertical offsets of the logarithmic apparent resistivity curves and is referred to as the static-shift effect (Jones, 1988), following a similar effect in seismology named "statics". These galvanic signatures are related to inescapable issues in observation of the electric field, wherein point-wise electric field observations, assumed during modelling and inversion, are replaced during MT surveys with voltage difference measurements along finite length dipoles (Poll et al., 1989; Pellerin and Hohmann, 1990), and by issues related to insufficient gridding resolution to describe the lateral variability of the near surface that affect both the electric and magnetic fields (Chave and Smith, 1994; Chave and Jones, 1997). Although the former of these may be handled by appropriate post-processing when modelling and inverting the field measurements, any near-surface inhomogeneity not parameterised in the modelling or inversion process, even at the electrode-scale size, will contribute to the galvanic signatures by distorting the local (primarily) electric fields. For land-based MT data, the magnetic effects of galvanic distortion only occur for a short frequency range of the order of half a decade at most (Chave and Smith, 1994; Chave and Jones, 1997).

Various methods have been proposed to quantify and correct for these static-shift effects, including continuous sampling and filtering of the electric channels (Torres-Verdin and Bostick, 1992), spatial filtering based on mapping of MT data (Berdichevsky, 1989), modelling of parametric homogeneous layers at depth (Jones, 1988), estimation of distortion-related parameters as unknowns during inversion (Sasaki and Meju, 2006; Miensopust, 2010; Avdeeva et al., 2015; De Groot-Hedlin, 1991; DeGroot-Hedlin, 1995), and finally the use of complementary EM geophysical methods (Sternberg et al., 1988; Pellerin and Hohmann, 1990; Miensopust et al., 2014). These methods can be broadly divided into methods that use intrinsic information from MT data and those that use extrinsic information from other geoscientific data. Whereas both families of methods can account for static shifts between MT modes at a single site and improve inter-station shifts, intrinsic information may not yield a correct resistivity in the case of both modes being distorted - as stated in Sternberg et al. (1988), "there is no reason to expect that either of the two MT polarisations will provide the correct resistivity.". In contrast, extrinsic methods using purely magnetic measurements (i.e. with no instruments using the subsurface as a component of their circuitry) by

definition are unaffected by the electric effects of galvanic distortion, and thereby provide a more correct resistivity estimate, albeit generally for much shallower depths than magnetotelluric measurements. The use of extrinsic information may, in some cases, be limited by the requirement that both the extrinsic information and MT data must illuminate some common depth volume within the Earth with a common current system in order to allow reconciliation of the resistivity structure. For example, if the near-surface is three-dimensional (3D), then the current system from regionally induced currents observed in MT is very different from the current system from locally induced currents from a small EM transmitter–receiver array, and any resistivities estimated by MT would correspond to a different volume than that sampled by the smaller array.

Fortunately, in the case of the Rathlin Basin broad-scale extrinsic resistivity information is available. As part of the regional Tellus ground and airborne geoscience mapping programme across both Northern Ireland and the Republic of Ireland, airborne frequency domain electromagnetic (FDEM) data were gathered over the target area ([Beamish, 2013](#)) in 2005 and 2006. [Sternberg et al. \(1988\)](#) and [Pellerin and Hohmann \(1990\)](#) describe how time domain electromagnetic (TDEM) data can be used to estimate and correct static-shift distortion of MT data, assuming that the MT data are one-dimensional (1D) or two-dimensional (2D) and in the correct geoelectric strike coordinate system, and we propose adapting their method to use the Tellus frequency domain airborne electromagnetic measurement (AEM) data for this purpose. Due to the high density of measurements often available, AEM data allow estimation of near-surface conductivity distributions at resolutions exceeding those of MT, making them an excellent choice for the correction of static-shift effects. The use of airborne EM data for static-shift correction has precedence, as outlined with airborne TDEM data by [Crowe et al. \(2013\)](#).

As three-dimensional inversion of MT data is becoming a more common practice, the effects of static-shift correction on resulting resistivity distributions must be considered. This article focuses on the implementation of this correction scheme for MT data by comparing models found by independent 3D MT inversion of the observed MT data and the static-shift-corrected MT data. In addition to comparing the model results, the statistical and spatial distribution of calculated static-shift corrections are examined and compared to previous works to verify their validity. Both the absolute resistivity and resistivity gradients are used to evaluate the differences between the two models, with the implications of the differences discussed in the context of the possible geothermal aquifer. Note that the approach presented here is primarily methodological in nature; the geological interpretation is brief and will be investigated at length in a future publication.

2.3 ELECTROMAGNETIC METHODS

EM methods include a wide variety of techniques that observe electromagnetic induction in the Earth and are most commonly used to image the subsurface distribution of electrical resistivity ρ (Ωm) or its inverse, electrical conductivity σ (Sm^{-1}), and, at high frequencies, electrical permittivity ε (Fm^{-1}). Subsurface materials are rarely homogeneous and can generally be described as a mixture

of materials with strongly differing properties, as detailed in Nover (2005) and Chave and Jones (2012). The bulk resistivity of a rock is commonly determined by very few of its constituents, with electrically the most important candidates at crustal depths being metallic conductors (sulfides, graphite, iron oxides), clays, and conductive fluids in pore spaces (both saline fluids and partial melts). Note that we use pore space in a general sense for primary and secondary porosity, including pores, fractures and conduits that may dominate the rock type under consideration. For low-enthalpy geothermal exploration in the upper crust, the most relevant property is the influence of electrolytic conduction by fluids in porous rocks. The relationship between the observed effective resistivity ρ , the pore fluid resistivity ρ_i , and the formation porosity ϕ is classically described for sandstones by Archie's Law (Archie, 1947), with generalisations discussed in Glover (2010). As Archie's Law assumes a clean sandstone matrix with well-established relationships between porosity and hydraulic permeability, its application may not always be appropriate, particularly if clay minerals are present (Mavko et al., 2009; Guéguen and Palciauskas, 1994; Zinszner and Pellerin, 2007).

In a broader sense, electrical conductivity is a proxy measure of hydraulic permeability rather than porosity, as the interconnection of conducting pathways facilitates electric current flow. Due to this strong dependence on the geometry of flow paths on the scale of interest, the relationship between permeability and porosity is highly nonlinear (amongst others, Raffensperger, 1996; Pape et al., 1999, 2000; Luijendijk and Gleeson, 2015). These dependencies have a close relationship with the type and geologic history of the rock considered (see, e.g., Bernabe et al., 2003), and the often complex development of geological units can lead to heterogeneities and preferential flow pathways at all scale lengths (Bjørlykke, 2010).

2.3.1 Magnetotelluric method

The MT method uses impedance transfer functions relating the electric and magnetic field components of vertically propagating EM source field plane waves to image the lateral and vertical resistivity distribution within the Earth. MT signal waves are generated by two sources, namely atmospheric electricity (generating signals of frequency > 10 Hz) and interactions of the Earth's magnetosphere with solar wind (generating signals of frequency < 10 Hz). Recent detailed reviews of MT methods, the underlying assumptions, and their application include Simpson and Bahr (2005), Berdichevsky and Dmitriev (2008), and Chave and Jones (2012).

Resistivity information at a range of depths is inferred by considering planar EM waves in the Earth at a range of frequencies, as their attenuation at a given frequency is a function of the resistivity ρ and magnetic permeability μ (Hm^{-1}) of the subsurface material, where the latter is generally assumed not to vary from that of free space, μ_0 . In a uniform half-space (i.e. a space

with no lateral or vertical resistivity variation) of resistivity ρ , the scale length δ in metres describing this attenuation,

$$\delta = \sqrt{\frac{2\rho}{\omega\mu}} \approx 503\sqrt{\rho/f}, \quad (2.1)$$

is termed the electromagnetic skin depth and describes the characteristic length over which the amplitude of an EM wave of frequency $\omega = 2\pi f$ decays by a factor of e^{-1} . This quantity is commonly used as a simple measure for the depth of investigation and radius of influence, although one must beware of its overuse in situations that depart from a uniform half-space, especially in the case of a multidimensional Earth (Jones, 2006).

The resistivity of a select volume of the Earth, as sampled by an EM wave of frequency ω , is determined from complex transfer functions that relate the amplitudes of the horizontal electric E_i (Vm^{-1}) and magnetic H_j (Am) field components that constitute the wave, defined as the complex MT impedance tensor \mathbf{Z} (Ω). This is generally formulated in the frequency domain, where the transfer function can be defined by the ratio of the fields:

$$Z_{ij}(\omega) = \frac{E_i(\omega)}{H_j(\omega)}. \quad (2.2)$$

By considering both orthogonal and parallel pairs of fields, an impedance tensor \mathbf{Z} with four components ($Z_{xx}, Z_{xy}, Z_{yx}, Z_{yy}$) can be defined:

$$\mathbf{Z} = \begin{pmatrix} Z_{xx} & Z_{xy} \\ Z_{yx} & Z_{yy} \end{pmatrix} \quad (2.3)$$

These impedances can be restated in more familiar magnitudes and units as an apparent resistivity ρ_a (i.e. equivalent half-space resistivity for a wave of that specific frequency for the orthogonal pairs Z_{xy} and Z_{yx}), and phase lead of the electric field over the magnetic field ϕ (which is $\pi/4$ for a uniform half-space for the orthogonal pairs), defined by:

$$\rho_{a,ij} = \frac{1}{2\pi\mu} |Z_{ij}|^2 \quad (2.4)$$

$$\phi_{ij} = \arg(Z_{ij}) = \tan^{-1} \left(\frac{\Im(Z_{ij})}{\Re(Z_{ij})} \right). \quad (2.5)$$

In MT surveying, the electrical field E is measured as a voltage difference over an appropriate distance rather than at a point. For the sampling of the magnetic field components, the electromagnetic properties of the volume sampled within a sensor are known and homogeneous (being the internal properties of the sensor itself), and the averaged field sampled through this sensor volume accurately represents a point magnetic field value (to within a length scale of that of the

sensor, typically 1.5 m for coil sensors used in broadband MT). However, the volumes sampled for the electric field components are of the order of 100 m (the typical bipole length in broadband MT (BBMT) surveys to acquire data in the frequency range of 100 to 0.01 Hz), with resistivity variations present within that length scale that may bias observations of the electric field. This distortion of primarily (but not exclusively) the electric field is one form of galvanic distortion and often manifests as frequency-independent multiplicative vertical offsets of MT apparent resistivity data for 1D or 2D cases (i.e. where impedance tensor diagonal components Z_{xx} and Z_{yy} are 0), when data are plotted as apparent resistivities on a log–log scale, hence the nomenclature of "static shift". As explained in, e.g., [Jones \(2011\)](#); [Chave and Jones \(2012\)](#), whereas real multipliers applied to an impedance tensor with 1D or 2D form affect only the magnitudes of the impedances, this is not the case if the impedance tensor has a 3D form with non-zero diagonal elements. Instead, the applied distortions cause mixing between the diagonal and off-diagonal components, affecting both the magnitudes and phases of the impedances.

2.3.2 Frequency domain AEM method

The basic theory for AEM can be found in [Ward and Hohmann \(1988\)](#). The FDEM method, as implemented for the Tellus AEM surveys, uses a pair of small coils as the transmitter–receiver (Tx-Rx) pair. The transmitter can be treated as a magnetic dipole that induces eddy currents in the subsurface at discrete frequencies, allowing the resistivity structure to be characterised by comparing the primary and secondary magnetic fields (H_p and H_s respectively). In the Tellus surveys Tx and Rx are oriented in a vertical, coplanar configuration, i.e. the coil axes are horizontal ([Leväniemi et al., 2009](#)), with magnetic dipole moments parallel to the flight direction.

AEM data take the form of ratios of the secondary magnetic fields (i.e. formed by current systems in the ground) to the primary magnetic fields (i.e. emitted by the transmitter coil), stated in parts-per-million. Both inphase (i.e. no phase change) and quadrature (i.e. 90° phase change) fields are considered; generally, the quadrature data are sensitive to the overall ground resistivity, whereas the inphase data are more sensitive to strong conductors. Unlike the magnetotelluric signal, the induced current systems and ensuing secondary magnetic fields of the AEM method are very much in the near-field region. As a result, the volume of Earth interrogated by the AEM signal cannot be easily reduced to a measure of skin-depth-type attenuation.

Although multidimensional modelling and inversion methods are available (see [Auken et al., 2014](#), for a recent review), AEM data are commonly treated as representative of a one-dimensional (1D) Earth, with spatial smoothing or other constraints along 2D flight lines possible to improve spatial continuity. One-dimensional modelling is usually performed based on analytical solutions for the layered Earth case, which are well known for most Tx-Rx configurations and can be found in many publications ([Keller and Frischknecht, 1966](#); [Ward and Hohmann, 1988](#); [Kaufman et al., 2014](#)). The particular analytical solution in a layered half-space for vertical, coplanar configuration of the transmitter and receiver coils as used here (i.e. parallel, horizontal magnetic dipoles) is found

in Minsley (2011). With the forward solution known, an inversion algorithm can be applied to determine a suitable resistivity model. The inversion of AEM data for this work uses the standard damped least-squares technique of Jupp and Vozoff (1975) as implemented in Airbeo (Raiche et al., 1985).

2.4 RATHLIN BASIN SURVEY

MT data were collected at 56 sites across part of the onshore Rathlin Basin (site locations shown in Figure 2.1) in May and June 2012. Seven parallel profiles were aligned perpendicular to the bounding Tow Valley Fault to the south-east (thick blue line in Figure 2.1), with profile and site separations each of 2 km in order to obtain a near-regular array of site locations, facilitating three-dimensional modelling and inversion. Both BBMT (i.e. from ≈ 300 Hz to 0.001 Hz) and audio-magnetotelluric (AMT) (i.e. from $\approx 10\,000$ Hz to 10 Hz) data were acquired at each site. Data were recorded with Phoenix Geophysics MTU-5A receivers, with either MTC-50 (for BBMT) or AMTC-30 (for AMT) induction coils used to sample the horizontal magnetic field components (H_x and H_y respectively). Vertical magnetic field components (H_z) were measured at almost all sites using either the appropriate induction coil or an AL-100 airloop, as deemed appropriate given the local ground conditions. The horizontal electric field components E_x and E_y were sampled by non-polarising lead-lead chloride (Pb–PbCl) PE4 Phoenix Geophysics electrodes arranged at each site in a cross configuration with electrode separations of typically 80 m. BBMT measurements were taken over a period of three nights at each site followed by an overnight measurement of AMT data.

Robust estimates of the frequency domain MT transfer functions were determined from the MT time series using commercial processing software from Phoenix Geophysics that implements the technique described in Jones and Jödicke (1984) and Jones et al. (1989). This approach is based on cascade decimation (Wight and Bostick, 1980), and uses a least trimmed squares algorithm (Rousseeuw, 1984; Rousseeuw and Leroy, 2003) to achieve the robustness of the estimate. Whilst a dedicated distant remote reference site was not used, the principle of remote referencing, as described in Gamble (1979) and Gamble et al. (1979), was applied by using the horizontal magnetic field components of each simultaneously acquired site as reference fields, and selecting the best available site as reference (typically five sites were recorded simultaneously). Finally, the AMT and BBMT data at each site were merged into a single response, spanning from 10 000 to 0.001 Hz at most sites.

Although data were acquired at an array of sites with the intent of 3D inversion, as the data were expected to be predominantly 2D in nature due to the expected strong lateral contrast across the bounding Tow Valley Fault, multisite, multi-frequency Groom & Bailey distortion analysis was applied to the data on a cross-basinal profile basis using the "strike" analysis tool (McNeice and Jones, 2001). The results of the analysis are presented in Figure 2.4 for four depth bands. Analysis of the data with respect to depth in "strike" shows that the data are predominantly 1D or 2D to

depths of ≈ 2 km, with increasing rms misfits beyond these depths indicative of either a change in strike direction (i.e. still a 2D structure, but with a different geoelectric strike direction) or a fully 3D structure. An estimate of the regional geoelectric strike azimuth was computed by arithmetically averaging the strike estimates from the deepest depth band (1780–3000 m) in the south-west half of the model, as these estimates represent portions of the model less affected by the coastal effect. The mean strike azimuth of the south-western part of the model is $\approx 43^\circ$ E, with a standard deviation of 10° . The mean geoelectric strike direction is coherent with the strike of the major structural feature, the Tow Valley Fault; however, it should be noted that as geoelectric strike directions inherently possess an ambiguity of $\pm 90^\circ$, the mean azimuth could also be interpreted as 47° W (i.e. a bearing of 313°). As the site profile azimuths were aligned perpendicular ($\approx 55^\circ$ W) to the mapped strike of the TVF in the area ($\approx 35^\circ$ E), both the inversion mesh and input data were rotated to a bearing of 315° (i.e. midway between the mean geoelectric strike direction and dip direction of the TVF). Note that the data were rotated without decomposition, to retain information that does not conform to the 2D assumption in Groom-Bailey decomposition. For a similar reason, the correction of static shifts was performed before rotation.

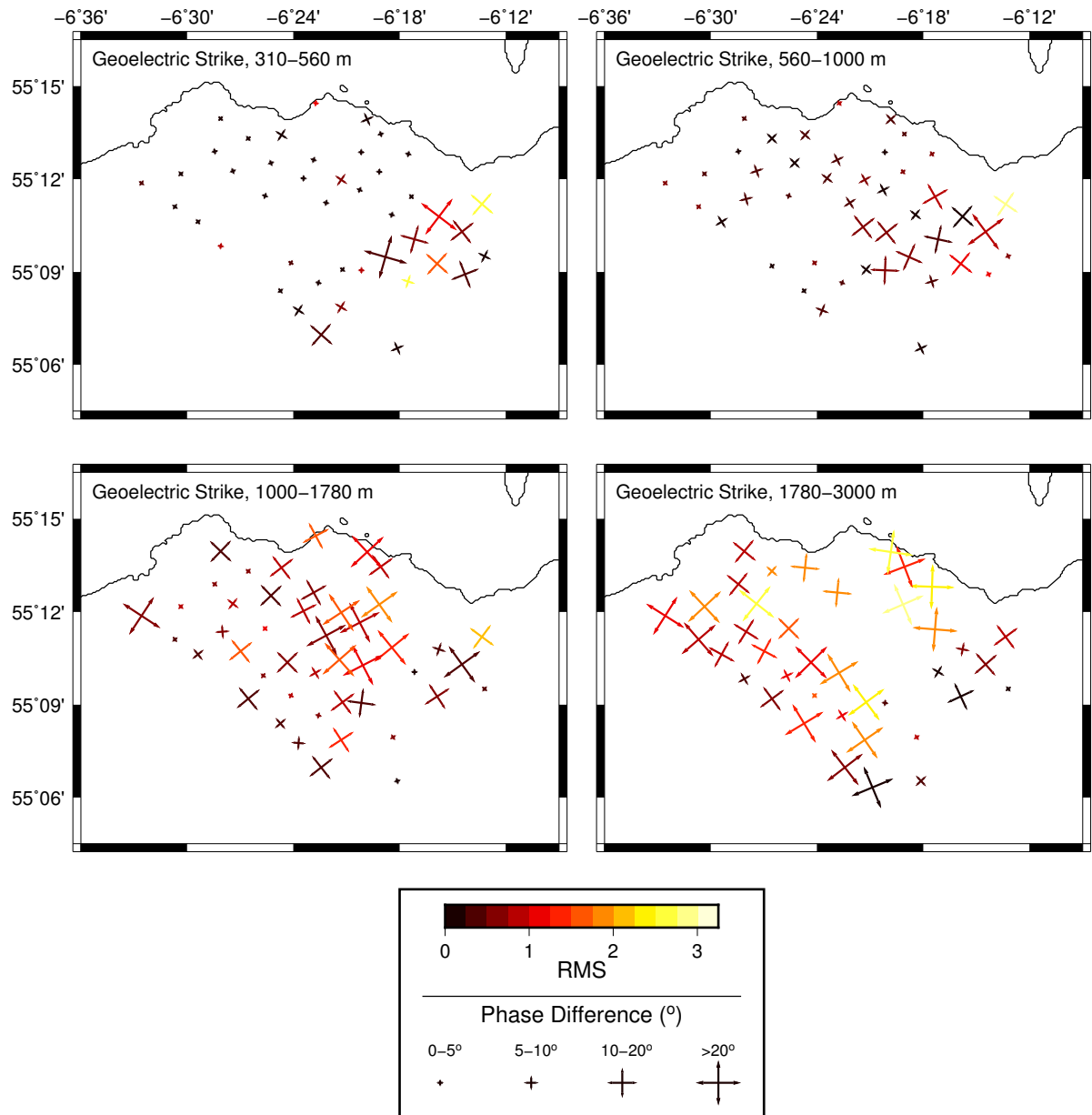


Figure 2.4.: Visualisation of dimensionality of MT data, decomposed using the "strike" analysis program [McNeice and Jones \(2001\)](#) over a range of depth bands (in metres below sea level). The orthogonal vectors at each MT site location indicate the azimuth of best-fitting geoelectric strike direction, coloured by the rms misfit between the observed MT response and the Groom-Bailey model response for the best-fit strike direction. The orthogonal pair of vectors is required as geoelectric strike estimates have a 90° ambiguity. The size of orthogonal vectors is classified by the phase difference, with larger vectors corresponding to larger phase differences. Small phase differences are associated with 1D resistivity structure, whereas larger phase differences occur with a 2- and 3D structure. Larger rms misfits indicate that the decomposition to a 2D structure is potentially invalid and can be caused by either significant noise contamination and distortion of the data or a 3D structure.

The MT responses were inverted for three-dimensional models using the ModEM 3D MT inversion program ([Kelbert et al., 2014](#); [Egbert and Kelbert, 2012](#)), with all four impedance tensor

elements and vertical transfer functions as input data. MT data were downsampled to a subset of 28 frequencies, spanning from 1000 to 0.001 Hz (displayed in Figure 2.5), with an increased sampling of frequencies in the range most sensitive to the target sediment depths (1–0.01 Hz). In order to avoid leverage bias in the search for optimum solutions that minimise rms misfit, poor-quality data (typically located near cultural noise sources) were manually identified and removed from the input data. The mesh used for inversion was $59 \times 68 \times 82$ cells in size (X,Y,Z) with the region of interest (the portion covered by MT sites) populated by cells of lateral extent 400 m by 400 m, with layer thicknesses logarithmically increasing beyond the depths required to accurately model bathymetry. Bathymetry was modelled by spanning the first 50 m depth interval with layers of 5 m, increasing to 25 m for the more distant (generally greater than 5000 m from coastline), deeper bathymetry, to a total depth of 300 m. Below the bathymetry, layers increased in thickness at a rate of increase of 1.01, increasing to a rate of 1.5 for depths beyond the volume of interest (i.e. beyond 4 km depth) to a total depth exceeding 1,500 km (i.e. at least 10 skin depths, given the initial half-space resistivity of $30 \Omega\text{m}$ and lowest frequency of 0.001 Hz). The highly efficient but approximate coast-effect forward modelling approach of Booker (described in [Burd et al., 2014](#)) was not used as some of our sites are located very close to the coast (well within one skin depth for moderate frequencies), requiring accurate modelling that could not be guaranteed with the approximate approach.

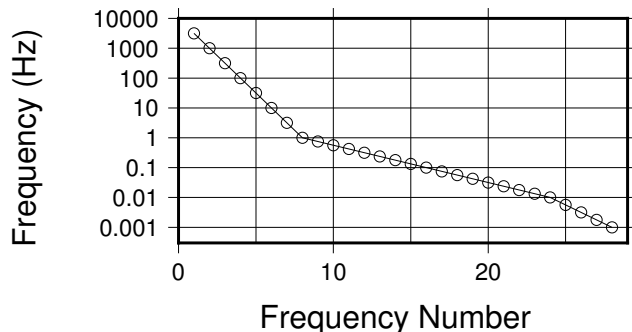


Figure 2.5.: Chart of frequency indices and values used in 3D inversion process. Frequency spacings per decade were 2 (for 3000 – 1 Hz), 8 (for 1 – 0.01 Hz), and 4 (for 0.01 – 0.001 Hz).

Inversion algorithms determine an appropriate model by iteratively adjusting a resistivity model, computing its forward MT responses, and comparing these responses to the observed data. Whereas the model steps vary depending on the precise algorithm implemented, there are several key parameters that influence an algorithm's behaviour, such as the data errors, type and degree of regularisation and initial starting and prior models. In particular, the distance between data and model responses, i.e. the sum of the squared residuals is used to measure the distance between the calculated and observed responses. To meet the assumptions of least-squares theory, these residuals must be standardised, i.e. scaled by the variance of the measurements in order to make them normally distributed over $\mathcal{N}(0, 1)$. In order to facilitate convergence of the inversion process, an error floor is commonly applied to input data for MT inversions, wherein the error provided for

inversion is defined as the greater of either the observed error or some function of the magnitude of the datum. Separate error floors were used for off-diagonal and diagonal impedance tensor components in this study of 5% and 20% of the mean magnitudes of (Z_{xy}, Z_{yx}) and (Z_{xx}, Z_{yy}) respectively. As the diagonal components observed were typically an order of magnitude smaller than the off-diagonal components due to generally 2D resistivity structures, the signal-to-noise ratio was significantly poorer, and applying a greater error floor here reduces the leveraging of the modelling process by noise-contaminated data.

The regularisation of an inversion describes the weighting between minimising the data residuals and some penalty function, commonly a roughness penalty that enforces smoothness in order to stabilise the resulting model. ModEM allows for the specification of separate regularisation parameters for the x , y and z directions, with higher values placing greater weight on the penalty function. Several values of these parameters were tested; however, varying regularisation in the z direction had a negligible effect on the model. Laterally isotropic values of 0.15, 0.3, and 0.45 were tested for the x and y directions, and whereas the overall model misfit did not vary significantly, lateral resistivity structure was strongly affected, with regularisation of 0.15 leading to discrete features with extreme resistivities (i.e. either very high or very low resistivity) beneath MT stations and poor continuity between sites. Resistivity structures in the models obtained with lateral regularisations of 0.3 and 0.45 correlated very well, with a slightly compressed range of resistivities present when regularisation was set to 0.45. In order to reduce over-smoothing of structural boundaries, final inversions were performed with lateral and vertical regularisation parameters of 0.3.

The starting model for each inversion was a $30 \Omega\text{m}$ half-space, with seawater to depths defined by coastal bathymetry fixed (i.e. invariant) at $0.3 \Omega\text{m}$ (marine sediments were not included). Final resistivity models were obtained by two consecutive inversion runs: a first model was determined by inversion from a uniform half-space starting model; then a second starting model was constructed by logarithmically averaging the resistivities in this first model with those of the starting half-space. The inversion of the averaged starting model was found to improve model fits significantly and result in resistivity distributions of greater range and contrast across interpreted structural boundaries. This work flow was found to preserve broad structural outlines in order to guide the inversion algorithm whilst suppressing finer features (typically associated with local minima in model space).

Frequency domain airborne electromagnetic data in our MT survey area were acquired as part of the regional Tellus survey described in [Beamish \(2013\)](#). The AEM data were obtained in 2005 and 2006 across Northern Ireland by the AEM-05 system described by [Leväniemi et al. \(2009\)](#), giving observations of both inphase and quadrature data at four frequencies (24 510, 11 962, 3 005, and 912 Hz). The entirety of Northern Ireland (barring high-flight regions above urban areas and steep topography) is covered by the Tellus AEM data set, which comprises parallel flight lines spaced 200 m apart on a bearing of 345° at a nominal altitude of 56 m, with a spatial sampling rate of one sample approximately every 15 m along the flight lines. The pre-processing work flow of the AEM data is detailed at length in [Beamish et al. \(2006\)](#) and [Leväniemi et al. \(2009\)](#). The inversion of

the FDEM data was performed using the one-dimensional Airbeo code from Amira International (Raiche, 1999) that implements the approach of Jupp and Vozoff (1975).

2.4.1 Correction of static shifts

The method proposed here for the correction of static-shift effects follows the approach of Pellerin and Hohmann (1990), adapted to using airborne FDEM data as extrinsic information. Earlier approaches took advantage of the downwards-propagating transient signal of the TDEM method to directly calculate an empirical, quasi-MT 1D response (Sternberg et al., 1988), and later work by Pellerin and Hohmann (1990) developed this approach by explicitly modelling the TDEM data to obtain a 1D resistivity model. The MT forward problem can be solved for this resistivity model and factors δ_{E_x} , δ_{E_y} that correct static shift between the calculated responses and observed data determined by taking the ratio of apparent resistivities. The resulting set of static-shift-corrected MT data may then be modelled as desired. We propose that the approach of Pellerin and Hohmann can be equally applied with FDEM data, subject to the same constraints, namely that there should be an overlap between the minimum depth of penetration of the MT sounding and the maximum depth of penetration of the extrinsic (to MT) information and that the dimensionality of the two methods should agree. The first constraint mandates the use of high-frequency AMT data rather than BBMT data to ensure overlapping volumes of sensitivity. A flowchart describing the steps taken in correcting the Rathlin Basin MT data with the Tellus AEM data is presented in Figure 2.6.

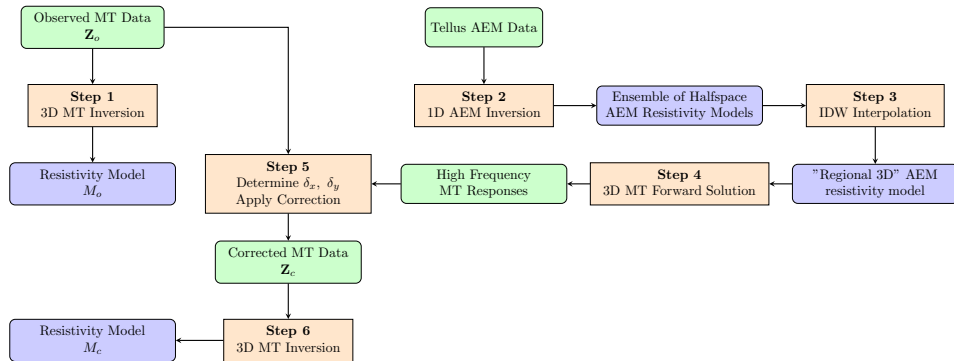


Figure 2.6.: Flowchart illustrating the steps required to a) find an original, uncorrected resistivity model M_o from MT data (Step 1 only), and b) find an improved, static-shift-corrected resistivity model M_c from MT data, with coincident airborne FDEM data (data from the Tellus project used for this study). For clarification, the MT data used in Step 5 are in their original coordinate system, whereas the MT data in Steps 1 and 6 are rotated to a bearing of 315° for inversion. IDW in Step 3 refers to inverse distance weighting.

The approach used here is predicated upon certain key assumptions about the near-surface geology and the induced galvanic distortion, and these assumptions clearly show the limits of the approach. Firstly, as mentioned we assume that the near-surface geology is 1D in structure, i.e. we can treat the off-diagonal impedance tensor elements Z_{xy} and Z_{yx} independently without rotating or otherwise preparing the data. Secondly, we assume that the galvanic distortion affects only the

electric field; as the total electric field is represented by E_x and E_y , we require only two corrective factors δ_{E_x} and δ_{E_y} to be applied to the two impedance tensor element pairs corresponding to E_x and E_y , namely (Z_{xx}, Z_{xy}) and (Z_{yx}, Z_{yy}) . Finally, whereas the cause of static-shift-type distortion of the MT data is the estimation of the electric field, the airborne FDEM data are observations of the magnetic field (directly proportional to the electric field). Hence, the FDEM data are unaffected by static-shift-type distortion, and any resistivity estimates computed from these data are closer to the true values. For clarity about the effect of the static-shift corrective factors, δ_{E_x} and δ_{E_y} are often presented here on a logarithmic scale; as the corrective factors transform to additive (or subtractive) changes of resistivity on a logarithm scale, their value is intuitively related to whether a correction to more resistive or more conductive true data is required. For example, a (multiplicative) static-shift corrective factor of $\delta_E = 3.16$, indicating that the true resistivity $\rho_T = \delta_E \rho_{obs} = 3.16 \rho_{obs}$ corresponds in logarithmic scale to an additive static-shift correction, i.e. $\log_{10}(\rho_T) = \log_{10}(\rho_{obs}) + 0.5$.

The first step of the implemented procedure is the inversion of the uncorrected MT data to obtain a baseline resistivity model for comparison M_o . The remaining steps describe how static-shift-corrected MT data Z_c were obtained by solving the MT forward problem for a model of the AEM data, and in turn inverted to obtain a corrected resistivity model M_c .

Step 1 3D MT inversion of observed MT data Z_o with the ModEM code to obtain model M_o . Both the inversion mesh and input data were rotated to a bearing of 315° for inversion.

Step 2 Modelling of each four-frequency AEM sounding within the survey area as a single-layer structure (i.e. half-space) with Airbeo ([Raiche, 1999](#)), resulting in an apparent resistivity value at each location best reproducing the observed AEM data.

Step 3 Interpolation of AEM half-space models by inverse-distance-weighted (IDW) averaging of log-resistivity values to populate the uppermost 200 m of an MT forward modelling mesh with cells of 170×170 m. Below the uppermost 200 m, the model reverts to a $100 \Omega\text{m}$ half-space.

Step 4 3D solution of MT forward problem for the resistivity model found in Step 3 with ModEM, resulting in a set of high-frequency synthetic MT responses at six frequencies from 10 000 to 1000 Hz for each MT sounding location. The frequencies chosen coincide with those of the downsampled MT data.

Step 5 Multiplicative static-shift corrective factors δ_{E_x} and δ_{E_y} found by taking the ratio of the apparent resistivities of the up to six high-frequency MT responses found in Step 4 to those of the observed data (i.e. $\delta_{E_x} = \rho_{a,xy}(\text{synthetic}) / \rho_{a,xy}(\text{observed})$) over the 10 000–1000 Hz band. Due to either noise contamination or non-1D behaviour (i.e. violating our assumptions), not all data in the compared frequency band were used; typically, comparison was made using three to four of the six data points that parallel the synthetic responses. The

corrective factors are applied to the entire bandwidth of the unrotated observed data to obtain $\rho_a(\text{corrected})$, with δ_{E_x} applied to all elements dependent on E_x , i.e. $\rho_{a,xx}$ and $\rho_{a,xy}$. δ_{E_y} is treated analogously.

Step 6 The static-shift-corrected data are used as input for 3D MT inversion with ModEM to obtain an improved resistivity model M_c . Both the inversion mesh and input data were rotated to a bearing of 315° for inversion.

Whereas multi-layered models that better reproduce the AEM data can also be determined using Airbeo, they were not used in favour of the half-space apparent resistivities for two principal reasons. Firstly, the interpolation of the apparent resistivities to a 3D MT mesh can be directly computed, whereas multi-layered models require more advanced approaches to reconcile variation in layer thicknesses unless these are explicitly set in the 1D inversion to facilitate interpolation. Secondly, the depth of sensitivity of the lowest frequency of the AEM data (912 Hz \approx 60 m, from forward modelling) has a moderately narrow overlap with the skin depth of the highest MT frequencies (10800 Hz, skin depth \approx 50 m for a typical near-surface resistivity of \approx 100 Ωm). Above this overlapping volume, the MT data remain sensitive to but poorly resolve resistivity contrasts, and for the purposes of our work, the added complexity in multi-layered AEM modelling does not significantly improve our results. A map of the half-space models found from the AEM data in Step 2 is shown in [Figure 2.7](#). As this work is reliant upon the depth of sensitivity of the FDEM data we assume that the causes of static shift encountered are locally one- or two-dimensional anomalies that perturb estimates of the electric field estimates E_i , causing frequency-independent static shifts of the MT impedance data. Additionally, as each electric field component is used to compute two forms of data (i.e. $\{Z_{ii}, Z_{ij} \propto E_i\}$), the same correction will be applied to data sharing a common electric field component. Groom and Bailey distortion analysis of the high-frequency MT data showed that the regional near-surface resistivity structure was 1D or 2D at most, validating this approach to correcting the static shift effects. We reiterate that for regions with regionally 3D structure, this approach would be invalid.

The statistical and spatial distributions of the static-shift multiplicative corrective factors δ_{E_x} and δ_{E_y} were examined for spatially coherent correlation and features that may be indicative of known regional-scale geological structures. The spatial distribution and magnitudes of the corrective factors across the survey area are shown in [Figure 2.8](#). Whereas some spatial correlation between static shifts and geology is apparent, static-shift variation mostly does not coincide with mapped surface geological boundaries, which invalidates the use of regional geological units as predictors of static shift. The histograms in [Figure 2.9](#) show the distributions of the logarithmic transforms of δ_{E_x} and δ_{E_y} , with statistical quantities shown in [Table 2.1](#) (the quantities of both $\log \delta_{E_x}$ and $\log \delta_{E_y}$ are tabulated, as are those of the mean static-shift correction at each site $\bar{\delta}_E$). The distributions of both δ_{E_x} and δ_{E_y} appear close to log-normal, with longer tails towards conductive corrections that likely indicate natural bias introduced by the sampling, such as the geographic location of the MT sites. The bivariate distribution of $\log \delta_{E_x}$ and $\log \delta_{E_y}$ from each site is shown in [Figure 2.10](#),

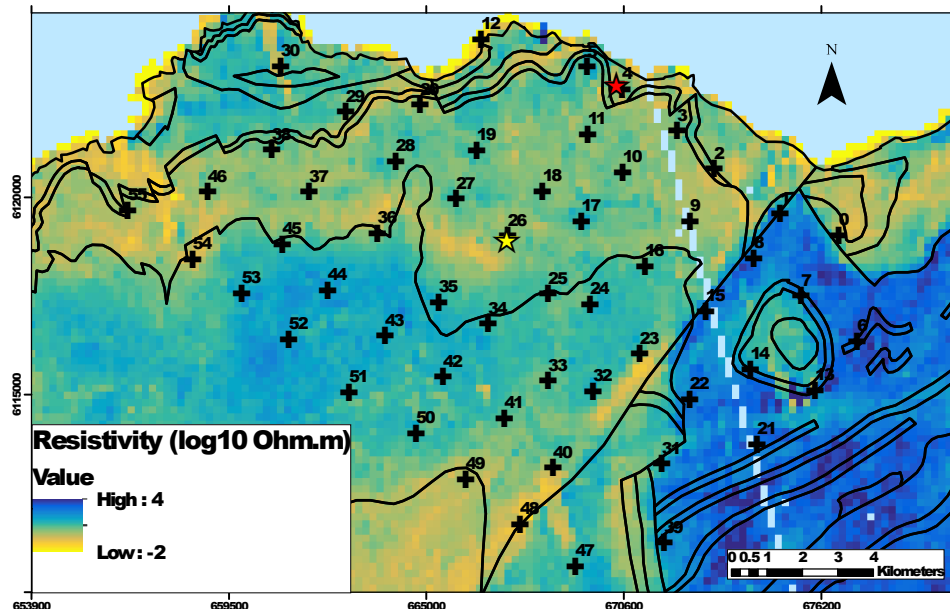


Figure 2.7.: Map of airborne FDEM half-space resistivity models, overlain with geological boundaries (solid black lines, as in Figure 2.1) and MT site locations (black cross symbols). The model exhibits good correlation with the mapped boundaries, as well as variation within each geological unit. Note that data from one flight line are missing, resulting in a white line in the figure. These absences were interpolated across in the synthetic model.

where the strong 45° (i.e. $\delta_{E_x} \approx \delta_{E_y}$) clustering indicates that the two electric field components at most sites are similarly affected by static-shift-type effects, with no evident regional preference for static shifts to one polarisation over the other.

Table 2.1.: Statistical measures of the \log_{10} of the corrective factors δ_{E_x} and δ_{E_y} (i.e. additive in logarithmic domain), as displayed in Figure 2.9. In addition to the means, medians and standard deviations of $\log_{10} \delta_E$, the means and medians of δ_E (i.e. multiplicative) are also shown. Note that δ_E is the site-wise mean static shift - i.e. the mean of δ_{E_x} and δ_{E_y} on a site-by-site basis.

	Mean (\log_{10})	Median (\log_{10})	σ (\log_{10})	Mean	Median
δ_{E_x}	-0.035	0.011	0.235	0.923	1.03
δ_{E_y}	-0.035	-0.020	0.236	0.923	0.955
$\delta_E = \frac{\delta_{E_x} + \delta_{E_y}}{2}$	-0.035	-0.012	0.225	0.923	0.974

From examination of the spatial and statistical distributions of δ_{E_x} and δ_{E_y} , the galvanic distortions present in these data show no consistent anisotropic behaviour and weak spatial correlation with surface geology. As the accepted theory is that galvanic distortion is typically caused by irresolvable near-surface resistivity inhomogeneities below the level of resolution of the AMT data, the weak spatial correlation with surficial geology is unlikely to be random and instead reflects the variation in heterogeneity of formations

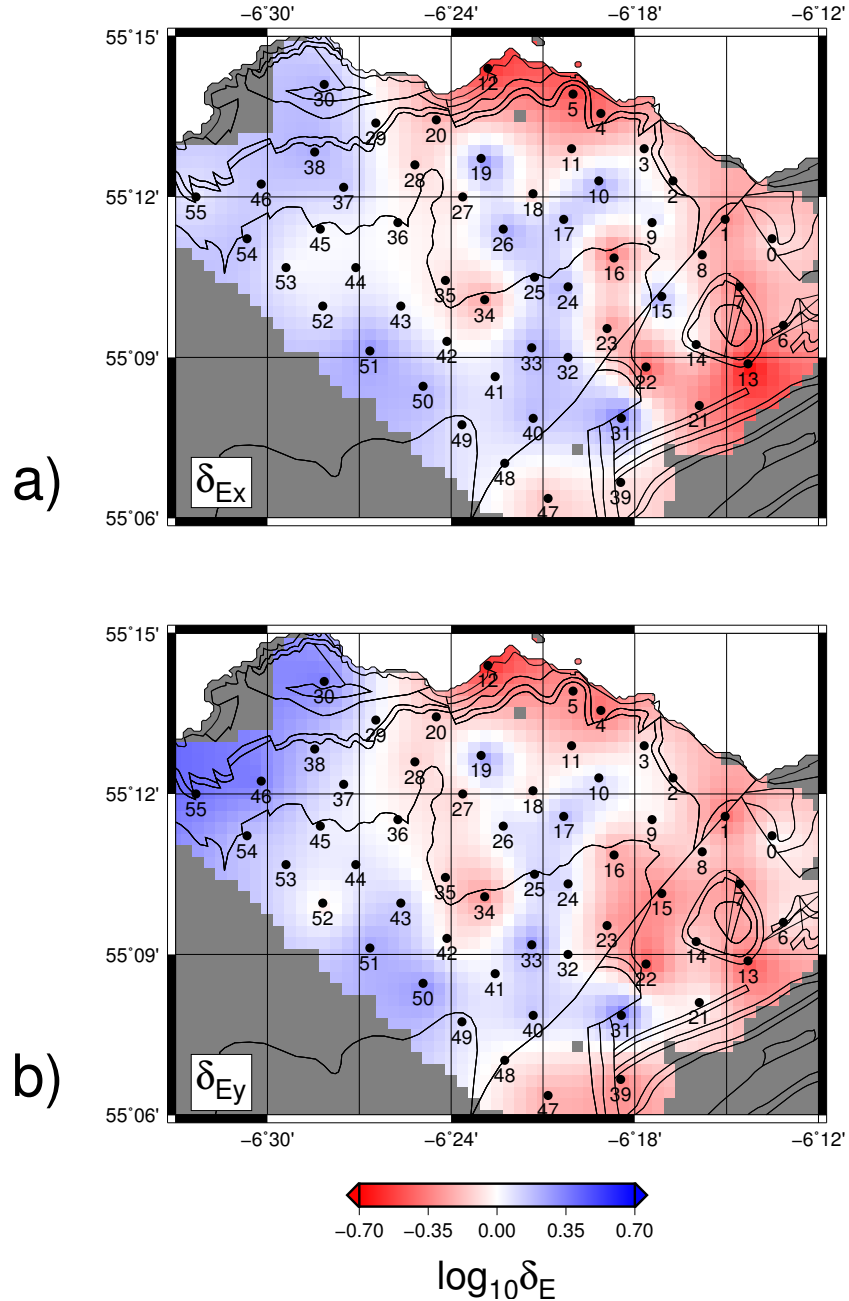


Figure 2.8.: Spatial distribution of static correction factors δ_{Ex} (a) and δ_{Ey} (b) in decades (i.e. as additive factors, where +0.5 corresponds to a multiplicative factor of $10^{0.5}, \approx 3$). Blue shading indicates resistive corrections to the data whereas red indicates conductive corrections. Note that for the majority of sites, δ_{Ex} and δ_{Ey} are similar in magnitude and polarity. The magnitudes of static corrections are generally less than 0.5 decades in size, corresponding to apparent resistivity estimates being shifted by factors of less than 3.

2.5 MODEL EVALUATION AND DISCUSSION

Initial comparison of the two models, one with (M_c) and one without (M_o) static-shift correction, shows greater resistivity contrasts and sharper delineation between resistive and conductive volumes

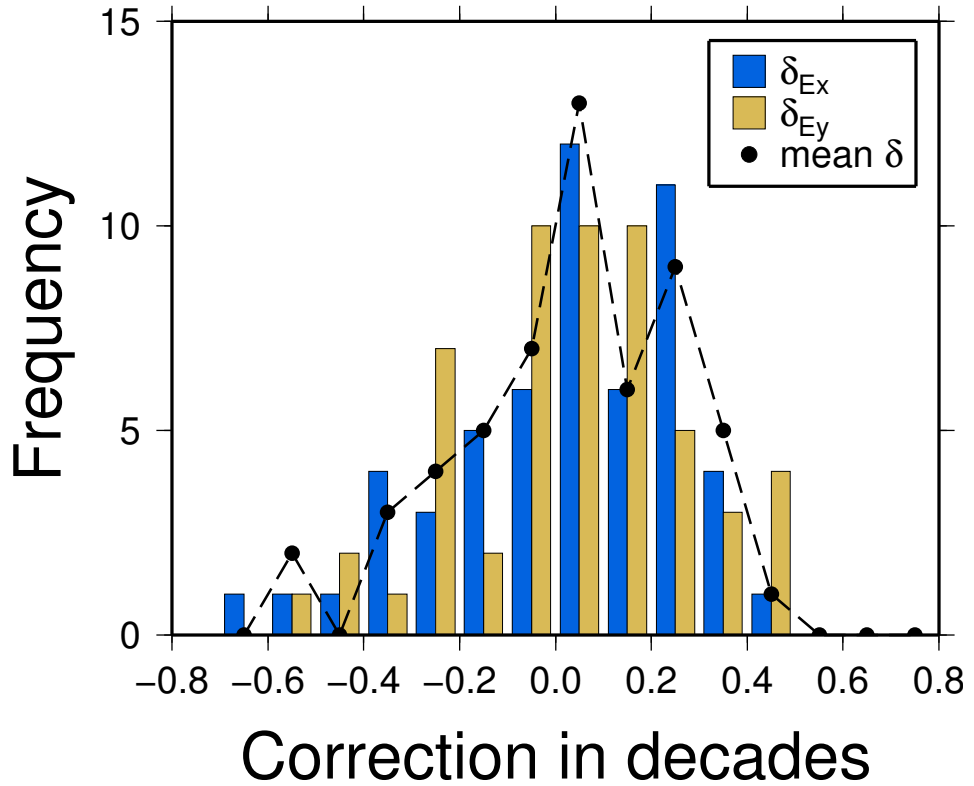


Figure 2.9.: Distribution of calculated static correction factors δ_{Ex} (blue) and δ_{Ey} (yellow) in decades (i.e. as additive factors, where +0.5 corresponds to a multiplicative factor of $10^{0.5}$, ≈ 3). Statistical quantities related to these distributions are tabulated in [Table 2.1](#).

in the corrected model M_c , and for these reasons M_c is preferred for interpretation and evaluation of structures in the Rathlin Basin. Due to the static-shift correction M_c also more likely better represents the correct resistivity distribution of the real Earth. [Figure 2.11–Figure 2.14](#) present the resistivity distribution ρ of horizontal and vertical slices taken through the preferred model M_c (profile locations are marked in [Figure 2.1](#)). Measures of model comparison are also shown on these figures and are discussed below (note that no images of the resistivity distribution of M_o are presented, as the resistivity differences with respect to M_c are subtle and difficult to perceive given the dynamic range of resistivities in the visualisation). The two models generally show good correlation of geoelectric structural geometries, but differ in the absolute resistivity estimates and the exact extent of these structures.

The resistivity structure of M_c is generally quite simple, with the most prominent feature being the extensive conductor, of a resistivity less than $10 \Omega\text{m}$, that lies between 900 and 2000 m depth and extends from the Tow Valley Fault in the south-east for a distance of up to 10 km towards the north-west.

We propose that this conductor primarily represents the conductive MMG, with a clearly delineated upper boundary. The interpretation of the lower boundary against the SSG (and equally, the boundary between the SSG and the EG sandstones) is hindered by both the smoothing effects of

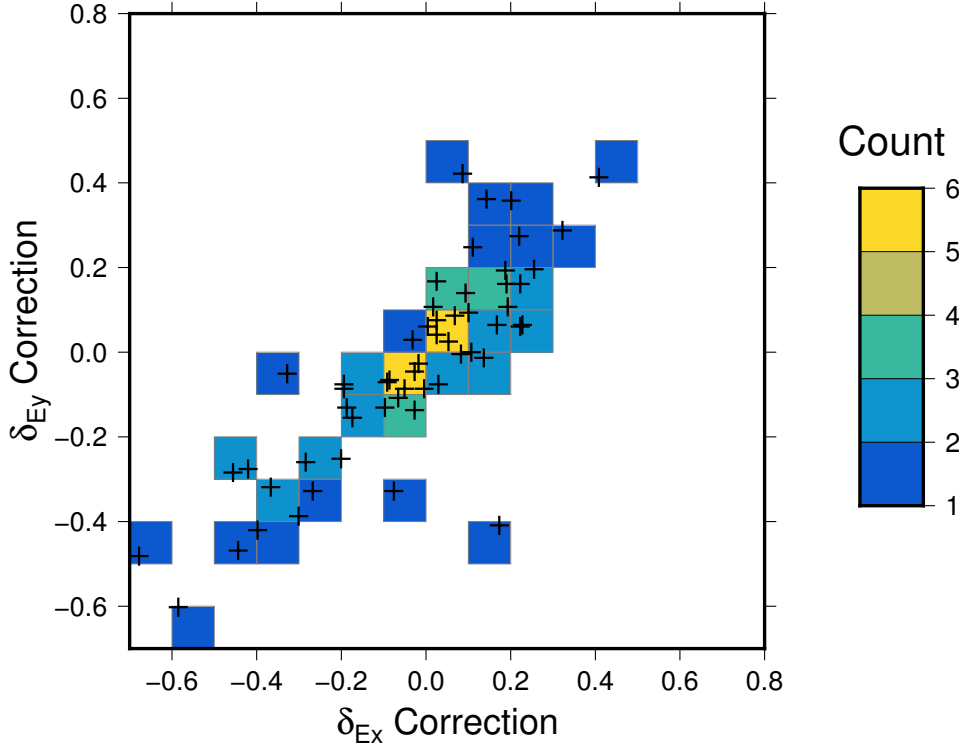


Figure 2.10.: Bivariate distribution of calculated static shift corrections δ_{Ex} and δ_{Ey} in decades (i.e. as additive factors, where +0.5 corresponds to a multiplicative factor of $10^{0.5}, \approx 3$), paired by site. The strong clustering and 45° trend (i.e. $\delta_{Ex} \approx \delta_{Ey}$) indicate that the orthogonal static shifts are generally similar sized across the survey area, with no observable regional trend of greater static shift of one polarisation.

the regularised inversion approach used and the fact that inductive EM responses are intrinsically sensitive to the tops of conductive units (and their integrated conductivity) rather than to the bottoms of conductive units (i.e. the tops of resistive units). The TVF, which forms the south-eastern boundary of the basin, is clearly defined, although the angles of dip modelled are slightly shallower than those modelled in Gibson (2004), again likely due to smoothing within the MT inversion process. The Dalradian metasedimentary horst is represented by the highly resistive volume in the south-east of the model and is visible at all depths and on both cross-basin profiles with a relatively homogeneous structure. All three profiles show the shallowest 500 m as moderately resistive, correlating well with the expected extent and thickness of the ALG basalts and UWFL. Minor conductors of $10 - 50 \Omega\text{m}$ occurring between depths of 300 and 600 m are interpreted as the LLG, although these depths are slightly greater than the depths observed in the PM1 borehole. The uppermost resistivities within the model correlate well with the mean of the resistivity measurements from the PM1 borehole for the ALG and underlying sediments, though clearly without the same vertical resolution.

In order to demonstrate the lateral heterogeneity of the basin and intra-basinal structures, Figure 2.15 shows the resistivity distribution of the basin portion of M_c as a set of layer-by-layer histograms, each histogram normalised by the number of counts for the mode of that layer. As the

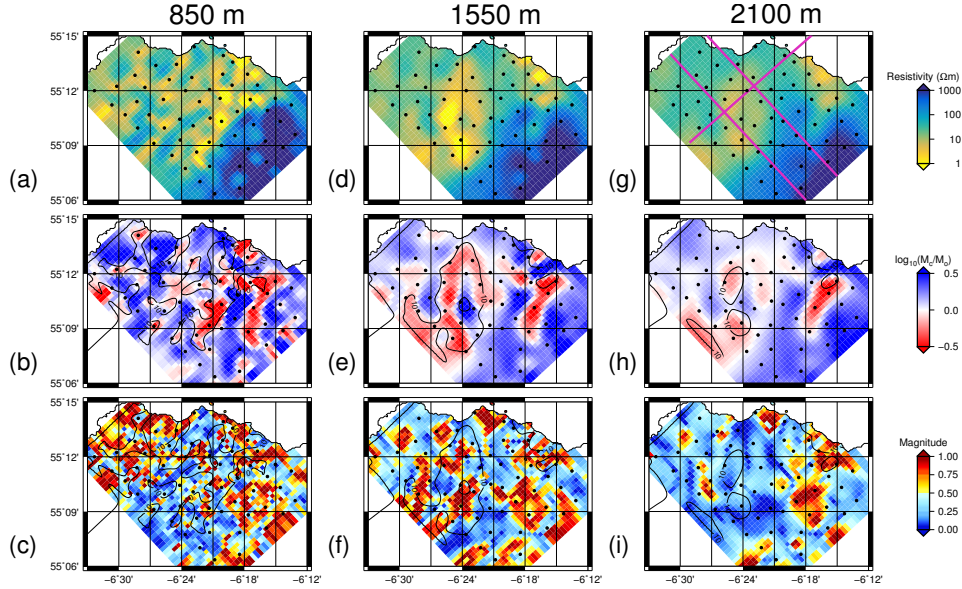


Figure 2.11.: Top row shows resistivity slices through the static-shift-corrected model M_c taken at 850 (a), 1550 (d), and 2100 (g) metres below sea level. Middle row shows the resistivity difference Δ between the models in decades ($\Delta(M_c, M_o) = \log_{10}(M_c/M_o)$) for the same depths, where red shows M_c more conductive than M_o , and blue more resistive. Bottom row shows the magnitude of the normalised cross-gradient (the cross-product of the gradient vectors of each model ∇M , as defined in Equation 2.7), as a diagnostic of structural similarity between the models, with 0 (blue) showing parallel gradient vectors (i.e. very similar structure) and 1 (red) showing orthogonal gradient vectors and structural disagreement. Note that the difference and cross-gradient plots are overlaid by the 10 Ωm contour from the corresponding resistivity slice. Magenta lines in subplot (g) indicate the location of Profiles A, B, and C.

model becomes much smoother below depths of approximately 2500 m, several tests were carried out to examine the sensitivity of the model responses to resistivity contrasts beyond these depths. The insertion of synthetic resistive bodies showed that the model responses are sensitive to them but unable to resolve resistivity contrasts below the conductive basin. It remains possible that older sediments with higher resistivity exist below this depth; however, the resistivity contrasts present within the MT data are insufficient to clarify their existence or extent.

Two diagnostic measures were used to assess the changes between M_c and the original model M_o , caused by static-shift correction. The first diagnostic measure is the logarithmic resistivity difference Δ between the two models,

$$\Delta(M_c, M_o) = \log_{10} \frac{\rho_{M_c}}{\rho_{M_o}}, \quad (2.6)$$

and the second is the normalised cross-gradient (NCG) of the two models, being the cross-product of each model's gradient vectors at each cell,

$$NCG(M_c, M_o) = \frac{|\nabla M_c \times \nabla M_o|}{|\nabla M_c||\nabla M_o|}. \quad (2.7)$$

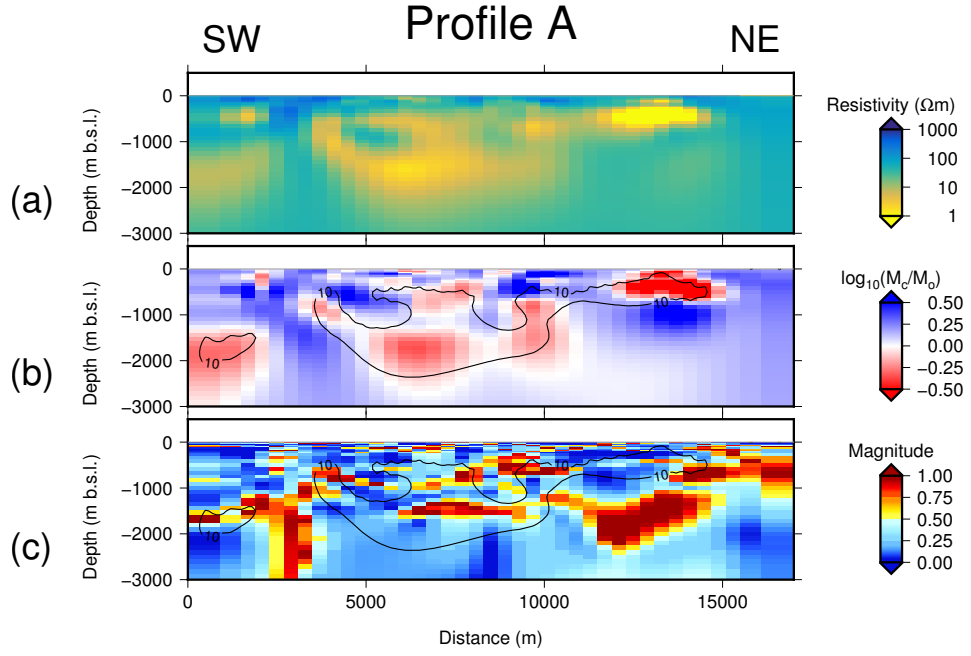


Figure 2.12.: Profile A taken along the axis of the concealed basin through the static-shift-corrected resistivity model M_c (location shown in [Figure 2.1](#) and [Figure 2.11g](#)). The resistivity is shown in **(a)**, the resistivity difference $\Delta(M_c, M_o)$ is shown in **(b)**, and the cross-gradient of M_c and M_o is shown in **(c)**. Contours on the difference and cross-gradient plots show the $10 \Omega\text{m}$ contour. For presentation a vertical exaggeration of 1.5 is used.

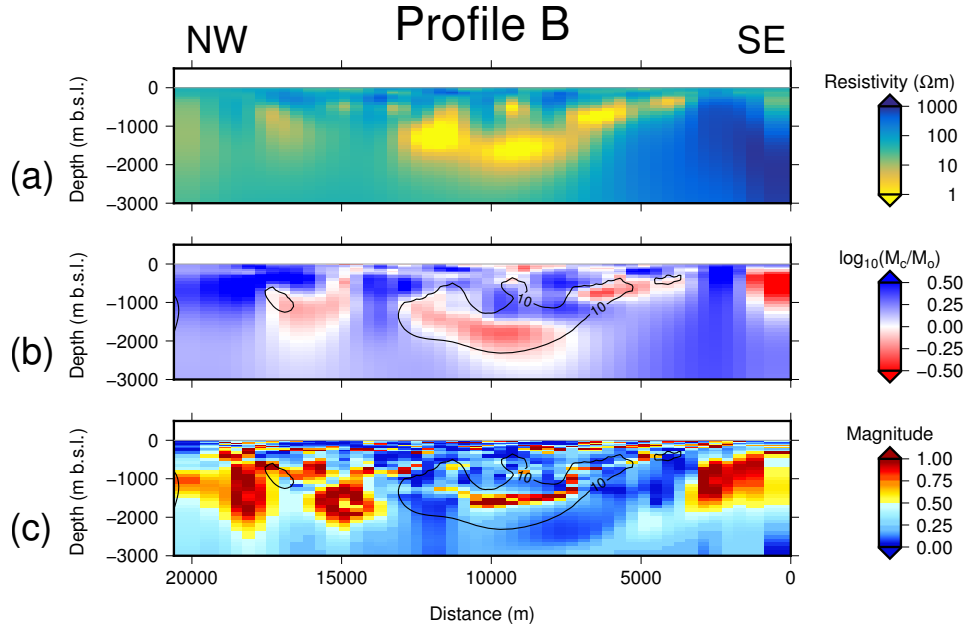


Figure 2.13.: Profile B taken across the static-shift-corrected resistivity model M_c (location shown in [Figure 2.1](#) and [Figure 2.11g](#)). The resistivity is shown in **(a)**, the resistivity difference $\Delta(M_c, M_o)$ is shown in **(b)**, and the cross-gradient of M_c and M_o is shown in **(c)**. Contours on the difference and cross-gradient plots show the $10 \Omega\text{m}$ contour. For presentation a vertical exaggeration of 1.5 is used.

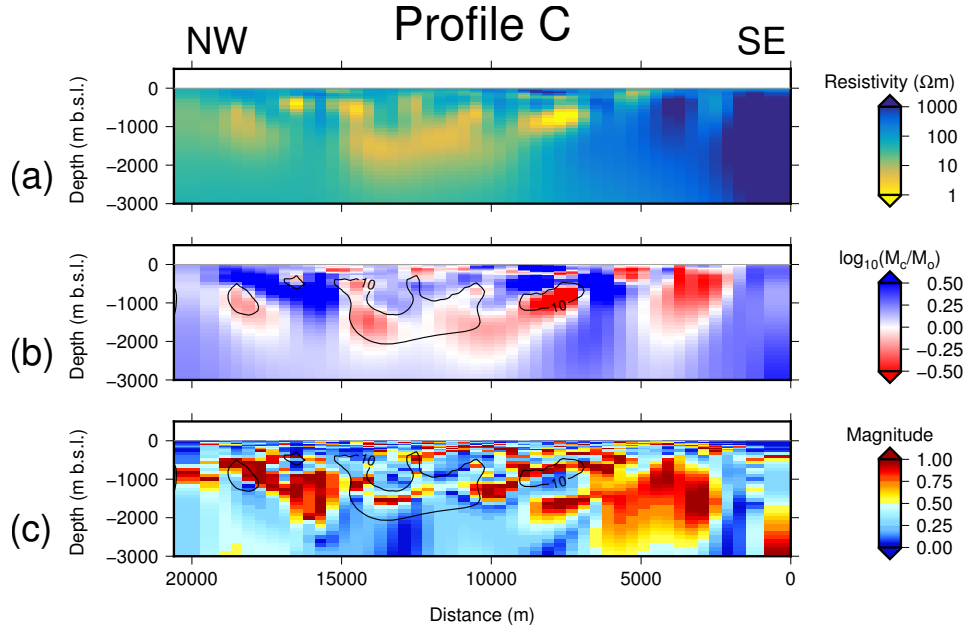


Figure 2.14.: Profile C taken across the static-shift-corrected resistivity model M_c (location shown in [Figure 2.1](#) and [Figure 2.11g](#)). The resistivity is shown in **(a)**, the resistivity difference $\Delta(M_c, M_o)$ is shown in **(b)**, and the cross-gradient of M_c and M_o is shown in **(c)**. Contours on the difference and cross-gradient plots show the $10 \Omega\text{m}$ contour. For presentation a vertical exaggeration of 1.5 is used.

The normalised cross-gradient was introduced in [Gallardo and Meju \(2003\)](#) in the context of joint inversion based on structural similarity and has been used by, e.g., [Schnaadt and Heinson \(2015\)](#) and [Rosenkjaer et al. \(2015\)](#) to highlight structural similarities and differences between resistivity models.

As the logarithmic resistivity difference Δ between M_c and M_o highlights discrepancies in the absolute resistivity values of the two models, it is more useful for observing contrasts in formation resistivities (i.e. locations where one model has a relative minimum or maximum) rather than comparing structural boundary locations. The figures presented show that the conductive features in M_c tend to be between 0.25 and 0.50 of a decade more conductive than their equivalent volumes in M_o , whereas the resistive features show similar tendencies towards greater resistivity in M_c . The largest vertical variations in Δ (i.e. from a local maximum to a local minimum or vice versa) are typically seen at the upper boundary of the MMG, making the interpretation of this boundary far less subjective in model M_c . The resistivity difference Δ also shows greater definition of the thin conductors interpreted as the LLG, which are difficult to delineate on the plots of resistivity alone due to weaker resistivity contrasts. The metasedimentary horst shows a range of both conductive and resistive contrasts; however, as this region shows greater geoelectrical heterogeneity and greater static-shift effects in the observed data, the cause of these differences is variations in the uncorrected data used to model M_o rather than the relatively uniform horst seen in M_c . The spatial distribution of Δ is insightful, particularly the distribution of points where $\Delta = 0$ (i.e. points where M_o and M_c have the same resistivity) which generally do not coincide with

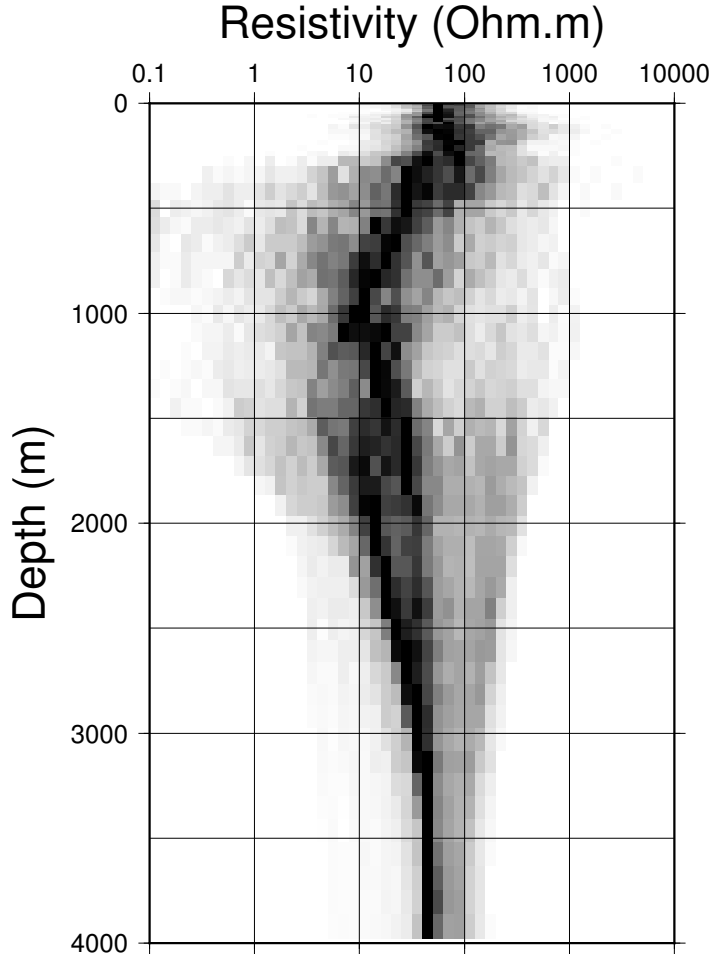


Figure 2.15.: Representative histogram model of the portion of the static-shift-corrected model M_c covering the Rathlin Basin only. Each layer represents the distribution of resistivities present in that layer of the model, normalised by the number of counts for the mode of that layer (black). Whereas a wide spread of resistivities is present from 300 m to 2500 m depth, the column of modal resistivities can be viewed as a "typical" 1D structure of the basin, with a distinct minimum of $\approx 10 \Omega\text{m}$ evident at 1100 m depth, the depth interval of the MMG observed in the Port More 1 borehole.

the resistivity minima or maxima of M_c , nor with the identifiable resistivity boundaries. Instead, these points in places indicate regions in which the structural geometries differ between models, such as thicker or thinner conductive bodies (e.g. at ≈ 800 m depth, 10000 m along Profile A, [Figure 2.12b](#), where the $\Delta = 0$ line occurs in the middle of a conductor). These differences in geometry are most noticeable as horizontal features in the uppermost 1000 m, where the models are constrained locally by single sites and the static-shift correction affects the model in a generally 1D manner. The lateral distribution of Δ at these shallow depths is a result of the pseudo-1D local scaling of the model differing from site to site; as such, we do not expect the distribution of Δ to replicate those of the static-shift corrections themselves (except for the trivial case of surficial and immediately subsurficial layers).

The NCG is largest where the gradient vectors (i.e. resistivity changes) of the two models are orthogonal, such as differences in structures and locations, or similar structure but differing magnitude of resistivity change (i.e. difference in curvature of the model). Both situations of elevated *NCG* are evident in the models, especially on the zero- Δ lines (i.e. where the resistivity models intersect and Δ reverses polarity, requiring significantly different gradient vectors), and at resistivity minima and maxima of M_c (and assumingly M_o , although not shown), indicating a difference in curvature due to slight offsets of critical resistivity points or large resistivity differences in co-located critical points. We note again that the significant variation in *NCG* values computed in the Dalradian horst likely reflects the heterogeneity of this block. Whereas the *NCG* was originally proposed as a means of determining structural similarity between models, our use of the *NCG* in this study suggests that it may also be used to assess the coincidence of similar structure with different resistivities.

The closeness of MT model responses to the data is commonly judged by the normalised root mean square error (nRMS), defined as

$$nRMS = \sqrt{N^{-1} \sum_{i=1}^N \tilde{r}_i^2}, \quad (2.8)$$

where \tilde{r} is the residual between calculated and observed data, normalised by the square root of its variance. In the case of a sufficient number of data N with approximately Gaussian and independent misfits, nRMS error should approach 1 for a model fitting to within 1 standard error; however, the application of an error floor to the observed misfits results in artificially lowered nRMS errors. Additionally, due to the global averaging of residuals an nRMS error is uninformative about which portion of data are poorly fit.

Regardless, the nRMS error remains a useful metric for comparing the relative goodness of fit of a succession of model responses to the same data set. The two models presented here reproduce the observed and corrected MT responses to similar degrees with overall nRMS of 1.77 and 1.96 for M_c , the corrected model (66 iterations total), and M_o , the original model (52 iterations total), respectively. [Figure 2.16](#) shows the distribution of misfit between the data and the model responses of M_c for the four impedance tensor elements at each frequency and site, allowing a better insight into which portions of the data are worse fit than can be drawn from a single nRMS value for the entire model. The measure of misfit displayed is the magnitude of the residual (the absolute value of the difference between the model response and observed datum), normalised by the errors used for inversion (the larger of the experimental errors or the applied error floor), similar to the overall nRMS defined in [Equation 2.8](#), with values of 1 or less indicating a residual smaller than the error (i.e. fit to within 1σ). In general, the off-diagonal components are well fit, with a handful of sites showing poorer fits with respect to phase components. As the model responses are noise-free and have internally consistent magnitude and phase behaviours, worse misfits to impedance phases in comparison to magnitudes imply that the affected portions of the data themselves may not entirely satisfy the assumption of being in the far-field region of the signal,

likely due to the proximity of a noise source. Interference from a local noise source contaminates both the magnitude and the phase of the data, and inverting such data can lead to a spurious model structure. Data that showed significant noise contamination (identified by phases trending towards 0°) were removed prior to inversion. The misfits of the diagonal impedance components show similar behaviour in that the magnitude is better fit than the phases; however, the differences in fit between magnitudes and phases are greater for the diagonals. Some increase in misfit is expected at the high-frequency limits due to the relocation of MT sites to the centre of their respective cells for computation; as the cells are 400 m wide within the survey area, the model is effectively 1D for forward computation of MT responses at such high frequencies, and diagonal impedances are 0 for such resistivity structure. As the observed diagonal MT data can be non-zero due to resistivity variations at scale lengths below those used for modelling purposes, the fit of these data can be improved by the use of a finer mesh, with a corresponding increase in computation time. At longer periods the misfits of diagonal phases are increased for the same reasons as the off-diagonal phases, namely noise contamination in the data; however, due to the generally smaller magnitudes of the diagonal MT data the signal-to-noise ratio can be considerably worse. It is possible that the error floor used for the diagonal components is perhaps too stringent, and lower misfits would be obtained with a higher error floor; however, as the observed data imply a predominantly 2D structure (as shown in [Figure 2.4](#)), such a change is unlikely to drastically change the final model.

Although examining the misfits of a single model's responses to the data set used in its determination in such a granular fashion is useful in determining which data components are poorly fit and possibly why, taking a similar approach in order to compare two models is not valid in this case. Due to the application of individual static-shift corrections to each site's MT data, the gradients of the respective data spaces of the models are significantly altered. As most inversion algorithms (the non-linear conjugate gradient method implemented in ModEM included) rely upon gradients within the data space to determine the direction of line searches as part of their optimisation, the static-shift corrections applied all but guarantee that the two inversions presented in this work are the products of different paths through their data spaces. Hence, although the overall mean nRMS estimates are similar, we cannot categorically state that any differences in misfit at the granular, individual datum level are not simply due to the different gradient progressions.

The key test of the two models lies in comparing the measured resistivity values from the PM1 borehole to the vertical resistivity columns from M_c and M_o corresponding to the location of the borehole ([Figure 2.17](#)). The input data for the two inversions differ solely in the application of static-shift corrections, assumed to only affect the magnitude of the data; considered as a purely 1D problem, such a shift results in the rescaling of both layer resistivities and thickness. The nRMS misfits of the two models' responses for this location are 0.97 (M_c) and 1.05 (M_o). The effect in 3D is more complicated, as the variation occurs in both lateral and vertical directions; however, some geometrical correlation and similar-shaped structures can still be expected in each of the two models. Note that we argue this based upon the perturbation of the data magnitudes, rather than the similar nRMS - as mentioned, such an assumption based on misfit is unreasonable.

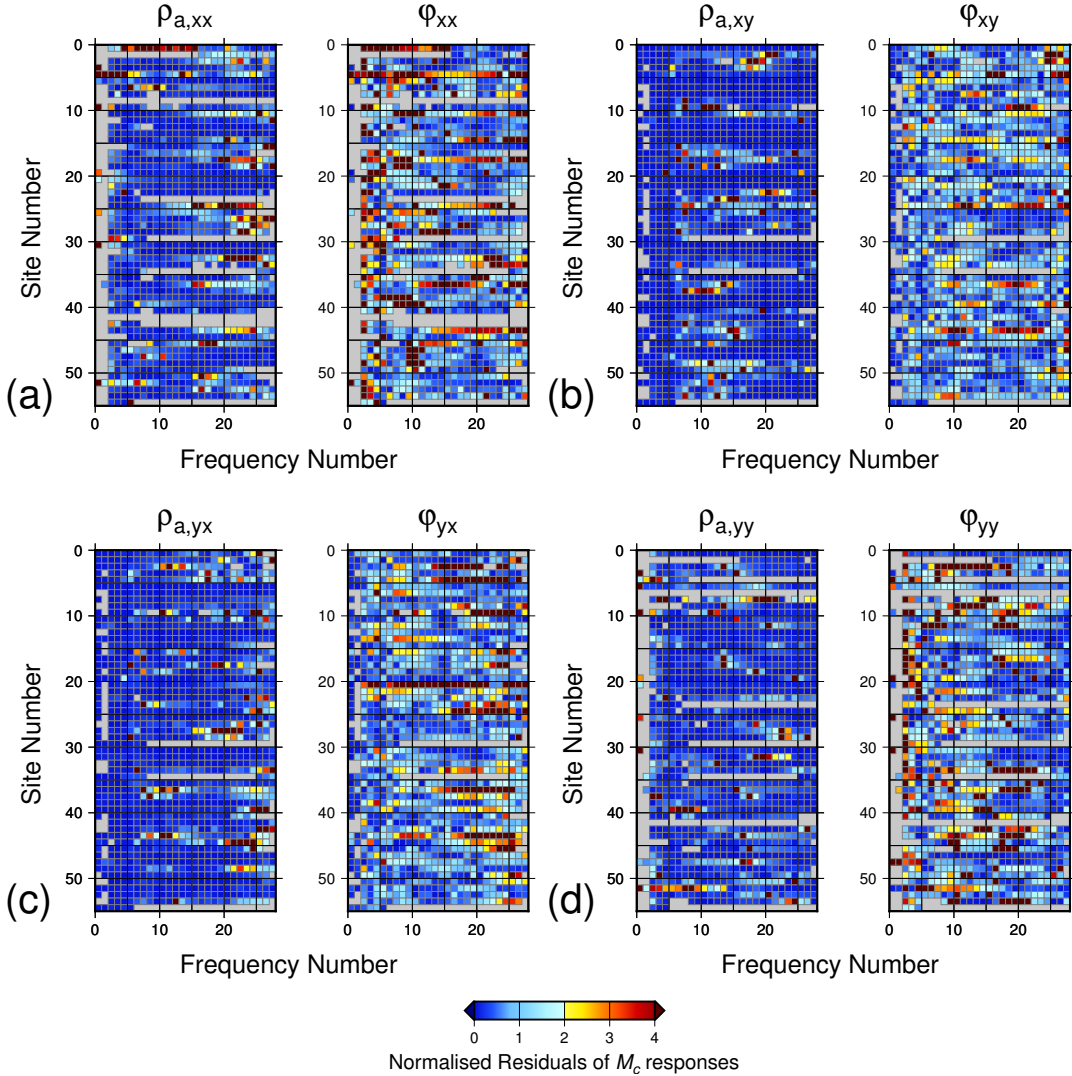


Figure 2.16.: Visualisation of the normalised residuals of the magnetotelluric responses of M_c compared to observed data at each site (numbered as per Figure 2.1) and inversion frequency number (as shown in Figure 2.5) for each element of the impedance tensor (a-d). The normalised residual is determined by taking the absolute value of the difference between model response and datum and normalised by the error used in inversion (i.e. the greater of the observed errors or the applied error floor). Normalised residuals of less than 1 indicate a residual smaller than the error. Note that misfits of apparent resistivity use the logarithmic difference to determine the residual. Values in grey represent the lower-quality data that were masked and not included in the inversion.

Additionally, for the uppermost extents of the model (i.e. at depths within the inductive volume of only a single MT site), it can be seen that the application of static-shift corrections results in similar effects to a 1D case, i.e. a model from data that have been statically shifted upwards to higher apparent resistivities will have increased resistivity–thickness products (thicker, more resistive layers). With this behaviour in mind, the two models M_c and M_o have very similar geometries at shallow depths (the uppermost 200 m), with the resistivities of M_c significantly closer to the mean

of the borehole measured resistivities. Due to the regularisation of the inversion process, neither model can adequately reproduce the highly variable near-surface variations measured through the ALG in the borehole. Comparison of the structures at deeper depths shows that whereas M_c has conductive layers at 300 and 1300 m depth, with resistivities of ≈ 3 and $15 \Omega\text{m}$, interpreted as the middle of the LLG sediments and the combined conductances of the MMG and SSG respectively, the equivalent conductors (assuming a scaled geometry) in M_o occur at 450 m and 1500 m, with resistivities of ≈ 20 and $\approx 8 \Omega\text{m}$. Similarly, the models show a resistor of ≈ 60 and $\approx 30 \Omega\text{m}$ at 600 and 750 m depth in M_c and M_o respectively.

The resistivity columns from the two models at the PM1 borehole site can also be compared on the basis of integrated conductances, i.e. the ratio of a layer's thickness and resistivity. In such a comparison, the LLG sediments are represented as conductances of 31 (M_c) and 13 (M_o) S, the interpreted dolerite sill sequence as conductances of 34 (M_c) and 23 (M_o) S, and the MMG or SSG sediments as conductances of 103 (M_c) and 100 (M_o) S. The greatest contrast in conductance is observed in the LLG, wherein M_c shows a conductance almost half an order of magnitude greater than M_o . The resistivity measurements in the PM1 borehole do not span the entire LLG interval; however, given the measured values the real conductance of the interval is likely greater still than the 31 S recovered in M_c . Hence, although M_c does not fully recover such a conductance, the elevated conductance in comparison to M_o , coupled with the near-identical lower conductances, indicates that M_c is closer to the real structure at this location.

Given the knowledge of the lithology and the measured borehole resistivities, we conclude that M_c is a categorically superior resistivity model in that, of the two models, it more accurately and correctly resolves the central depths and resistivity values of the lithological units encountered. Critically, the limited borehole resistivity data in the MMG and SSG suggest that resistivity increases slightly with depth between the two units, and whereas the resistivity column of M_o more closely matches the absolute resistivity values, the column of M_c better approximates the trend of the observed borehole resistivities. Without further external information to verify the models with, the smaller differences between the M_o model resistivity column and the borehole resistivity measurements of the target sediments cannot lead to the acceptance of the entire model, as the shallower structure is poorly recovered. Conversely, M_c , the static-shift-corrected model, correlates well with the borehole lithological boundaries from the PM1 borehole and shows a trend in resistivity with depth that matches the trend evident in the wireline resistivity measurements.

Changes in resistivity at depth from static-shift correction have strong implications for the interpretation of the reservoir potential of the area. Assuming Archie's Law holds and depending on the cementation exponent m (formation dependent, but typically ≈ 2 for reservoir formations), a relative change in resistivity f_ρ between two models ρ_c and ρ_o (i.e. $\rho_c = f_\rho \rho_o$) corresponds to a change in estimated porosity of $\phi_c = f_\phi \phi_o$, where $f_\phi \propto \sqrt[m]{f_\rho}$. The relationship between porosity and hydraulic permeability is known to be complex and highly nonlinear; it would be highly speculative to quantify how the resistivity perturbations from correction of static-shift effects would affect any attempt to estimate hydraulic permeability. At this stage, given the paucity of borehole

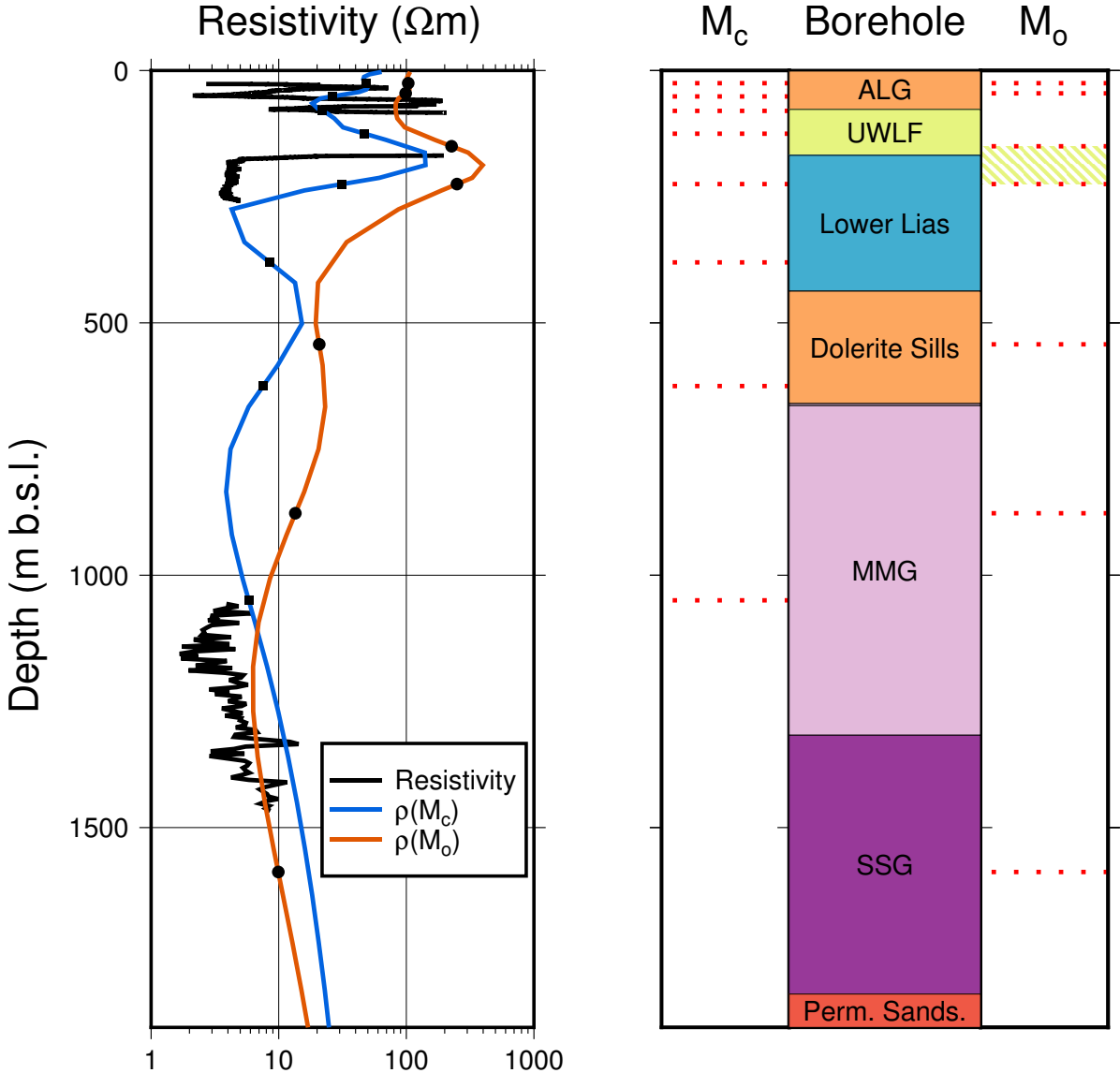


Figure 2.17.: Left-hand panel shows the resistivity columns from both M_c (blue) and M_o (orange) adjacent to the Port More 1 borehole, plotted with the observed normal resistivity data. Due to the regularisation in the inversion process, neither model can reproduce the high variability of resistivities within the ALG observed in the uppermost 100 m of normal resistivity data. Note that the resistivity column of M_c approaches the observed low resistivities of the LLG and reproduces the trend observed in the MMG and SSG resistivities, albeit with resistivities approximately half a decade greater. In contrast, the resistivity column of M_o correlates poorly with the observed normal resistivity data, with overestimated resistivities and layer thicknesses. Right-hand panel shows interpreted structure of each resistivity column (patterned, on either side), with the observed borehole lithology in the centre column. The interpreted M_c structure shows significantly improved correlation with the observed lithology; in particular, the upper boundary of the MMG against the dolerite sills is recovered much closer to the true depth in M_c than in M_o . The static-shift correction factors δ_{E_x} and δ_{E_y} applied at this site were 0.40 and 0.38 (-0.40 and -0.42 in decades) respectively.

information and unfavourable geoelectric setting (in which the conductive MMG directly overlies the moderately less conductive SSG and EG reservoir targets), the modelled resistivity distribution cannot be used to extend the knowledge of the hydraulic properties of the reservoir targets beyond what is reported from the boreholes within the Rathlin Basin with any useful level of confidence.

The quasi-1D correction of static-shift effects applied here affects the resulting three-dimensional models to significantly greater depths than expected, with differences between the corrected and uncorrected resistivity models of up to half an order of magnitude present at depths of up to 2000 m (see, for example, the constant depth slice at 2100 m depth in [Figure 2.11](#)) that do not correlate with the spatial distribution of applied static-shift corrections ([Figure 2.8](#)). Whereas the structural geometries are very similar between the two models (especially in the shallow regions constrained by single MT sites), interpretations of the target sediment locations in the models differ in significant ways, with both depth to sediments and absolute resistivity affected. As such, it is clear that when seeking accurate resistivity and depth estimates in three-dimensional modelling of MT data, galvanic distortion must be accounted for as its effects are subtle but pervasive.

2.6 CONCLUSIONS

An approach for the correction of static-shift-type galvanic distortion in MT data utilising airborne FDEM data has been tested that follows the use of TDEM data in previous methods. The new approach was tested on an MT data set from Northern Ireland, using a publicly available regional data set of airborne frequency domain electromagnetic data to create a set of corrected MT data. Three-dimensional inversion of each magnetotelluric data set recovers structures with similar geometries; however, structures in the near-surface show scaling of resistivity–thickness products proportional to the static-shift correction applied. When compared to geophysical borehole logs it is clear that the model from static-shift-corrected data reproduces the observed resistivity with significantly greater fidelity. Significant suborders of magnitude variations in resistivity are caused in the model by the correction of the static-shift components of galvanic distortion, not only in the near-surface but extending down to the target sediment depths (≈ 1500 m). As the test area is a prospective geothermal exploitation site (a sedimentary aquifer with elevated temperatures), electrical resistivity could be used to infer the heterogeneous distribution of hydraulic properties within the reservoir; however, the suborder of magnitude perturbations caused by inadequate consideration of galvanic distortion would lead to a gross misestimation of these physical properties.

The model determined by the inversion of static-shift-corrected data was found to better recover the resistivity structure observed in a nearby borehole in comparison to the model from observed data. Based on these observations, we conclude that airborne FDEM data provide sufficiently accurate resistivity estimates to allow the correction of static-shift effects in MT data. Note that this approach as discussed here is valid only for locales where the near-surface resistivity distribution is approximately one-dimensional. Given the often regional acquisition and open availability of such AEM data, it is hoped that the approach demonstrated here could be further tested with

other MT surveys. Pending further case studies, FDEM could in future be considered as another alternative method to evaluate and correct static-shift-type distortion. Additionally, whereas our approach assumes one-dimensional, single-layer models for the AEM data in deriving the static-shift corrections, future advances could investigate what effect more advanced AEM modelling (i.e. multiple layers or, where applicable due to AEM acquisition specifications, full 3D modelling) would have on the computed forward MT responses and associated static-shift corrections.

2.7 CODE AVAILABILITY

Aside from the processing codes used to convert the measured MT time series data to robust impedance data (implemented in propriety programs from Phoenix Geophysics), codes used in this article are available for academic and non-commercial purposes. The Airbeo program for AEM modelling is part of the P223 software suite of Amira International, assembled by CSIRO, and available from Amira International's website. The Strike program for distortion analysis of MT data can be obtained by contacting AG Jones, the co-author of [McNeice and Jones \(2001\)](#). The ModEM code for three-dimensional inversion of MT data is available for non-commercial use from its authors' website, hosted by Oregon State University.

2.8 DATA AVAILABILITY

Two types of geophysical data were modelled for this article, namely, airborne FDEM and MT data. The airborne FDEM data set is publicly available under the Tellus Project, and accessible from the project's website. The initial Tellus Project collected airborne geophysics and surface samples across Northern Ireland, and subsequent projects have expanded the data set to cover a significant portion of Ireland.

The collection of the MT data, as part of the IREtherm Project, was funded by Science Foundation Ireland; as a publicly-funded project the data are intended to be publicly available. IREtherm data will be uploaded to the European Plate Observing System (EPOS - www.epos-ip.org) Data Centres, upon the data centres' completions, however, in the interim period MT data can be provided by the authors upon request.

2.9 AUTHOR CONTRIBUTION

R. Delhaye, A.G. Jones and M.R. Muller designed the MT acquisition plan, with contributions from D. Reay in terms of prior geological and geophysical knowledge. R. Delhaye and M.R. Muller carried out the acquisition, with the assistance of the acknowledged IREtherm MT Team. MT data processing was done by R. Delhaye, under instruction from A.G. Jones and M.R. Muller. The workflow for AEM modelling and MT static shift correction was planned and executed by R. Delhaye and V. Rath. MT inversions performed by R. Delhaye, with instructive direction from A.

Jones and V. Rath. Manuscript prepared by R. Delhaye and V. Rath, with insightful comments and review from A. Jones and M. Muller.

2.10 ACKNOWLEDGEMENTS

We would like to acknowledge Science Foundation of Ireland for the financial support for the IREtherm project (10/IN.1/I3022) to A. G. Jones and particularly the student support to R. Delhaye. MT data acquisition was only possible with the assistance of the IREtherm MT Team (S. Blake, T. Farrell, C. Hogg, J. Vozar, C. Yeomans). G. Egbert, A. Kelbert, and N. Meqbel are very gratefully thanked for making their ModEM code available to the community, especially N. Meqbel for installing it on our clusters and those of the Irish Centre for High-End Computing (ICHEC). The Geological Survey of Ireland and the Geological Survey of Northern Ireland are thanked for providing access to Tellus project data and other complementary information. M. Dessaix of the GSNI is especially thanked for his assistance with the latter. Amira International is thanked for providing open access to the P223 modelling suite. We also acknowledge the work of the Geological Survey of Ireland-funded project GSI-sc-04, "Spatially constrained Bayesian inversion of frequency and time domain airborne electromagnetic data from the Tellus projects" in advancing the available tools and utilities for the handling of Tellus project airborne data. ICHEC is thanked for providing the computational capability required for us to perform our inversions. Lastly, we gratefully thank A. Junge and an anonymous reviewer for their comments and suggestions for improving this paper.

Edited by: C. Krawczyk.

Reviewed by: A. Junge and one anonymous referee

2.A COMPARISON WITH INVERSION OF NON-ROTATED DATA AND MESH

In order to establish if the choice of mesh and data rotation significantly influences the resulting models, a further comparative inversion was performed using non-rotated data and mesh. The non-rotated mesh comprised $64 \times 80 \times 82$ cells in size (X,Y,Z), with cells in the central portion of the model of lateral extent 400 m by 400 m. The layer thicknesses, initial half-space resistivity of $30 \Omega\text{m}$, bathymetry and smoothing factors were kept identical to the rotated mesh used within the article. Similarly, the same selection of data and error floors as used for the rotated data were applied to the non-rotated data. The resulting models, M_c (i.e. inverted from static shift-corrected, non-rotated data) and M_o (i.e. inverted from original, non-rotated data), had normalised RMS misfits of 2.14 (63 iterations) and 2.17 (60 iterations) respectively.

Figures [Figure 2.18](#), [Figure 2.20](#), [Figure 2.22](#) and [Figure 2.24](#) present the diagnostic images of resistivity, Δ (the logarithmic resistivity difference), and the normalised cross-gradient value for the two models M_c and M_o determined for rotated data and meshes. In contrast, [Figure 2.19](#), [Figure 2.21](#), [Figure 2.23](#) and [Figure 2.25](#) present the same diagnostic images for the comparative

models N_c and N_o determined for non-rotated data and meshes. By examining the resistivity plots of N_c in comparison to the resistivity plots of M_c , it is clear that the non-rotated N models recover generally similar structures to their rotated M counterparts, with an extensive central conductor in N_c of similar extent to the central conductor in M_c associated with the Permian and Triassic sediments. Similarly, both M and N models feature a large resistor in the south-east associated with the Dalradian metasedimentary block. Although it is apparent that the non-rotated models have resolved slightly less structure at depth than the rotated models, the discussion presented here is not intended to be a comprehensive overview of the topic of model and data rotation. For detailed investigation of the effects of rotation on MT inversion, the reader is referred to other works such as [Tietze and Ritter \(2013\)](#).

As the mesh and data rotation does affect 3D inversion results, it is the changes in Δ , the logarithmic difference between N_c and N_o , that are of most interest to this research. The small variations between the resistivity images of N_c and M_c have the consequence that the distributions of Δ are not expected to be identical, as can be clearly seen. The rotated models M show elevated values of Δ , extending to greater depths than in the non-rotated models N . With the caveat that the resistivity distributions cannot be declared equivalent between the M and N models (i.e. the differences observed between N and M models cannot be categorically defined as purely due to rotation), it appears that rotation of the inversion mesh and data exaggerate the effects of static shift correction on the resulting model. For example, if the depth slices from 1550 m are considered, the distributions of Δ for the rotated models M generally show magnitudes that are elevated approximately a quarter of an order of magnitude greater than those of the non-rotated models N . It should be noted that even with the reduced magnitudes of Δ in the non-rotated N models, the effects of static shift correction still propagate to 2 km depth within the models.

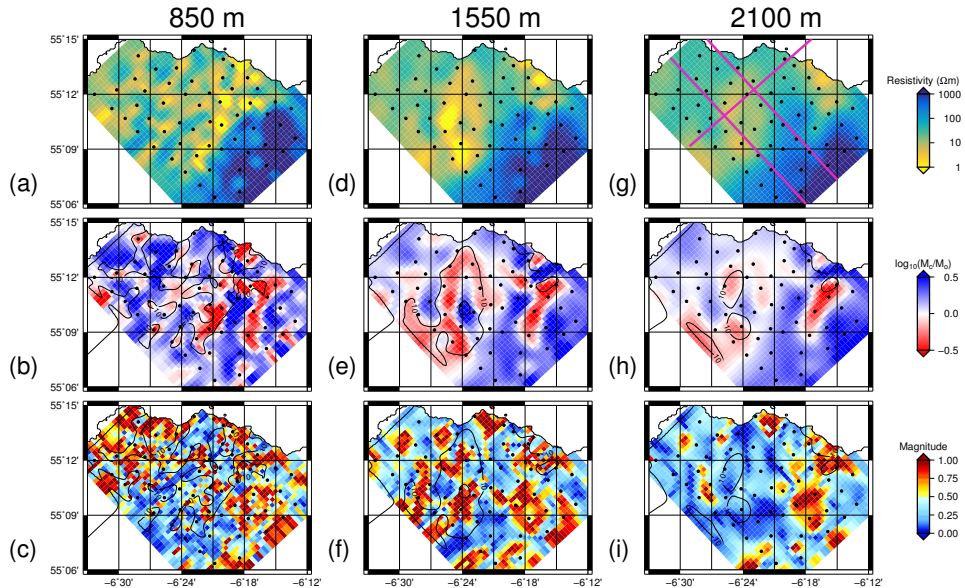


Figure 2.18.: Top row shows resistivity slices through the rotated, static-shift-corrected model M_c taken at 850 (a), 1550 (d), and 2100 (g) metres below sea level. Middle row shows the resistivity difference Δ between the non-rotated models in decades ($\Delta(M_c, M_o) = \log_{10}(M_c/M_o)$) for the same depths, where red shows M_c more conductive than M_o and blue more resistive. Bottom row shows the magnitude of the normalised cross-gradient (the cross-product of the gradient vectors of models ∇M_c and ∇M_o) as a diagnostic of structural similarity between the models, with 0 (blue) showing parallel gradient vectors (i.e. very similar structure), and 1 (red) showing orthogonal gradient vectors and structural disagreement. The difference and cross-gradient plots are overlaid by the 10 Ωm contour from the corresponding resistivity slice. Magenta lines in subplot (g) indicate the location of Profiles A, B, and C.

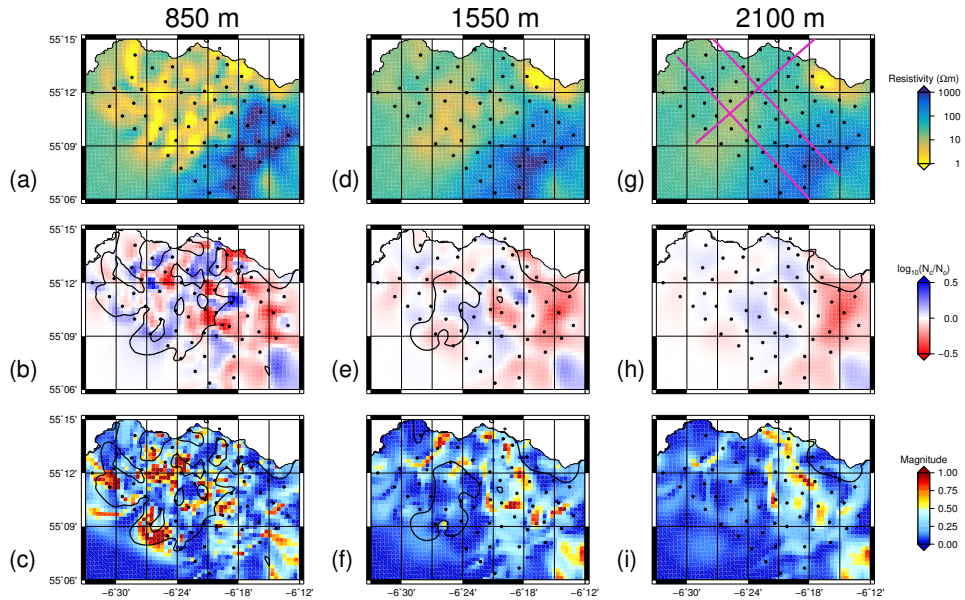


Figure 2.19.: Top row shows resistivity slices through the non-rotated, static-shift-corrected model N_c taken at 850 **(a)**, 1550 **(d)**, and 2100 **(g)** metres below sea level. Middle row shows the resistivity difference Δ between the non-rotated models in decades ($\Delta(N_c, N_o) = \log_{10}(N_c/N_o)$) for the same depths, where red shows N_c more conductive than N_o , and blue more resistive. Bottom row shows the magnitude of the normalised cross-gradient (the cross-product of the gradient vectors of models ∇N_c and ∇N_o) as a diagnostic of structural similarity between the models, with 0 (blue) showing parallel gradient vectors (i.e. very similar structure) and 1 (red) showing orthogonal gradient vectors and structural disagreement. The difference and cross-gradient plots are overlaid by the 10 Ωm contour from the corresponding resistivity slice. Magenta lines in subplot **(g)** indicate the location of Profiles A, B and C.

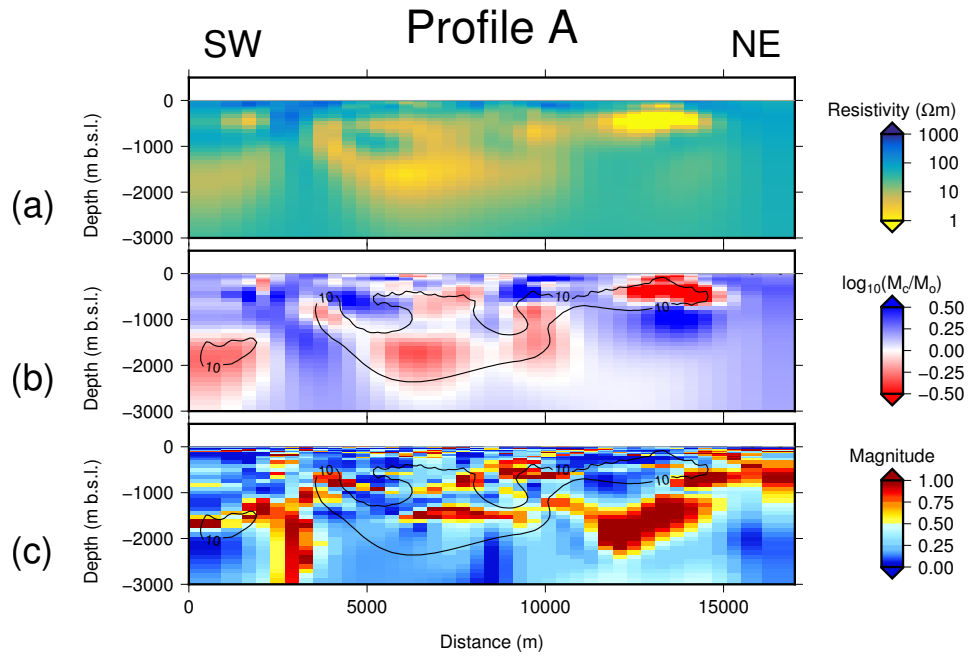


Figure 2.20.: Profile A taken along the axis of the concealed basin through the static-shift-corrected resistivity model M_c (location shown in Figures [Figure 2.11g](#) and [Figure 2.19g](#)). The resistivity is shown in **(a)**, the resistivity difference $\Delta(M_c, M_o)$ is shown in **(b)**, and the cross-gradient of M_c and M_o is shown in **(c)**. Contours on the difference and cross-gradient plots show the $10 \Omega\text{m}$ contour. For presentation a vertical exaggeration of 1.5 is used.

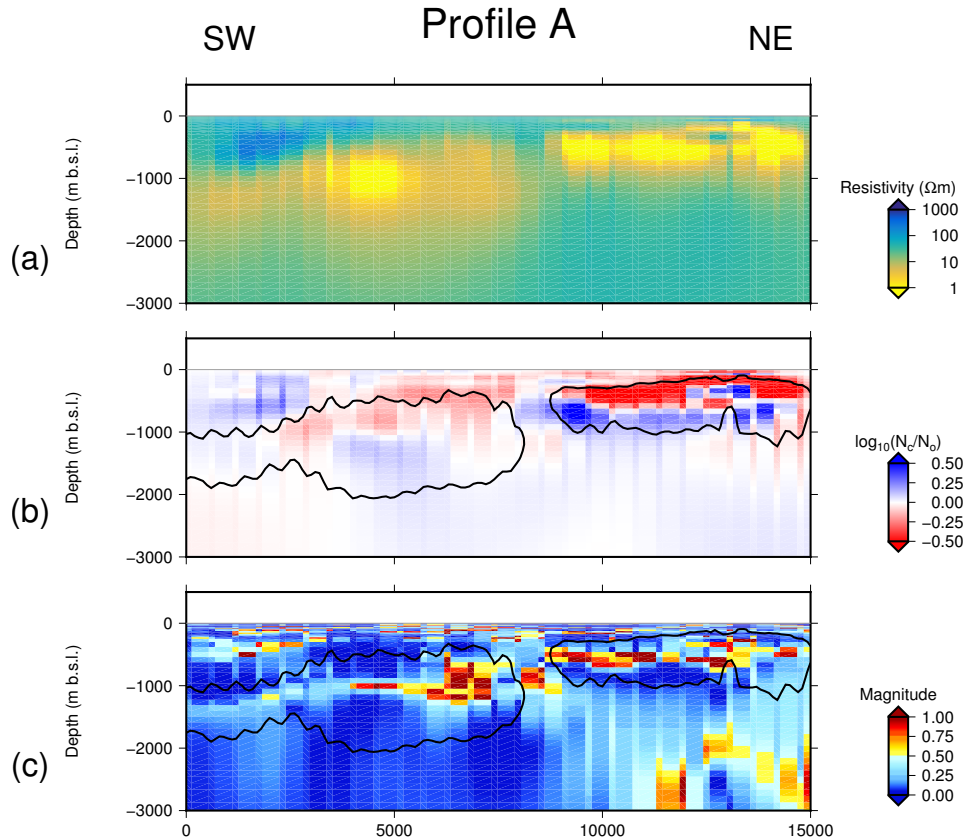


Figure 2.21.: Profile A taken along the axis of the concealed basin through the non-rotated, static-shift-corrected resistivity model N_c (location shown in Figures [Figure 2.11g](#) and [Figure 2.19g](#)). The resistivity is shown in **(a)**, the resistivity difference $\Delta(N_c, N_o)$ is shown in **(b)**, and the cross-gradient of N_c and N_o is shown in **(c)**. Contours on the difference and cross-gradient plots show the $10 \Omega\text{m}$ contour. For presentation a vertical exaggeration of 1.5 is used.

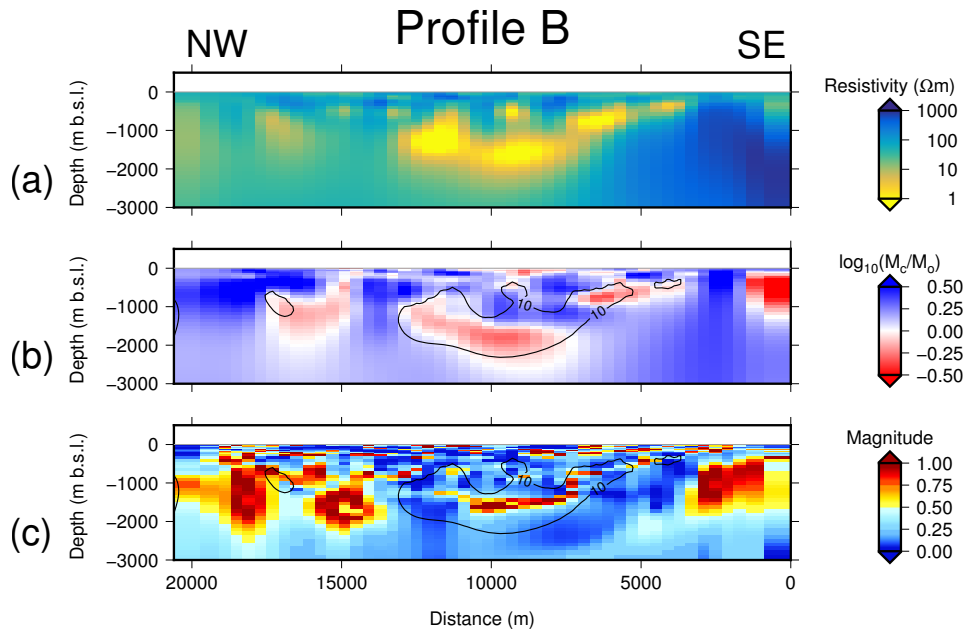


Figure 2.22.: Profile B taken across the static-shift-corrected resistivity model M_c (location shown on Figures [Figure 2.11g](#) and [Figure 2.19g](#)). The resistivity is shown in **(a)**, the resistivity difference $\Delta(M_c, M_o)$ is shown in **(b)**, and the cross-gradient of M_c and M_o is shown in **(c)**. Contours on the difference and cross-gradient plots show the $10 \Omega\text{m}$ contour. For presentation a vertical exaggeration of 1.5 is used.

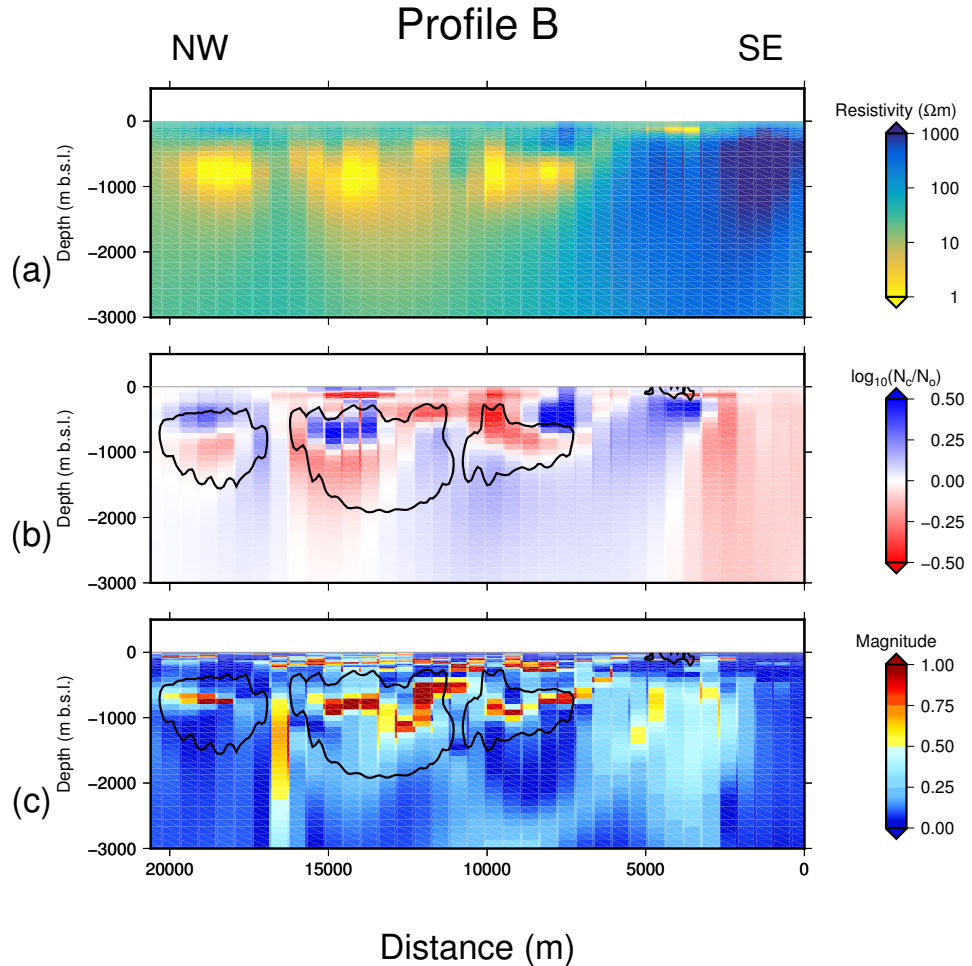


Figure 2.23.: Profile B taken across the non-rotated, static-shift-corrected resistivity model N_c (location shown in Figures [Figure 2.11g](#) and [Figure 2.19g](#)). The resistivity is shown in **(a)**, the resistivity difference $\Delta(M_c, M_o)$ is shown in **(b)**, and the cross-gradient of N_c and N_o is shown in **(c)**. Contours on the difference and cross-gradient plots show the $10 \Omega\text{m}$ contour. For presentation a vertical exaggeration of 1.5 is used.

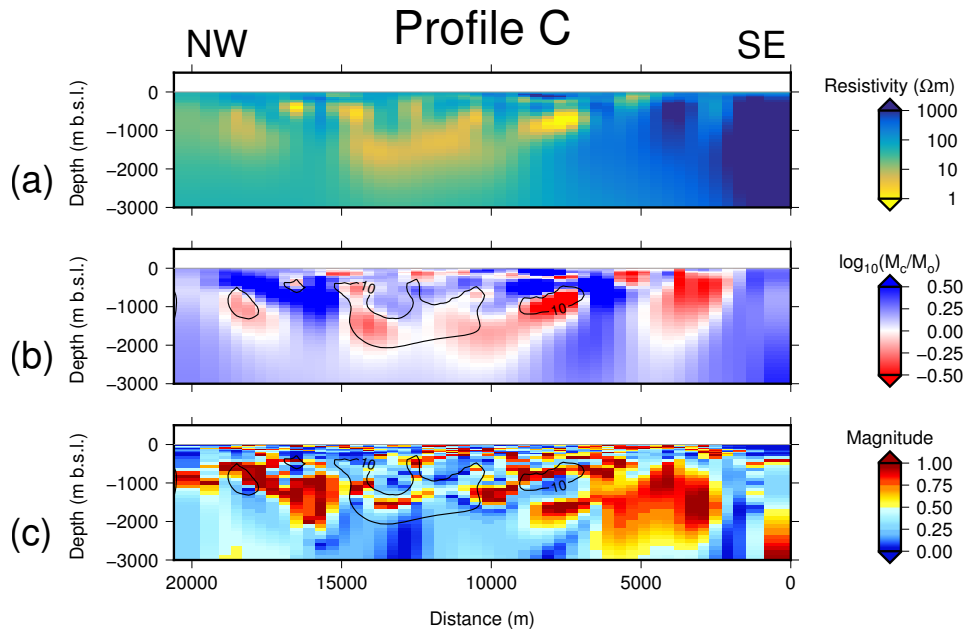


Figure 2.24.: Profile C taken across the static-shift-corrected resistivity model M_c (location shown in Figures [Figure 2.11g](#) and [Figure 2.19g](#)). The resistivity is shown in **(a)**, the resistivity difference $\Delta(M_c, M_o)$ is shown in **(b)**, and the cross-gradient of M_c and M_o is shown in **(c)**. Contours on the difference and cross-gradient plots show the $10 \Omega\text{m}$ contour. For presentation a vertical exaggeration of 1.5 is used.

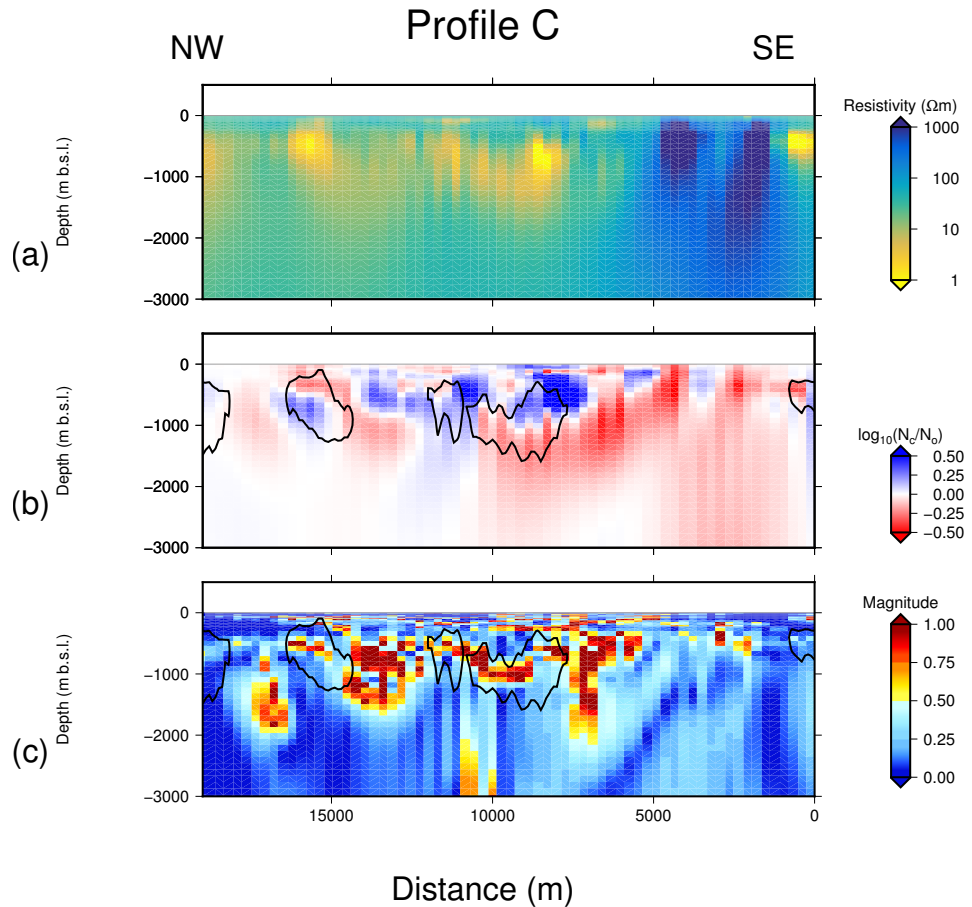


Figure 2.25.: Profile C taken across the non-rotated, static-shift-corrected resistivity model N_c (location shown on Figures [Figure 2.11g](#) and [Figure 2.19g](#)). The resistivity is shown in **(a)**, the resistivity difference $\Delta(N_c, N_o)$ is shown in **(b)**, and the cross-gradient of N_c and N_o is shown in **(c)**. Contours on the difference and cross-gradient plots show the $10 \Omega\text{m}$ contour. For presentation a vertical exaggeration of 1.5 is used.

3

QUANTITATIVE GEOTHERMAL INTERPRETATION OF ELECTRICAL RESISTIVITY MODELS OF THE RATHLIN BASIN, NORTHERN IRELAND

3.1 ABSTRACT

In the evaluation of low– to medium–enthalpy geothermal resources on the island of Ireland, some of the most interesting targets are the deep sedimentary basins of Northern Ireland. The deepest of these is the Rathlin Basin, where Permian and Triassic reservoir sediments are known to exist to at least 2300 m depth. Two deep boreholes within the basin provide evidence of elevated temperatures at depth that are atypical within Ireland, prompting further geophysical exploration of the basin as one component of the IRETHERM project. The magnetotelluric (MT) method was selected as the investigative geophysical tool as it is capable of sensing and defining electrically conductive porous sediments beneath overlying resistive strata, in this case flood basalt sequences. MT data were acquired on a rectangular grid of 39 sites across almost half of the onshore basin to investigate the composition and spatial variation of the basin’s formations.

One-dimensional stochastic inverse modelling of the observed MT data was with a reversible-jump Markov chain Monte Carlo 1D inversion code, resulting in ensembles of models for each site. The use of model ensembles rather than single models avoids the pitfall of over-reliant interpretation on non-unique resistivity models, increasing the robustness of the interpretation. Interpreted models compare very favourably with nearby deep borehole records, and interpolation of the complete set of ensemble interpretations results in a conservative reservoir volume of approx. 32 km^3 of combined Permian and Triassic sandstones beneath the MT survey.

Based upon new, high quality temperature data available in the Ballinlea 1 borehole, an approximate estimation of thermal energy in place as a function of final reservoir temperature has been performed for the interpreted MT resistivity model volume. A final minimum temperature of 25 °C (being the temperature that comparable estimates have been made for adjacent geothermal prospects) results in a minimum estimated Indicated Geothermal Reserve (IGR) of $2.9 \times 10^{18} \text{ J}$

This chapter has been published as: R. Delhaye, V. Rath, A. G. Jones, M. R. Muller, and D. Reay. Quantitative geothermal interpretation of electrical resistivity models of the Rathlin Basin, Northern Ireland. *Geothermics*, 77C: 175–187, 2019.

beneath the MT survey area. The modelling results suggest that exploitation of the maximum volume of sediments would occur for a final temperature of $\approx 55^{\circ}\text{C}$.

3.2 INTRODUCTION

The Rathlin Basin is a significant sedimentary depocentre in Northern Ireland (Figure 3.1), comprising a succession of Carboniferous to Cretaceous strata. Permian and Triassic sandstone formations within the basin are known to act as hydrocarbon reservoir formations offshore, in the Irish Sea to the east (Richardson and Neymeyer, 2013). Equilibrated temperature measurements in two local boreholes - Port More 1 (PM1) and Ballinlea 1 (B1), respectively - in the basin show elevated geothermal gradients in comparison to the mean regional gradient, suggesting that the porous sediments function as a geothermal aquifer. As hydrothermal fluid is typically saline and thus conducts electrons well, if the porous sediments are saturated with a hydrothermal brine and the fluid is sufficiently connected, they should be electrically distinct to the surrounding basal material and overlying aquitard formation and be resolved using appropriate deep-probing electromagnetic methods.

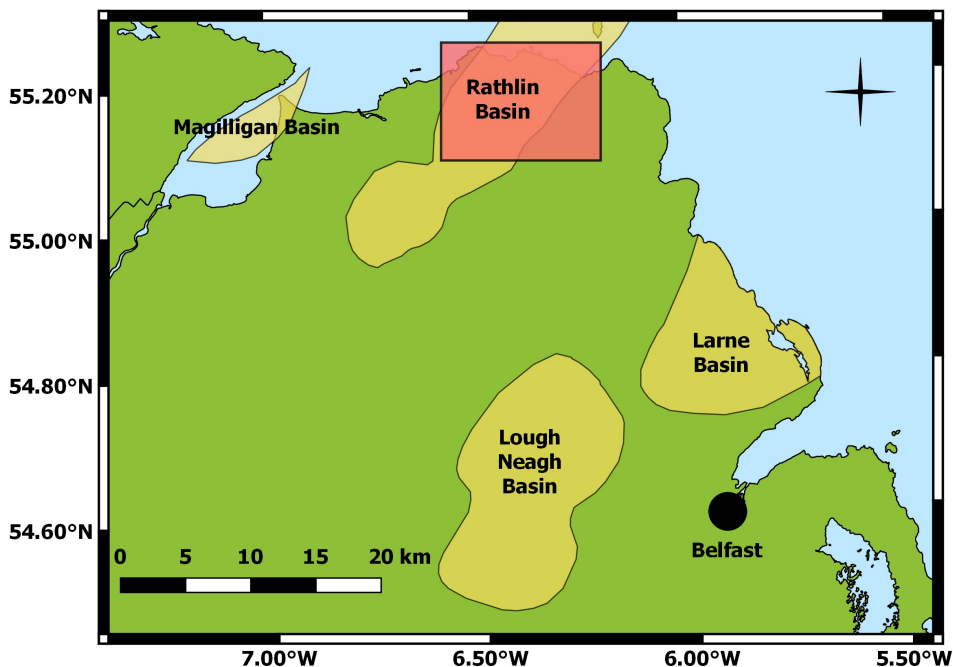


Figure 3.1.: Regional map of onshore sedimentary basins (yellow) within Northern Ireland (Belfast shown for location). The area of research considered in this article is shown by the red rectangle over the Rathlin Basin.

Several sets of geophysical data have previously been acquired across the basins of Northern Ireland, including gravity data, seismic reflection data, and most recently regional airborne geophysical data (aeromagnetic, radiometric and frequency-domain electromagnetic data). However, both the seismic reflection data and aeromagnetic data are dominated by the regionally present Antrim Lava group due to (1) its negative acoustic impedance contrast with respect to the underlying stratigraphy and irregular internal geometry at its base, and (2) its significant magnetic signature, respectively. Regional gravity data have been modelled, with results published in Mitchell (2004) that attribute a maximum depth of ≈ 4 km to the base of the Permian and Triassic sediments; the authors of Mitchell (2004) note that this model assumes relatively low density Carboniferous sediments as observed in the adjacent Magilligan Basin to the west (see Figure 3.1). If the Carboniferous sediments within the Rathlin Basin are of higher density than those of the Magilligan Basin then a greater thickness of the lower density Permian and Triassic formations would be required to remain consistent with the observed gravity anomaly.

Existing resistivity wireline logs from one of the boreholes confirm the electrical distinction of formations, suggesting that methods sensing lateral and vertical variation in electrical conductivity may be very productive. Hence, natural-source electromagnetic surveying using the magnetotelluric (MT) method of exploration of the onshore portion of the basin was carried out to evaluate the low- to medium-enthalpy geothermal potential of the Rathlin Basin.

In order to improve the accuracy of recovered resistivities from the modelling of MT data, the MT data were treated prior to inversion modelling for a form of galvanic electric field distortion known as "static-shift". MT data are affected by near-surface resistivity structure below the resolution of the method, resulting in biased estimates of the electric field, and accordingly MT impedances ("static-shift"-type distortion, as described in e.g. Berdichevsky and Dmitriev, 1976; Jones, 1988; Chave and Jones, 2012). A number of approaches have been developed to compensate for this distortion, and as our survey area fortunately falls within the area covered by the regionally available airborne EM data from the Tellus Project (Young, 2016), we successfully adapted the method of Pellerin & Hohmann (Pellerin and Hohmann, 1990). The method of Pellerin & Hohmann (Pellerin and Hohmann, 1990) originally modelled ground-based time domain EM measurements to find a simple near-surface one-dimensional (1D) structure, and MT data were shifted to match the responses of this simple structure. We have adapted this approach by modelling airborne frequency domain EM (FDEM) data in place of the ground-based time domain EM data; specifically, we determine a best-fitting single layer half-space resistivity model from the four frequency data at each measurement location, then collate these individual models into the top layers of a 3D resistivity forward model. The magnitudes of the MT responses from the forward model (i.e. the apparent resistivities) are compared with those of the observed data, and corrective factors δ_{E_x} , δ_{E_y} were found to reconcile the observed to calculated magnitudes. Full details of our approach to static-shift correction are presented in Delhayé et al. (2017).

This study presents the results of one-dimensional (1D) modelling of the MT data acquired over the northern half of the onshore part of the Rathlin Basin, and a geothermal interpretation of the

basin in the context of existing geological and geophysical constraints. It follows the methodological study of static-shift correction of relevant MT data presented in [Delhaye et al. \(2017\)](#). Comparisons of models from the static-shift-corrected and original MT data show improved recovery of layer depths and thicknesses when compared to borehole information in this area, and hence all the results presented here were derived from the static-shift corrected MT data. In this paper we present an overview of the current knowledge of the basin, followed by an interpretation of 1D resistivity models derived from the MT data over the basin with respect to the existing knowledge. In conjunction with new temperature data acquired within the basin, the interpreted resistivity models are used to estimate the geothermal reservoir volume and associated geothermal heat energy in place.

3.3 TECTONIC AND GEOLOGIC SETTING

The surficial geology of the Rathlin Basin is dominated by Paleogene volcanics that conceal much of Northern Ireland's older geological formations. A map showing the surficial geology of the survey area is presented in [Figure 3.2](#), together with borehole and MT site locations, modelling profiles, and the surface trace of the major Tow Valley Fault. The geology of the Rathlin Basin is described in detail in [Mitchell \(2004\)](#). The Rathlin Basin lies within one of the seven identifiable terranes that comprise modern-day Ireland; specifically, the basin lies within a region consisting of mid- to late-Neoproterozoic (1000–545 Ma) metamorphic and metasedimentary rocks collectively termed the Dalradian Supergroup. Due to extensive deformation and metamorphism associated with the Grampian orogeny (475–470 Ma), the Dalradian rocks are expected to have reduced levels of hydraulic porosity and permeability, and hence elevated electrical resistivities. During the subsequent Variscan orogenic cycle (350–250 Ma), regional shear and stress reactivated the pre-existing Caledonian (490–390 Ma) Tow Valley Fault (TVF). The resulting normal and dextral strike-slip faulting created the rift basin that would later fill with Carboniferous, Permian and Triassic aged sediments to become the Rathlin Basin.

3.4 STRATIGRAPHY

Stratigraphic information relevant to our study is mainly derived from the two deep boreholes within the basin, Port More 1 and Ballinlea 1 (locations in [Figure 3.2](#); see [Figure 3.3](#) for Port More 1 borehole stratigraphy). As the base of the Rathlin Basin sedimentary fill has not yet been reached by drilling, Carboniferous sediments encountered in the Ballinlea 1 borehole are assumed to be the basal lithology sediments. The assumption of basal sediments is supported by the presence of Carboniferous formations in the adjacent, shallower Magilligan Basin (locality in [Figure 3.1](#)). Above the Carboniferous strata lie two Permian formations, the early-Permian Enler (EG) and Belfast (BG) groups, of interest as the formations have been observed to have favourable hydraulic properties for hydrocarbon reservoirs ([Naylor and Shannon, 2011](#)). The BG is overlain by

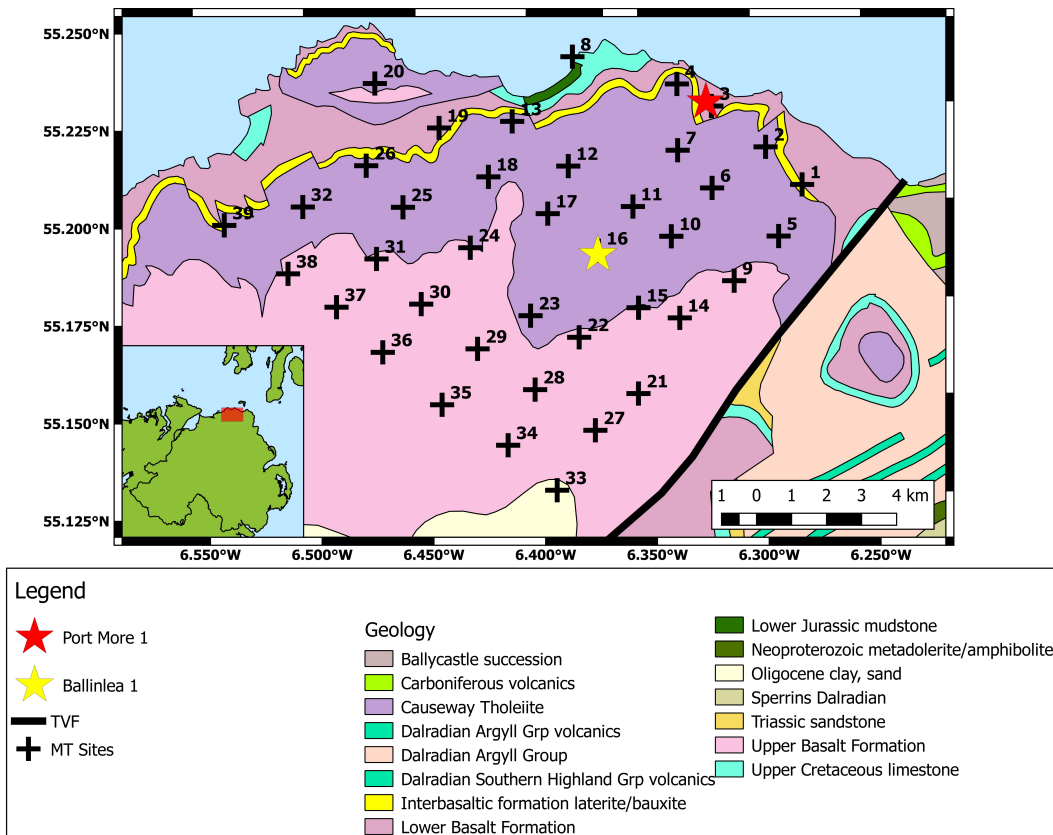


Figure 3.2.: Surficial geology of the Rathlin Basin survey area in Northern Ireland, overlain by magnetotelluric (MT) acquisition sites (numbered black pluses) and borehole locations (PM1, red star on the north-east coast, B1, yellow star further inland). The bold black line shows the location of the Tow Valley Fault. (For interpretation of the references to colour in this figure legend, the reader is referred to the web version of the article.)

the early-Triassic Sherwood Sandstone Group (SSG), with hydraulic properties comparable to the underlying BG. The SSG is overlain by the late-Triassic Mercia Mudstone group (MMG), which in turn is overlain by the early-Jurassic Lower Lias group (LLG) mudstones. However, the PM1 borehole encountered a significant thickness of dolerite and basalt sills between the LLG and MMG formations, and the spatial extent of these intrusions is unknown across the basin. The youngest sediments within the basin are early-Cretaceous Ulster White Limestone formation (UWLF) chalcites, overlying the LLG. Finally, the entire basin is concealed beneath the Antrim Lava group (ALG) of Paleogene flood basalts, which forms part of the North Atlantic Igneous Province ([Mitchell, 2004](#)). The age ranges of these formations are shown in [Table 3.1](#).

3.5 BOREHOLES

To date two near-vertical boreholes have been drilled to significant depth within the onshore Rathlin Basin, namely, the aforementioned Port More 1 (PM1, 1967) and Ballinlea 1 (B1, 2008) boreholes

Table 3.1.: Ages and petrographic descriptions of the formations in the Rathlin Basin. Age is listed by both epoch and millions of years. Values and descriptions taken from [Mitchell \(2004\)](#)

Formation	Epoch	Age (Ma)	Petrography
Antrim Lava group (ALG)	Paleocene	61–58	Basalt, tuff layers
Ulster White Limestone formation (UWLF)	Early Cretaceous	85–69	Chalk, some flint
Lower Lias Waterloo mudstones (LLG)	Early Jurassic	199–182	Mudstone, thin limestone
Dolerite sills	Paleocene	61–58	Dolerite, basalt
Mercia Mudstone group (MMG)	Late Triassic	247–209	Mudstone, siltstone
Lagavarra Formation (LF)	Late Triassic	247–209	Sandstone, siltstone, thin mudstone
Sherwood Sandstone group (SSG)	Early Triassic	252–247	Fine-grained sandstone
Belfast group (BG)	Late Permian	260–252	Sandstones, claystones, marls
Enler group (EG)	Early Permian	290–272	Fine-grained sandstone

(locations in [Figure 3.2](#)), with measured total depths of \approx 1900 and \approx 2700 m below surface respectively. Wireline log data, detailed lithological logs and temperature measurements to 1481 m depth are publically available from the PM1 borehole. Equilibrated (i.e. at sufficient post-drilling time such that borehole fluids are in thermal equilibrium with adjacent rock - an equilibration period of 10–20 times the drilling time has been suggested by [Bullard \(1947\)](#); [Beardmore and Cull \(2001\)](#)) temperature measurements from the B1 borehole have also been recently acquired by Schlumberger on behalf of Rathlin Energy (UK) Ltd.

3.5.1 Port More 1 borehole

The PM1 borehole was drilled in 1967 to a near-vertical depth of 1900 m below surface to explore for coal and evaporite minerals at depth within the Rathlin Basin ([Wilson and Manning, 1978](#)). Based on modelling of the then-available gravity data, the borehole was predicted to intersect Carboniferous lithologies at a depth of \approx 1500 m. However, a succession of dolerite sills was encountered in the hole ([Figure 3.3](#)), the elevated density of which had a strong effect on the gravity anomaly used to estimate the expected depths. As a consequence, the Permian and Triassic sediments extend to far greater depth than predicted from the gravity model, and the base of the Permian sequence was not reached by the depth at which drilling terminated due to technical difficulties.

In addition to the lithological sequence itself ([Figure 3.3](#)), several sets of geophysical data were also acquired from downhole measurements. Gamma ray and neutron porosity data were logged from the surface to 1481 m depth (the base of the borehole was not reached due to technical difficulties), with DC resistivity and self-potential logs also acquired through the Mercia Mudstone

and Sherwood Sandstone groups (MMG and SSG, respectively) from 1050 to 1450 m. Equilibrated temperature data were measured in the uppermost 600 m of the borehole, with interval geothermal gradient estimates ranging from 20 K km^{-1} in the Ulster White Limestones to 50 K km^{-1} in the Lower Lias and dolerite sills. Although Wilson and Manning (1978) accounted for paleoclimate effects (Beardmore and Cull, 2001), due to the shallow depths of temperature measurement these geothermal gradients shed little insight on the deeper formations of interest.

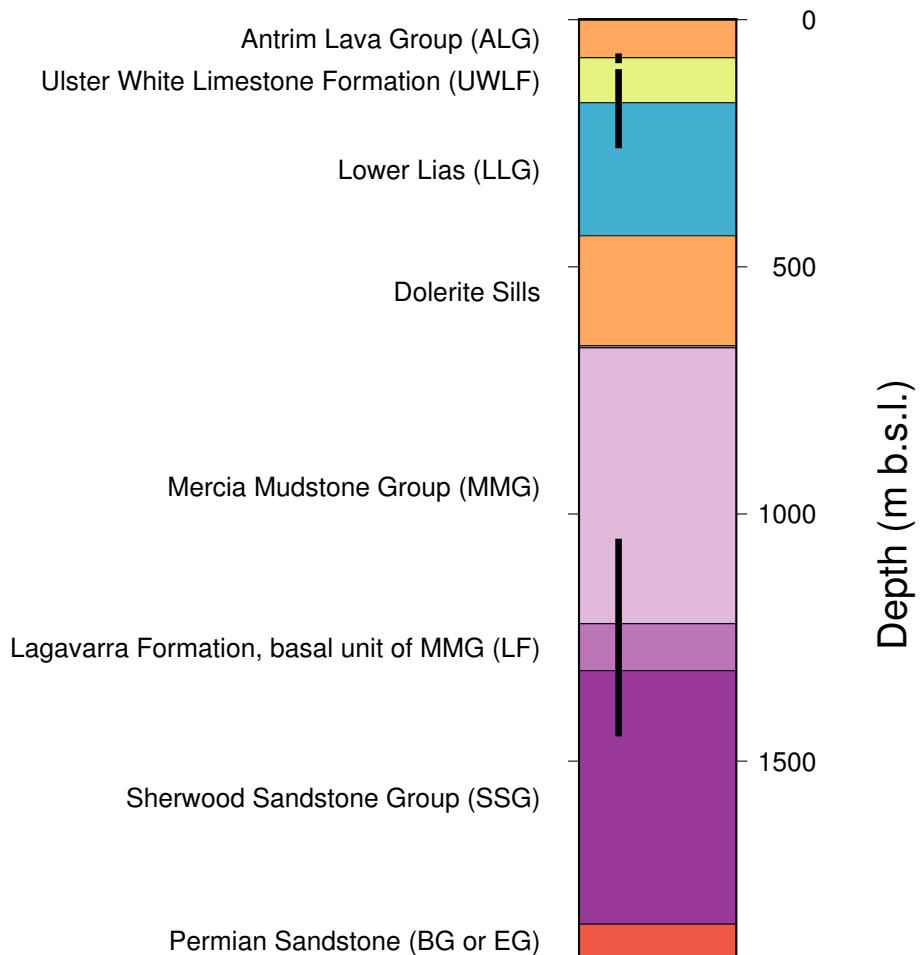


Figure 3.3.: Formations encountered in the PM1 borehole (see Figure 3.2 for location). The borehole terminated at 1900 m depth, within Permian sandstones. It is unclear whether the Permian sandstones are of the Belfast (hydraulically favourable) or Enler group (less hydraulically favourable). Due to technical difficulties regarding the diameter of the hole, wireline logs were only acquired in several depth ranges; these intervals are marked by the solid black vertical lines.

3.5.1.1 DC resistivity log

DC resistivity wireline logs sample the near-hole resistivity distribution of the borehole over the length of a "sonde", the downhole tool, producing resistivity data at a resolution far greater than achievable by MT or any other surface electrical or electromagnetic geophysics (Ellis and Singer, 2008), but sampling only a small volume ($< 1 \text{ m}$) around the borehole, whereas MT and other

EM methods produce a volumetrically integrated average from the surface to the depth of interest. The resistivity log was acquired over the depth interval from 1050 to 1450 m in the PM1 borehole (denoted by vertical black bar in Figure 3.3), which covers the lower portion of the Mercia Mudstone group (MMG) and the upper portion of the Sherwood Sandstone group (SSG). The resistivity data are plotted in Figure 3.4 (left column). Although the data are highly variable within each formation, reflecting the highly localised sampling of heterogeneous material, clear differences between the formation samples are evident. Furthermore, the 95 m thick Lagavarra Formation (LF), which forms the base of the MMG, comprises a mix of sandstone and mudstone layers, and by treating this formation as a separate unit the resistivity differences remain. Histograms of each of these sample groups are also shown in Figure 3.4 (right column), as are the respective logarithmic median resistivities of 3.2 Ωm (MMG), 4.8 Ωm (LF), and 6.2 Ωm (SSG).

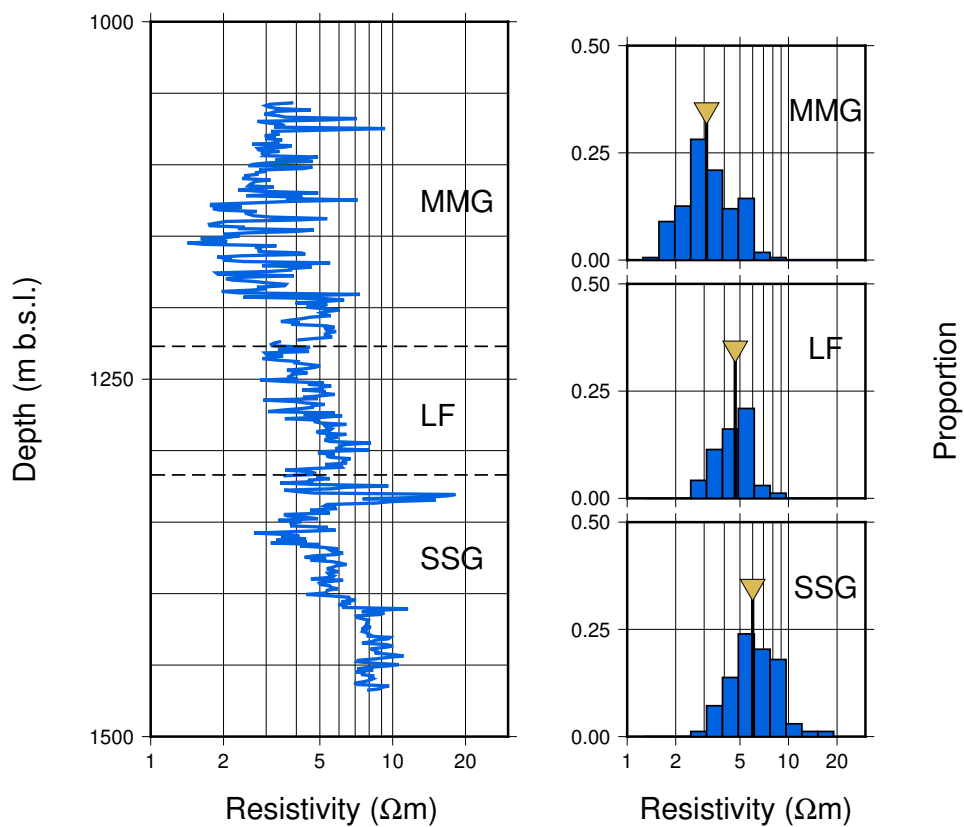


Figure 3.4.: Left-hand subfigure shows measured resistivity data with depth from 1050 to 1450 m in PM1 borehole, sampling from the Mercia Mudstone group (MMG) into the underlying Sherwood Sandstone group (SSG). The basal Lagavarra Formation (LF) within the MMG is also labelled. The MMG and LF formations are relatively consistent in their resistivities, with a slight increase in resistivity below 1150 m, whereas the SSG tends to continue to increase in resistivity. In order to examine further the increase in resistivity with depth, the log-resistivity distributions from each of the three units are shown in the right-hand subfigures. Given the differences in central tendency of each formation, the units can be assumed to have distinct median resistivities (marked by vertical black line with yellow triangles). (For interpretation of the references to colour in this figure legend, the reader is referred to the web version of the article.)

Although downhole resistivity tools and MT each give information about the resistivity of the Earth, the two methods rarely return the same information due to differences in sampling methodologies and underlying physics. Downhole tools typically observe resistance to near-vertical DC currents across distances <1 m, whereas the MT method infers resistance to inductive (time-varying), near-horizontal electric fields over distance scales of the depths of interest, typically tens to thousands of metres. In addition to the difference in scale, the orientation of the electric fields can also play a part due to electrical anisotropy within the media themselves. As a result, for the purposes of MT modelling the borehole resistivity measurements are limited to that of supporting qualitative information on the relative resistivities of the sediments.

3.5.1.2 *Neutron porosity log*

The neutron porosity log measures the absorption of emitted neutrons by the rock formation, and is strongly sensitive to the presence of hydrogen - typically, the presence of clays, shales, or formation waters in pore spaces. As high concentrations of hydrogen are found in multiple different forms, older neutron porosity data are reported in American Petroleum Institute (API) units rather than a percentage porosity ([Scott, 1984](#)). It should be noted that an increase in API units of neutron porosity corresponds with a *decrease* in hydrogen content (i.e. a decrease in neutron porosity indicates an increase in clay, shale, water or oil content of the formation).

[Figure 3.5](#) (left column) shows the neutron porosities (in orange) and electrical resistivities (in blue) observed in the PM1 borehole across the sedimentary units of interest. Normalised correlations between these quantities are also shown for the MMG, LF and SSG, with a correlation of 1 indicating that resistivity and neutron porosity fluctuate in unison with the specified lag. This is exemplified by the cross-correlations of the MMG and SSG, each of which spikes to ≈ 0.8 with zero lag. As there is a well-documented empirical relationship (Archie's Law) between a sandstone formation's effective porosity and effective resistivity (defined in [Archie \(1947\)](#), discussed at length in [Glover \(2010\)](#), and specifically for relevant Irish lithologies in [Campanyà et al. \(2015\)](#)), the strong positive correlation between neutron porosity (recalling the inverse relationship between neutron porosity and percentage porosity) and resistivity implies that the fluid content of pore spaces has a lower resistivity than the surrounding sandstone or mudstone matrix. As the MMG formation is known to have generally poorer hydraulic properties we interpret the strong correlation between MMG neutron porosity and resistivity as indicative of elevated clay content, whereas for the known porous and permeable SSG unit we interpret the correlation as indicative of elevated porosity or permeability.

3.5.1.3 *Laboratory porosity and permeability measurements*

Laboratory measurements of porosity and hydraulic permeability taken from SSG core samples from the PM1 borehole are presented in [Wilson and Manning \(1978\)](#). The measured porosities and hydraulic permeabilities are plotted in [Figure 3.6](#), colour coded by the depth at which the respective samples were recovered. Note that the permeability measurements were corrected for Klinkenberg effects, i.e. corrections have been applied to compensate for viscosity and density differences

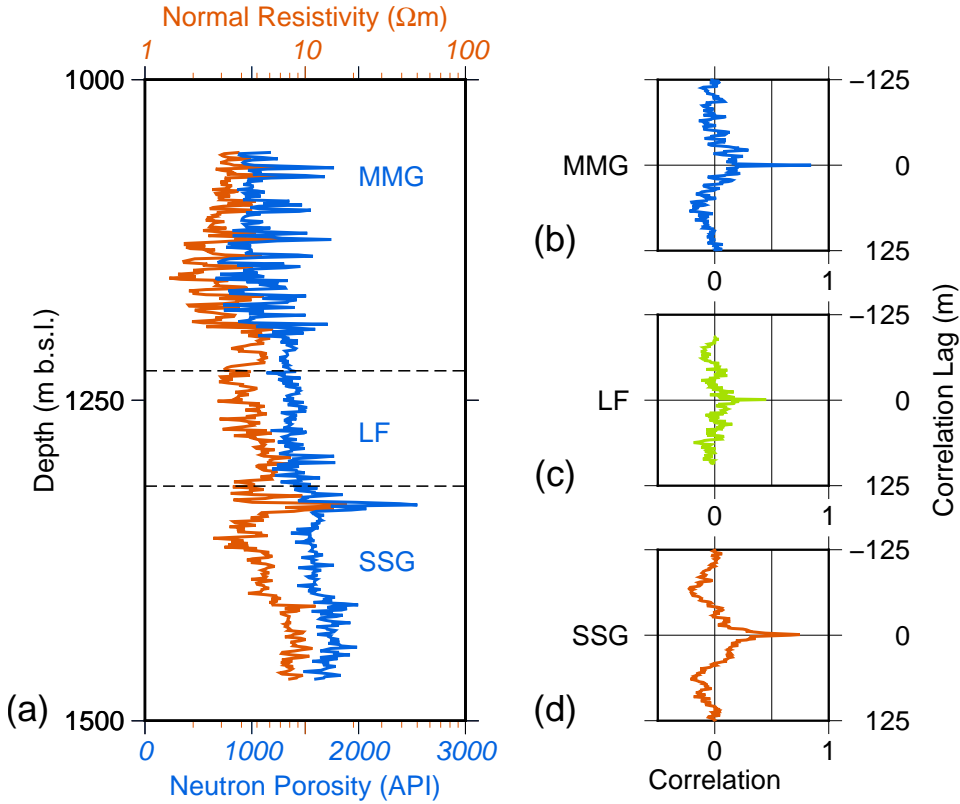


Figure 3.5.: Left-hand subfigure shows the measured neutron porosity (in American Petroleum Institute - API - units) in blue, and the measure wireline resistivities in orange from the deeper section of the PM1 borehole. Note that neutron porosity data when presented in API units has a negative correlation with true percentage porosity. The right-hand subfigures show the normalised correlation between the neutron porosity and resistivity in each of the three formations marked (i.e. MMG, LF, and SSG), where a correlation of 1 describes two data sets that fluctuate in perfect unison. Both the MMG and SSG show strong correlations between neutron porosity and resistivity, implying that the formations' resistivities are strongly affected by porosity or clay content. The reduced correlation peak amplitude of the LF implies that the properties are more weakly linked, with some other factor influencing one or both of porosity and resistivity.

between the gas used in laboratory measurements and the expected pore fluids. Klinkenberg correction also accounts for the Klinkenberg effect, where in low flow (i.e. low permeability) situations a gas will not encounter the same boundary effects within pores as a liquid (Klinkenberg, 1941). The change in relationship between porosity and log-permeability above moderate permeabilities (i.e. $\Phi > 18\%$) is typical of clastic rocks, and arises from the development of sufficient flow velocities so as to create boundary layers within the flow paths that impede some of the flow Chilingarian and Wolf (1975); Bernabe et al. (2003).

3.5.2 Ballinlea-1 borehole

Equilibrated temperature measurements in the B1 Borehole on behalf of Rathlin Energy (UK) Ltd., confirm the elevated temperatures previously reported within the basin, shown in Figure 3.7. The

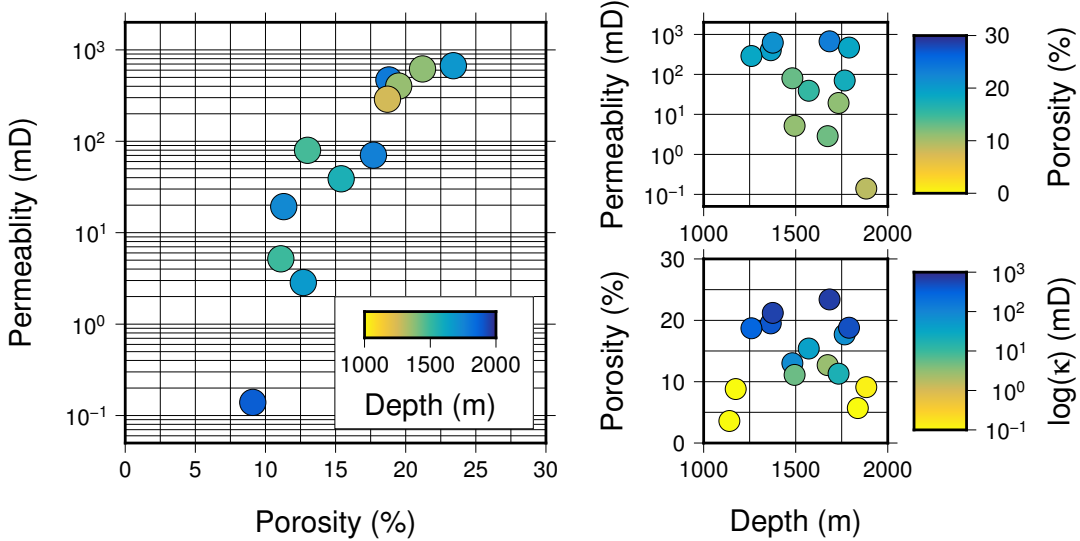


Figure 3.6.: Left figure: distribution of percentage porosities against Klinkenberg-corrected (i.e. a correction that accounts for the slightly different behaviours of the gas used in laboratory measurements, and the *in situ* liquids expected) permeabilities in twelve core samples taken from the SSG and underlying Permian (Belfast or Enler) sandstones from the PM1 borehole, coloured by estimated depth of recovery. The near-linear relationship between percentage porosity and the logarithm of permeability, with a change in gradient (here at approx. 17 % porosity), is common in clastic rocks due to changes in flow conditions with increasing pathway volumes. Right-upper figure: distribution of permeabilities against estimated depth of recovery. Right-lower figure: distribution of porosities against estimated depth of recovery. Note that neither permeability nor porosity has a distinct relationship with depth. (For interpretation of the references to colour in this figure legend, the reader is referred to the web version of the article.)

temperature data allow estimation of geothermal gradients by piecewise divided differences (i.e. approximating the first vertical derivative of temperature). The relationship between temperature gradients ∇T (geothermal gradients in this case, in Km^{-1}), thermal conductivity λ ($\text{Wm}^{-1}\text{K}^{-1}$), and heat flux density Q (in this case, assumed to be near-vertical, Wm^{-2}), is described by Fourier's Law, given as Equation 3.1,

$$Q = -\lambda \nabla T. \quad (3.1)$$

The thermal conductivity of a lithological unit is primarily dependent on its quartz content and porosity. Provided that there is no significant advective fluid flow, interval geothermal gradient estimates can be taken as a proxy for the inverse of the lithological unit's thermal conductivity. It should be noted that the relationship between thermal conductivity and geothermal gradient can be biased by lingering paleoclimate effects on the temperature field (Beardmore and Cull, 2001; Bodri and Cermak, 2007), however, as the target sediments occur at depths greater than 1 km the paleoclimate effect is likely small (i.e., $< 5 \text{ mWm}^{-2}$ change in heat flow density). As long as adjacent formations have contrasting thermal conductivities, variations in geothermal gradient estimate should be consistent with the formation boundaries. Such a comparison for the observed B1 temperature measurements is shown in Figure 3.7, although visually some of the formations are

thermally indistinct from one another at this scale (i.e. the Lower Lias, MMG and any intermediate dolerite sills). In particular, the SSG and BG formations are thermally indistinct (i.e., the units have very comparable geothermal gradients of $\approx 24 \text{ K km}^{-1}$), as they have similar composition and porosities. However, the deeper, Permian EG formation has a decreased geothermal gradient in comparison to the BG formation. Assuming a constant heat flux, the decrease in geothermal gradient from the BG to EG units suggests a corresponding increase in thermal conductivity, likely due to a decrease in either clay content or porosity in the EG (when compared to the BG), or an increase in quartz content in the EG.

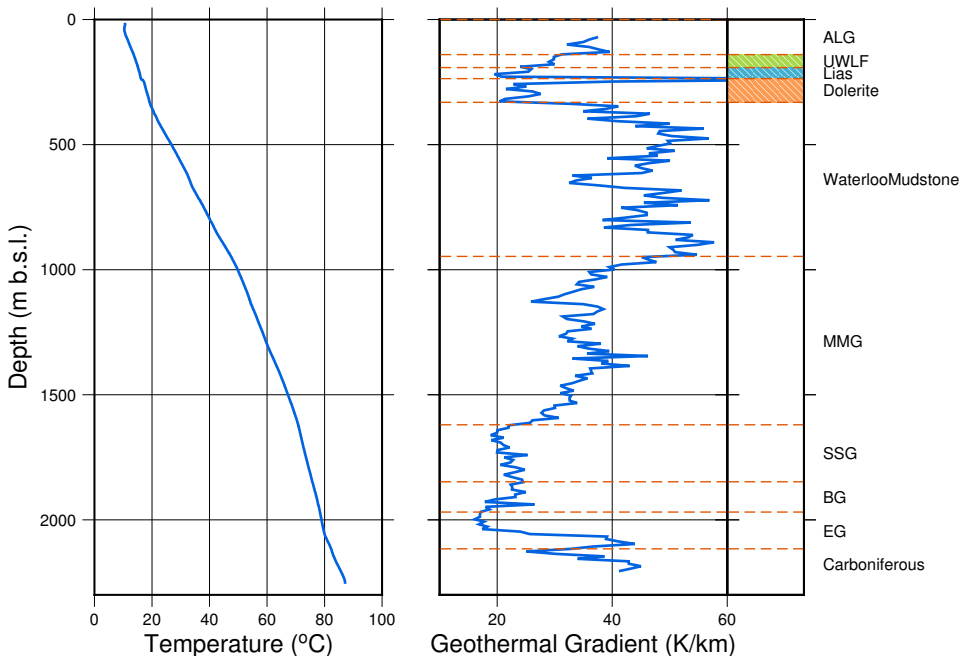


Figure 3.7.: Left-hand panel shows observed temperatures (blue) with depth in the B1 borehole. Observed data were measured in 2015, with sufficient post-drilling time (≈ 7 years) that the temperatures are assumed to be in thermal equilibrium with the surrounding formations. Central panel shows first difference of the temperature data, giving estimates of the geothermal gradient within each formation (assumed to be approximately constant for a unit with "homogeneous" thermal conductivity). Right panel shows formations observed in the B1 borehole. (For interpretation of the references to colour in this figure legend, the reader is referred to the web version of the article.)

3.6 MAGNETOTELLURIC EXPLORATION

The magnetotelluric (MT) method is a geophysical technique that images subsurface electrical resistivity structure by examining the attenuation of electromagnetic (EM) waves within the Earth, and is well described in e.g., Chave and Jones (2012). At the frequencies of the MT method, this attenuation through a body of rock is dependent upon three factors, namely, the frequency of the wave, the electrical resistivity of the rock volume, and the magnetic permeability of the rock volume (generally, insignificantly different to that of free space, although at high frequencies over granitic

plutons one must consider magnetic permeability, e.g., Kao and Orr (1982a,b)). Hence, sampling EM waves with a range of frequencies allows for the derivation of an electrical resistivity model that reproduces the observed MT responses. The electrical resistivity of a volume of Earth material is sensitive to a wide range of factors, including mineral composition, alteration, temperature, and the presence and distribution of fluids. In particular, for the purpose of evaluating the Rathlin Basin as a possible geothermal aquifer, it was expected that the presence of saline geothermal waters in the elevated porosities of the Permian and Triassic sandstones would be manifest as elevated observed electrical conductivities (equivalently, a reduction in observed electrical resistivity).

MT data were acquired over half of the onshore basin area that includes the two boreholes in order to extend understanding of basin structure beyond the two boreholes and mapped geophysical data. MT data were acquired at a total of 39 sites north-west of the bounding Tow Valley Fault (TVF), at locations shown in [Figure 3.2](#). In addition to correction of static-shift type distortion in the MT data, Delhaye et al. (2017) also presents the results of dimensionality analysis by use of the *strike* analysis tool (McNeice and Jones, 2001), implying approximately 1D resistivity structure within the uppermost 3000 m. Although 3D inverse models of the Rathlin Basin MT data are presented in Delhaye et al. (2017), they have been disregarded in favour of 1D inversion of invariant data for this work. This judgement is based primarily upon the sub-optimal acquisition site spacings with respect to the geological targets of interest and general resistivity trends. As the majority of resistivity structure resolved in the 3D models of Delhaye et al. (2017) are within the uppermost 2 km, a large proportion of resolved structure is within the inductive region of only a single site. The advantages of 3D inversion in modelling lateral resistivity structure cannot be fully exploited without overlapping data coverage from adjacent sites, resulting in a "3D resistivity model" that consists of effectively independent models of each site's data interpolated between sites by the inversion algorithm. Given the 1D resistivity structure indicated by dimensionality analysis, it is reasonable to invert the computed 1D data in a strictly 1D sense, and interpolate these models separately, although interpretation is limited to horizontal boundaries. Identifying lateral resistivity structure at scale lengths smaller than the MT site spacings is not feasible based upon the work presented here. The main issue with interpreting pseudo-3D models based upon interpolation of 1D models is the effect of static shift-type distortion, however, in our case such static-shift effects have been addressed (Delhaye et al., 2017).

Monte Carlo inversion of MT data was proposed in 1979 by Jones and Hutton (1979), and has advanced since then. Transdimensional Markov Chain Monte Carlo approaches (MCMC hereafter) have been proposed by several authors (Brodie and Jiang, 2018; Mandolesi et al., 2018) as a means to explore the non-uniqueness and range of plausible 1D inverse models. For sufficiently long Markov chains the ensemble will approximate the posterior probability density (PPD) of the true resistivity-depth model, and conclusions can be drawn about the likelihood of certain model features. Transdimensional implementations of MCMC modelling include the dimensionality of the problem (i.e., the number of layers) as an additional simulated parameter (Green, 1995). For investigation of the Rathlin Basin MT data, four chains of 10 million (i.e., 10^7) models were

computed with the reversible-jump MCMC code of Brodie and Jiang (2018) for each MT site. Model ensembles were computed for invariant MT data (i.e., the geometric mean of apparent resistivities, and arithmetic mean of phases) with assumed error floors of 5% (ρ_a) and $2^\circ(\phi)$, with models defined by a domain of depth bins ranging to 5000 m depth. Misfits of models are defined in a standard chi-squared manner (Equation 3.2). This formulation of misfit assumes that the errors ε_i are normally distributed, and hence a misfit equal to the number of data implies that the average datum is reproduced with a residual equal to the error. We note that the assumptions of misfit are inherently violated by the application of an error floor, however, it remains a useful measure of the progression of the Markov chain as it clearly visualises when the chains converge to a region of model space of minimal misfit.

$$\delta(m) = \sum_{i=1}^N \left(\frac{d_i - d_r}{\varepsilon_i} \right)^2 \quad (3.2)$$

The complete results and model ensemble parameters for each MT site can be found in the supplementary material. To illustrate the format and interpretation of the ensembles, we present the respective ensembles for the two sites adjacent to the PM1 and B1 boreholes. Each ensemble is presented in a similar manner, with the input and invariant data plotted against a best-fitting model's responses, a histogram of the number of layers in each model within the ensemble, and a plot of the misfit progression of the model chain. The posterior probability density function (PDF) of the resistivity and depth distribution of the ensemble is plotted, normalised by the mode of each depth bin to highlight modal behaviours of the ensemble, with statistical measures overlain. Finally, interpreted formations and any comparative information are displayed for each site. Model ensembles have been interpreted on a formation basis by considering primarily the modes and medians of each ensemble, with means and 10th-percentiles used in some cases. The 90th-percentile line is less useful as modelled resistivities tend to be virtually unbounded at the resistive end of the spectrum than at the conductive end, as evident by the skewed distribution of 10th- and 90th-percentile lines with respect to medians (by definition, the 50th-percentile line). This is due to induction studies being sensitive to the integrated conductivity of conductive layers and insensitive to the actual resistivity of resistive layers, save for defining a minimum bound (see, e.g., Jones, 1999).

Figure 3.8 and Figure 3.9 display the model ensembles for the sites adjacent to the PM1 and B1 boreholes, with the respective formation logs (note that surficial basalts are implied, and not explicitly interpreted). Note that as neither ensemble clearly resolves the top of the EG formation, the encountered depths from boreholes have been included to aid later interpolation. Both ensembles have interpretations generally consistent with the borehole formation log, with the exception of the intrusive dolerite sill intercepted in the PM1 borehole (and the aforementioned EG boundary). Due to the possibly extreme resistivity contrasts between the highly conductive LLG sediments and the igneous sills, clear interpretation of similar sills is difficult across the basin, as although some ensembles feature distinct resistive bands with similar appearances to the dolerite sill in the

B1 borehole, it remains possible that further sills are concealed within the formations of other ensembles. The igneous intrusions appear limited to Jurassic and younger formations, however, and hence are not considered further for the interpretation of the target sediments (i.e., the SSG and BG sediments).

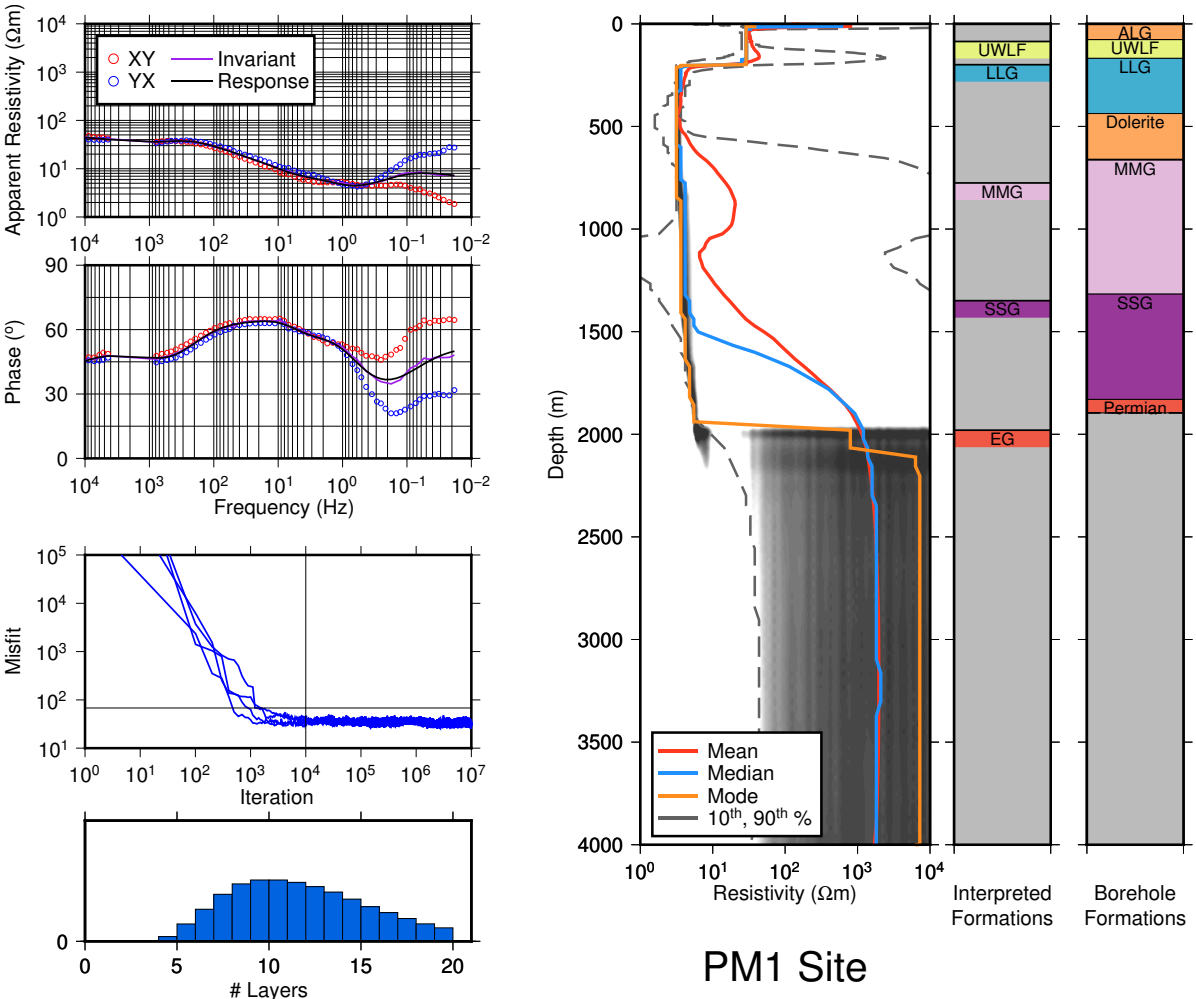


Figure 3.8.: Display of MCMC model ensemble for site adjacent to the PM1 borehole. Left column includes plots of data and model responses, misfit progression for MCMC chain (with 10 000 burn-in chain and ideal misfit marked), and histogram of number of layers in the ensemble models. Central plot shows a shaded heatmap of the logarithmic PPD of the model density, normalised by the mode of each depth bin. Statistical measures of the ensemble are overlain on the heatmap. Right columns show the formation tops as interpreted from the ensemble, compared to the formation sequence observed in the PM1 borehole (as shown in Figure 3.3).

Based upon the comparison between ensemble interpretations and borehole formation logs, and continuity of formation depths and thickness between adjacent ensemble interpretations, we consider that the interpreted SSG reservoir thicknesses are sufficiently precise for the purposes of an order-of-magnitude geothermal resource estimation. Figure 3.10 presents interpolated surfaces corresponding to the interpreted tops of the MMG, SSG, and EG units, with the EG assumed as the base of a potential reservoir, and the thickness distribution for the combined SSG and BG reservoir

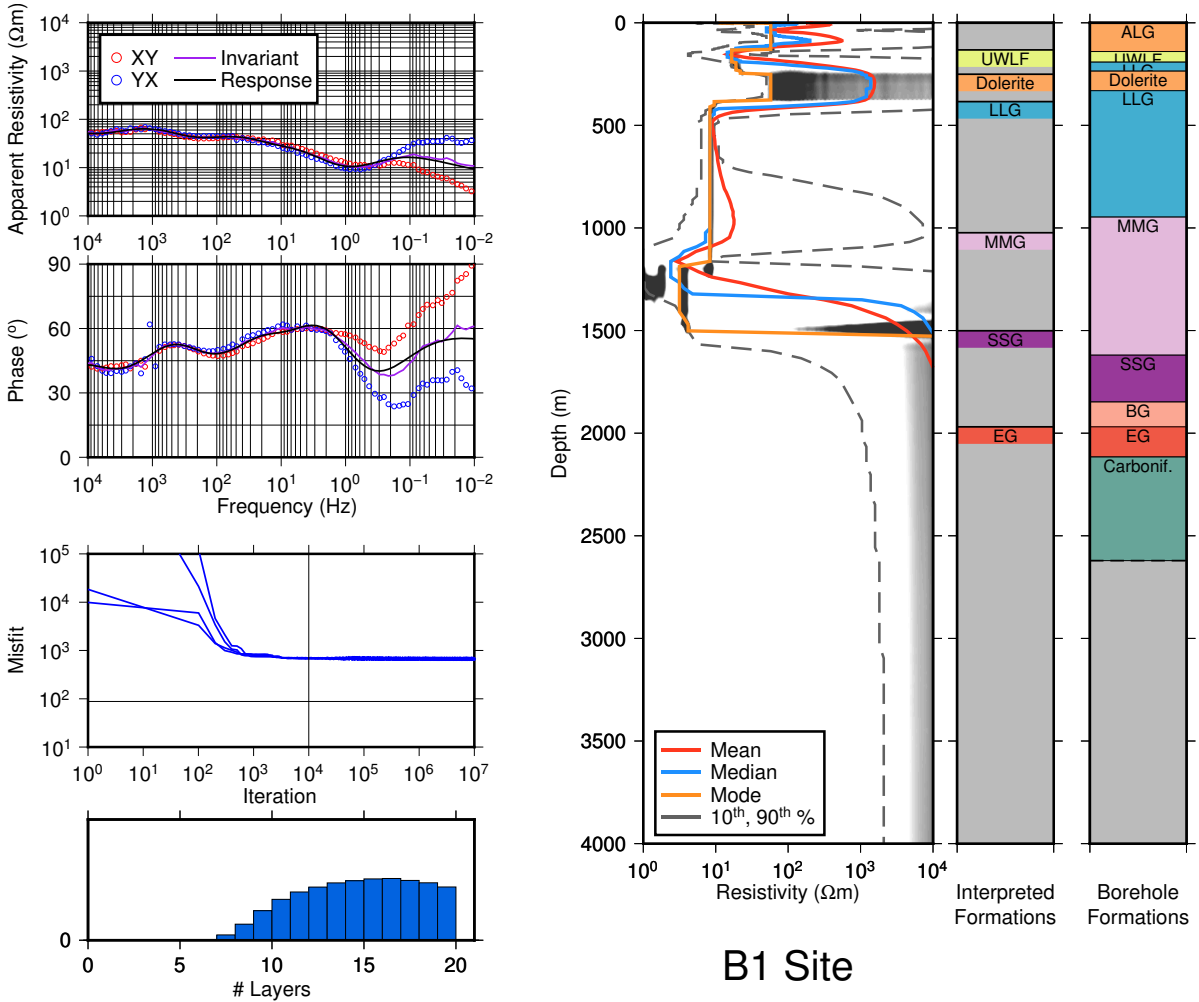


Figure 3.9.: Display of MCMC model ensemble for site adjacent to the B1 borehole. Left column includes plots of data and model responses, misfit progression for MCMC chain (with 10 000 burn-in chain and ideal misfit marked), and histogram of number of layers in the ensemble models. Central plot shows a shaded heatmap of the logarithmic PPD of the model density, normalised by the mode of each depth bin. Statistical measures of the ensemble are overlain on the heatmap. Right columns show the formation tops as interpreted from the ensemble, compared to the formation sequence observed in the B1 borehole (as shown in Figure 3.7).

volume is presented in Figure 3.11. For the purpose of quantitative geothermal resource estimation we have truncated the assumed reservoir extent based upon the EG interpretation, resulting in an assumed reservoir of thickness between 100 m and 400 m, with a total volume of 32 km^3 .

3.7 INDICATED GEOTHERMAL RESERVE ESTIMATION

From existing knowledge of the Rathlin Basin and new insights gained from the MT resistivity models presented here, it is possible to classify the Rathlin Basin as an Indicated Geothermal Reserve (as defined in Lawless, 2010) by estimating the exploitable volume of reservoir rocks V ,

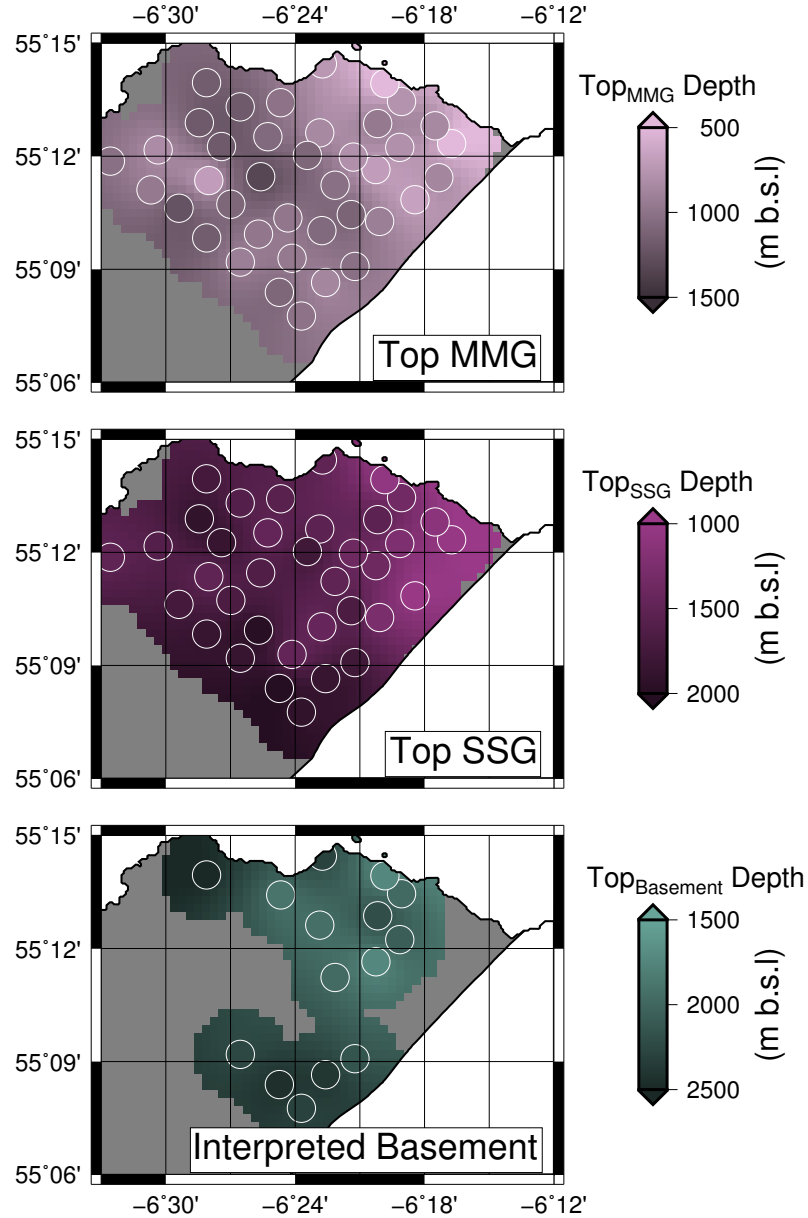


Figure 3.10.: Depth distributions of the three stratigraphic horizons of principal interest, namely, the tops of the Mercia Mudstone group (MMG), Sherwood Sandstone group (SSG), and the Enler Group of Permian sandstones (EG). White circles mark locations where the boundary was identifiable. The horizons are masked by grey in regions greater than two kilometres from an MT site with an identifiable corresponding boundary, to clarify the resolution extent.

and in turn the thermal energy in place Q_{th} . Note that precise quantification of the geothermal prospects in the Rathlin Basin is difficult due to limited information on thermal and hydraulic properties; regardless, by appropriate assumptions an order-of-magnitude estimate of the heat in place can be made.

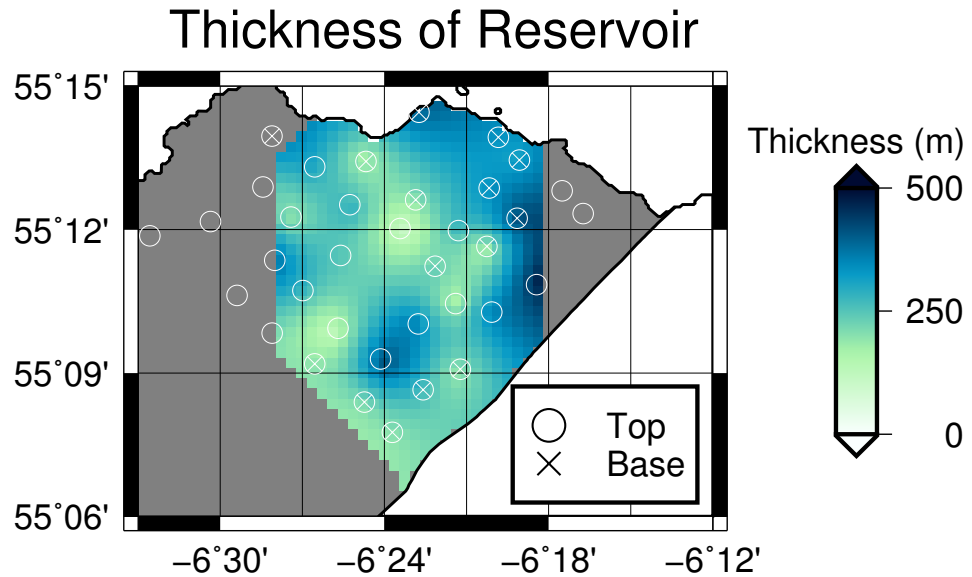


Figure 3.11.: Distribution of assumed Sherwood Sandstone Group reservoir formation, interpreted from [Figure 3.10](#), where 'Top' markers are the locations of resistivity models at which Top SSG can be interpreted. Similarly, 'Base' markers denote locations of resistivity models at which Top EG can be interpreted. After truncating the volume adjacent to the TVF to compensate for the subvertical basin boundary, the assumed reservoir has a volume of 32 km³.

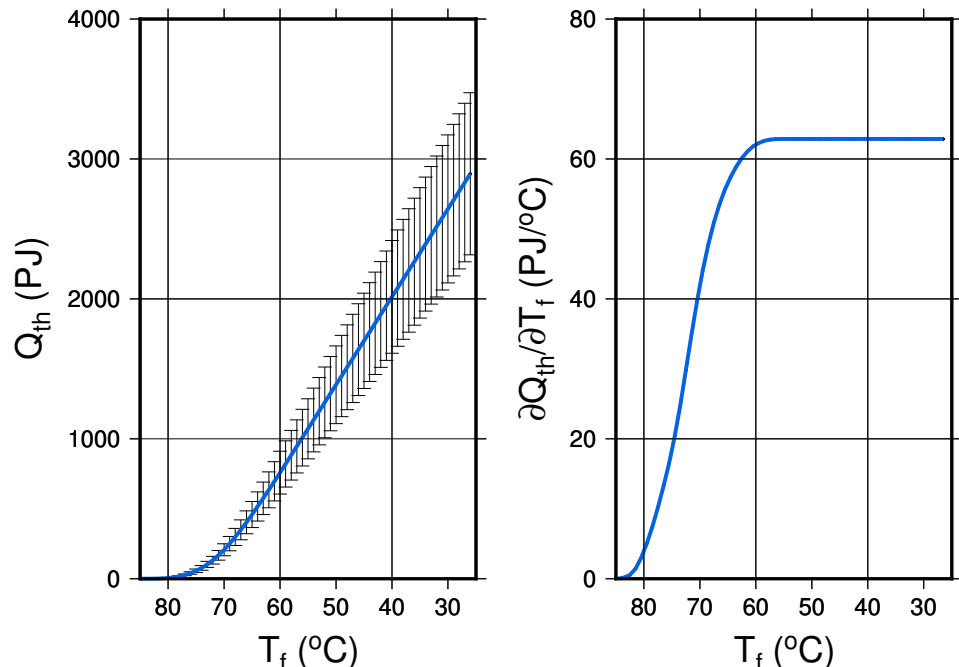


Figure 3.12.: Visualisation of the thermal energy in place available as a function of final reservoir temperature, following the approach detailed in [Lawless \(2010\)](#). Left-hand panel shows the thermal energy Q_{th} and uncertainty (typically $\pm 30\%$) in petajoules (i.e. $\times 10^{15}$ J) versus final temperature T_f , and right-hand panel shows the change of Q_{th} with decreasing T_f . Reducing T_f always corresponds to an increase in Q_{th} ; however, as can be seen from the gradient plot on the right the relationship is non-linear until T_f is sufficiently low to allow exploitation of the full volume, i.e. for $T_f <= 50$ °C.

The method of estimation used here follows that presented in Lawless (2010) for estimating Q_{th} as a function of temperature change ($T_i - T_f$) and porosity, as shown in Equation Equation 3.3.

$$Q_{th} = V \times \{[(C_r \rho_r (1 - \Phi)(T_i - T_f)] + [C_w \rho_w \Phi(T_i - T_f)]\} \quad (3.3)$$

In this equation, C_w is the specific heat capacity of water, assumed constant at $4181 \text{ Jkg}^{-1}\text{C}^{-1}$, and C_r is the specific heat capacity of the rock matrix, taken as $816 \text{ Jkg}^{-1}\text{C}^{-1}$ for a similar Permian sandstone in the UK (Richardson and Neymeyer, 2013). The porosity Φ was taken as $14 \pm 1.5\%$, i.e. the mean of the laboratory measurements shown in Figure 3.6. The density of the rock matrix, ρ_r was taken as $2450 \pm 50 \text{ kgm}^{-3}$ (Mitchell, 2004), whereas the density of water ρ_w was treated as a function of temperature (as defined in Adams and Bachu, 2002). As the two target formations (i.e. the SSG and BG sandstones) have the same observed geothermal gradient ($\approx 24 \text{ K km}^{-1}$, from Figure 3.7), for geothermal estimation purposes they can reasonably be treated as a single unit, with a range of initial temperatures T_i linearly interpolated from the appropriate section of observed temperature measurements shown in Figure 3.7.

The formation depths interpreted in the previous section were interpolated over an appropriate portion of the survey area to estimate the total volume for the target SSG and BG sediments, and uncertainties of 20 m were attributed to the depths of each boundary. As the Dalradian horst south-east of the TVF represents a significant volume of non-sedimentary material at depth due to its sub-vertical dip between 25 and 56° to the north-west (modelled from gravity data by Gibson, 2004), this volume must be accounted for to avoid overestimating the sediment volume. The TVF was assumed to be planar with a dip of 40° (the mean dip reported by Gibson, 2004), resulting in a triangular prism that models the displacement of sediments at depth. The volume of the triangular prism was then subtracted from the total sediment volume to approximate the absence of sediments due to fault loss adjacent to the TVF. Finally, the reservoir volume was fractionally adjusted to compensate for the discrepancy between the formation-level interpretation and lithology-level reality; as a significant fraction of the SSG intercepted in the PM1 borehole is conglomerate rather than sandstone, it would be inappropriate to neglect that such conglomerate is less likely to contribute to a reservoir. Based upon the thicknesses of conglomerate and sandstone encountered in the PM1 borehole (i.e., 148 m of conglomerate in the 579 m thick SSG interval), the volume presented previously in Figure 3.10 was reduced by a further 25 % to account for the viable proportion of the reservoir (note that in reality the SSG-BG interval likely represents several smaller reservoirs due to conglomerates acting as barriers to permeability).

Final reservoir temperatures T_f were varied from 85°C down to 25°C , and the results with error estimates (typically $\approx \pm 30\%$) are plotted in Figure 3.12, in the left-hand panel. The lower boundary of $T_f = 25^\circ\text{C}$ was selected to facilitate comparison with existing estimates of geothermal potential in the adjacent Larne basin (Pasquali et al., 2010; Busby, 2014). The stored heat in place Q_{th} increases as the final temperature decreases, an expected result as the volume of viable (i.e. at a temperature greater than T_f) reservoir rocks increases. The non-linearity of Q_{th} for small ($T_i - T_f$) arises as only a small amount of the reservoir has a sufficiently high initial temperature

T_i ; as $(T_i - T_f)$ increases, more of the reservoir is usable, and Q_{th} rises due to the increases in both V and $(T_i - T_f)$. Modelling of the Rathlin Basin for a $T_f = 25$ °C gives an estimated Q_{th} of 2900 ± 600 PJ for the assumed geothermal reserve; to place this Q_{th} estimate in context, the nearby Larne Basin has been estimated to have $Q_{th} = 1800$ PJ in place for the same T_f (Pasquali et al., 2010; Busby, 2014).

A comparison of the volume exploited V , and the rate of change $\partial V / \partial T_f$, to the final temperature T_f is shown in Figure 3.13. As seen by the change in volume with respect to T_f , a target T_f of 55 °C is required to exploit the entire assumed reservoir volume. Exploitation beyond this T_f returns increasing Q_{th} as a linear function of T_f , without the exponential increase due to increasing reservoir volume, and this diminishing returns may limit geothermal exploitation. The geographic distribution of Q_{th} as estimated for $T_f = 25$ °C is presented in Figure 3.14, with elevated densities of Q_{th} centrally and to the east of the survey area due to thicker sediments in these areas.

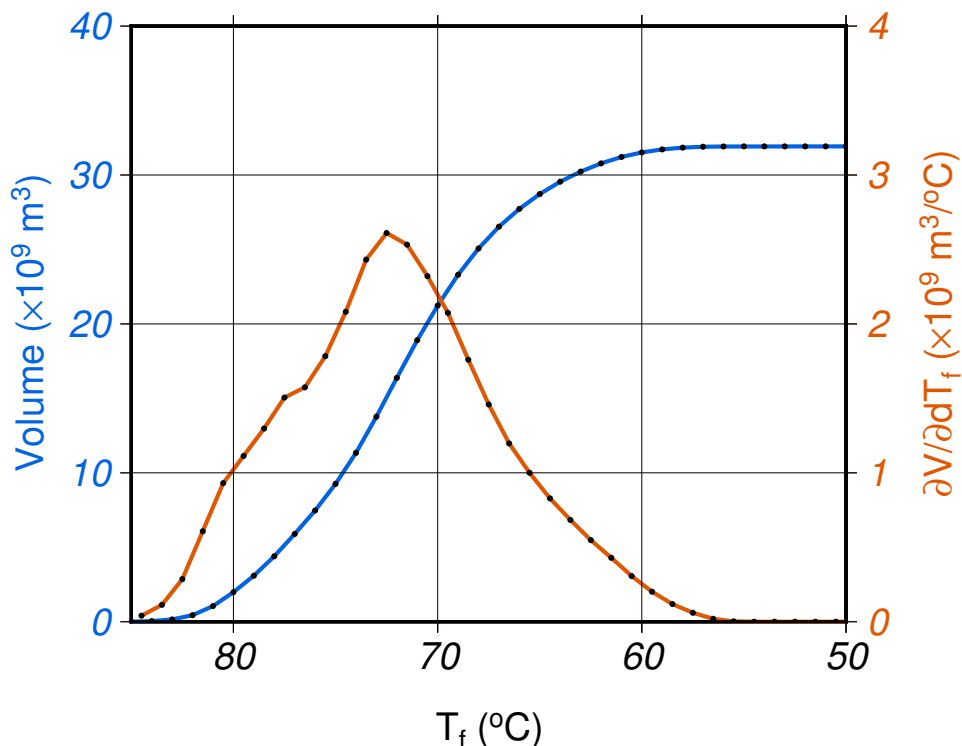


Figure 3.13.: Diagnostic display of the volume of reservoir sediments at or above the final reservoir temperature T_f (blue), and the increase in reservoir volume with respect to final temperature ($\partial V / \partial T_f$, orange). As temperature is assumed as a linear function of depth, the initial increase in $\partial V / \partial T_f$ from 85 to 73 °C is due to both lateral and vertical (i.e., thickness) expansion of the accessible volume. For $T_f < 73$ °C, $\partial V / \partial T_f$ decreases as the areal extent approaches its limit. In order to maximise exploitation of the reservoir, a target $T_f = 55$ °C is suggested, as exploitation beyond this has diminished thermal energy returns.

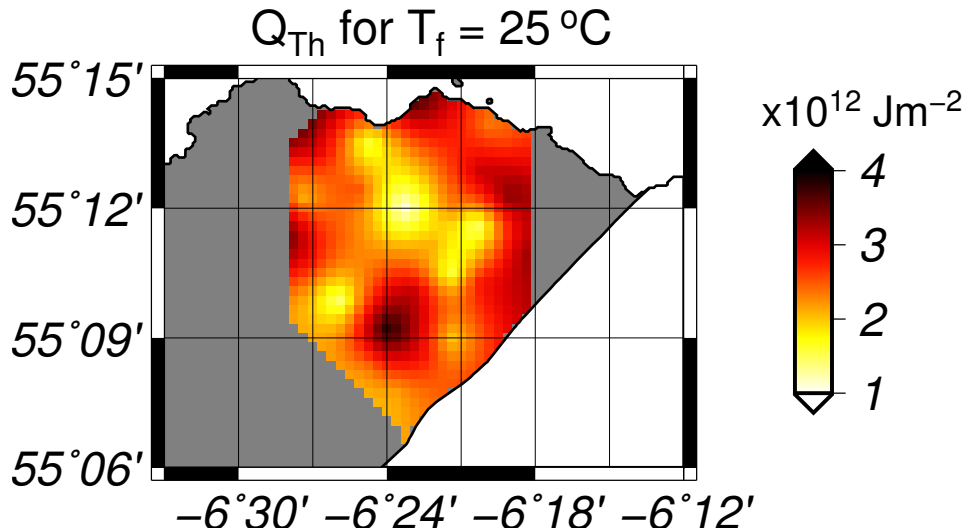


Figure 3.14.: Geographic distribution of areal density of geothermal energy in place Q_{th} , as computed for $T_f = 25$ °C. The density of geothermal energy in place is elevated towards the centre and eastern portions of the research area, where the reservoir sediment thicknesses are elevated compared to the remainder of the basin.

3.8 IMPLICATIONS AND DISCUSSION

At the time of MT data acquisition, existing geophysical models (Mitchell, 2004; Naylor and Shannon, 2011) suggested a depth to the base of Permian sandstones of up to 4000 m, with the PM1 resistivity measurements indicated that the MMG is more conductive than the underlying SSG and BG sandstones. Resistivity measurements from the PM1 borehole suggest that the general resistivity contrasts between the MMG and underlying SSG & BG formations are minor (i.e., a resistivity contrast of 0.3 in \log_{10} units). However, the results of this work indicate that the MMG found within the Rathlin Basin is slightly more resistive when modelled by MT data, and the basin as a whole, or at least the permeable (conductive) parts of the basin, is shallower than predicted. Resistivity models from inversion of MT data sets adjacent to the two deep boreholes can be interpreted into structures comparable to borehole knowledge, however, as the data from some of the MT sites have poor signal quality, recovery of the low-resistivity contrast boundaries of interest was not possible at all sites. Additionally, as the MT method is unable to resolve accurately the actual resistivity of a resistive formation beneath a conductor, but only set a minimum value on it, we also cannot be certain that the resistivities estimated for the SSG and BG are sufficiently accurate for porosity estimation.

A major consequence of the shallow, conductive resistivity structure is that due to the nominal 2 km MT site spacing, most of the resistivity structure modelled in the survey area relies upon single MT sites. As a result, we limited the modelling to 1D inversion to avoid interpretation of shallow (i.e. < 1500 m) resistivity structure between MT sites that will, in all likelihood, be more controlled by the smoothing terms of 3D inversion modelling objective function rather than the fit

to the data themselves, given by the misfit term in the objective function. However, limiting the modelling to 1D inversion may be less appropriate for longer period MT data, as previous work has shown such data to have characteristics indicative of 3D resistivity basement structure (Delhaye et al., 2017).

Given that the survey area covers less than half of the onshore basin, the entire Rathlin Basin presents a significant geothermal resource in comparison to other onshore geothermal resources in Northern Ireland. However, the most significant aspect of a geothermal reservoir after temperature is the network of pathways of fluid migration, i.e., the hydraulic permeability; in the case of clastic rocks such as the SSG or BG, the distribution of hydraulic permeability can vary significantly across a region, greatly altering the viable reservoir volume. As the limited results from core samples shown in Figure 3.6 exhibit a large range of permeabilities, it can be inferred that the distribution of permeability within the basin is complex and significant in limiting intra-reservoir flow. Intra-basin faults have been mapped in the Rathlin Basin by other geophysical methods (Gibson, 2004), and these may function as impermeable barriers to flow, compartmentalising and limiting the continuity of the reservoir. Additional porosity and hydraulic permeability data from new boreholes is essential to obtaining more robust, statistical geothermal models, particularly as there have been some concerns raised regarding the appropriateness of Klinkenberg corrections for the SSG in Britain (Bloomfield and Williams, 1995).

The elevated geothermal conditions within the Rathlin Basin, when compared to the remainder of Ireland, are known solely from borehole temperature measurements in the two deep boreholes, and quantitative analysis is only possible from the equilibrated temperature measurements from the B1 borehole. More accurate estimation of both the heat flux distribution and total heat in place of the basin would require further temperature observations in additional boreholes, and ideally laboratory measurements of formation thermal conductivities. Regardless, although computed by a simplistic bulk approach, the estimates of geothermal heat in place presented here show that the Permo-Triassic sediments within the Rathlin Basin represent a large heat resource.

3.9 CONCLUSIONS

Investigation of the onshore Rathlin Basin by means of an MT survey has expanded understanding of reservoir sediment distribution within the basin well beyond that previously known from boreholes and other geophysical data. Careful modelling of the observed MT data reveals that a portion of the Mercia Mudstone group (the layer immediately above the target Sherwood Sandstone group and Belfast group sandstones) is more electrically conductive than the underlying target sandstones. Due to the resistivity configuration of the target being located below a conductor, the resistivity estimates of the underlying sediments cannot be relied upon to be accurate, and another form of interpretation was required to distinguish between lithological layers.

MT data were inverted in a reversible-jump MCMC manner, with the resulting model ensembles interpreted on a formation basis. Interpretations of the model ensembles compare favourably to

adjacent deep boreholes, and hence formation interfaces were interpolated between the MT sites to form layer boundary estimates across the area. A conservative volume estimate of 32 km^3 of target SSG and BG sandstones was computed from the interpolated boundaries, corresponding with the area where both the top SSG and top Carboniferous lithological boundaries were successfully defined.

Estimation of thermal energy in place as a function of final reservoir temperature T_f suggest an Indicated Geothermal Resource of $\approx 2.9 \times 10^{18} \text{ J}$ (i.e. 2,900 PJ) for a final temperature of 25°C , with the majority of BG and SSG sandstones engaged by final temperature approaching 50°C . This estimated resource places the Rathlin Basin as a greater IGR than adjacent contemporaneous basins. However, at this stage we are limited to estimating an Indicated Geothermal Resource by the scarce boreholes and geophysical information available; consideration of the Rathlin Basin as a Measured Geothermal Resource would require additional geophysical, geological and temperature information.

3.10 ACKNOWLEDGMENTS

This work was supported by Science Foundation of Ireland [grant 10/IN.1/I3022 awarded to AGJ], as part of the IREtherm project. MT data acquisition was only possible with the assistance of the IREtherm MT Team (S. Blake, T. Farrell, C. Hogg, J. Vozar, C. Yeomans). Rathlin Energy (UK) Ltd. are gratefully thanked for providing temperature and lithological information from the B1 borehole. R. Brodie (Geoscience Australia) is thanked for making the rjMCMC 1D inversion code available for use. We thank an anonymous reviewer for comments and suggestions that improved the manuscript.

3.A EXAMINATION OF 1D MT MODEL BOUNDARY TOLERANCES

As a measure of uncertainty in the assumed boundary depths for computation of the Indicated Geothermal Resource within the Rathlin Basin, synthetic 1D forward testing has been performed for each 1D MT model used in the basin interpolation and interpretation. To enable such testing, MT models determined by Occam inversion were reduced from 45 layers to $\approx 7\text{-}8$ layers by use of the layered 1D inversion tool in WinGLink (an implementation of *minim*, Fischer and Le Quang, 1981), wherein layer thicknesses as interpreted from the vertical derivative of $\log \rho$ were fixed, and best-fitting interval resistivities determined by the inversion. A comparison of the Occam inverse model and corresponding *minim* model at the PM1 borehole site is shown in [Figure 3.15](#). Note that replication of the observed MT data by the responses of the *minim* model is not the intent of the comparison being carried out, rather, only the effect of perturbing the boundary depth on a model's response is of interest.

The depth of the boundary interpreted as the top of the SSG interval in the *minim* model was perturbed slightly by an incremental change dh of up to $\pm 100 \text{ m}$ in order to examine the effect on

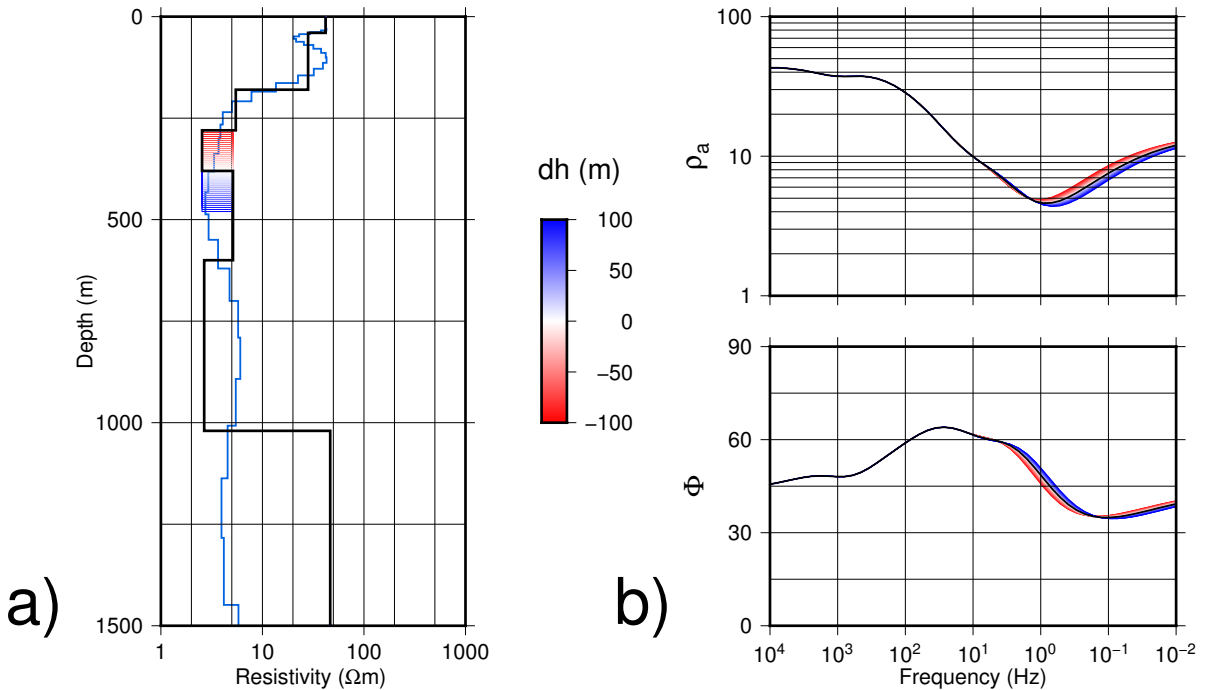


Figure 3.15.: a) Comparison of original Occam inverse model (blue line) with *minim* model (black line), and *minim* model perturbed with shifts dh to boundary (red-to-blue lines). b) 1D MT forward responses of *minim* model (black line) and dh -perturbed models (red-to-blue lines). (For interpretation of the references to colour in this figure legend, the reader is referred to the web version of the article.)

the forward responses of the altered models, in comparison to the responses of the original *minim* model. A root-mean-square deviation in response (expressed as a percent change) was computed for each dh between -100 m (i.e., shallower boundary depth) and $+100$ m (i.e., deeper boundary depth), and the resulting distribution of deviation as a function of dh was considered. The responses and distribution of percent deviation for the PM1 borehole site are also shown in Figure 3.15 as an example of the process. Figure 3.16 presents the distribution of percentage deviation for all the sites interpreted in this manner. By considering these results, if a maximum tolerable deviation of 5% of a model's responses is assumed, then dh of up to ± 20 m are possible at the majority of sites.

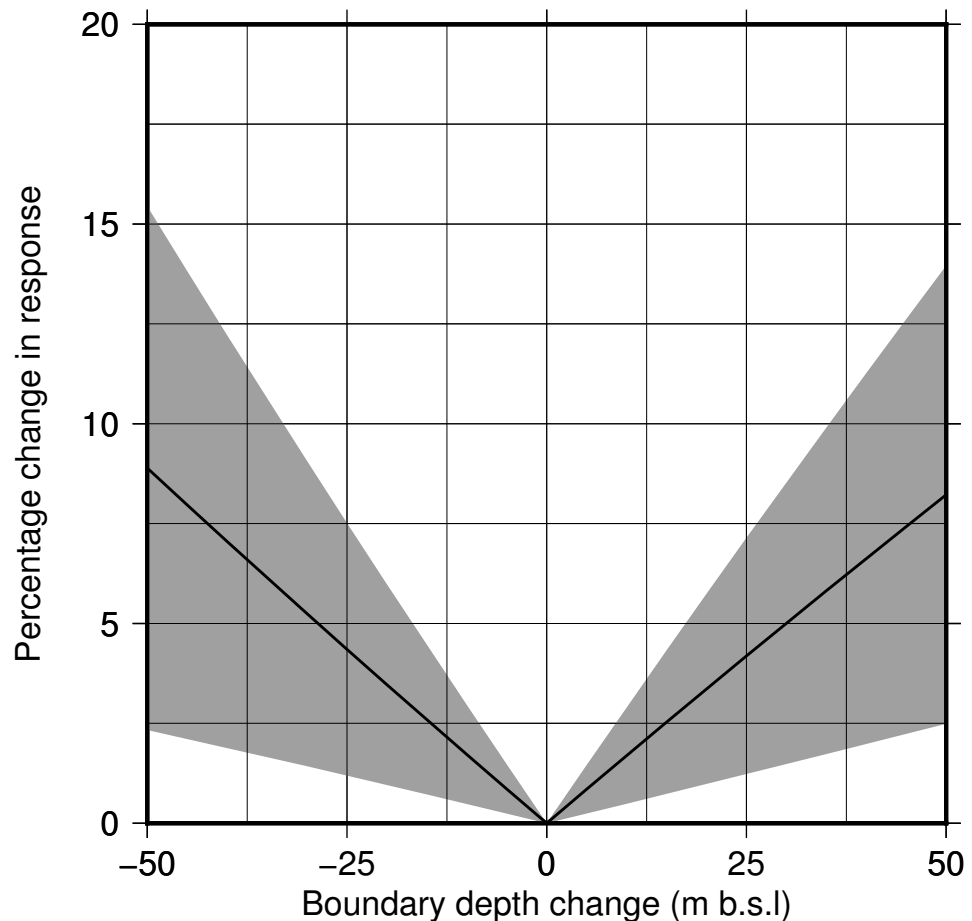


Figure 3.16.: Plot of total percentage changes in 1D model MT responses as a function of dh change in SSG boundary depth. The mean percentage change of all models is shown by the black line, and the grey region represents one standard deviation. In order to ensure a maximum of 5% change in response (hence, uncertainty of boundary depth) for each model, a tolerance of $\approx \pm 20$ m is required.

4

ESTABLISHING THE SENSITIVITY OF A 3D MAGNETOTELLURIC MODEL OF RATHLIN BASIN, NORTHERN IRELAND

4.1 ABSTRACT

Deep Permian and Triassic sandstones located in the north-east of Ireland are of considerable interest for both geothermal and hydrocarbon exploitation. In order to image these sediments beneath the Rathlin Basin in Co. Antrim, Northern Ireland, magnetotelluric (MT) data were collected from 55 acquisition stations located in profiles across the onshore portion of the basin. Although the geological structure of the basin is expected to consist of a subhorizontally layered sedimentary basin, magnetotelluric modelling of the target sediments is complicated by the basin's coastal environment, and the slight resistivity contrasts between the basin sediments.

We present a three-dimensional inverse model of the resistivity distribution beneath the basin, and thoroughly examine the sensitivity of this model as a proxy for the relevance of model portions to the observed data. Doing so allows delineation of the transition of the model from data-controlled to regularisation-controlled, and adds confidence to the interpretation of resistivity structure. Examining both the resistivity and sensitivity distributions of our model shows that the near-surface basalts and Lower Lias Sandstones are well-recovered. However, at depths beyond 1,000 m the sensitivity distribution becomes laterally inhomogeneous, with variation that contrasts with that observed in the resistivity distribution and suggests resistivity structure that is more determined by regularisation than by data residual. By considering both resistivity and distribution, an interpretation can be reached that correctly takes into account the smoothing effect of the inversion.

This chapter is yet to be published; authors would include Delhaye, R., Rath, V., Jones, A.G., Muller, M.R., and Reay, D.

4.2 INTRODUCTION

Buried underneath the expanse of flood basalts in Northern Ireland are three sedimentary basins with sedimentary fill of substantial interest for geothermal and hydrocarbon exploration, namely, the Larne, Lough Neagh, and Rathlin Basins (Goodman et al., 2004). The Rathlin Basin is so far the poorest known of the three; however, from the few deep boreholes and other geophysical information it is believed to hold both the thickest succession of sediments of interest and the most elevated geothermal setting (i.e. increased temperature with depth). This combination of heat and hydraulic properties suggests that the Rathlin Basin may represent a considerable thermal resource (Reay and Kelly, 2010); however, greater understanding of the thickness and extent of the sediment structure is required before deciding on any further drilling or exploitation. Two formations in particular are of interest for geothermal interests due to elevated porosities and hydraulic permeabilities: the early-Triassic Sherwood Sandstone Group and late-Permian Belfast Group of sandstones.

4.2.1 *Geological Setting*

The Rathlin Basin consists primarily of late-Palaeozoic and Mesozoic sediments, and is generally concealed beneath Palaeogene flood basalts. The surficial geology of the island, the distribution of MT acquisition sites, and the basin's location within Northern Ireland are shown in [Figure 4.1](#). The Port More 1 borehole (PM1) lies near the coast on the mainland (location also marked in [Figure 4.1](#)), and was drilled to a depth of 1897 m (Wilson and Manning, 1978). The stratigraphy encountered at PM1 is expected to be broadly similar to that encountered across the basin, with a thin (i.e. 100 m or less) surficial layer of Antrim Lava Group (ALG) basalts over a thin layer of the Ulster White Limestone Formation (UWLF). Both formations are expected to be dense and resistive. Beneath the UWLF lies \approx 200 m of conductive, less-dense Jurassic Lower Lias Group (LLG) mudstones (the Waterloo Mudstone formation). Below the LLG an unexpected thick (\approx 330 m) succession of dolerite and basalt sills were encountered; wireline resistivity measurements in PM1 suggest these sills are relatively resistive, and likely denser than the overlying and underlying sediments. The deep fill of the basin beyond the sills is a mix of the mid-Triassic Mercia Mudstone, early-Triassic Sherwood Sandstone, and late-Permian Belfast and Enler Sandstone Groups; the PM1 borehole terminated in Permian sandstones, although it is unclear precisely which group. A diagram of this stratigraphy is shown in [Figure 4.2](#).

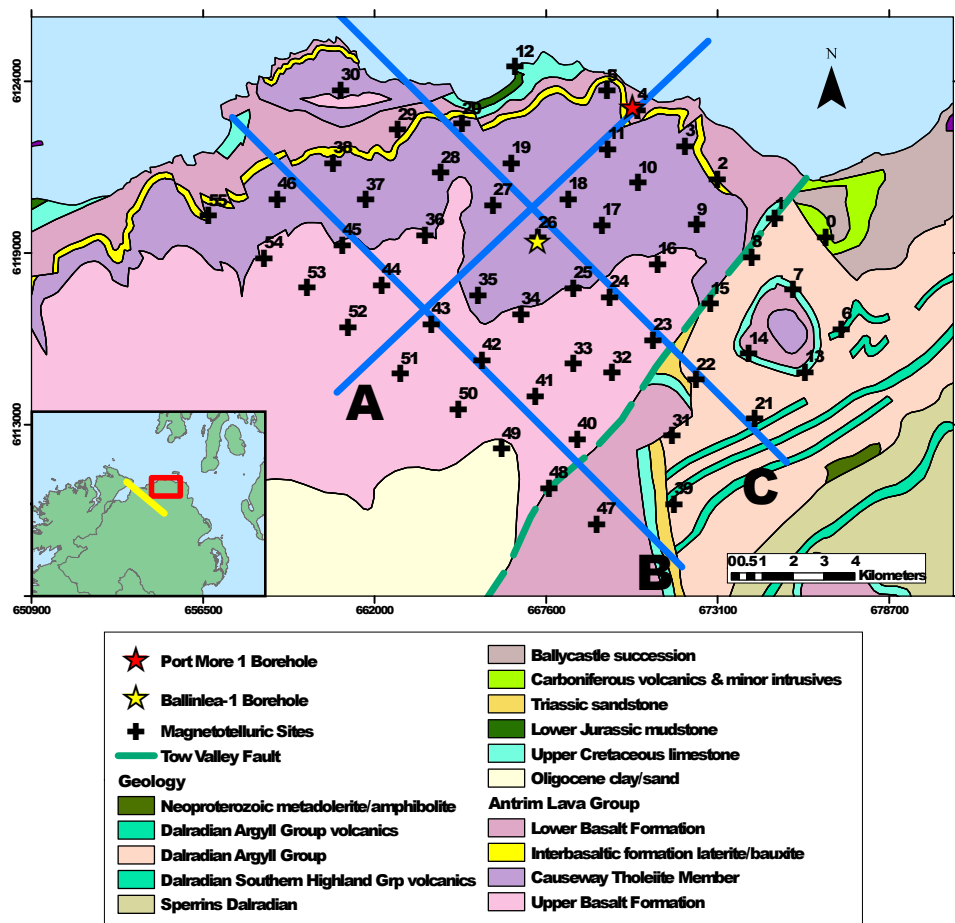


Figure 4.1.: Geological map of Rathlin Basin area, overlain with magnetotelluric acquisition sites numbered and denoted by black crosses. Note the large areal extent of the Antrim Lava Group basalts, with minimal surface expression of the underlying sedimentary basin. Profiles A, B and C denote the locations corresponding to Figure 4.4 – Figure 4.6. Inset map shows the northern half of Ireland, with the location of the magnetotelluric survey area shown by the red rectangle.

4.3 METHODOLOGY AND RESULTS

4.3.1 Magnetotelluric Theory

The magnetotelluric method (MT) is a geophysical method of investigation that allows estimation of the Earth's electrical resistivity structure by modelling the attenuation of natural or man-made electromagnetic waves in the subsurface (Simpson and Bahr, 2005; Chave and Jones, 2012). The attenuation of EM waves in a conductive medium depends upon the electromagnetic properties of the medium (i.e. the electrical resistivity and magnetic permeability), and the frequency of the wave itself. The magnetic permeability is assumed to not vary from that of free space, leaving the other two factors as controls over the penetration of MT signal waves (with lower frequencies and higher resistivities leading to greater penetration depths). The relationship between the signal wave frequency ω , the electrical resistivity ρ , and the magnetic permeability μ is described by the

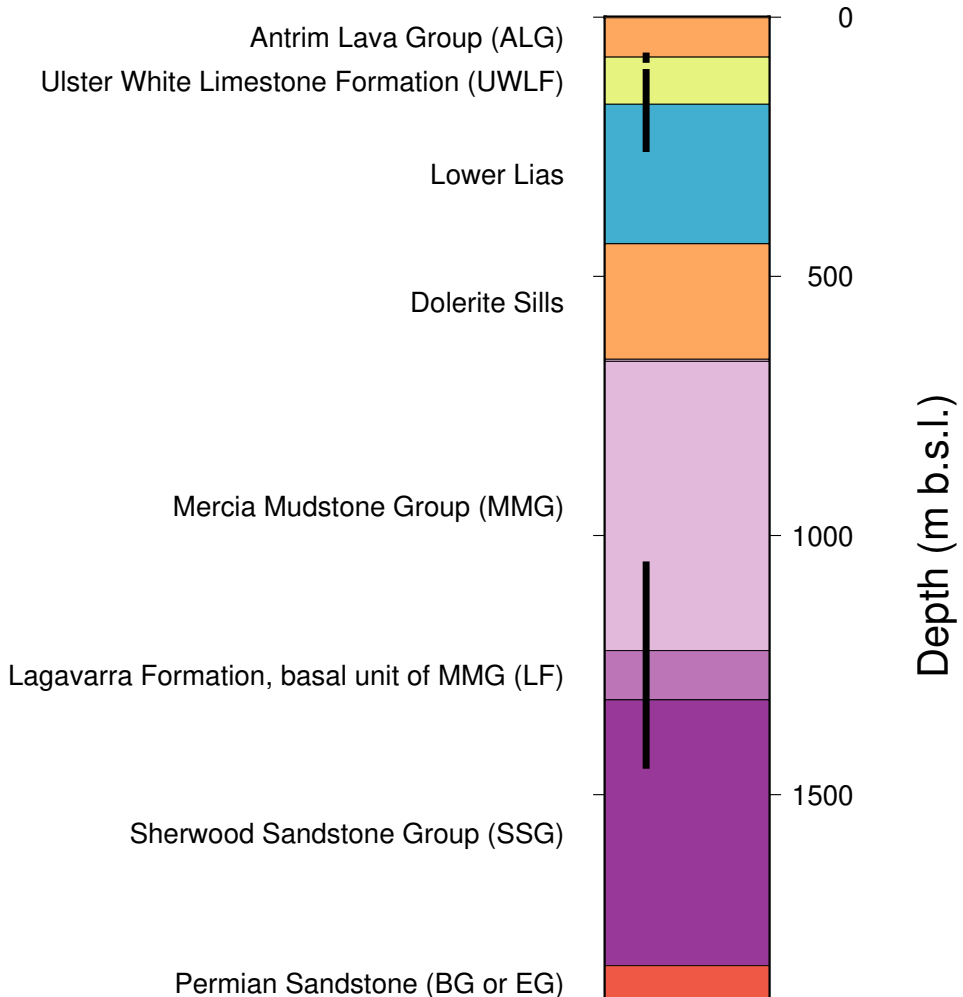


Figure 4.2.: Bulk lithologies encountered in the PM1 borehole (see [Figure 4.1](#) for location). The borehole terminated at 1896 m depth, within the Permian Enler Group Sandstones. Solid black vertical lines indicate depths at which wireline resistivity data were measure.

electromagnetic skin depth δ . The skin depth is defined as the scale length over which the wave amplitude decays by e^{-1} , and can be approximated by $\delta \approx 503\sqrt{\rho/f}$ for a half-space of constant resistivity ρ .

MT data are defined by impedance transfer functions (Z_{ij}) that relate the sampled horizontal electric (E_i) and magnetic (H_j) fields. Four transfer functions are generally defined as the electric and magnetic fields are measured in two orthogonal directions; these can be arranged in tensor form as shown in [Equation 4.1](#), where $Z_{ij} = E_i/H_j$. Assuming that the co-ordinate axes are correctly aligned, the form of the impedance tensor reflects the dimensionality of the underlying resistivity structure.

$$\mathbf{Z} = \begin{pmatrix} Z_{xx} & Z_{xy} \\ Z_{yx} & Z_{yy} \end{pmatrix} \quad (4.1)$$

In addition to the impedance transfer functions, two further transfer functions that relate each of the horizontal magnetic field components to the vertical magnetic field component. The two magnetic transfer functions comprise the tipper function, defined as follows.

$$\mathbf{T} = \begin{pmatrix} T_{zx} \\ T_{zy} \end{pmatrix}; \text{ where } T_{zx} = \frac{H_z}{H_x}, T_{zy} = \frac{H_z}{H_y} \quad (4.2)$$

4.3.2 Magnetotelluric Data Acquisition and Analysis

The research presented here is based upon MT data collected and modelled previously in [Delhayé et al. \(2017\)](#); principle notes on the data and inversion are reproduced here for convenience. MT data were collected using Phoenix Geophysics magnetotelluric equipment at 55 locations on seven profiles across an onshore portion of the basin, as shown in [Figure 4.1](#). Broadband MT data (BBMT, i.e. from 300 to 0.01 Hz) were acquired over three nights at each location, followed by one night of audiometalluric data (AMT, i.e. from 10000 to 1 Hz) acquisition. The range of data collected was chosen to provide resistivity information from the very near-surface to sufficient depths that encompass the target sediments. Data were processed and merged into combined data sets by appropriate Phoenix Geophysics software. Static-shift-type distortions are observed in a number of the MT site records, and in order to compensate for the static-shift effects we have applied the method presented in [Delhayé et al. \(2017\)](#), using regional airborne electromagnetic data gathered during the Tellus Project ([Beamish, 2013](#)). This method of static-shift correction assumes that static-shift effects are related solely to electric field observations. Hence, by modelling the airborne EM data, computing forward MT responses from the models, and taking the ratio of these responses to the observed data, frequency-independent factors are determined that compensate for the static-shifts.

The ModEM 3D inversion program (as presented in [Egbert and Kelbert, 2012; Kelbert et al., 2014](#)) was used for the inverse modelling of the MT data. The 3D model was determined over a mesh of $59 \times 68 \times 82$ cells (with x, y, z defined as positive east, north, and downwards), commencing from a $30 \Omega\text{m}$ halfspace. Cells in the central portion of the model had a uniform width of 400 m, and layers of fine (5–10 m) thickness cover the bathymetry, increasing to approximately 80 m across the depths of interest (i.e. from 500 to 3000 m depth). In order to account for the surrounding conductive sea with the required precision, bathymetry was implemented in the model as cells of fixed resistivity ($0.33 \Omega\text{m}$), in accordance with bathymetry taken from Shuttle Radar Topography Mission (SRTM) 1 data. Twenty-eight frequencies per site were used as input for inversion of both the off-diagonal (i.e. Z_{xy} and Z_{yx}) and diagonal (i.e. Z_{xx} and Z_{yy}) impedance tensor elements, covering from 10,000 to 0.001 Hz, with clearly noise-affected data omitted from the inversion process. Vertical magnetic transfer function ("tipper") data were also included at the same frequencies.

Inversion algorithms commonly assess the fit of a model by comparing the distance between the computed responses and the input data to the errors of the data. In order to avoid leveraging the models due to poor data with overly small error estimates, an error floor schema was applied to the input data, wherein errors are redefined as the larger of the observed data, or a defined percentage of the mean of the data magnitudes. For the inverse model presented here, error floors were applied to off-diagonal data as 5% of the corresponding (i.e., same site/frequency) off-diagonal data magnitudes (i.e., the mean of Z_{xy} and Z_{yx}), whereas the error floors applied to diagonal data were applied as 20% of the diagonal data magnitudes. An absolute error floor of 0.03 was assumed for tipper data. The continuity of resistivity structure found by inversion is strongly affected by the regularisation of the particular algorithm (i.e. the weighting between fitting input data and a smoothing function); for the model presented, smoothing values of 0.30 were used to maintain model continuity between MT site locations. The final model responses show a normalised RMS (i.e. the distance between model responses and observed data, normalised by errors used for inversion) of 1.77.

The 3D resistivity model examined here for the Rathlin basin data is presented as three horizontal slices (850 m, 1550 m, and 2100 m depth respectively) in [Figure 4.3](#), and three profiles ([Figure 4.4](#), [Figure 4.5](#), and [Figure 4.6](#), respectively). The horizontal slices in [Figure 4.3](#) show resistivity structure that mostly agrees with expectations, i.e., at shallower depths of down to 1500 m, the central basinal area is dominated by conductivity associated with the clastic sediments of the LLG, MMG and SSG, with resistive increases beyond 2000 m depth as the basin bottoms out. The south-east margins of the basin are clearly marked by a large increase in resistivity associated with the metasedimentary Dalradian supergroup.

[Figure 4.4](#), [Figure 4.5](#) and [Figure 4.6](#) show transects of the resistivity distributions along and across the basin. All three profiles clearly show immediately near-surface basalts and Ulster White chalks as strong resistors, with conductive features in the uppermost 500 m of the model, interpreted as LLG mudstones, and at depths of between 1200 m and 2500 m, interpreted as the Permo-Triassic sandstones. Profiles B and C also show clearly the resistive Tow Valley Fault Zone margin to the south-east, with a contrast of several orders of magnitude in resistivity. The north-east extent of Profile A lacks the deeper conductive zones associated with the SSG

4.3.3 Model Jacobian Sensitivity

At the conceptual level, inverse problems such as the inversion of magnetotelluric data can be posed as a minimisation problem where the minimum of an objective function $A(\mathbf{m})$ is sought ([Zhdanov, 2002](#); [Tikhonov and Arsenin, 1977](#)). In order to handle the ill-posed nature of the problem, a regularisation term α is included to enforce conditions upon the solution (in the context of geophysical modelling, α is frequently a gradient or Laplacian function to smooth the result). The objective function can then be presented in [Equation 4.3](#), where $A(\mathbf{m})$ is the objective function to be minimised, \mathbf{d} are the observed data, \mathbf{m} is the model, and $\hat{\mathbf{F}}$ is the forward operator to compute

a model's responses, with $\|\hat{\mathbf{F}}\mathbf{m} - \mathbf{d}\|^2$ hence representing a residual between observed data and model responses.

$$A(\mathbf{m}) = \|\hat{\mathbf{F}}\mathbf{m} - \mathbf{d}\|^2 + \alpha \|\mathbf{m}\|^2 \quad (4.3)$$

If [Equation 4.3](#) is considered with respect to the behaviour of \mathbf{m} , it is apparent that \mathbf{m} will not solely be determined by the proximity of its responses to the observed data, but also by whatever regularisation is applied.

In order to evaluate portions of the 3D model that are relatively more sensitive to the MT data, some authors (e.g., [Zhdanov, 2002](#); [Schwabenberg et al., 2002](#)) have proposed the use of the Jacobian matrix that relates a resistivity model's elements and magnetotelluric responses. The Jacobian matrix, also called the sensitivity matrix ([Schwabenberg et al., 2002](#)), consists of the partial derivative of model responses (i.e., complex impedances or magnetic transfer functions) with respect to perturbations of the model parameters (i.e., resistivity or conductivity). For a model with m_j resistivity elements, and Z_i responses, the sensitivity matrix \mathbf{J} comprises an $i \times j$ matrix, with element J_{ij} representing the partial derivative (note that the model parameters are typically varied on a logarithmic rather than linear scale):

$$J_{ij} = \frac{\partial Z_i}{\partial \log m_j} \quad (4.4)$$

As the Jacobian matrix elements are strictly the relationship between the model and model responses, then low sensitivities in a portion of the model imply that the resistivity structure is algorithmically influenced more strongly by the regularisation term than by the data-fitting term. In and of itself, \mathbf{J} is not intuitive to examine, as in addition to variation over many orders of magnitude, the elements of \mathbf{J} are also vector quantities (i.e., both negative and positive quantities are possible). However, certain operations can be applied that facilitate interpretation and comparison of the elements of the sensitivity matrix. Firstly, the elements of \mathbf{J} should be weighted by the corresponding data errors both to reduce elements to dimensionless quantities, allowing the comparison of impedance and magnetic transfer function responses, and to downweight elements that correspond with data with high errors. Secondly, the effect of varying model cell size (i.e., model mesh dimensions) can be suppressed by weighting the log-sensitivities with an appropriate scale factor. [Schwabenberg et al.](#) used the area of each 2D model element as a scale factor; it follows that weighting for our 3D resistivity model should instead use the volume of model elements as a scale factor. It should be noted that although the dependence of the Jacobian on element volumes is inherent to the computation of an inverse, for interpretation purposes some form of "sensitivity density" function is preferable. Downweighting the elements of the Jacobian by the volumes of the respective model elements achieves the desired re-scaling.

Formally, for a model element m_j of volume V_j , and data d_i with associated error e_i (note that due to the normalisation by error, $\partial d_i / \partial m_j$ has only the dimensions of $\Omega^{-1} m^{-1}$, and may hence

represent an impedance or a magnetic transfer function), the error- and volume-adjusted sensitivity J_{eV} (hereafter referred to as the adjusted-sensitivity) is determined by:

$$J_{eV}(i, j) = \frac{1}{e_i V_j} \frac{\partial d_i}{\partial m_j} \quad (4.5)$$

The integrated sensitivity of each model element (Zhdanov, 2002) can also be considered by computing the Euclidean norm of J_{eV} with respect to the data. The resultant vector can be reshaped to provide a sensitivity structure of the same dimensions as the model. The integrated sensitivity associated with a model element $\Sigma J_{eV}(m_j)$ is defined by:

$$\Sigma J_{eV}(m_j) = \sqrt{\sum_i \left[\frac{1}{e_i V_j} \frac{\partial d_i}{\partial m_j} \right]^2} \quad (4.6)$$

Given the number of elements in the Jacobian matrices (4,999,240,864 for the model and data selection presented), the Jacobian elements are first examined by histograms of the elements' magnitudes. Additionally, given that MT inversion meshes have extensive padding to avoid modelling edge effects, histograms of elements that correspond to the core portion of the model only are also presented, where exterior padding model cells and cells beyond 3 km depth are neglected to reduce the model to the central 109,242 elements. Figure 4.7 displays the effects of the two forms of adjustment (i.e., by data error and by element volume) on the magnitude distribution of the Jacobian. The distribution of the unweighted Jacobian has two peaks at magnitudes of 10^{-5} and 10^{-3} , with a long tail towards smaller values (particularly in the padding cells). In addition to converting the Jacobian to dimensionless values, adjusting the magnitudes by the corresponding data errors separates the two peaks by several further orders of magnitude. Magnitudes are also increased by the error adjustment, as the errors are significantly smaller than the data values. Lastly, the volume adjustment significantly penalises Jacobian elements that correspond to the exterior padding cells, as the padding cells have significantly greater volumes. Figure 4.8 reveals that the two peaks in Jacobian magnitude correspond to the two forms of magnetotelluric data involved, i.e., impedance and vertical magnetic transfer (tipper) data. For the inversion presented here an absolute minimum error (error floor) of 0.03 was assumed for all tipper data (i.e., an error from 5% to 100% and beyond of the tipper datum magnitudes, given that tipper data rarely exceed 0.6 in magnitude, and half are ≈ 0.03 or less), whereas 5% or 20% of the impedance magnitude was used for each impedance datum. If an assumed relative error floor for one channel of data (in this case, tipper data, although it could equally apply to diagonal impedance data in other cases) is systematically greater than other channels, the error-weighting of the Jacobian (i.e., J , unweighted) results in down-weighted sensitivities. At this stage the disparity in magnitudes appears to suggest that to obtain a change in tipper of comparable magnitude to those computed for impedances would require either larger resistivity variations or larger anomaly volume. Hereafter only the error- and volume-adjusted Jacobian (i.e., J_{eV} , the adjusted sensitivity) is discussed.

The visualisation of J_{eV} as an image in [Figure 4.9](#) was constructed from treating the data vector and model element vector of the Jacobian as a coordinate system, with data treated as a linear vector by nested iteration over frequency (from highest to lowest), then data type (Z_{xx} , Z_{xy} , Z_{yx} , Z_{yy} , T_x , T_y), then by site. Model elements are treated as a linear vector by nested over the z -direction first, then the x -direction and y -direction. The resulting image shows a reduction in sensitivity with depth (i.e., a decrease from left to right) for data of high-to-moderate frequency (low-to-moderate number). Additionally, a strong contrast in magnitude is evident between sensitivities associated with tipper data and those associated with impedance, with contrasts of ≈ 5 – 10 orders of magnitude. Due to the strong contrast in sensitivity between impedance and tipper components, the histograms of $\log_{10} J_{eV}$ in [Figure 4.10](#) show two distinct peaks at -7 and -13 , the majority of which are associated with cell elements within the core of the model (i.e., not padding cells). The long tail of smaller magnitudes not present in the core suggests that the padding cells have been correctly suppressed by volume-weighting of the Jacobian.

Examination of the histograms of integrated sensitivities in [Figure 4.11](#) shows the sensitivities related to the core volume of the model comprise the most sensitive region of the histogram, as would be expected. However, no clear division is evident between the summed sensitivities of the core model and those of the exterior padding portion of the model. Given the continuity between core and entire model histograms, no clear sensitivity value that could be used as a threshold to accept or reject resistivity structures is evident, and another criterion for acceptance would be required.

4.3.4 Examination by Jacobian Sensitivity

Due to its definition and relation of model elements to model responses, the integrated sensitivity distribution can be applied as an additional tool to evaluate the resistivity model. As the MT method is well-known to be more sensitive to conductors than resistors, a degree of correlation is expected in the spatial variations of the resistivity and sensitivity distributions; hence, the most immediate result is that any model portion with a high conductivity but low sensitivity should be noted as either exaggerated or created by inversion regularisation.

To demonstrate this concept, corresponding layers and profiles of the integrated sensitivity distribution are also presented on [Figure 4.3](#), [Figure 4.4](#), [Figure 4.5](#), and [Figure 4.6](#). The behaviour of integrated sensitivity with depth is generally a smooth decrease with depth, with higher sensitivities within the basinal region rather than the Dalradian horst to the south-east. The expected behaviour is broadly observed on the shallow 850 m slice, however, at depths of 1,550 m and 2,100 m, the basinal region east of $-6^{\circ}21'$ has notably lower sensitivity than the remainder of the basin. This decreased sensitivity can be understood as the data within this region is more impacted by cultural noise due to the town of Ballycastle and its surrounds; as a result much of it was not used in inversion, i.e., the omitted data represent rows that are absent from J . The affected region has elevated resistivity in comparison to the remainder of the basin, and in conjunction with the

reduced sensitivity we cannot conclusively interpret this portion of the model with regards to the presence or absence of the sediments of interest.

The three profiles of integrated sensitivity all feature their highest sensitivities in the uppermost 1000 m, within the central portion that lies beneath the MT sites, with sensitivities that generally decrease with depth. Large zones of reduced sensitivity are present on all three profiles, particularly beneath the north-eastern end of Profile A at depths below 2,000 km, and on profiles B and C beneath the Tow Valley Fault Zone. Additionally, some zones of lower sensitivity are present at or beneath conductive features, such as the deeper (1500 m) conductor on Profile A at 7,000 m profile distance. Such insensitive features that coincide with conductive features are of immediate interest and decrease the validity of model interpretation at the respective location.

The results shown here indicate that analysis of the sensitivity essentially does not contribute to the interpretation of additional structures in the model. Rather, the sensitivity must be used in conjunction with the resistivity model as a key to which portions of resistivity and conductivity have been determined by minimisation of the data residual term (i.e., higher sensitivity), and which portions are determined by the regularisation term and smooth (i.e., lower sensitivity). Hence, the result of sensitivity analysis on the interpretation of the model is a more conservative, limited interpretation of the extent of the existing understanding.

4.3.5 SVD Truncation of the Jacobian Sensitivity

In order to simplify the evaluation of the 3D MT model based upon the adjusted sensitivities, we consider the sensitivity matrix in its singular-value decomposed (SVD) form. The SVD of an m -by- n matrix A decomposes A into three separate matrices, that can be recombined to obtain the original matrix, i.e., $A = USV^T$ (Kaipio and Somersalo, 2006). The three matrices are U , an m -by- m matrix consisting of the eigenvectors of AA^* , S , an m -by- n diagonal matrix of "singular values" in descending order, and V , an n -by- n matrix consisting of the eigenvectors of A^*A . SVD is very closely related to the Principal Component Analysis approach to data describing data, in which a set of principal components (defined by $T = US$) are defined such that each principal component accounts for the most possible variance in the remaining data. As the diagonal elements of S are ordered by descending magnitude, and hence account for descending amounts of data variance, then the SVD can be used as a form of low-pass filter by using a truncated form of S to reconstruct A containing the sensitivity components that are most stable. Figure 4.12 presents the singular value distribution S of the sensitivity matrix, with the ratios of successful singular values presented beneath the main plot. A significant downwards decrease in the progression of S can be seen at approximately the 10,000th singular value, and we propose that S be truncated to this breakpoint before reconstructing a filtered Jacobian matrix J_{SVD} .

For comparison with Figure 4.10, histograms of the truncated-SVD reconstruction $J_{10,000S}$ are presented in Figure 4.13, with the distributions corresponding to the core model cells overlain. The truncated-SVD reconstruction completely recovers the original high sensitivity distribution associ-

ated with impedance data (i.e., $\log_{10}|J_{eV}| > -10$). The long tail to low sensitivities observed in the original Jacobian is not fully recovered in the truncation, however, due to the vanishingly small magnitudes the loss is not appreciable. [Figure 4.14](#) displays histograms of the corresponding integrated sensitivity reconstructions $\Sigma J_{10,000S}$; note that due to the large dynamic range of the constituent elements, ΣJ_{eV} is primarily dependent upon impedance sensitivities, and hence although the lower sensitivity components of J_{eV} are not well-replicated in $J_{10,000S}$, the summed Jacobian matrices ΣJ_{eV} and $\Sigma J_{10,000S}$ are comparable. We conclude that for the purposes of evaluating the MT model, truncation based upon singular value progression can result in a functionally identical Jacobian sensitivity matrix. Although this approach does not appear to immediately offer an accept/reject-type criterion for model evaluation, the truncated SVD form of the Jacobian can offer a significant logistical benefit due to the potentially great reduction in data storage requirements.

4.4 DISCUSSION

With the relationship between the objective function and the Jacobian in mind, analysis of the weighted Jacobian as a sensitivity matrix is a useful evaluation tool for the resistivity model. In particular, analysis of ΣJ showed that some conductive regions at depths of interest within the resistivity model may not be well constrained by the data, with sensitivities much decreased in comparison to similar depths elsewhere in the model. However, we would not describe sensitivity analysis by this method to be a fully finished tool, as certain issues would need to be addressed. Chief amongst the issues is the very significant gap in Jacobian sensitivities J_{eV} corresponding to tipper data in comparison with those corresponding to impedance data, as evident in the histograms in [Figure 4.10](#). Although the mismatch in relative errors of impedance and magnetic transfer data (i.e., 5% of off-diagonal impedance magnitude c.f. $>5\%$ of magnetic transfer magnitude) exacerbates the difference in sensitivity magnitudes, a several order-of-magnitude difference in location of peaks of impedance and magnetic transfer function remains present even in the histogram of unweighted Jacobian magnitudes in [Figure 4.7](#). Given that the Jacobian represents the effect on model responses by small perturbations to the model on an element-wise basis, the fractional changes in vertical magnetic transfer function responses compared to impedance responses may be a by-product of the method of computation. Vertical magnetic transfer data are significant in regions of significant lateral resistivity contrast such as fluid-saturated fault zones or dikes. Given that the model elements within the volume of interest considered here are generally 400 m by 400 m across, but 20 to 30 m thick, then the fractional perturbation of resistivity of a single model element involved in the Jacobian computation may simply not be at the scale of lateral resistivity contrasts that give rise to the observed vertical magnetic transfer function, particularly as MT site locations tend towards the centre of model elements (i.e., at distance from the lateral boundaries). It may also be that the aspect ratios of model elements used in this work (i.e., an element is typically five to ten times wider than it is thick) are poor for the purposes of estimating the Jacobian sensitivity of vertical magnetic transfer data. Synthetic forward modelling is required to establish baseline

expectations of the relative magnitudes of **T** and **Z** sensitivities before drawing further conclusions on the reasons behind discrepancies in the relative magnitudes of **T** and **Z** sensitivities in inversion of field data. Such investigation could also examine if variation of model element geometries affect **T** and **Z** sensitivities at different rates.

Due to the dominance of **Z** sensitivities in the integrated sensitivity ΣJ , truncation of the SVD by the largest 10,000 singular values recovers $\Sigma J_{10,000S}$ that is mostly equivalent to ΣJ_{eV} , with little filtering evident. However, the continued presence of the sensitivity structures suggests that the truncated SVD validates the robustness of the sensitivity features and allows for more confident analysis of the sensitivity. A well-known benefit of the SVD truncation is a significant decrease in size of the U , S and V matrices. For the case presented here, i.e., $J_{10,000S}$, the original matrix U_0 is $328,984 \times 15,196$ in size (strictly an SVD decomposition would be $328,984 \times 328,984$, however the columns beyond 15,196 contain only zeroes, S_0 is $328,984 \times 15,196$ in size, and V_0 is $15,196 \times 15,196$ in size. If $J_{10,000S}$ is considered, then the matrices are significantly smaller, i.e., $U_{10,000S}$ can be reduced to $328,984 \times 10,000$, and both $S_{10,000S}$ and $V_{10,000S}$ can be reduced to $10,000 \times 10,000$ in size. In terms of a total number of variables, the SVD truncation represents a reduction to approximately 70% of the original size. Note that truncation to a further reduced number of singular values will have a greater reduction in storage and memory requirements; far greater efficiency could be achieved with fewer singular values, however, the effect on the reconstructed Jacobian would require careful examination.

[Figure 4.4](#), [Figure 4.5](#) and [Figure 4.6](#) show numerous small (i.e., one or two cells) low-sensitivity (i.e., $\Sigma J < 10^{-3}$) anomalies at shallow to moderate depths with poor lateral continuity. The causes of these anomalies are unclear, as the normalisation by data errors and cell volumes are identical to the cells adjacent to the anomalies. The anomalies also appear to be smeared vertically, which suggests that the anomalies may originate from vertical smoothing within the 3D inversion. Specifically, if a column within the model has a portion with lower sensitivity than elsewhere in the column, then the vertical smoothing portion of inversion may propagate a reasonable resistivity through the low sensitivity portion. Hence, in addition to clarifying the large-scale sensitivity structure, examining a model's sensitivity can also shed light on more minor portions of the resistivity that have been interpolated from smoothing functions.

It is important to note that as low-sensitivity anomalies often coincide with acceptable resistivity structure, the resistivity structure may be interpreted with a false level of confidence, e.g., the north-east end of Profile A at depths below 2,000 m depth. For MT resistivity models with more complicated resistivity structures than the model presented here, examination of the sensitivity distribution should be considered to verify interpretations made from the resistivity. Specifically, caution should be maintained of otherwise-interpretable model features that coincide with low integrated sensitivities, as such features have higher degrees of constraint by regularisation in place of model residuals.

4.5 CONCLUSIONS

In an effort to validate interpretation of a 3D resistivity model, we have analysed the Jacobian-derived sensitivity of the model with respect to its MT responses. Appropriate weighting of the sensitivities by data errors and model cell volumes reduces the relationship between the adjusted sensitivity and MT responses to one that more accurately reflects whether a model element's resistivity is more strongly determined by the data residual, or by the regularisation term applied during the inversion process. Additionally, truncated Singular Value Decomposition of the Jacobian was considered as a way to determine an acceptance/rejection criterion; although the results of this are not conclusive, the logistical and computational gains of such truncation should not be overlooked.

The results of comparing the sensitivity and resistivity distributions show that the approach suggested here adds considerable interpretive information about the validity of individual resistivity structures within the model. Although the computation of the entire Jacobian is an expensive process, the additional structural confidence can drastically change how a model is perceived, and ultimately will improve the final interpretation.

4.6 ACKNOWLEDGMENTS

We would like to acknowledge the financial support to RD from the IREtherm project funded by Science Foundation of Ireland (10/IN.1/I3022) to AGJ. MT data were acquired with the assistance of C. Hogg, S. Blake, C. Yeomans, T. Farrell, and M. Muller. We acknowledge use of the SRTM elevation data available from the U.S. Geological Survey. Gary Egbert, Anna Kelbert and Naser Meqbel are very gratefully thanked for making their ModEM code available to the community, and especially Naser Meqbel for installing it on our clusters and those of the Irish Centre for High- End Computing (ICHEC). The Geological Survey of Ireland and the Geological Survey of Northern Ireland are thanked for providing access to Tellus Project data and other complementary information. M Dessisa of the GSNI is especially thanked for his assistance with the latter. Amira International is thanked for providing open access to the P223 modelling suite. ICHEC is thanked for providing the computational capability required for us to perform our inversions.

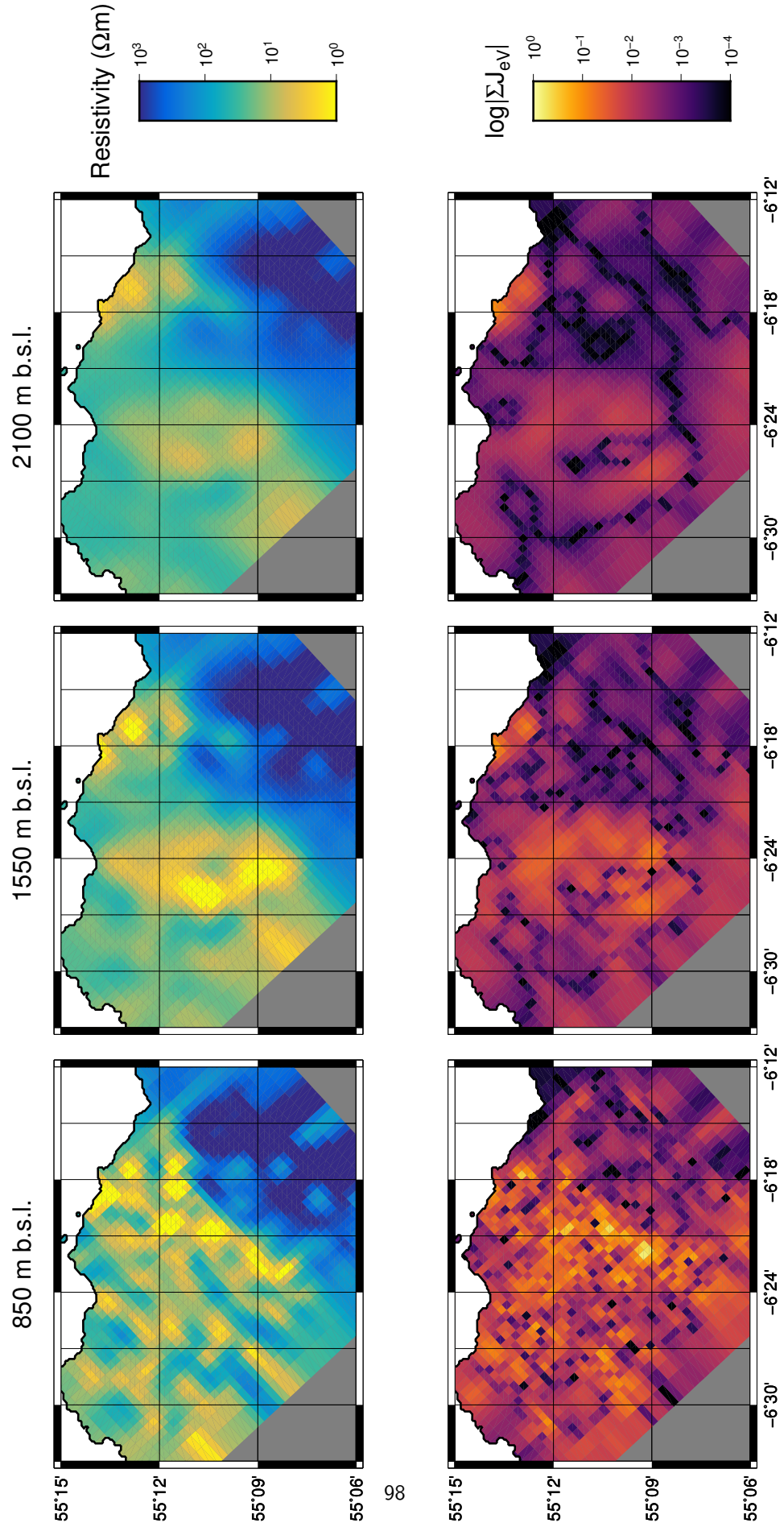


Figure 4.3.: Upper row: horizontal slices through the 3D resistivity model. Lower figure: horizontal slices through the integrated sensitivities ΣJ_{eV} of the model

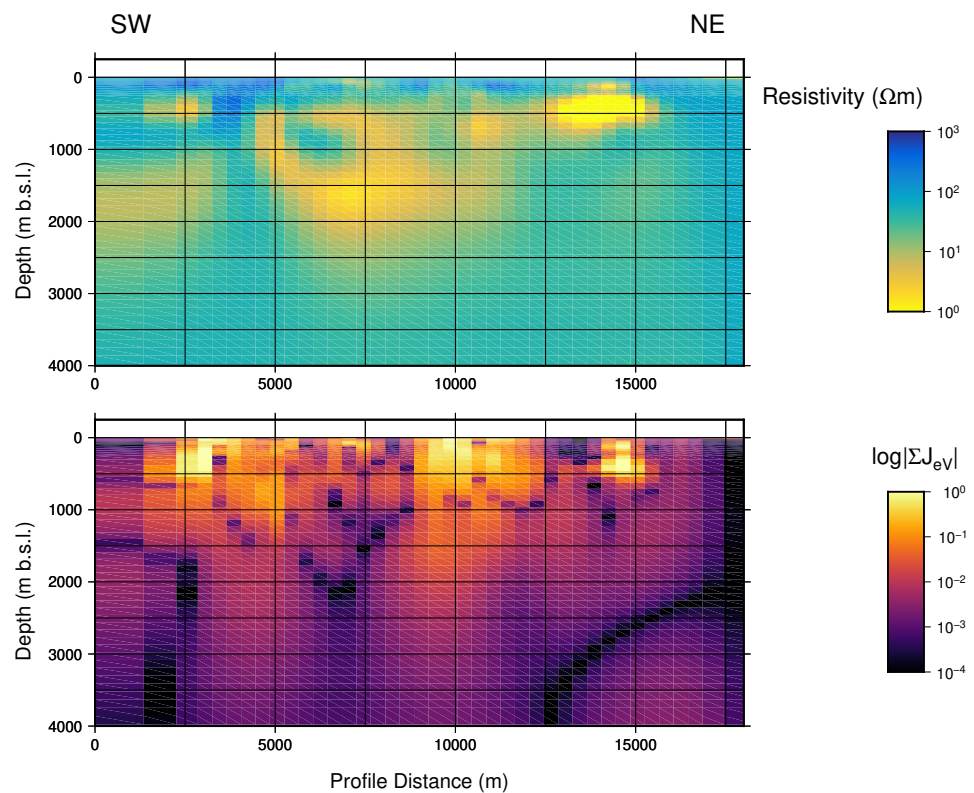


Figure 4.4.: Upper: resistivity distribution along Profile A (axial along basin). Lower: integrated sensitivity distribution along Profile A.

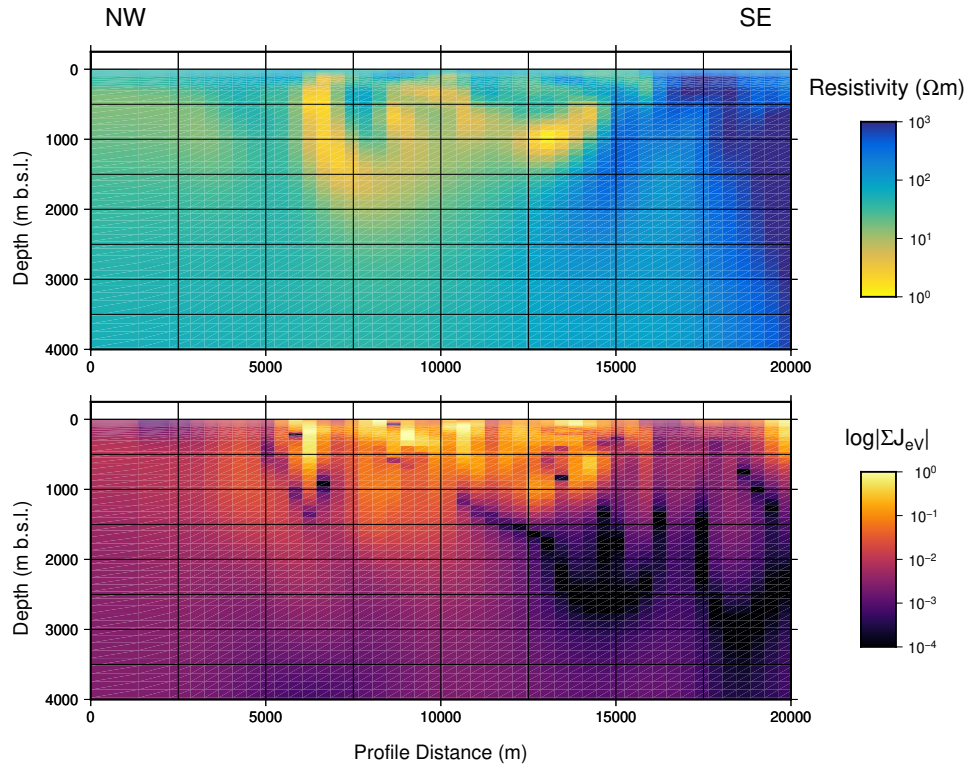


Figure 4.5.: Upper: resistivity distribution along Profile B (transverse across basin). Lower: integrated sensitivity distribution along Profile B.

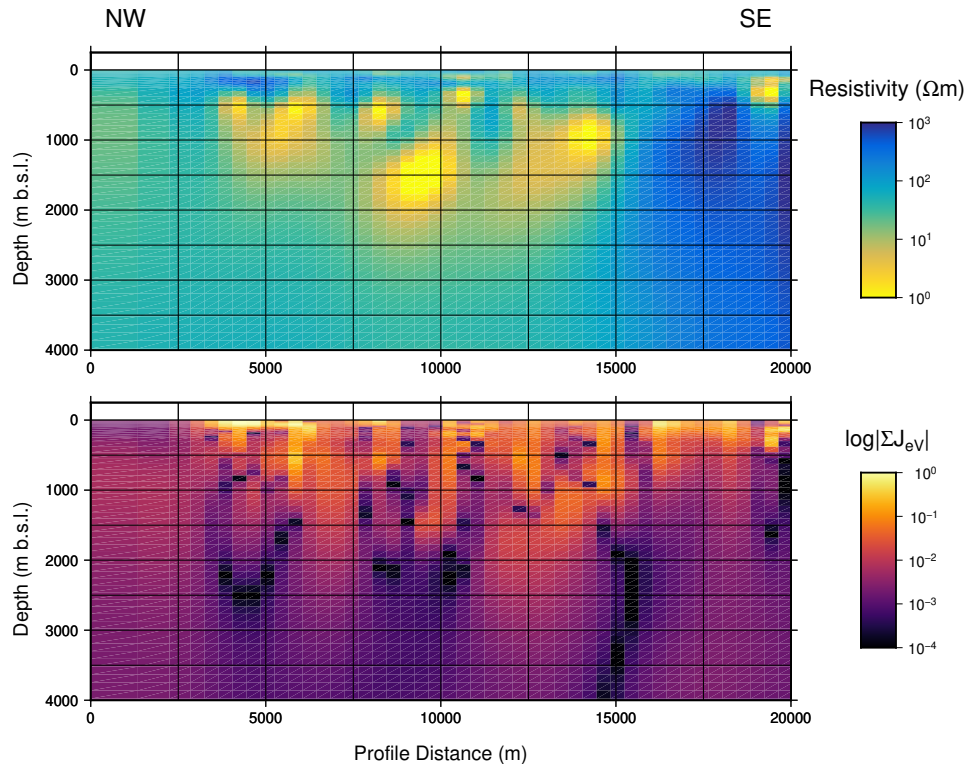


Figure 4.6.: Upper: resistivity distribution along Profile C (transverse across basin). Lower: integrated sensitivity distribution along Profile C.

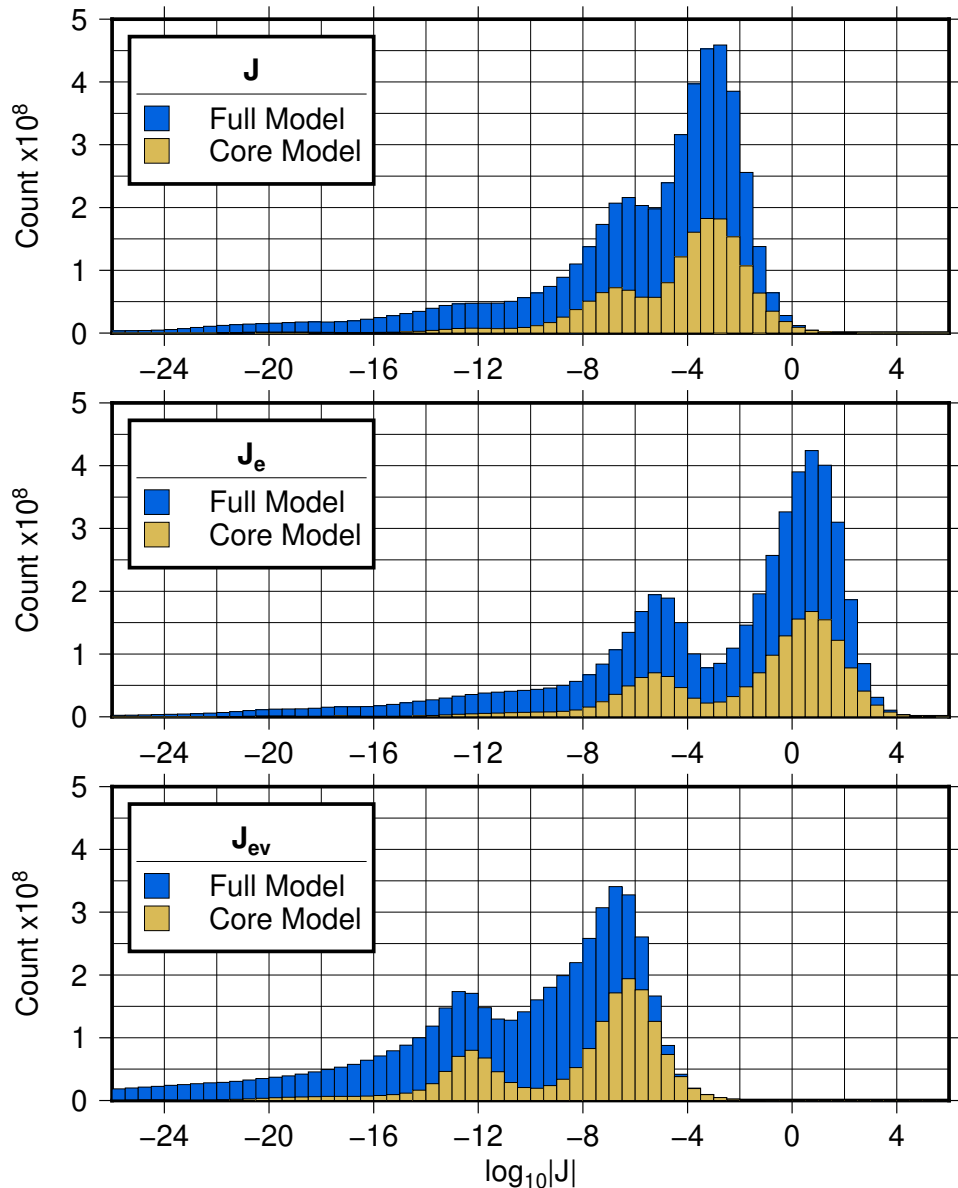


Figure 4.7.: Comparative histograms of the magnitude distributions of: (top) the original Jacobian elements, (middle) the error-adjusted Jacobian elements, and (bottom) the error- and volume-adjusted Jacobian elements. Each histogram also shows the distribution of magnitudes of Jacobian elements corresponding to the central core of the model (i.e., with padding cells stripped).

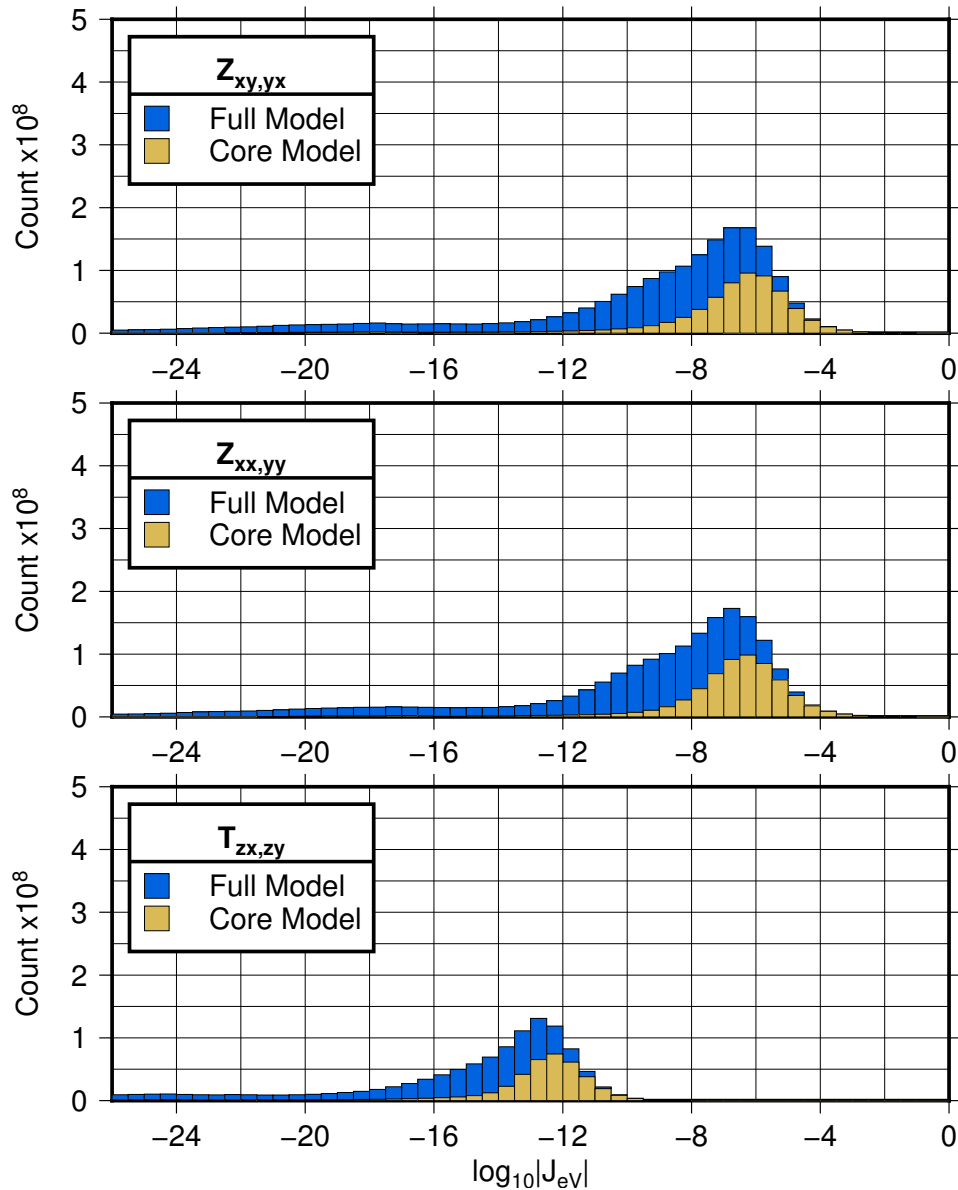


Figure 4.8.: Comparative histograms of the magnitude distributions of error- and volume-adjusted Jacobian elements that correspond to: (top) off-diagonal impedance data, (middle) diagonal impedance data, and (bottom) tipper data. Each histogram also shows the distribution of magnitudes of Jacobian elements corresponding to the central core of the model (i.e., with padding cells stripped). The disparity in magnitudes suggests that obtaining a change in tipper of comparable magnitude would require either larger resistivity variations or larger anomaly volume.

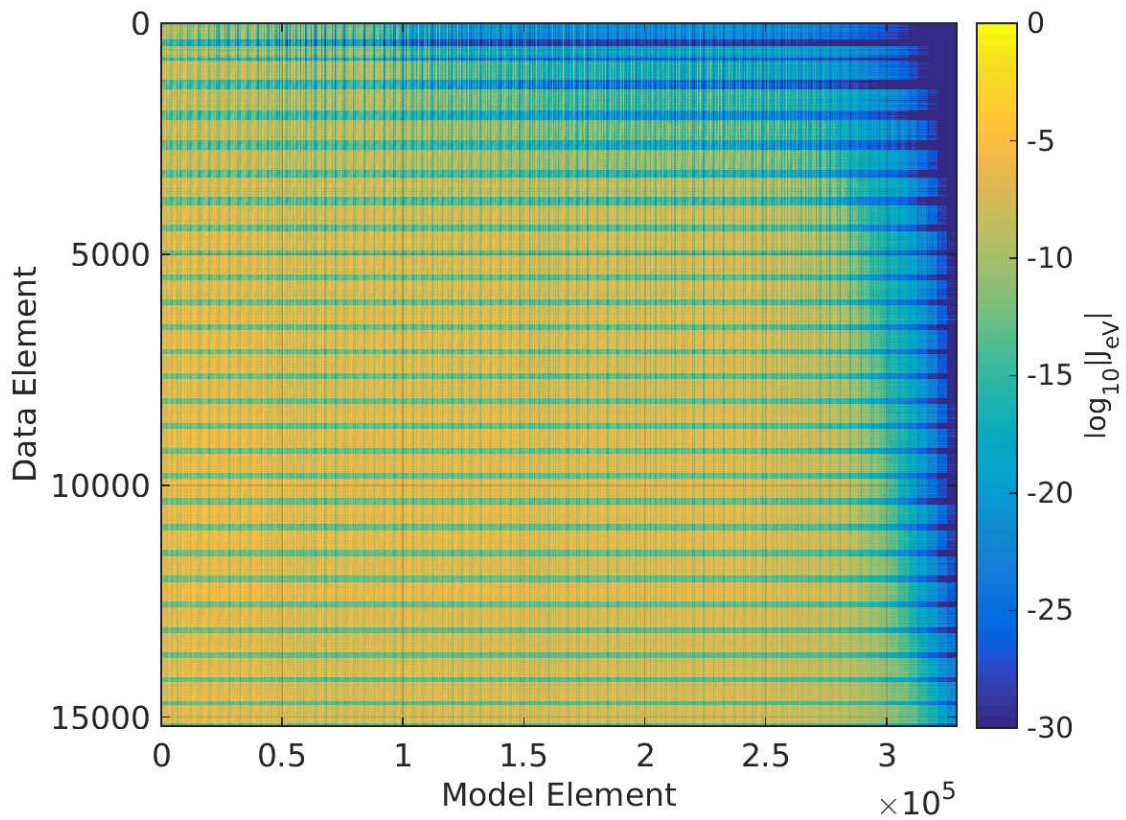


Figure 4.9.: Visualisation of adjusted sensitivities of the 3D MT model, with both data and model elements linearised as axes. The linearised data are sorted by site, then component, then increasing period, whereas the linearised model is sorted by layer. Tipper data have generally lower sensitivities, resulting in distinct horizontal banding in the image.

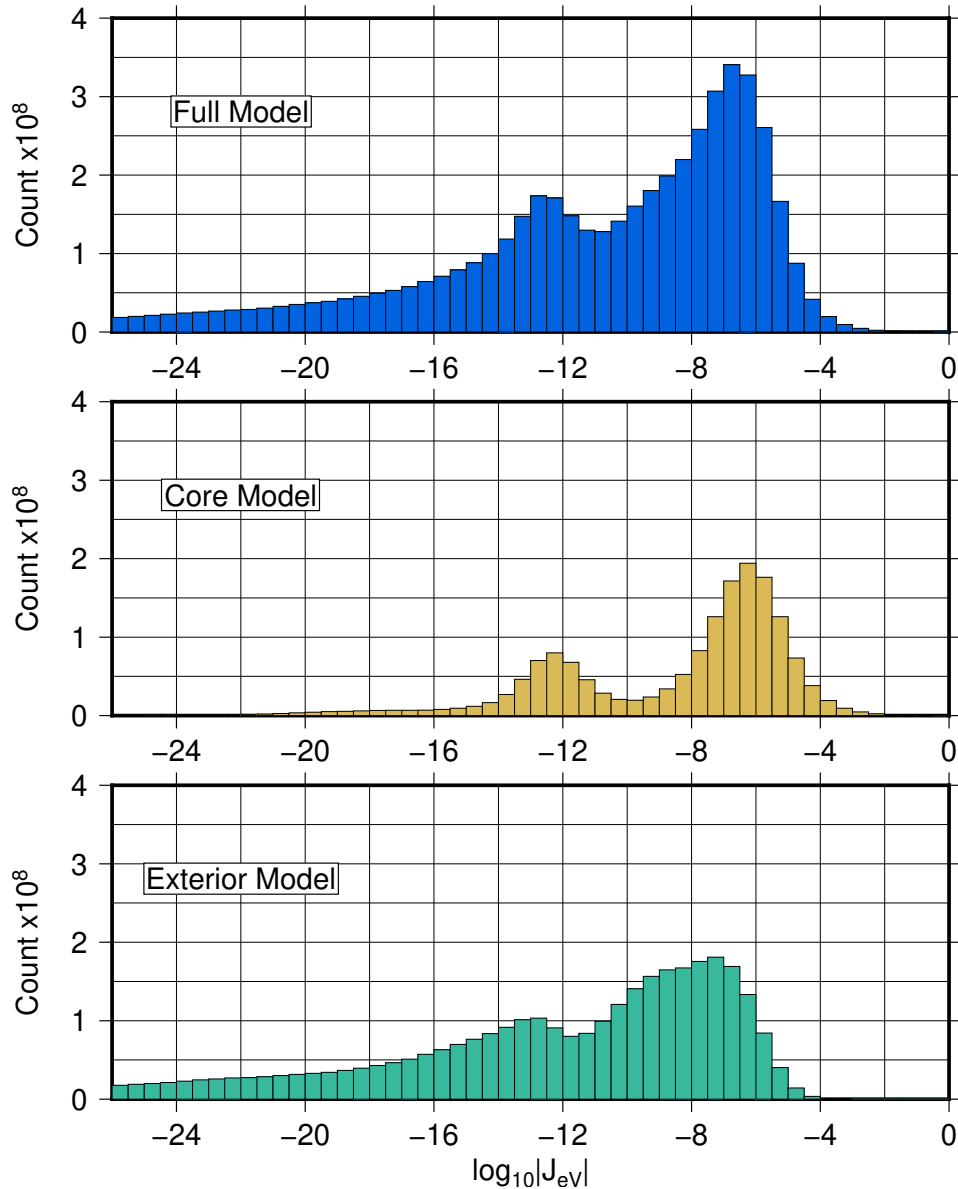


Figure 4.10.: Top: histogram of adjusted sensitivities of the 3D MT model. Middle: histogram of adjusted sensitivities of the core portion of the model (i.e., outer padding cells and cells beneath 3 km depth excluded). Bottom: histogram of adjusted sensitivities of the exterior cells of the model.

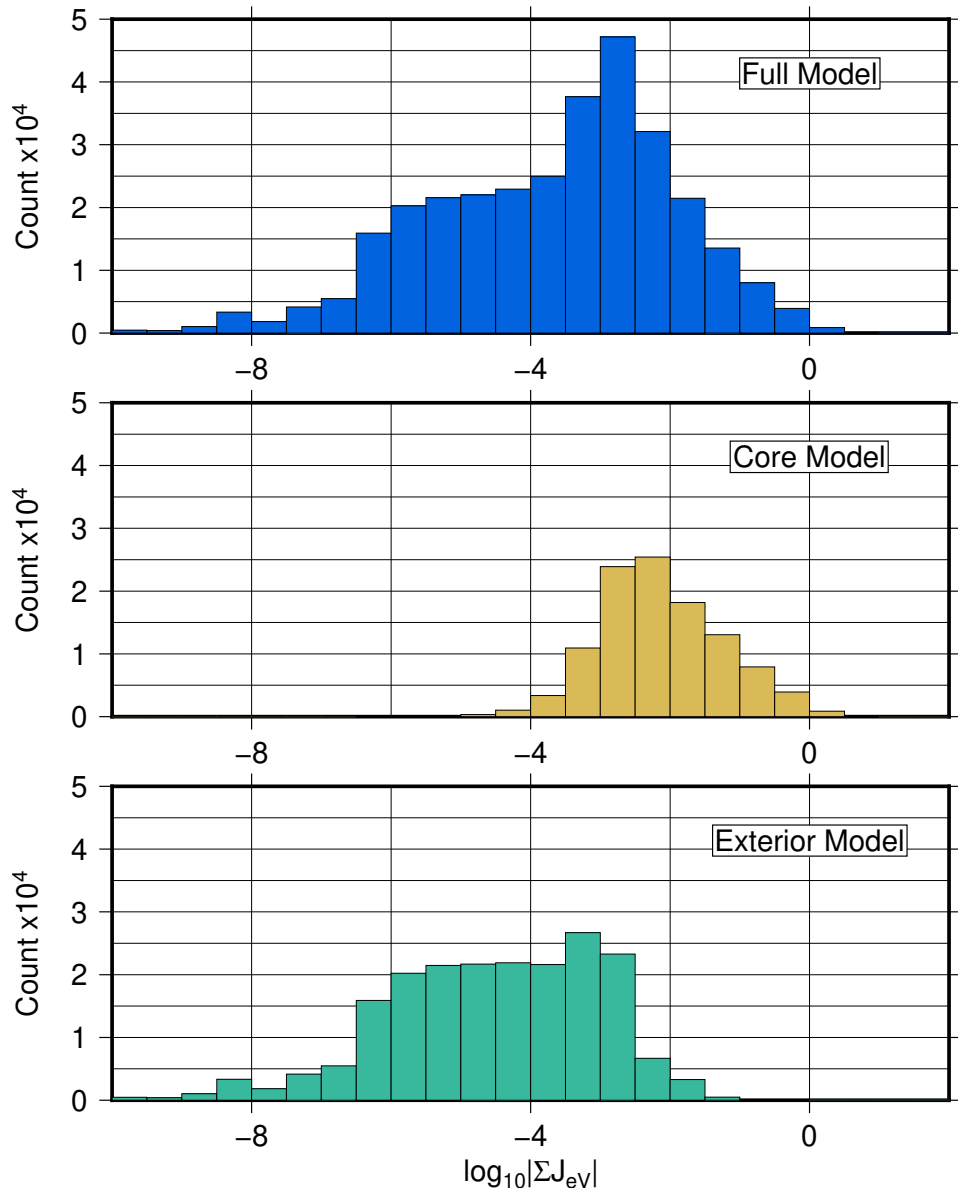


Figure 4.11.: Top: histograms of integrated sensitivities of the 3D MT model. Middle: histogram of integrated sensitivities of the core portion of the model (i.e., outer padding cells and cells beneath 3 km depth excluded). Bottom: histogram of adjusted sensitivities of the exterior cells of the model.

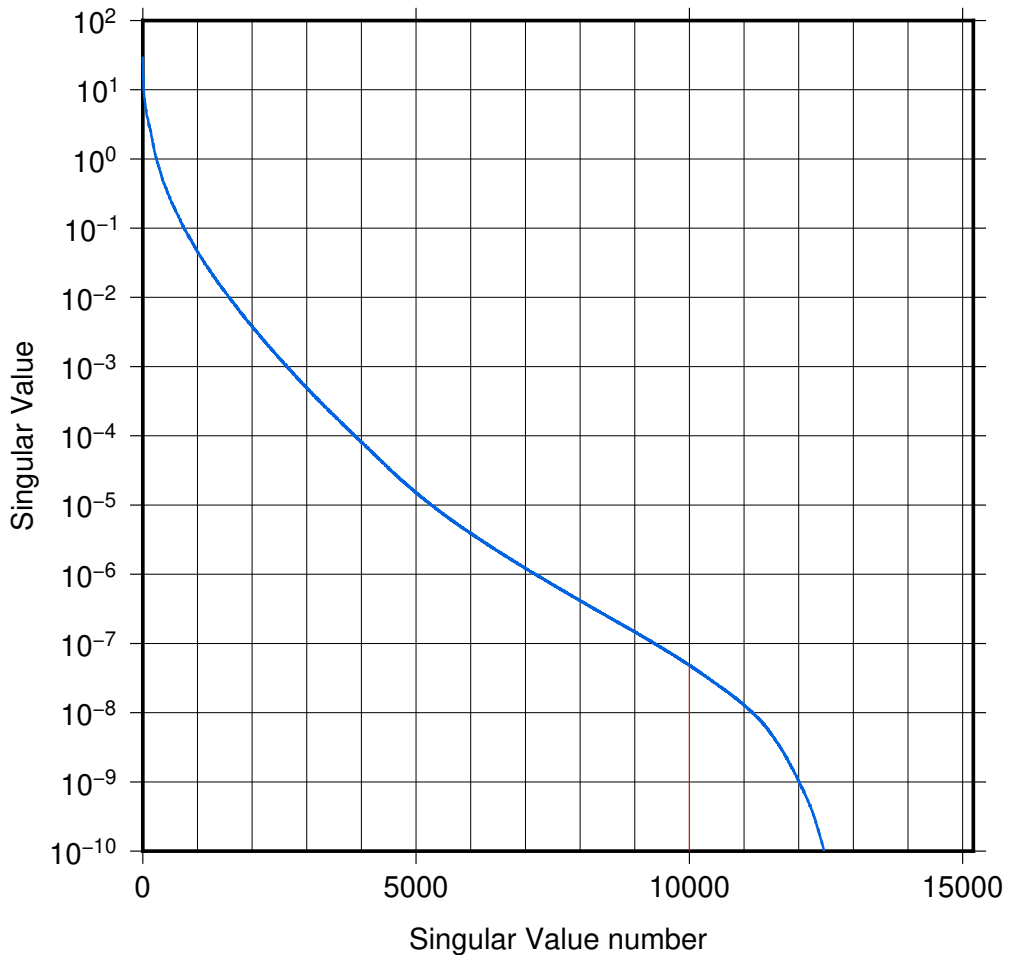


Figure 4.12.: Singular values of the SVD-decomposed Jacobian matrix for the Rathlin Basin MT model are presented in the upper plot. The break points at the 10,000th singular value is marked with a red line.

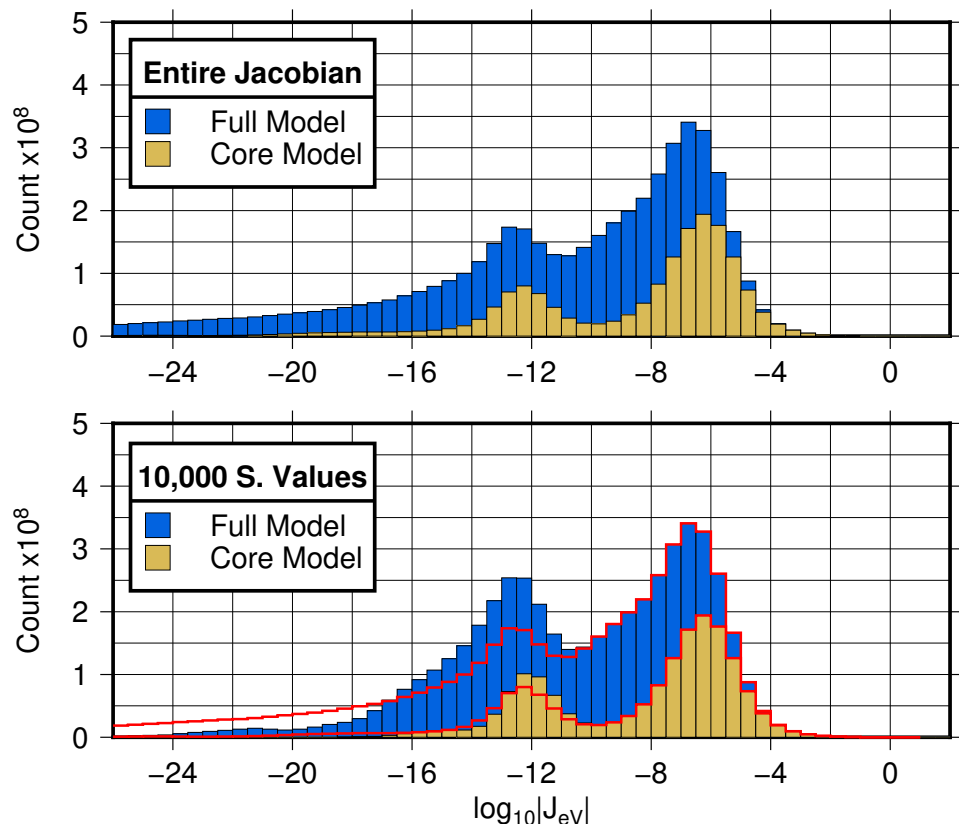


Figure 4.13.: Comparative histograms of the original adjusted sensitivities of the complete Jacobian, and the reconstructed Jacobian matrix $J_{10,000S}$. The histograms of the reconstructed Jacobian has the outline of the complete Jacobian's histogram shown in red.

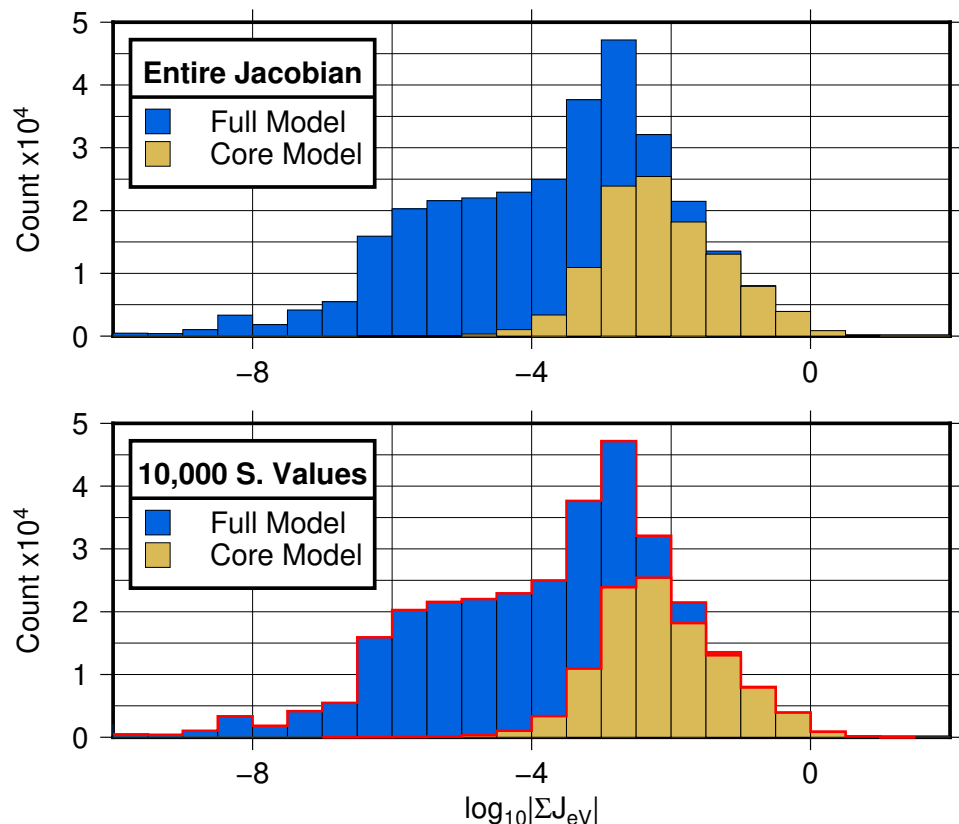


Figure 4.14.: Comparative histograms of the integrated sensitivities of the complete Jacobian, and the reconstructed Jacobian matrix $\Sigma J_{10,000S}$. The histograms of the reconstructed Jacobian has the outline of the complete Jacobian's histogram shown in red.

5

CONCLUSIONS

The work presented in this thesis endeavours to improve knowledge of the sedimentary Rathlin Basin in Northern Ireland by determination of electrical resistivity models from new MT data. The resulting treatment and modelling of the MT data has lead to a new methodology for treatment of static-shift distortion of MT data, and 1D resistivity models that allow estimation of the geothermal resource present within the onshore Rathlin Basin. Additionally, an approach to manipulating the Jacobian sensitivity of the 3D resistivity model has resulted in a potential tool to assess the confidence with which resistivity structures should be interpreted.

5.1 REVISITING THE RESEARCH QUESTIONS

The chapters of this thesis were organised in order to answer three research questions. Each research question was addressed by a separate chapter in this thesis.

5.1.1 *How can regional airborne EM data from the Tellus Project be used in static shift correction of MT data?*

The Tellus Project airborne frequency-domain EM data set represents an enormous resource of near-surface resistivity information; as such, it is of considerable value in the context of accounting for static-shift type distortion of MT data. [Chapter 2](#) presents a methodology for doing so that follows the steps previously laid out for time-domain EM data, modified to account for the different data type and acquisition (i.e. airborne flight lines rather than co-located terrestrial sites). The methodology involves 1D modelling of the regionally available, high resolution Tellus airborne EM data, and computation of synthetic MT responses at locations that correspond to MT site locations, allowing corrections for static shift distortions to be calculated. The application of corrections determined by this method leads to significant changes in the resulting MT model, as would be expected from any other static-shift treatment that involves perturbations of the data. Critically, the model determined from static-shift corrected data shows a distinct improvement in recovered structure when compared to models from uncorrected data, measured against the lithological boundaries observed in borehole records. The results obtained in this portion of the

thesis support the conclusion that airborne EM data present a promising option for large-scale correction of static-shift distortion, in areas where the near-surface can generally be assumed to be laterally homogeneous.

5.1.2 *What can be inferred about the geothermal potential of Rathlin Basin from MT models?*

Chapter 3 describes how the static-shift corrected resistivity MT data of the onshore Rathlin Basin (determined in [Chapter 2](#)) have been modelled in 1D, with the set of models interpreted in the context of hosting a potential geothermal aquifer. The resistivity models were interpreted according to the vertical derivative of resistivity, as the structural features of principle interest are resistivity contrasts between sub-horizontal sedimentary layers. The approach successfully recovered structure consistent with the two deep boreholes within the basin, and in particular, a conductor associated with the target Sherwood Sandstone Group and Permian sandstones was identified. In conjunction with thermal information from the Ballinlea 1 borehole and laboratory measurements of hydraulic properties of the reservoir rocks taken from the Port More 1 borehole, the depth and thickness distribution of the target sandstones allows computation of an Indicated Geothermal Resource. The IGR defined in this method (as proscribed in [Lawless \(2010\)](#)) is $\approx 2.9 \times 10^{18}$ J (i.e. 2,900 PJ), computed for a final reservoir temperature of 25 °C (note that the IGR is also considered as a function of temperature in the chapter). To place the computed density of geothermal energy in place over the Rathlin Basin of between 1 and 4×10^{10} J m⁻² in context, a similar measure of the Dogger Basin beneath Paris, France, estimates a geothermal potential of 2.5×10^{10} J m⁻² ([Jaudin et al., 2009](#)); as the Dogger Basin is currently exploited for space heating, the potential of the Rathlin Basin is clear.

As defined in the Australian Geothermal Lexicon, an Indicated Geothermal Resource is defined as the "part of a Geothermal Resource which has been demonstrated to exist through direct measurements that indicate temperature and dimensions so that Recoverable Thermal Energy (in units of PJ_{th} or MW_{th}-years) can be estimated with a reasonable level of confidence". Insofar as is possible with the current geophysical and geological information, we consider this IGR estimate as the limiting case of what may be defined without further data acquisition.

5.1.3 *What additional value can be added to 3D model interpretation by also considering the sensitivity of model responses?*

The 3D resistivity model determined in [Chapter 2](#) was considered further in [Chapter 4](#), focusing on the application of the Jacobian matrix relating the model parameters to model MT responses. Appropriate treatment of the Jacobian clarifies that some portions of the model have conductive features coincident with low sensitivity zones; such conductors should be interpreted with lower confidence as their conductivity has a comparatively greater reliance upon the regularisation. An attempt was also made to define an acceptance criterion based upon a sensitivity distribution

determined by truncation of the SVD of the Jacobian matrix (acting as a filter function); although unsuccessful, the truncated SVD form has significantly eased storage and computational demands. The results of this study suggest that sensitivity analysis is a highly useful method for adding confidence to model interpretation, and although expensive, should be more commonly used.

5.2 RECOMMENDATIONS FOR FURTHER RESEARCH

Based upon the results and points of consideration from the research presented in this thesis, the author has identified several avenues for further research to build upon the conclusions. These are presented below, broadly categorised into methodological and specific suggestions (i.e. in regards to geothermal exploration and exploitation of the Rathlin Basin).

5.2.1 *Methodological Recommendations*

ADVANCEMENT OF FDEM MODELLING FOR STATIC SHIFT CORRECTION Although the modelling of AEM data in 1D frameworks (i.e. as half-spaces or layers) has shown good results in the work presented here for correction of static-shift effects, the approach could be easily extended to include 2D or 3D modelling of the AEM. Such modelling in greater than 1D frameworks could produce satisfactory static-shift corrections in regions with more complicated near-surface resistivity structure than those encountered in the Rathlin Basin.

However, moderate issues would need to be addressed as part of advancing the AEM modelling or static-shift correction calculation. In particular, the modelling of AEM in a 2D framework requires reconciliation of the linear AEM resistivity model with the orthogonal MT response directions in a potentially different co-ordinate system. Such problems with data alignment would be avoided by moving to a 3D modelling framework. The use of 3D inverse modelling was tested with the Tellus AEM data; however, the lateral gap between adjacent flightlines proved to be too great and prevented the solution of meaningful structure.

POST-INVERSION MODEL APPRAISAL An optimum way of appraising (in a non-interpretative context, rather than in comparison to geological information) inversion models, with more granularity than a single nRMS value, remains to be generally adopted across the MT community. Examination of the sensitivity (as defined as the sum of the Jacobian over all model responses, weighted by the data errors and element volumes) may provide one avenue to do so; however, the computation of the complete Jacobian for a moderately sized 3D model remains a not-insignificant task.

Additionally, although the normalised cross-gradient measure used in this thesis has performed well in comparison of MT models, alternative objective measures may also exist. I have considered correlation of models by Fourier transform, however, the initial hurdle is how best to handle the irregularly spaced vertical layers.

FURTHER INVESTIGATION OF INVERSE MODEL SENSITIVITY ANALYSIS The sensitivity analysis applied in Chapter 4 suggests that some of the modelled conductors within the Rathlin Basin should be interpreted with reduced confidence due to the influence of the algorithmic regularisation and smoothing. Singular value decomposition of the full Jacobian was attempted to evaluate if breakpoints in the singular value magnitudes would provide clear sensitivity thresholds for model area acceptance. Regrettably, insofar as the SVD approach has been successful in drastically reducing the required information, the desired thresholds have not been determined. However, the compressional benefits of the SVD should facilitate future research in this area. Alternatively, the Jacobian could be summed over the data axis rather than the model axis, with suitable weighting, in order to gauge the relative importance of each data component.

5.2.2 Recommendations for the Assessment of the Rathlin Basin

VALIDATION OF INTERPRETED LAYER BOUNDARIES Verification of the MT model's interpretation is limited by the existence of only two deep boreholes, in addition to the slight resistivity contrasts between layers of interest. If no large-scale lateral resistivity variations are present within the target layers, the current interpretation of the MT model is agreeable with existing constraints. However, such regional homogeneity is unlikely, and any geological constraint from additional boreholes within the survey area would provide valuable insight into the model's current validity.

Additionally, near-surface resistivities were significantly lower than expected, adversely affecting the modelling of the resistivity structure within the shallowest ≈ 1500 m between MT sites. The acquisition of additional MT sites interspersed between the existing sites would greatly clarify the uppermost layer boundaries, especially the top of the MMG. As a first step, such additional research need not be on nearly the scale - rather, even an additional three sites between the two existing boreholes would be tremendously insightful, giving a shorter profile with 1 km site spacings.

UPGRADE INDICATED GEOTHERMAL RESOURCE ESTIMATE In accordance with the definitions stated in the Australian Geothermal Lexicon, an Indicated Geothermal Resource (IGR) is "...that part of a Geothermal Resource which has been demonstrated to exist through direct measurements that indicate temperature and dimensions so that Recoverable Thermal Energy (in units of PJ_{th} or $MW_{th}\text{-years}$) can be estimated with a reasonable level of confidence.". The criteria for this definition have been achieved by the Ballinlea 1 borehole temperature measurements and 3D MT modelling. However, the estimates associated with an IGR are limited by a lack of petrophysical knowledge regarding reservoir continuity. In order to upgrade an IGR to a Measured Geothermal Resource, estimates of how much recoverable thermal energy are present must take into account hydraulic properties (i.e. permeability) that affect

well deliverability. Hydraulic property knowledge at the stage of the research presented here was limited to nine core samples from the Port More 1 Borehole, with lab measurements taken in the 1970s. Without additional samples or measurements between new boreholes within the target sediments, there is insufficient evidence to allow estimation of a Measured Geothermal Resource.

IMPROVE OVERALL DEPICTION OF IRISH REGIONAL HEAT FLOW From the outset of the IREtherm Project, an ongoing concern has been the limited knowledge of region-scale thermal structure. As outlined in the introduction, current knowledge is based upon the sparse deep boreholes and surface heat flow measurements. Given the extensive (and increasing) coverage of Ireland by the Tellus Project and its subsequent expansive projects, spectral analysis of the aeromagnetic data could be applied in order to estimate the Curie Point Depth (CPD) beneath much of Ireland (Tanaka et al., 1999). With appropriate assumptions about the magnetised minerals in Irish crustal rock, the CPD distribution can provide a useful background map of geothermal gradient (i.e., without contribution from crustal heat sources), independent of the sources of current uncertainty. Further research on applying such an approach to Ireland is ongoing (Delhaye and Mather, 2018).

5.3 IN CONCLUSION

The research presented in this thesis occurred as part of the IREtherm Project, in order to investigate the geothermal potential of the Rathlin Basin. Magnetotelluric and airborne frequency-domain electromagnetic data have been used to determine electrical resistivity models that reproduce the sediments of interest. New methodological approaches have been developed and applied in order to improve the models, resulting in significant improvement and clarification of models. In particular, the new static-shift correction approach taken in this research has improved the recovery of sedimentary layers in comparison to deep boreholes, whereas visualisation of the integrated sensitivity of the 3D resistivity model presents a new means of assessing the dependence of model structure on input data rather than algorithmic smoothing.

Resistivity models of the onshore Rathlin Basin has allowed the estimation of an Indicated Geothermal Resource of 2,900 PJ, an IGR that is significantly greater than similar estimates presented for adjacent basins. It should be noted that this estimate of heat energy in place is an outside estimate that assumes total recovery of the energy, and does not take into account the hydraulic permeability nor inefficiency of extraction. Regardless, this IGR estimate represents a valuable contribution towards the goal of IREtherm insofar as is possible to achieve with geophysics alone.

Sensitivity analysis of the 3D resistivity model has clarified that most of the model can be interpreted with confidence, however, the regions beneath the Tow Valley Fault, and surrounding the town of Ballycastle show reduced sensitivity that should limit interpretation. The method shows promise for aiding assessment of other models, particularly in cases where different subsets of data

are used for inversion. For example, if a project region has several phases of data collection, the Jacobian sensitivities of cumulative model (i.e., with additional data added) should highlight which model portions are most affected by the additional sites.

The modelled reservoir sediments in the Rathlin Basin beneath mainland Ireland and assumed beneath Rathlin Island support the original hypothesis of a significant geothermal resource in Northern Ireland. The estimated IGR of 2,900 PJ represents a sizeable amount of heat energy, particularly if one considers that this estimate does not include any additional volume from offshore to the north-east and beneath Rathlin Island, nor from further west towards the Foyle Basin.

BIBLIOGRAPHY

- J. J. Adams and S. Bachu. Equations of state for basin geofluids: algorithm review and intercomparison for brines. *Geofluids*, 2(4):257–271, 2002. (Cited on page [78](#).)
- G. E. Archie. Electrical resistivity an aid in core-analysis interpretation. *AAPG Bulletin*, 31:350–366, 1947. ISSN 0149-1423. doi: 10.1306/3d93395c-16b1-11d7-8645000102c1865d. (Cited on pages [24](#) and [68](#).)
- K. Árnason. The static shift problem in MT soundings. In *Proceedings of the World Geothermal Congress, 15–19 April 2015 in Melbourne, Australia*, 2015. (Cited on pages [10](#), [11](#), and [12](#).)
- E. Auken, A. Vest Christiansen, C. Kirkegaard, G. Fiandaca, C. Schamper, A. A. Behroozmand, A. Binley, E. Nielsen, F. Effersø, N. B. Christensen, K. Sørensen, N. Foged, and G. Vignoli. An overview of a highly versatile forward and stable inverse algorithm for airborne, ground-based and borehole electromagnetic and electric data. *Exploration Geophysics*, 46(3):223–235, 2014. doi: 10.1071/EG13097. (Cited on page [26](#).)
- A. Avdeeva, M. Moorkamp, D. Avdeev, M. Jegen, and M. Miensopust. Three-dimensional inversion of magnetotelluric impedance tensor data and full distortion matrix. *Geophysical Journal International*, 202(1):464–481, 2015. doi: 10.1093/gji/ggv144. (Cited on pages [11](#) and [22](#).)
- K. Baba, A. D. Chave, R. L. Evans, G. Hirth, and R. L. Mackie. Mantle dynamics beneath the east Pacific rise at 17°S: Insights from the Mantle Electromagnetic and Tomography (MELT) experiment. *Journal of Geophysical Research: Solid Earth*, 111(B2), 2006. (Cited on page [xiii](#).)
- D. Beamish. The bedrock electrical conductivity structure of Northern Ireland. *Geophysical Journal International*, 194(2):683–699, Aug. 2013. ISSN 1365-246X. doi: 10.1093/gji/ggt073. (Cited on pages [23](#), [31](#), and [89](#).)
- D. Beamish, R. J. Cuss, M. Lahti, C. Scheib, and E. Tartaras. The Tellus airborne geophysical survey of Northern Ireland: Final processing report. Internal Report IR/06/136, British Geological Survey, Nottingham, UK, 2006. (Cited on page [31](#).)
- C. J. Bean and F. Martini. Sub-basalt seismic imaging using optical-to-acoustic model building and wave equation datuming processing. *Marine and Petroleum Geology*, 27(2):555–562, Feb. 2010. ISSN 02648172. doi: 10.1016/j.marpetgeo.2009.09.007. (Cited on page [20](#).)
- G. R. Beardmore and J. P. Cull. *Crustal heat flow: a guide to measurement and modelling*. Cambridge University Press, 2001. (Cited on pages [65](#), [66](#), and [70](#).)

- M. Berdichevsky. Methods used in the U.S.S.R. to reduce near-surface inhomogeneity effects on deep magnetotelluric sounding. *Physics of The Earth and Planetary Interiors*, 53(3-4):194–206, Mar. 1989. ISSN 00319201. doi: 10.1016/0031-9201(89)90003-4. (Cited on pages [11](#) and [22](#).)
- M. Berdichevsky and V. Dmitriev. Distortion of magnetic and electric fields by near-surface lateral inhomogeneities. *Acta Geod. Geophys. Montan. Acad. Sci. Hung*, 11:447–483, 1976. (Cited on pages [12](#) and [62](#).)
- M. N. Berdichevsky and V. I. Dmitriev. *Models and Methods of Magnetotellurics*. Springer, Berlin-Heidelberg, Germany, 2008. (Cited on page [24](#).)
- Y. Bernabe, U. Mok, and B. Evans. Permeability-porosity relationships in rocks subjected to various evolution processes. *Pure and Applied Geophysics*, 160:937–960, 2003. (Cited on pages [24](#) and [69](#).)
- K. Bjørlykke. *Petroleum Geoscience: From Sedimentary Environments to Rock Physics*. Springer, Berlin-Heidelberg, Germany, 2010. (Cited on page [24](#).)
- J. Bloomfield and A. Williams. An empirical liquid permeability–gas permeability correlation for use in aquifer properties studies. *Quarterly Journal of Engineering Geology and Hydrogeology*, 28(Supplement 2):S143–S150, 1995. (Cited on page [81](#).)
- L. Bodri and V. Cermak. *Borehole climatology: a new method how to reconstruct climate*. Elsevier, Oxford, 2007. (Cited on page [70](#).)
- R. Brodie and W. Jiang. Trans-dimensional Monte Carlo inversion of short period magnetotelluric data for cover thickness estimation. *ASEG Extended Abstracts*, 2018(1):1–7, 2018. (Cited on pages [xiv](#), [72](#), and [73](#).)
- E. C. Bullard. The time necessary for a bore hole to attain temperature equilibrium. *Geophysical Supplements to the Monthly Notices of the Royal Astronomical Society*, 5(5):127–130, 1947. doi: 10.1111/j.1365-246X.1947.tb00348.x. (Cited on page [65](#).)
- A. I. Burd, J. R. Booker, R. Mackie, A. Favetto, and M. C. Pomposiello. Three-dimensional electrical conductivity in the mantle beneath the Payún Matrú Volcanic Field in the Andean backarc of Argentina near 36.5°S: evidence for decapitation of a mantle plume by resurgent upper mantle shear during slab steepening. *Geophysical Journal International*, 198(2):812–827, Aug. 2014. ISSN 1365-246X. doi: 10.1093/gji/ggu145. (Cited on page [30](#).)
- J. Busby. Geothermal energy in sedimentary basins in the UK. *Hydrogeology Journal*, 22(1): 129–141, 2014. (Cited on pages [1](#), [78](#), and [79](#).)
- J. Campanyà, A. G. Jones, J. Vozár, V. Rath, S. Blake, R. Delhaye, and T. Farrell. Porosity and permeability constraints from electrical resistivity models: Examples using magnetotelluric

- data. In *Proceedings of the World Geothermal Congress 2015, 15–19 April 2015 in Melbourne, Australia*, 2015. (Cited on page [68](#).)
- R. M. Carruthers, D. Beamish, R. E. Heaven, I. Legg, I. Mitchell, D. Reay, and A. S. D. Walker. Regional interpretation of gravity and aeromagnetic data from Northern Ireland. Technical Report WK/96/05/C, British Geological Survey, 1997. (Cited on page [5](#).)
- A. D. Chave and A. G. Jones. Electric and magnetic field galvanic distortion decomposition of BC87 data. *Journal of geomagnetism and geoelectricity*, 49(6):767–789, 1997. ISSN 0022-1392. doi: 10.5636/jgg.49.767. (Cited on page [22](#).)
- A. D. Chave and A. G. Jones. *The magnetotelluric method theory and practice*. Cambridge University Press, 2012. ISBN 9780521819275. doi: 10.1017/cbo9781139020138. (Cited on pages [7](#), [17](#), [21](#), [22](#), [24](#), [26](#), [62](#), [71](#), and [87](#).)
- A. D. Chave and J. T. Smith. On electric and magnetic galvanic distortion tensor decompositions. *J. Geophys. Res.*, 99(B3):4669–4682, Mar. 1994. doi: 10.1029/93jb03368. (Cited on page [22](#).)
- G. V. Chilingarian and K. H. Wolf. *Compaction of coarse-grained sediments, I*, volume 18. Elsevier, 1975. (Cited on page [69](#).)
- D. Colombo, T. Keho, E. Janoubi, and W. Soyer. Sub-basalt imaging with broadband magnetotellurics in NW Saudi Arabia. In *Expanded Abstracts of the SEG San Antonio 2011 Annual Meeting, 18–23 September 2011, in San Antonio, Texas*, volume 619–623, 2011. (Cited on page [20](#).)
- S. C. Constable, R. L. Parker, and C. G. Constable. Occam's inversion: A practical algorithm for generating smooth models from electromagnetic sounding data. *Geophysics*, 52(3):289–300, 1987. doi: 10.1190/1.1442303. (Cited on page [xiv](#).)
- M. Crowe, G. Heinson, and T. Dhu. *Magnetotellurics and airborne electromagnetics - a combined method for assessing basin structure and exploring for unconformity-related uranium*, pages 1–5. 2013. doi: 10.1071/ASEG2013ab225. (Cited on page [23](#).)
- C. D. De Groot-Hedlin. Removal of static shift in two dimensions by regularized inversion. *Geophysics*, 56(12):2102–2106, Dec. 1991. ISSN 1942-2156. doi: 10.1190/1.1443022. (Cited on pages [11](#) and [22](#).)
- C. DeGroot-Hedlin. Inversion for regional 2-D resistivity structure in the presence of galvanic scatterers. *Geophysical Journal International*, 122(3):877–888, Dec. 1995. ISSN 1365-246X. doi: 10.1111/j.1365-246X.1995.tb06843.x. (Cited on pages [11](#) and [22](#).)
- R. Delhayé and B. Mather. Mapping of Curie point depth distribution beneath Ireland from Tellus aeromagnetic data. In *Geophysical Research Abstracts*, volume 20, 2018. (Cited on page [113](#).)

- R. Delhaye, V. Rath, A. G. Jones, M. R. Muller, and D. Reay. Correcting for static shift of magnetotelluric data with airborne electromagnetic measurements: a case study from Rathlin Basin, Northern Ireland. *Solid Earth*, 8(3):637–660, 2017. doi: 10.5194/se-8-637-2017. (Cited on pages [62](#), [63](#), [72](#), [81](#), and [89](#).)
- R. Delhaye, V. Rath, A. G. Jones, M. R. Muller, and D. Reay. Quantitative geothermal interpretation of electrical resistivity models of the Rathlin Basin, Northern Ireland. *Geothermics*, 77C: 175–187, 2019.
- G. D. Egbert and A. Kelbert. Computational recipes for electromagnetic inverse problems. *Geophysical Journal International*, 189(1):251–267, Apr. 2012. doi: 10.1111/j.1365-246x.2011.05347.x. (Cited on pages [xiv](#), [29](#), and [89](#).)
- D. V. Ellis and J. M. Singer. *Well Logging for Earth Scientists*. Springer, PO Box 17, 3300 AA Dordrecht, The Netherlands, 2 edition, 2008. (Cited on page [66](#).)
- G. Fischer and B. Le Quang. Topography and minimization of the standard deviation in one-dimensional magnetotelluric modelling. *Geophysical Journal International*, 67(2):279–292, 1981. (Cited on page [82](#).)
- L. A. Gallardo and M. A. Meju. Characterization of heterogeneous near-surface materials by joint 2D inversion of DC resistivity and seismic data. *Geophysical Research Letters*, 30(13), 2003. doi: 10.1029/2003GL017370. 1658. (Cited on pages [xii](#) and [41](#).)
- T. D. Gamble. Magnetotellurics with a remote magnetic reference. *Geophysics*, 44:53–68, Jan. 1979. doi: 10.1190/1.1440923. (Cited on pages [10](#) and [27](#).)
- T. D. Gamble, W. M. Goubau, and J. Clarke. Error analysis for remote reference magnetotellurics. *Geophysics*, 44(5):959–968, 1979. doi: 10.1190/1.1440988. (Cited on pages [10](#) and [27](#).)
- X. Garcia and A. G. Jones. Atmospheric sources for audio-magnetotelluric (AMT) sounding. *Geophysics*, 67(2):448–458, 2002. (Cited on page [8](#).)
- P. J. Gibson. Geophysical characteristics of the Tow Valley Fault Zone in North-East Ireland. *Irish Journal of Earth Sciences*, 22:1–13, 2004. (Cited on pages [7](#), [19](#), [38](#), [78](#), and [81](#).)
- P. W. J. Glover. A generalized Archie's law for n phases. *Geophysics*, 75(6):E247–E265, 2010. doi: 10.1190/1.3509781. (Cited on pages [24](#) and [68](#).)
- R. Goodman, G. L. I. Jones, J. Kelly, E. Slower, and N. O'Neill. Geothermal energy resource map of Ireland, final report. Technical report, Sustainable Energy Authority of Ireland, Dublin, Ireland, 2004. (Cited on pages [1](#), [2](#), [3](#), [17](#), [19](#), and [86](#).)
- P. J. Green. Reversible jump Markov chain Monte Carlo computation and Bayesian model determination. *Biometrika*, 82(4):711–732, 1995. (Cited on page [72](#).)

- Y. Guéguen and V. Palciasuskas. *Introduction to the physics of rocks*. Princeton University Press, New Jersey, 1994. (Cited on page 24.)
- S. Hautot, R. T. Single, J. Watson, N. Harrop, D. A. Jerram, P. Tarits, K. Whaler, and G. Dawes. 3-D magnetotelluric inversion and model validation with gravity data for the investigation of flood basalts and associated volcanic rifted margins. *Geophysical J. International*, 170:1418–1430, 2007. doi: 10.1111/j.1365-246X.2007.03453.x. (Cited on page 20.)
- B. Heincke, M. Jegen, M. Moorkamp, and R. W. Hobbs. Joint-inversion of magnetotelluric, gravity and seismic data to image sub-basalt sediments offshore the Faroe-Islands. *SEG Technical Program Expanded Abstracts*, 2014:770–775, 2014. (Cited on page 20.)
- C. Hepworth and I. S. Sanders, editors. *The Geology of Ireland: Second Edition*. Dunedin Academic Press Ltd., 2 edition, Apr. 2009. ISBN 1903765722. (Cited on page 17.)
- F. Jaudin, M. Le Brun, V. Bouchot, and C. Dezayes. French geothermal resources survey, brgm contribution to the market study in the lowbin project. Technical report, BRGM report RP-57583-FR, 2009. (Cited on page 110.)
- M. D. Jegen, R. W. Hobbs, P. Tarits, and A. Chave. Joint inversion of marine magnetotelluric and gravity data incorporating seismic constraints. preliminary results of sub-basalt imaging off the Faroe Shelf. *Earth and Planetary Science Letters*, 282:47–55, 2009. (Cited on page 20.)
- A. Jones. Imaging the continental upper mantle using electromagnetic methods. *Lithos*, 48:57–80, 1999. (Cited on page 73.)
- A. Jones and R. Hutton. A multi-station magnetotelluric study in southern Scotland - ii. Monte-Carlo inversion of the data and its geophysical and tectonic implications. *Geophysical Journal of the Royal Astronomical Society*, 56:351–368, 1979. (Cited on page 72.)
- A. Jones and H. Jödicke. Magnetotelluric transfer function estimation improvement by a coherence-based rejection technique. In *SEG Technical Program Expanded Abstracts 1984*, SEG Technical Program Expanded Abstracts, pages 51–55. Society of Exploration Geophysicists, Jan. 1984. doi: 10.1190/1.1894081. (Cited on pages 10 and 27.)
- A. G. Jones. Static shift of magnetotelluric data and its removal in a sedimentary basin environment. *Geophysics*, 53(7):967–978, 1988. doi: 10.1190/1.1442533. (Cited on pages 11, 22, and 62.)
- A. G. Jones. Electrical properties of the lower continental crust. In *Continental Lower Crust*, volume 23, pages 81–143. Elsevier Amsterdam, 1992. (Cited on page 21.)
- A. G. Jones. Electromagnetic interrogation of the anisotropic Earth: Looking into the Earth with polarized spectacles. *Physics of the Earth and Planetary Interiors*, 158(2-4):281–291, Oct. 2006. ISSN 00319201. doi: 10.1016/j.pepi.2006.03.026. (Cited on page 25.)

- A. G. Jones. Three-dimensional galvanic distortion of three-dimensional regional conductivity structures: Comment on "three-dimensional joint inversion for magnetotelluric resistivity and static shift distributions in complex media" by Yutaka Sasaki and Max A. Meju. *J. Geophys. Res.*, 116 (B12):B12104+, Dec. 2011. doi: 10.1029/2011jb008665. (Cited on page 26.)
- A. G. Jones, A. D. Chave, G. Egbert, D. Auld, and K. Bahr. A comparison of techniques for magnetotelluric response function estimation. *Journal of Geophysical Research*, 94(B10):14201–14213, 1989. doi: 10.1029/jb094ib10p14201. (Cited on pages 10 and 27.)
- D. L. B. Jupp and K. Vozoff. Stable iterative methods for the inversion of geophysical data. *Geoph. J.Roy. Astr. Soc.*, 42:957–976, 1975. (Cited on pages 27 and 32.)
- J. Kaipio and E. Somersalo. *Statistical and computational inverse problems*, volume 160. Springer Science & Business Media, 2006. (Cited on page 94.)
- D. Kao and D. Orr. Magnetotelluric response of a uniformly stratified earth containing a magnetized layer. *Geophysical Journal International*, 70(2):339–347, 1982a. (Cited on page 72.)
- D. Kao and D. Orr. Magnetotelluric studies in the Market Weighton area of eastern England. *Geophysical Journal International*, 70(2):323–337, 1982b. (Cited on page 72.)
- Kaufman, D. Alekseev, and M. Oristaglio. *Principles of Electromagnetic Methods in Surface Geophysics*. Elsevier, Amsterdam, NL, 2014. (Cited on page 26.)
- A. Kelbert, N. Meqbel, G. D. Egbert, and K. Tandon. ModEM: A modular system for inversion of electromagnetic geophysical data. *Computers & Geosciences*, 66:40–53, May 2014. ISSN 00983004. doi: 10.1016/j.cageo.2014.01.010. (Cited on pages xiv, 29, and 89.)
- G. V. Keller and F. C. Frischknecht. *Electrical methods in geophysical prospecting*. Pergamon Press, Oxford, UK, 1966. (Cited on page 26.)
- L. J. Klinkenberg. The permeability of porous media to liquids and gases. *Drilling and Production Practice*, pages 200–213, 1941. (Cited on page 69.)
- J. Lawless. Geothermal lexicon for resources and reserves definition and reporting. *Australian Geothermal Energy Group*, 2010. (Cited on pages xii, 14, 75, 77, 78, and 110.)
- H. Leväniemi, D. Beamish, H. Hautaniemi, M. Kurimo, I. Suppala, J. Vironmäki, R. J. Cuss, M. Lahti, and E. Tartaras. The JAC airborne EM system: AEM-05. *Journal of Applied Geophysics*, 67(3):219–233, Mar. 2009. ISSN 09269851. doi: 10.1016/j.jappgeo.2007.10.001. (Cited on pages 26 and 31.)
- M. Loewer. Investigation of the geothermal energy potential of the Lough Neagh Basin, Northern Ireland, using magnetotelluric and gravity modelling. Master's thesis, ETH Zurich, Zurich, Switzerland, 2011. (Cited on page 1.)

- E. Luijendijk and T. Gleeson. How well can we predict permeability in sedimentary basins? Deriving and evaluating porosity-permeability equations for noncemented sand and clay mixtures. *Geofluids*, 15(1-2):67–83, 2015. doi: 10.1111/gfl.12115. (Cited on page 24.)
- E. Mandolesi, X. Ogaya, J. Campanyà, and N. P. Agostinetti. A reversible-jump Markov chain Monte Carlo algorithm for 1D inversion of magnetotelluric data. *Computers & Geosciences*, 113: 94–105, 2018. (Cited on page 72.)
- F. Martini, W. W. Hobbs, C. J. Bean, and R. Single. A complex 3D volume for sub-basalt imaging. *First Break*, 23:41–51, 2005. (Cited on page 20.)
- G. Mavko, T. Mukerji, and J. Dvorkin. *The Rock Physics Handbook. Tools for Seismic Modelling of Porous Media*. Cambridge University Press, Cambridge, UK, 2009. (Cited on page 24.)
- N. McCann. An assessment of the subsurface geology between Magilligan Point and Fair head, Northern Ireland. *Irish Journal of Earth Sciences*, 9(1):71–78, 1988. ISSN 07901763, 20090064. (Cited on pages 5 and 7.)
- G. W. McNeice and A. G. Jones. Multisite, multifrequency tensor decomposition of magnetotelluric data. *Geophysics*, 66(1):158–173, Jan. 2001. ISSN 1942-2156. doi: 10.1190/1.1444891. (Cited on pages xiv, 27, 29, 49, and 72.)
- M. P. Miensopust. *Multidimensional Magnetotellurics. A 2D case study and a 3D approach to simultaneously invert for resistivity structure and distortion parameters*. PhD thesis, Faculty of Science, National University of Ireland, Galway, 2010. (Cited on pages 11 and 22.)
- M. P. Miensopust, A. G. Jones, G. P. Hersir, and A. M. Vilhjálmsdóttir. The Eyjafjallajökull volcanic system, Iceland: insights from electromagnetic measurements. *Geophysical Journal International*, 199(2):1187–1204, Nov. 2014. doi: 10.1093/gji/ggu322. (Cited on pages 12 and 22.)
- B. J. Minsley. A trans-dimensional Bayesian Markov chain Monte Carlo algorithm for model assessment using frequency-domain electromagnetic data. *Geophysical Journal International*, 187(1):252–272, Oct. 2011. ISSN 1365-246X. doi: 10.1111/j.1365-246x.2011.05165.x. (Cited on page 27.)
- W. I. Mitchell. *The Geology of Northern Ireland : Our Natural Foundation*. Geological Survey of Northern Ireland, Belfast, UK, 2004. ISBN 0852724543. (Cited on pages 4, 5, 17, 19, 21, 62, 63, 64, 65, 78, and 80.)
- G. Muñoz. Exploring for geothermal resources with electromagnetic methods. *Surv. Geophys.*, 35: 101–122, 2014. doi: 10.1007/s10712-013-9236-0. (Cited on page 17.)
- D. Naylor and P. Shannon. *Petroleum geology of Ireland*. Dunedin Academic Press Ltd, Edinburgh, UK, 2011. (Cited on pages 3, 4, 5, 18, 20, 63, and 80.)

- G. Nover. Electrical properties of crustal and mantle rocks - a review of laboratory measurements and their explanation. *Surveys in Geophysics*, 26(5):593–651, Sept. 2005. ISSN 0169-3298. doi: 10.1007/s10712-005-1759-6. (Cited on page 24.)
- H. Pape, C. Clauser, and J. Iffland. Permeability prediction based on fractal pore-space geometry. *Geophysics*, 64(5):1447–1460, 1999. (Cited on page 24.)
- H. Pape, C. Clauser, and J. Iffland. Variation of permeability with porosity in sandstone diagenesis interpreted with a fractal pore space model. *Pure Applied Geophysics*, 157:603–619, 2000. (Cited on page 24.)
- R. Pasquali, N. O'Neill, D. Reay, and T. Waugh. The geothermal potential of Northern Ireland. In *Proceedings of the World Geothermal Congress 2010, 25–30 April 2010 in Bali, Indonesia, 2010*, 2010. (Cited on pages 1, 14, 19, 78, and 79.)
- L. D. Pellerin and G. W. Hohmann. Transient electromagnetic inversion; a remedy for magnetotelluric static shifts. *Geophysics*, 55(9):1242–1250, Sept. 1990. ISSN 1942-2156. doi: 10.1190/1.1442940. (Cited on pages 11, 22, 23, 32, and 62.)
- H. E. Poll, J. T. Weaver, and A. G. Jones. Calculations of voltages for magnetotelluric modeling of a region with near-surface inhomogeneities. *Phys. Earth Planet. Inter.*, 53:287–297, 1989. (Cited on page 22.)
- J. P. Raffensperger. Numerical simulation of basin-scale hydrochemical processes. In M. Y. Corapcioglu, editor, *Advances in Porous Media*, volume 3, pages 185–305. Elsevier, New York, 1996. (Cited on page 24.)
- A. Raiche. A flow-through Hankel transform technique for rapid, accurate Green's function computation. *Radio Sci.*, 34(2):549–555, Mar. 1999. doi: 10.1029/1998rs900037. (Cited on pages 32 and 33.)
- A. P. Raiche, D. L. B. Jupp, H. Rutter, and K. Vozoff. The joint use of coincident loop transient electromagnetic and Schlumberger sounding to resolve layered structures. *Geophysics*, 50(10): 1618–1627, 1985. doi: 10.1190/1.1441851. (Cited on pages xiv and 27.)
- D. Reay and J. Kelly. Deep geothermal energy resource potential in Northern Ireland. *European Geologist*, 29:14–18, 2010. (Cited on pages 1, 17, 19, and 86.)
- I. Richardson and A. Neymeyer. Deep geothermal review study: Final report. Technical report, Department of Energy & Climate Change (DECC), 1 Victoria Street, London, SW1H 0ET, United Kingdom, 2013. (Cited on pages 61 and 78.)
- W. Rodi and R. L. Mackie. Nonlinear conjugate gradients algorithm for 2-D magnetotelluric inversion. *Geophysics*, 66(1):174–187, Jan. 2001. doi: 10.1190/1.1444893. (Cited on pages xiii and xiv.)

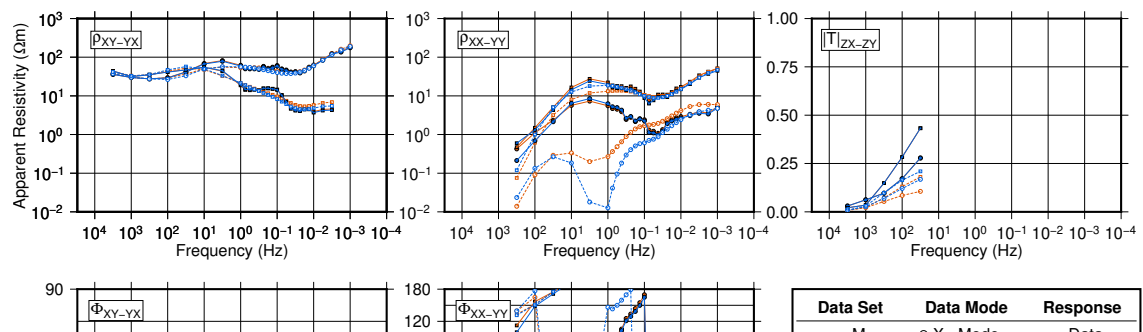
- G. K. Rosenkjaer, E. Gasperikova, G. A. Newman, K. Arnason, and N. J. Lindsey. Comparison of 3D MT inversions for geothermal exploration: Case studies for Krafla and Hengill geothermal systems in Iceland. *Geothermics*, 57:258–274, 2015. (Cited on pages [xii](#) and [41](#).)
- P. J. Rousseeuw. Least median of squares regression. *Journal of the American Statistical Association*, 79(388):871–880, Dec. 1984. doi: 10.1080/01621459.1984.10477105. (Cited on pages [10](#) and [27](#).)
- P. J. Rousseeuw and A. M. Leroy. *Robust Regression and Outlier Detection*. Wiley-Interscience, 1 edition, Oct. 2003. ISBN 0471488550. (Cited on pages [10](#) and [27](#).)
- Y. Sasaki and M. A. Meju. Three-dimensional joint inversion for magnetotelluric resistivity and static shift distributions in complex media. *J. Geophys. Res.*, 111,:B05101, 2006. doi: 10.1029/2005JB004009. (Cited on pages [11](#) and [22](#).)
- S. Schnaidt and G. Heinson. Bootstrap resampling as a tool for uncertainty analysis in 2-D magnetotelluric inversion modelling. *Geophysical Journal International*, 203(1):92–106, 2015. (Cited on pages [xii](#) and [41](#).)
- K. Schwalenberg, V. Rath, and V. Haak. Sensitivity studies applied to a two-dimensional resistivity model from the central andes. *Geophysical Journal International*, 150(3):673–686, 2002. ISSN 1365-246X. doi: 10.1046/j.1365-246X.2002.01734.x. (Cited on page [91](#).)
- J. H. Scott. Computer analysis of digital well logs. Technical Report 879, U.S. Geological Survey, 12201 Sunrise Valley Drive, Reston, VA 20192, USA, 1984. scott1984. (Cited on page [68](#).)
- S. Sihelník. Investigation of compressed air energy storage potential in the Larne Basin, Northern Ireland, using magnetotelluric and gravity methods. Master's thesis, ETH Zurich, Zurich, Switzerland, 2011. (Cited on page [1](#).)
- F. Simpson and K. Bahr. *Practical Magnetotellurics*. Cambridge University Press, Cambridge, UK, 2005. (Cited on pages [7](#), [17](#), [24](#), and [87](#).)
- K. Spitzer. Magnetotelluric static shift and direct current sensitivity. *Geophysical Journal International*, 144(2):289–299, Feb. 2001. ISSN 0956540X. doi: 10.1046/j.1365-246x.2001.00311.x. (Cited on page [11](#).)
- B. K. Sternberg, J. C. Washburne, and L. Pellerin. Correction for the static shift in magnetotellurics using transient electromagnetic soundings. *Geophysics*, 53(11):1459–1468, Nov. 1988. ISSN 1942-2156. doi: 10.1190/1.1442426. (Cited on pages [11](#), [22](#), [23](#), and [32](#).)
- A. Tanaka, Y. Okubo, and O. Matsubayashi. Curie point depth based on spectrum analysis of the magnetic anomaly data in east and southeast asia. *Tectonophysics*, 306(3):461 – 470, 1999. ISSN 0040-1951. doi: [https://doi.org/10.1016/S0040-1951\(99\)00072-4](https://doi.org/10.1016/S0040-1951(99)00072-4). (Cited on page [113](#).)

- K. Tietze and O. Ritter. Three-dimensional magnetotelluric inversion in practice - the electrical conductivity structure of the San Andreas Fault in Central California. *Geophysical Journal International*, 195(1):130, 2013. doi: 10.1093/gji/ggt234. (Cited on page 51.)
- A. N. Tikhonov and V. Y. Arsenin. *Solutions of ill-posed problems*, volume 14. Winston, 1977. (Cited on page 90.)
- C. Torres-Verdin and F. X. Bostick. Principles of spatial surface electric field filtering in magnetotellurics; electromagnetic array profiling (EMAP). *Geophysics*, 57(4):603–622, Apr. 1992. ISSN 1942-2156. doi: 10.1190/1.1443273. (Cited on pages 10 and 22.)
- S. H. Ward and G. W. Hohmann. *Electromagnetic Methods in Applied Geophysics*, volume 1, Theory, pages 131–312. 1988. (Cited on page 26.)
- P. Wessel, W. H. F. Smith, R. Scharroo, J. Luis, and F. Wobbe. Generic Mapping Tools: Improved version released. *Eos, Transactions American Geophysical Union*, 94(45):409–410, 2013. ISSN 2324-9250. doi: 10.1002/2013EO450001. (Cited on page xiv.)
- D. Wight and F. X. Bostick. Cascade decimation—A technique for real time estimation of power spectra. In *Acoustics, Speech, and Signal Processing, IEEE International Conference on ICASSP '80, 9–11 April 1980, Denver, Colorado*, volume 5, pages 626–629. IEEE, Apr. 1980. doi: 10.1109/icassp.1980.1170868. (Cited on pages 10 and 27.)
- H. E. Wilson and P. I. Manning. *Geology of the Causeway Coast*. British Geological Survey, Nottingham, UK, 1978. (Cited on pages 19, 65, 66, 68, and 86.)
- M. Young. *Unearthed: impacts of the Tellus surveys of the north of Ireland*. Royal Irish Academy, 2016. (Cited on page 62.)
- M. S. Zhdanov. *Geophysical inverse theory and regularization problems*, volume 36. Elsevier, 2002. (Cited on pages 90, 91, and 92.)
- B. Zinszner and F. M. Pellerin. *A Geoscientist's Guide to Petrophysics*. Editions Technip, Paris, France, 2007. (Cited on page 24.)

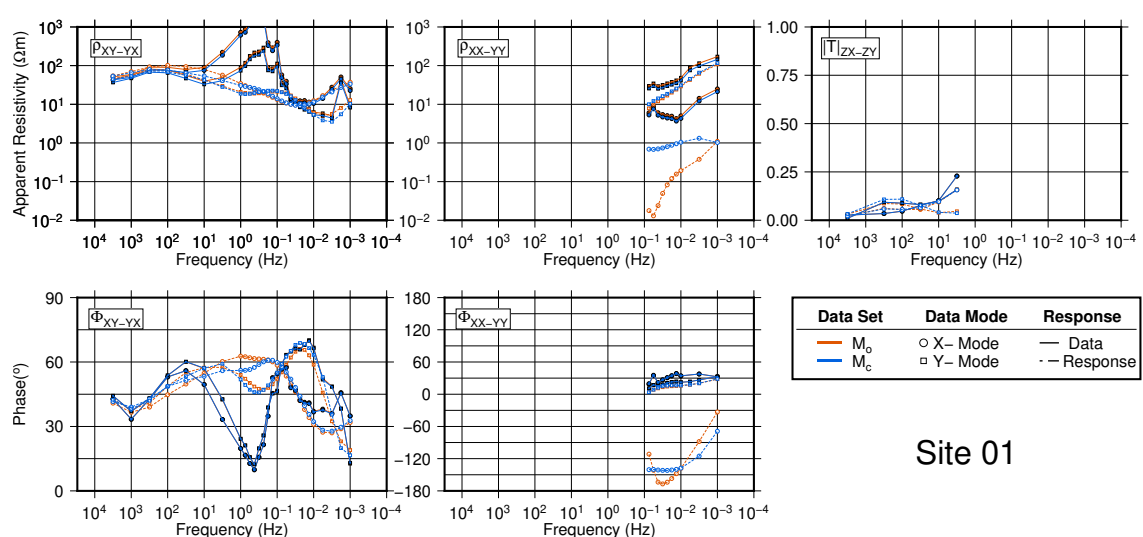
Part I
APPENDICES

A

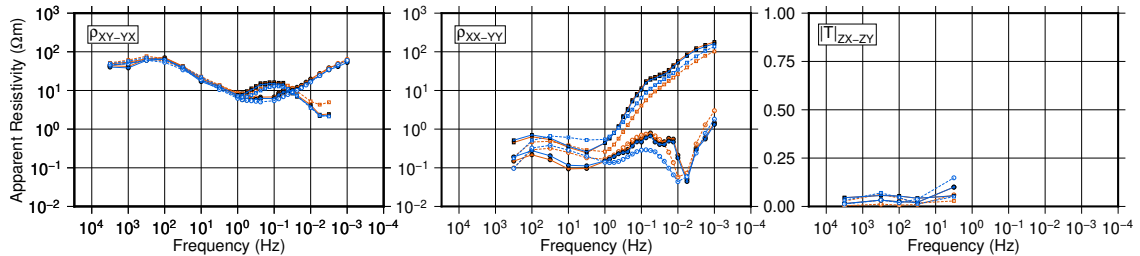
CHAPTER 2 DATA AND RESPONSES



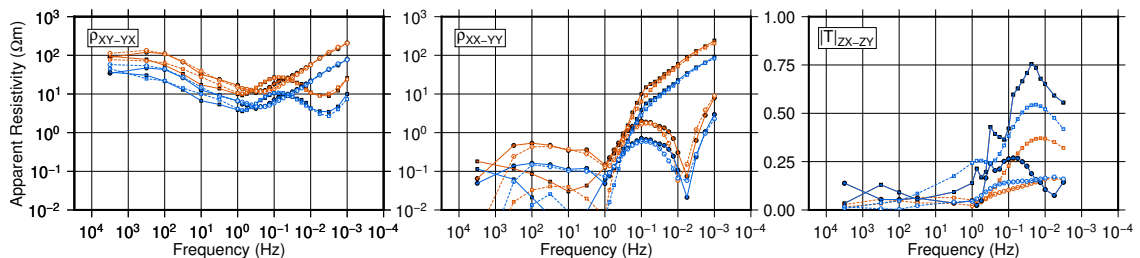
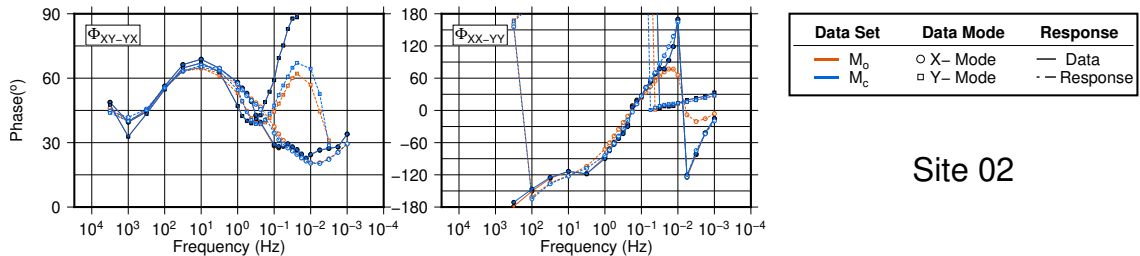
Site 00



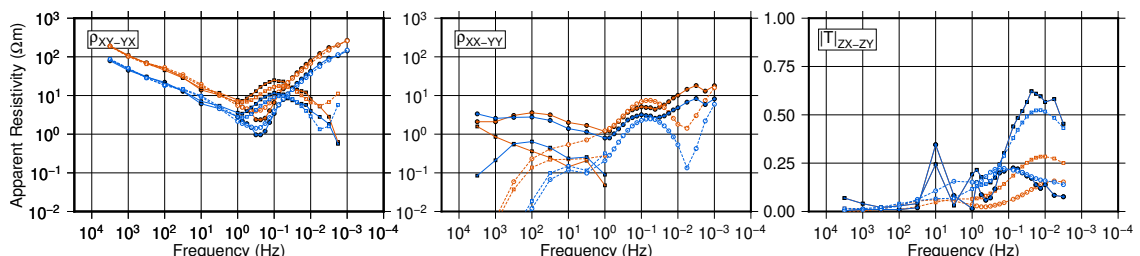
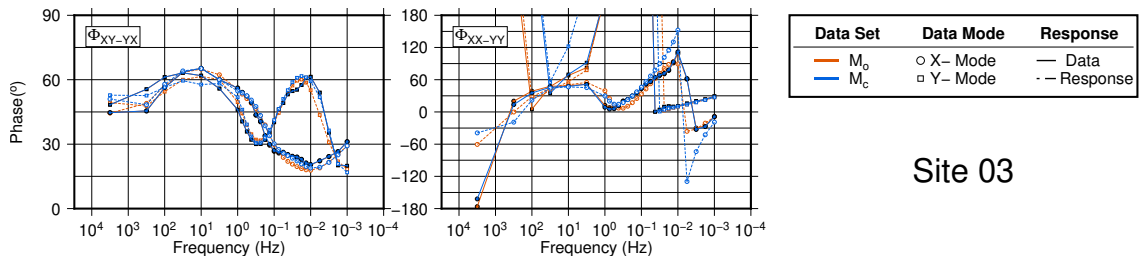
Site 01



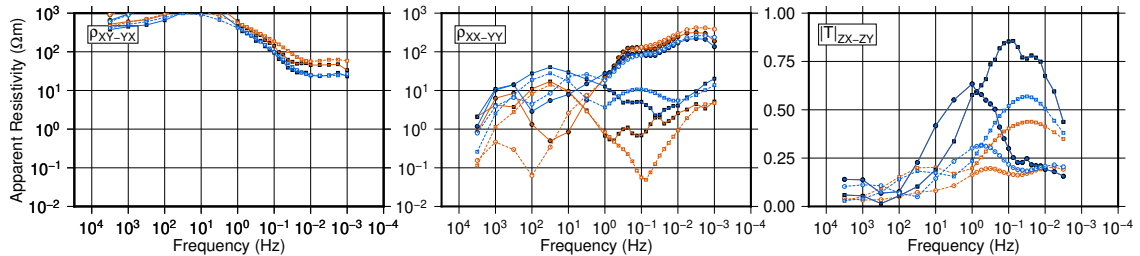
Site 02



Site 03

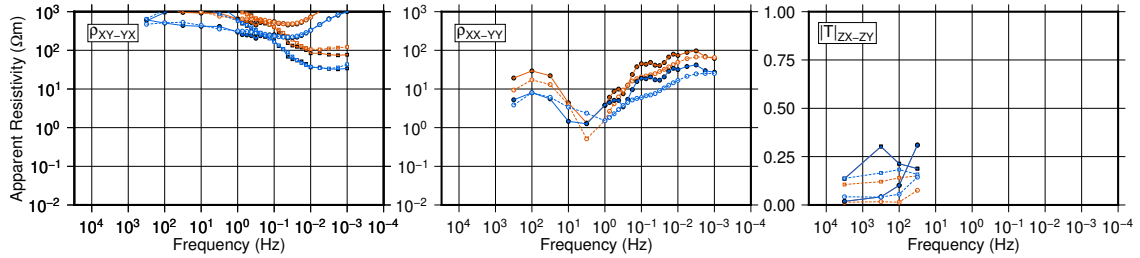
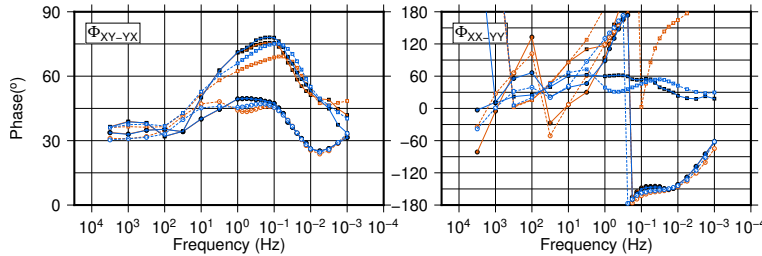


Site 04



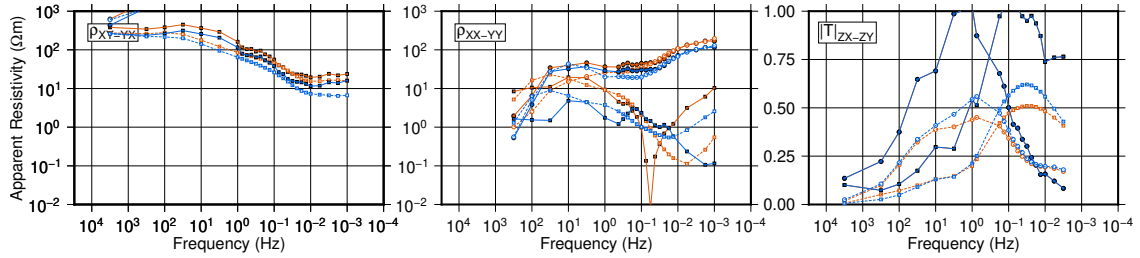
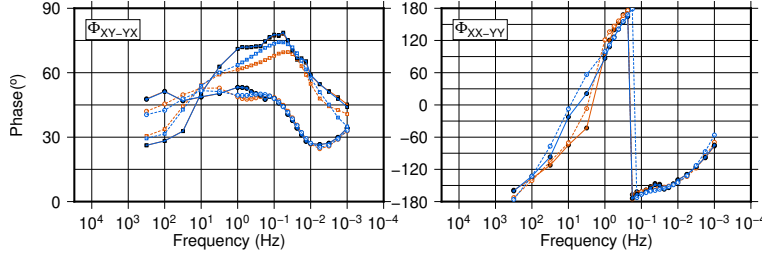
Data Set	Data Mode	Response
M_o	○ X- Mode	— Data
M_c	□ Y- Mode	- - Response

Site 05



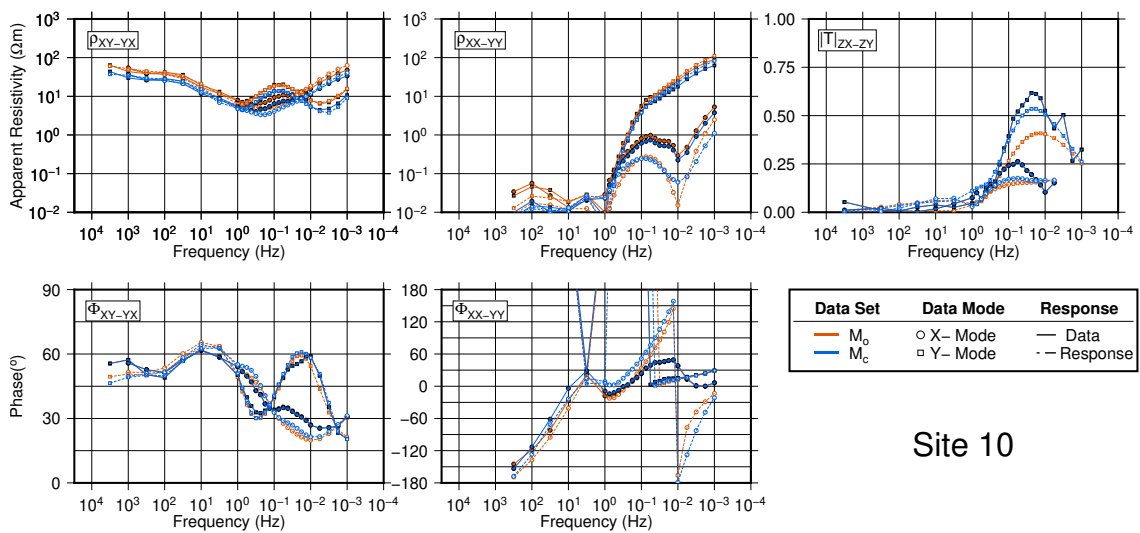
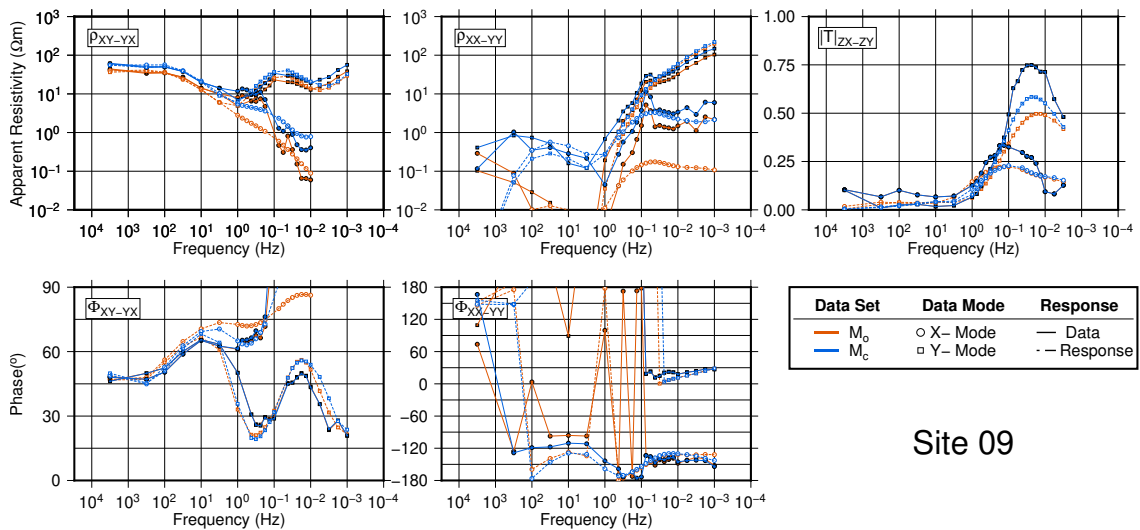
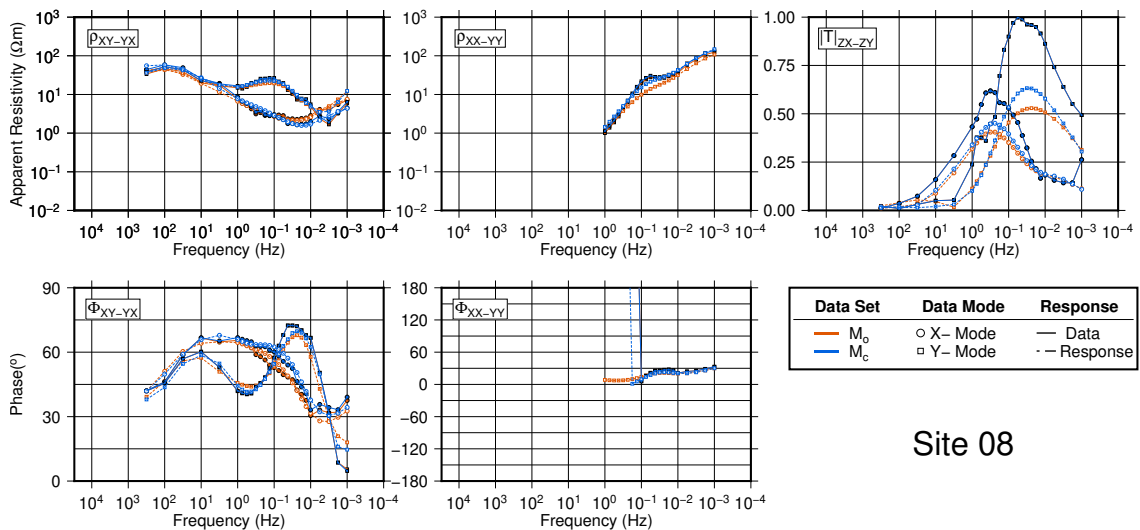
Data Set	Data Mode	Response
M_o	○ X- Mode	— Data
M_c	□ Y- Mode	- - Response

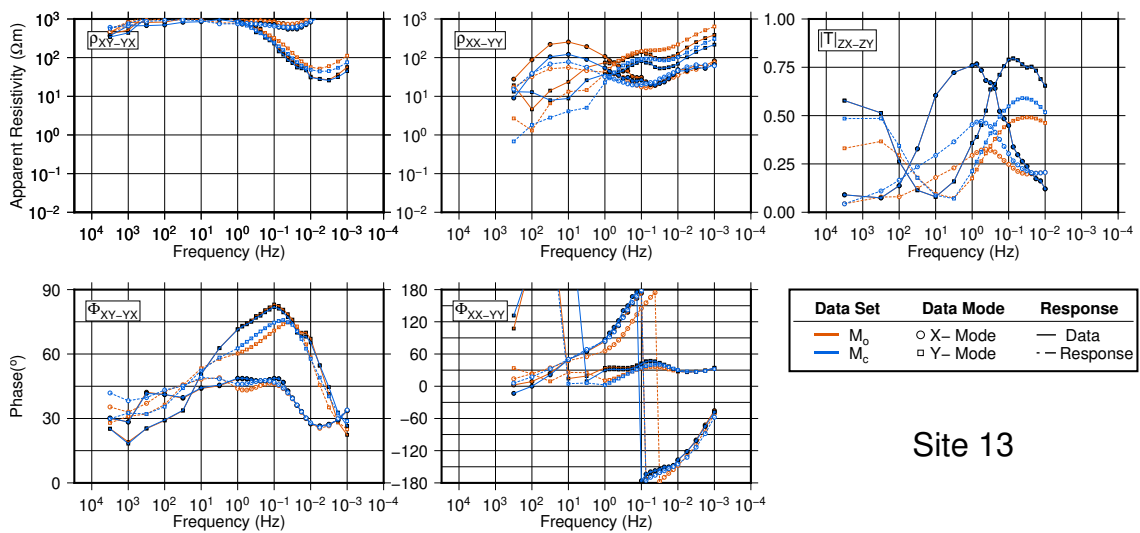
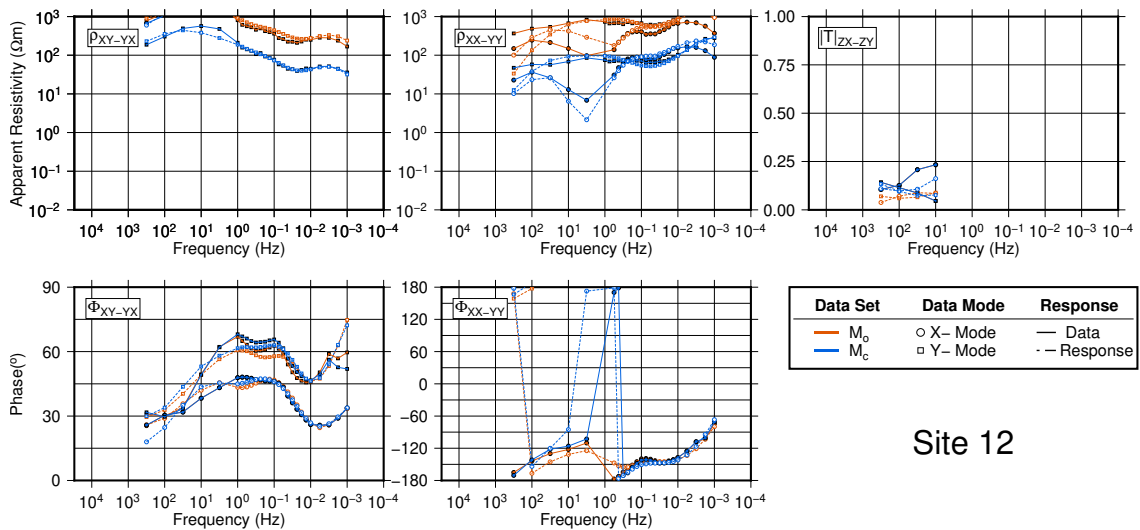
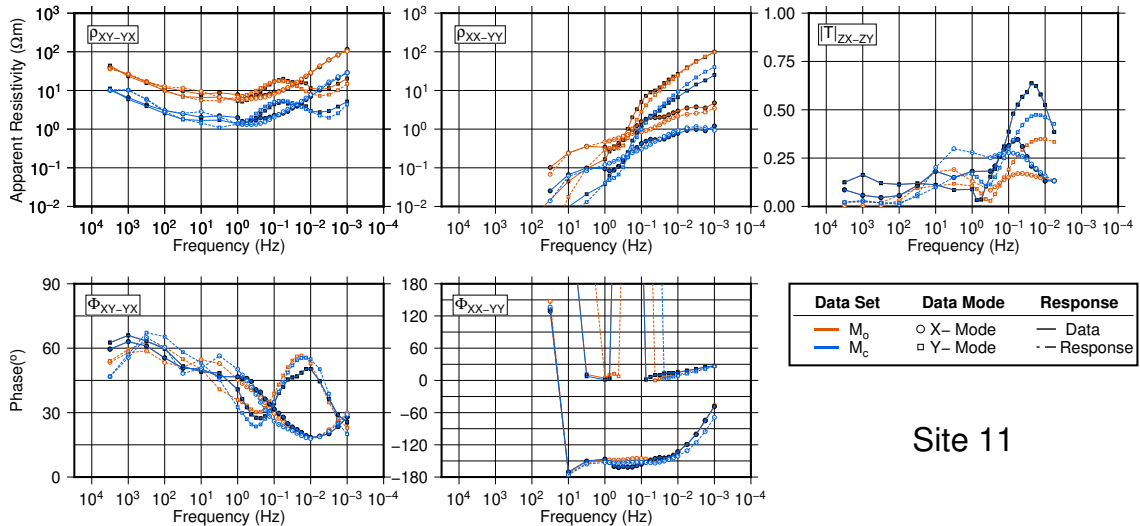
Site 06

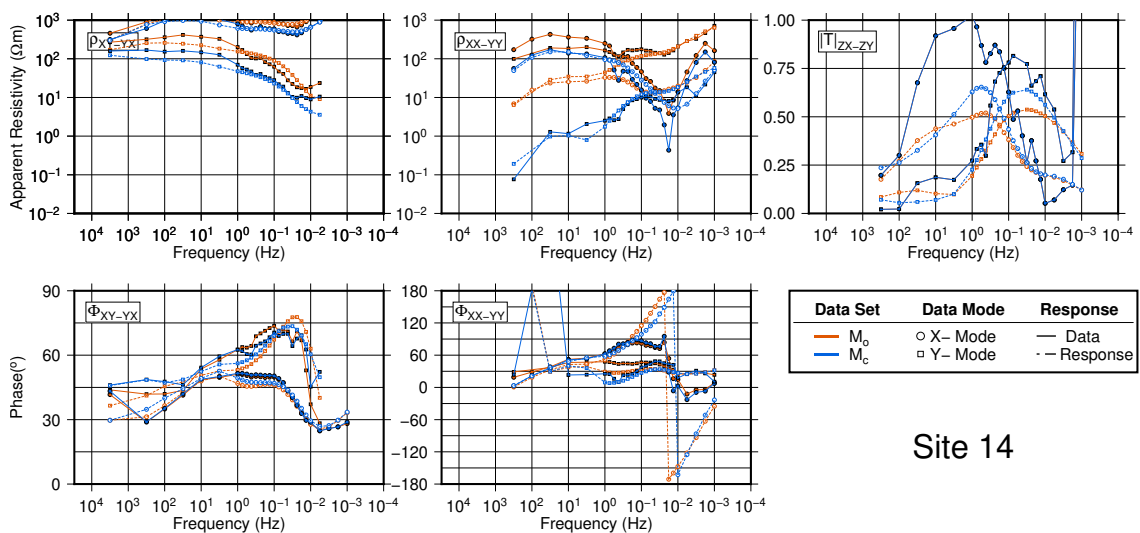


Data Set	Data Mode	Response
M_o	○ X- Mode	— Data
M_c	□ Y- Mode	- - Response

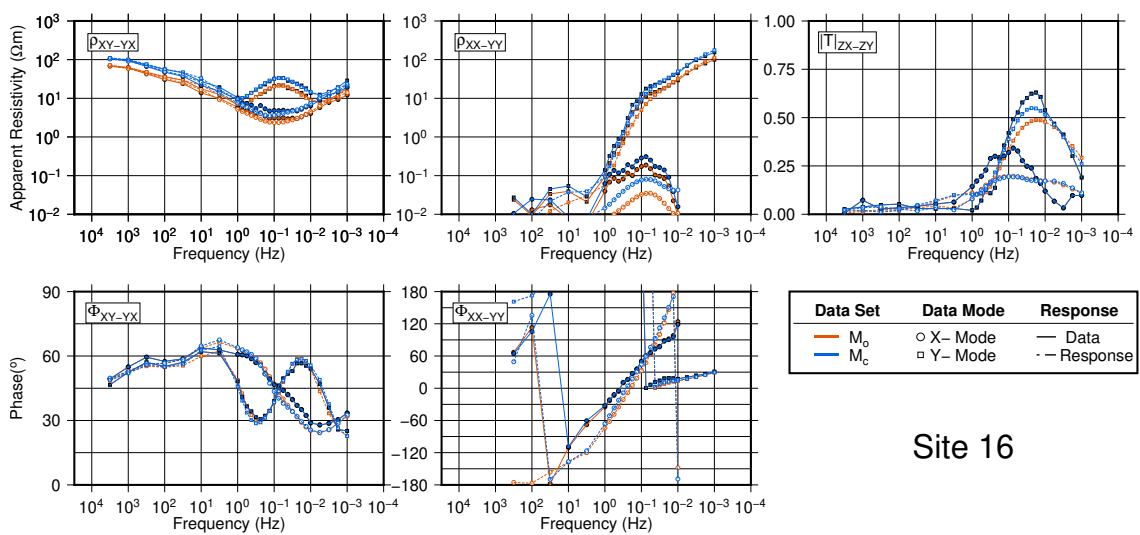
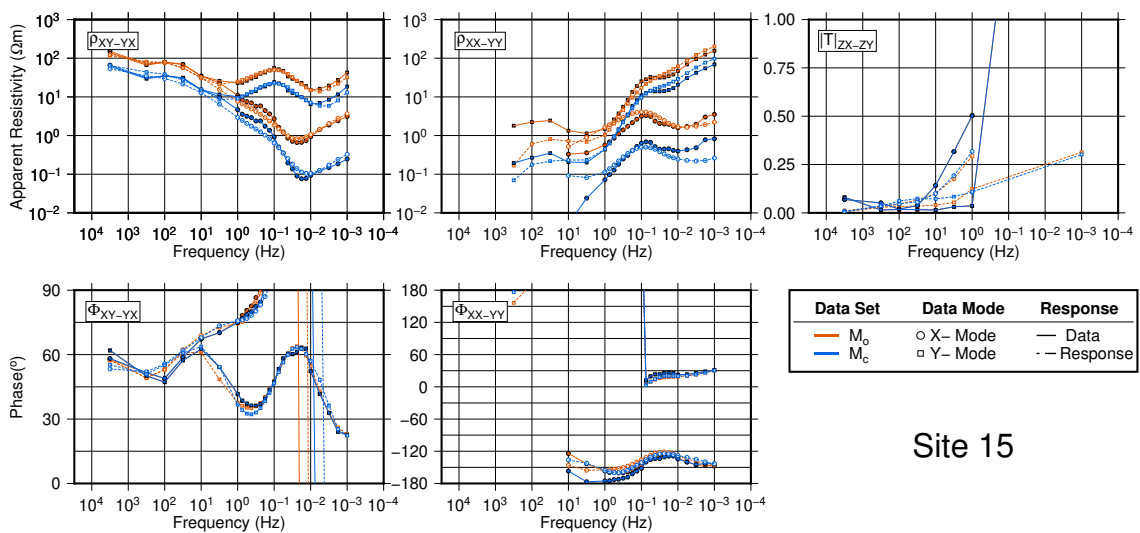
Site 07

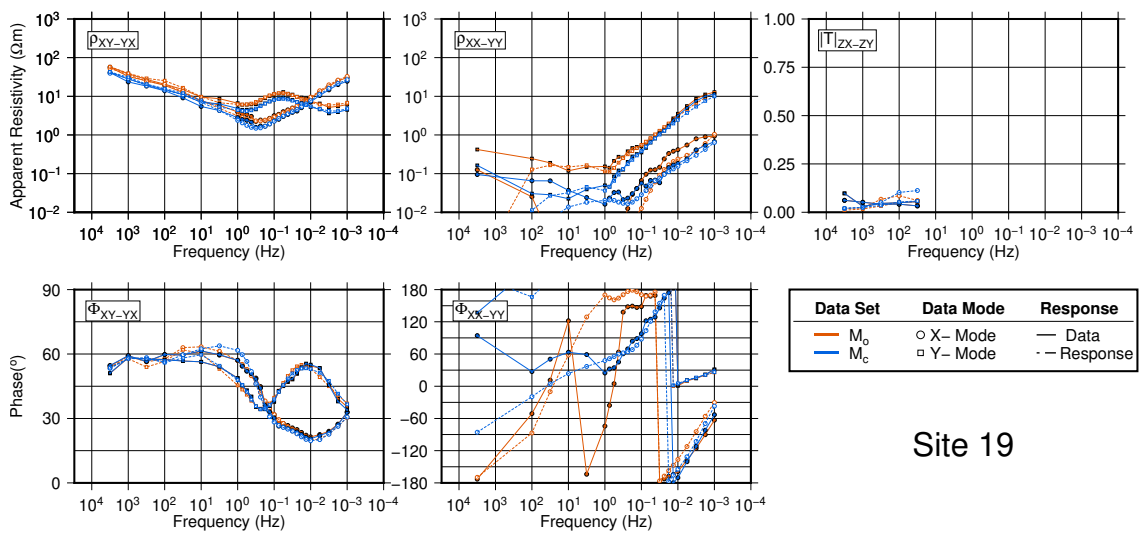
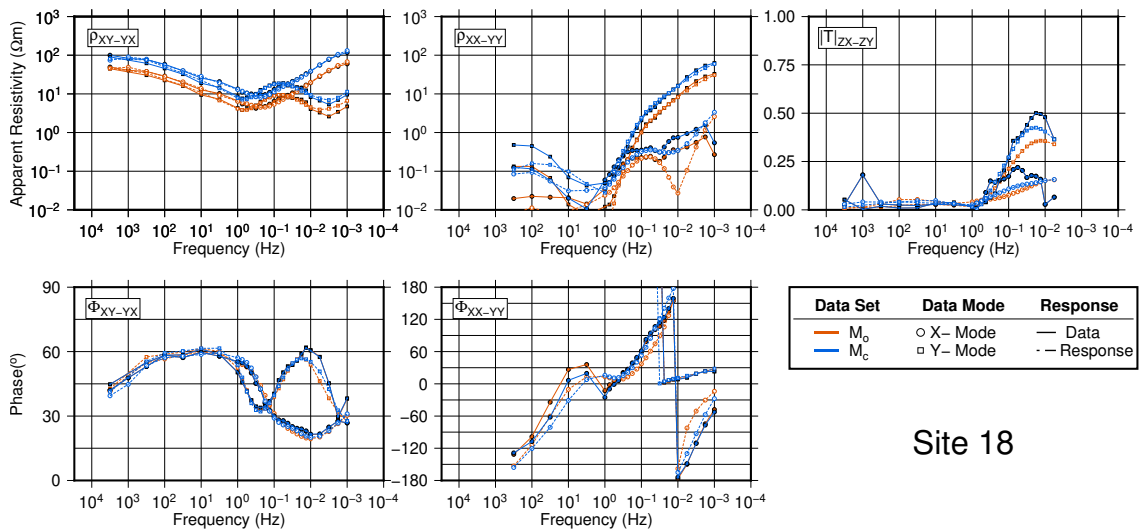
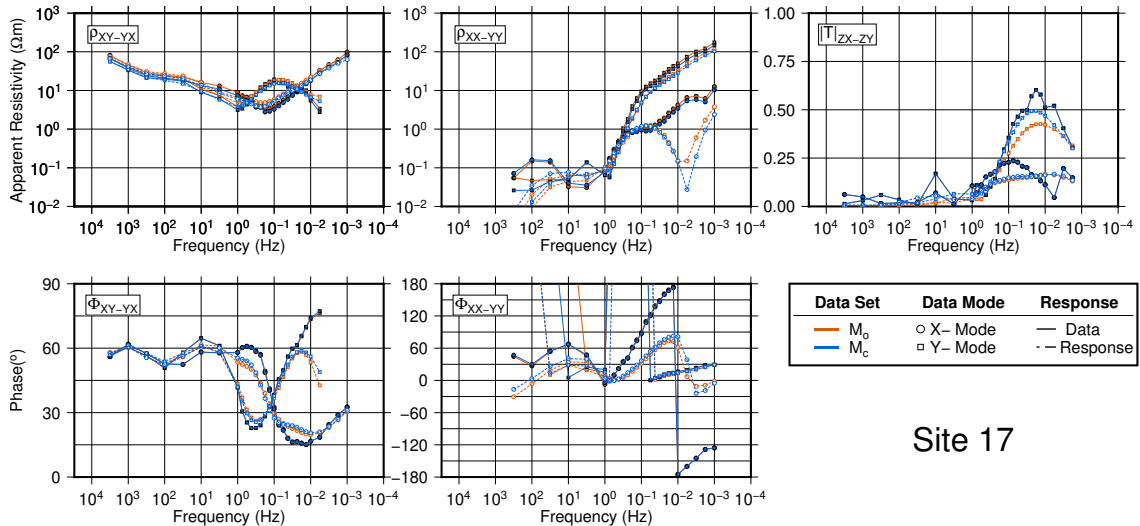


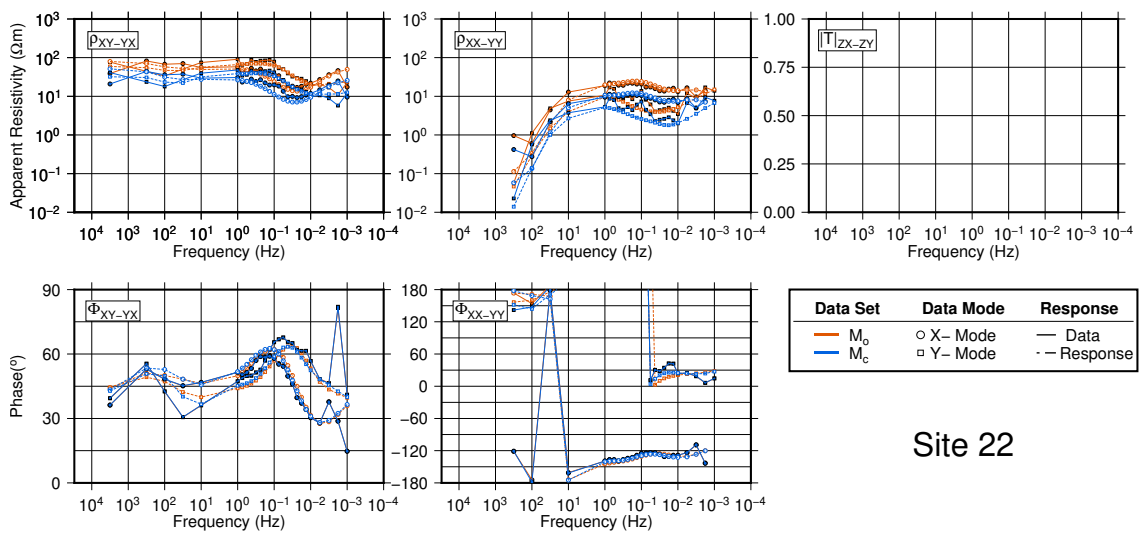
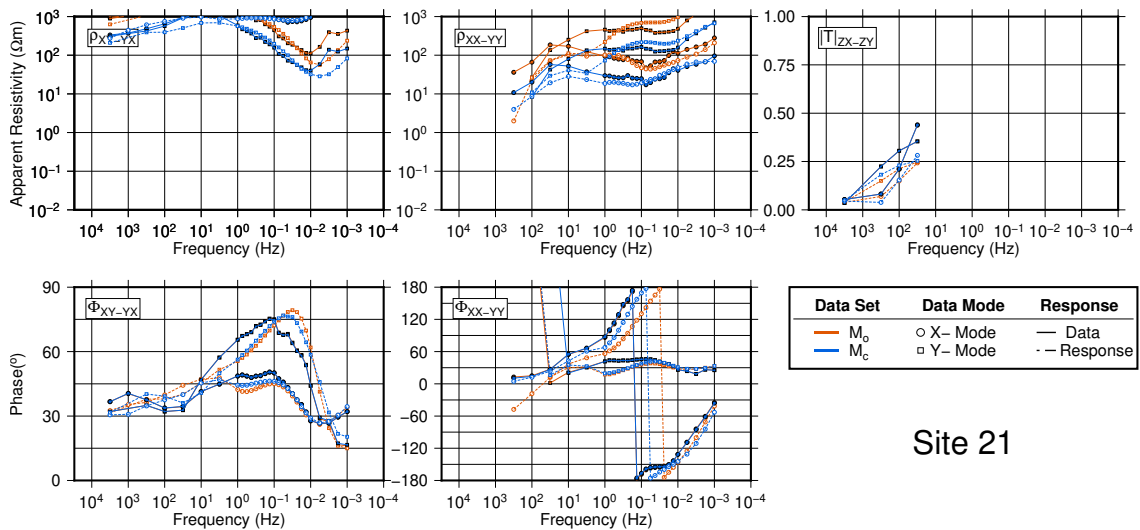
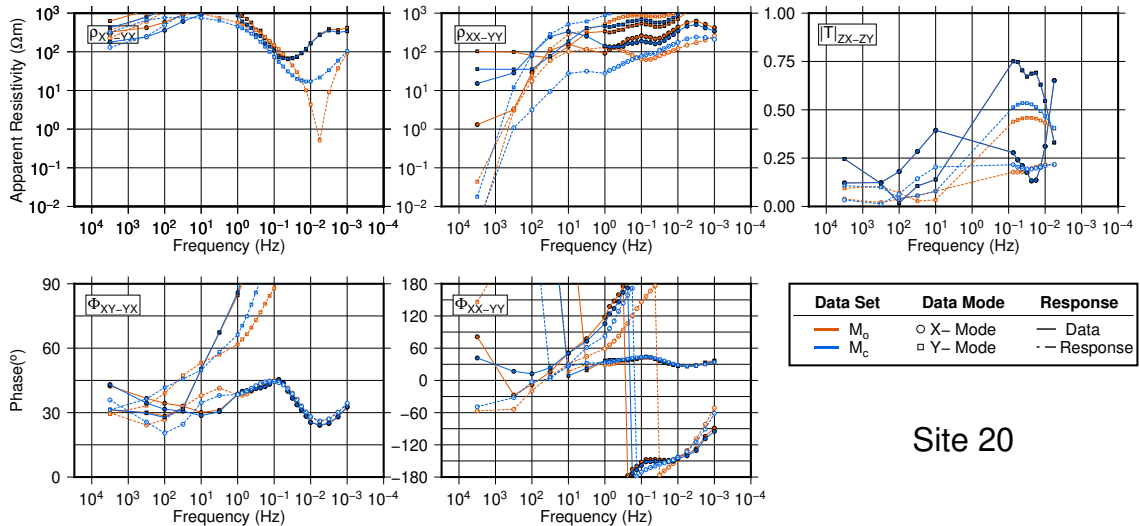


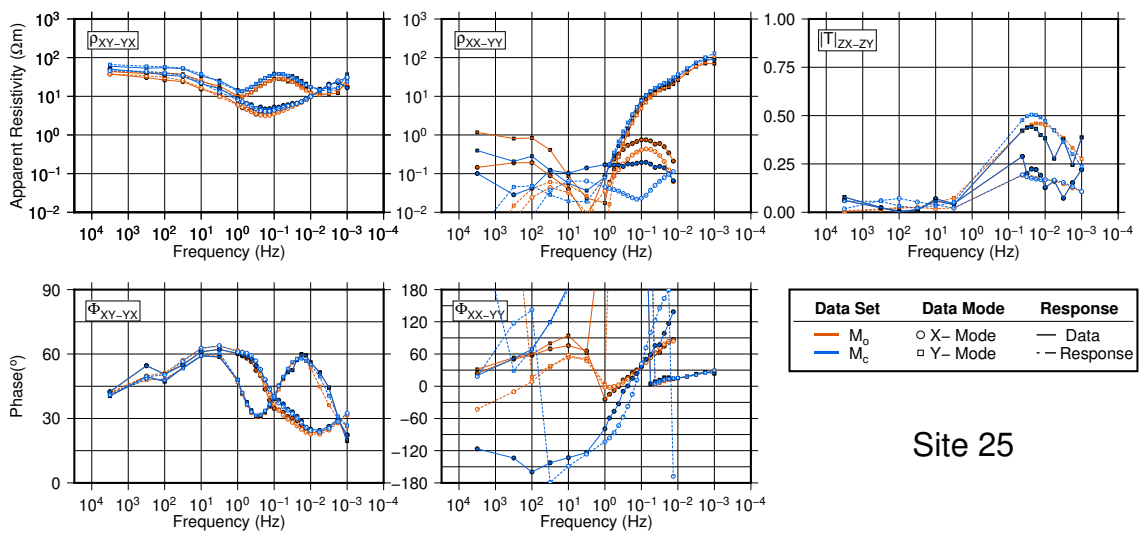
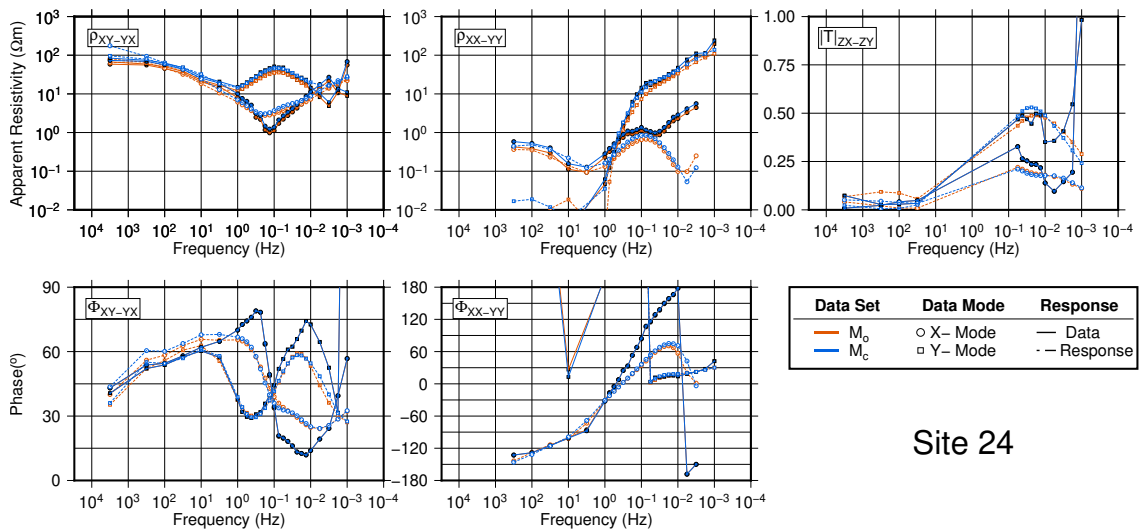
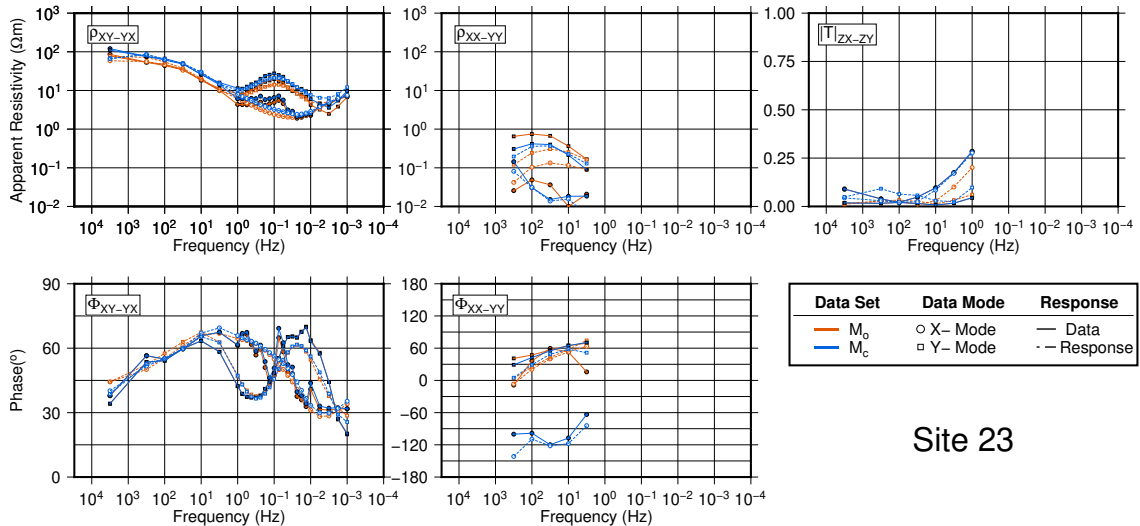


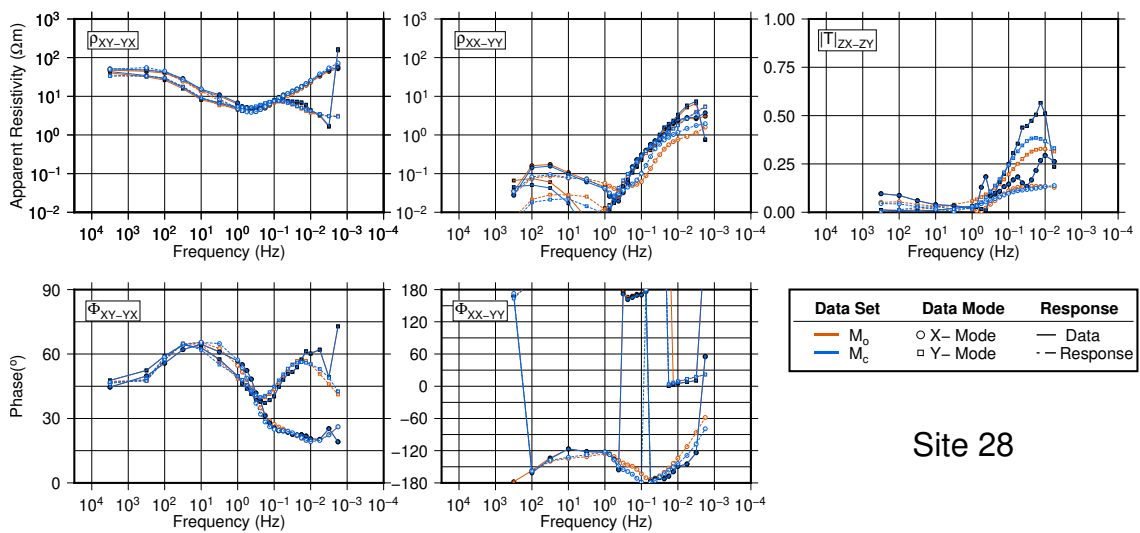
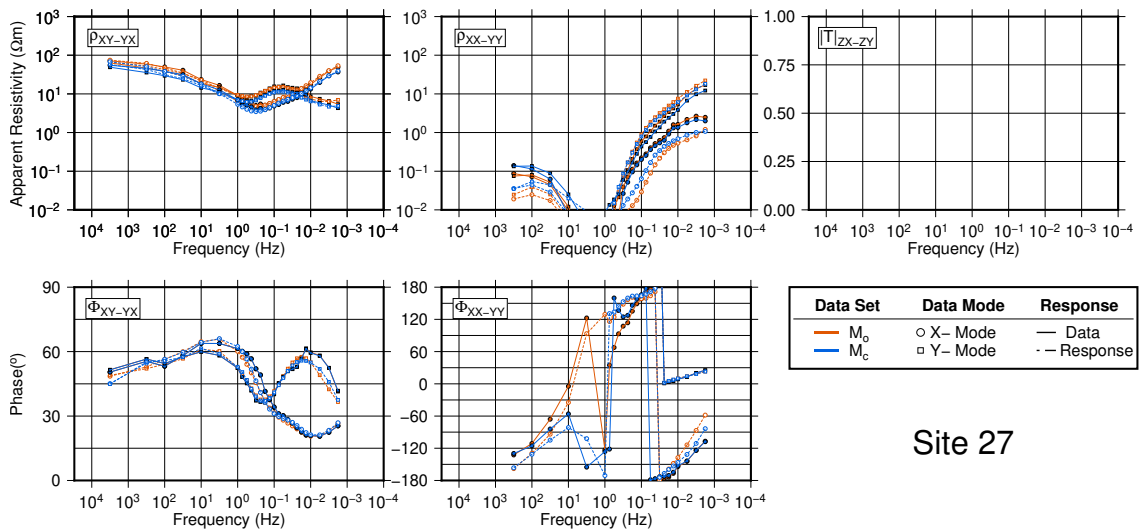
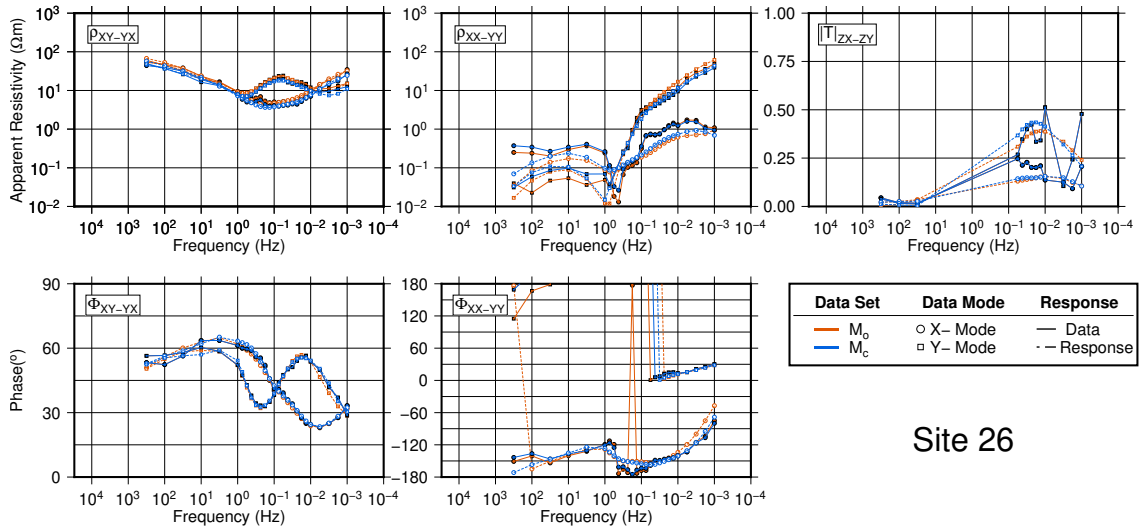
Site 14

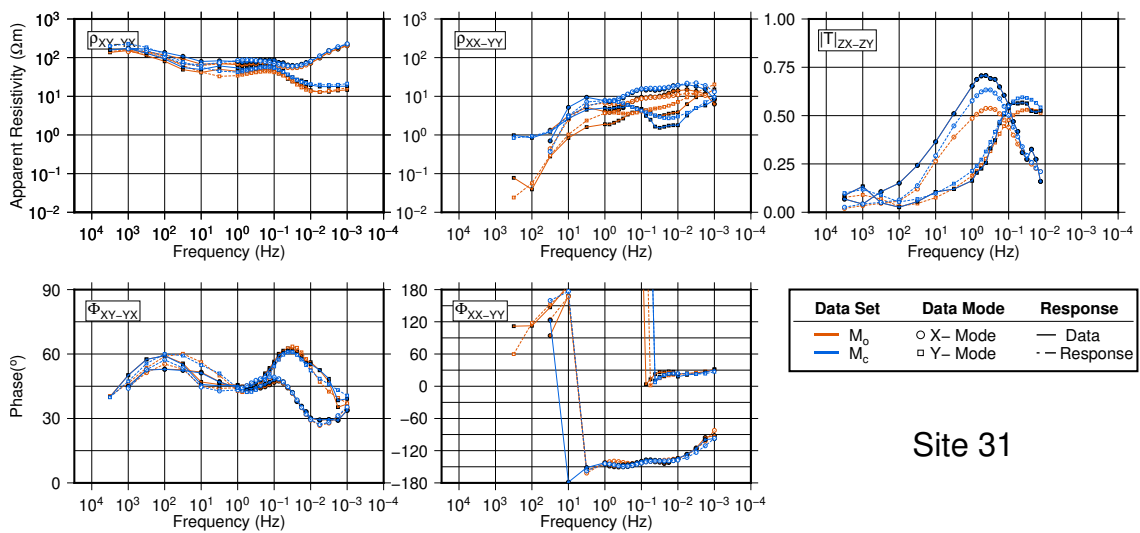
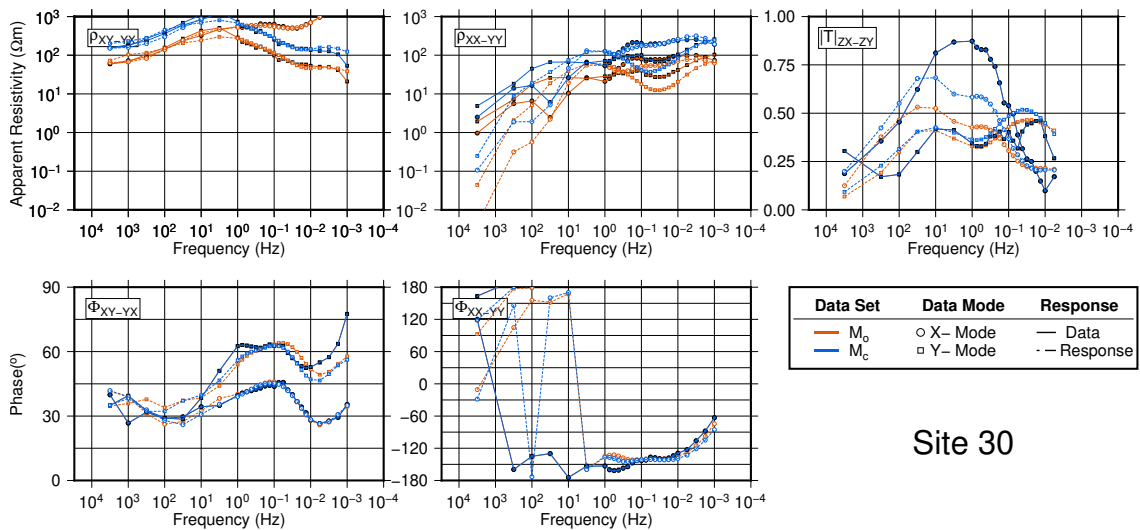
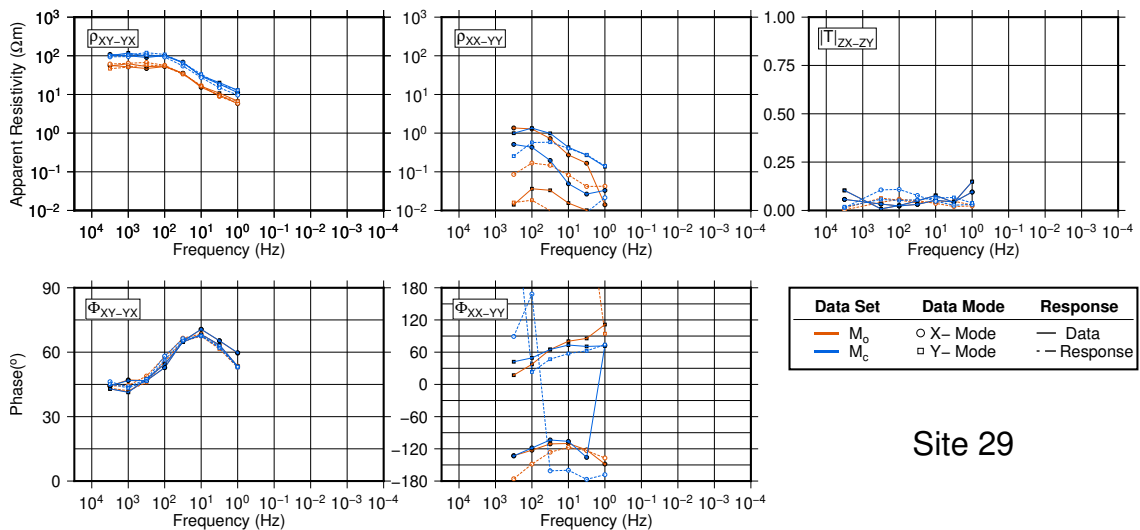


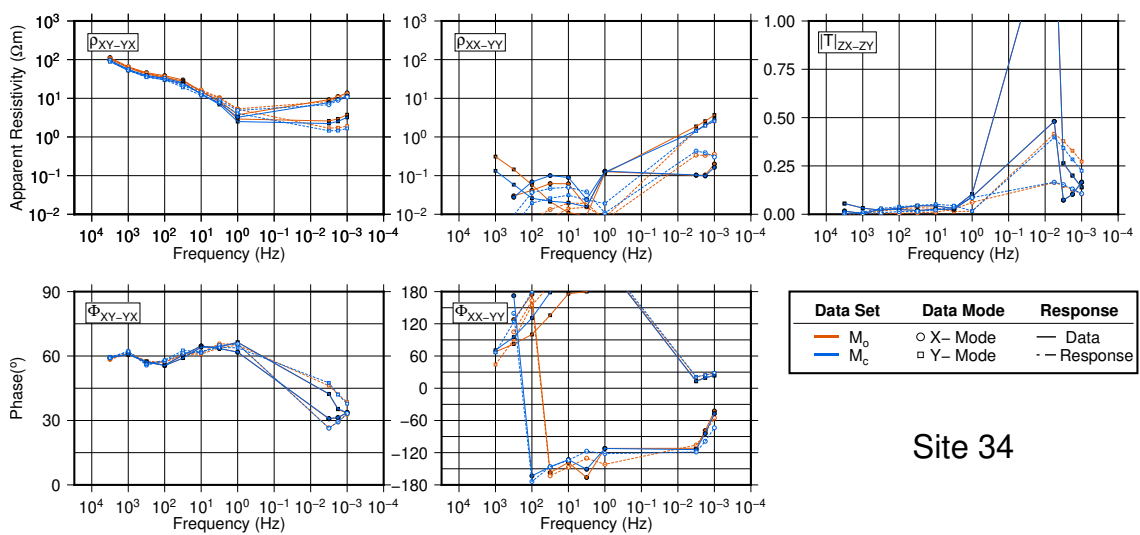
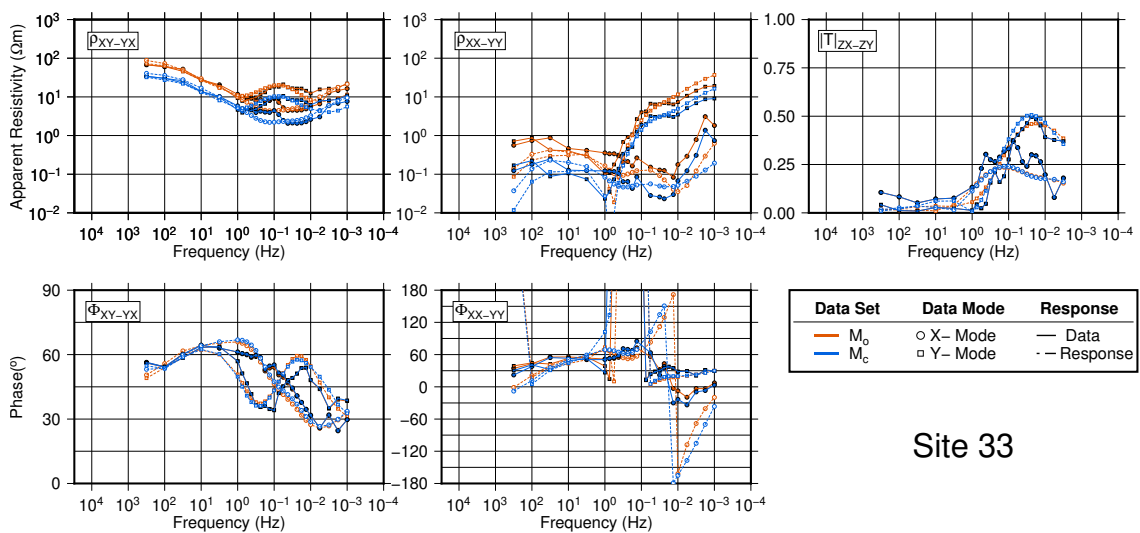
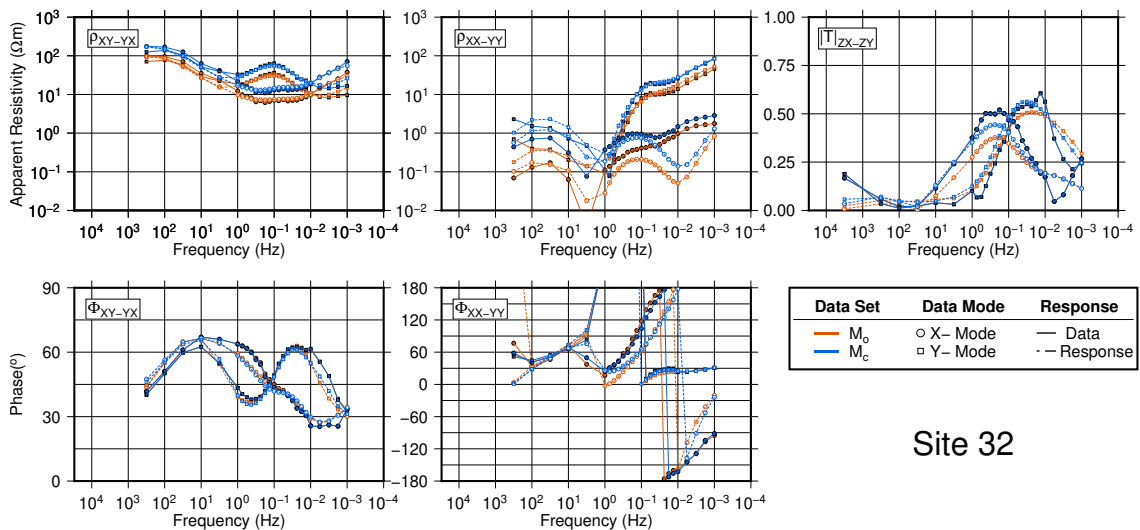


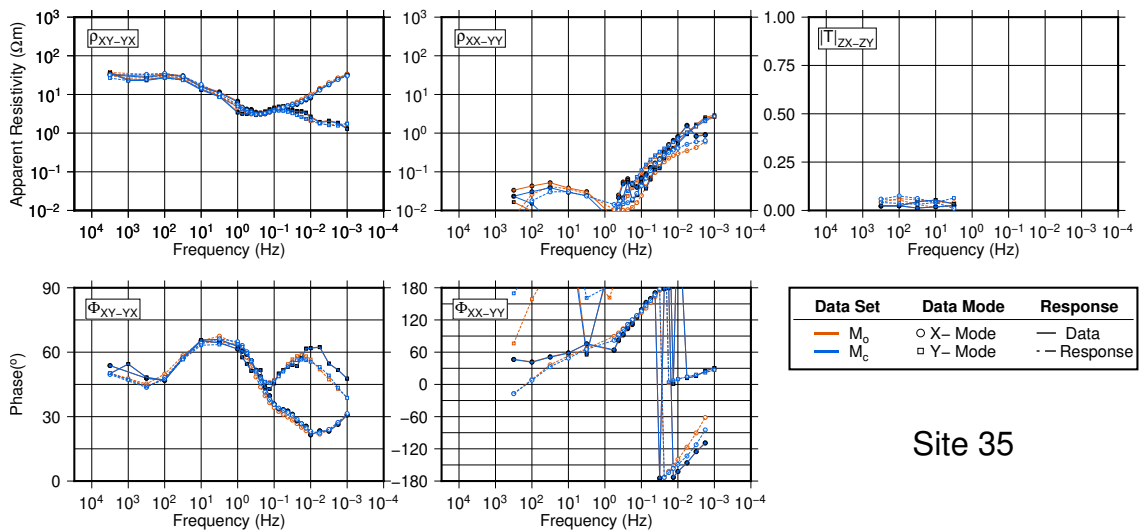




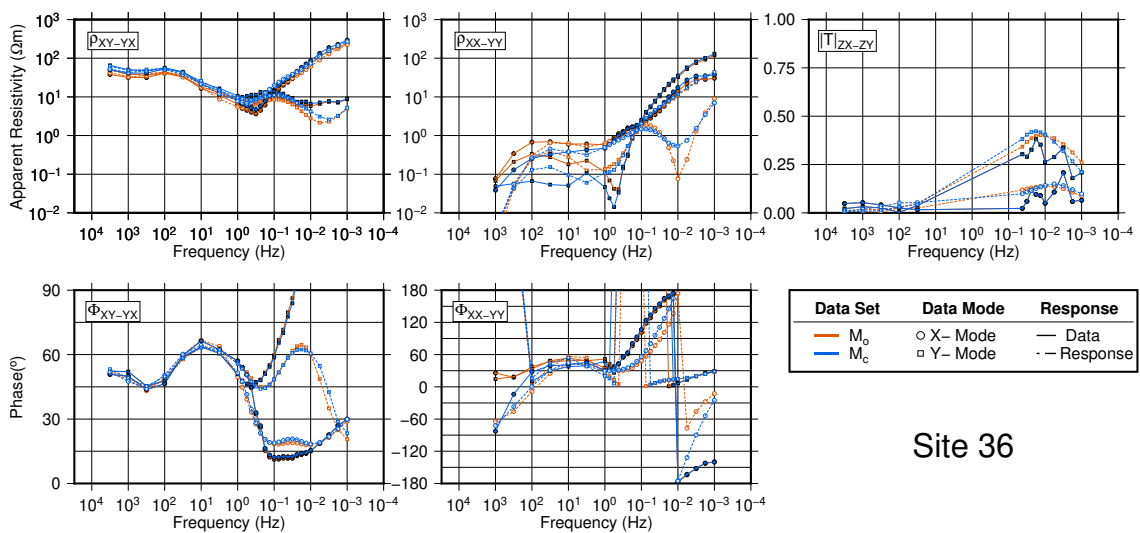




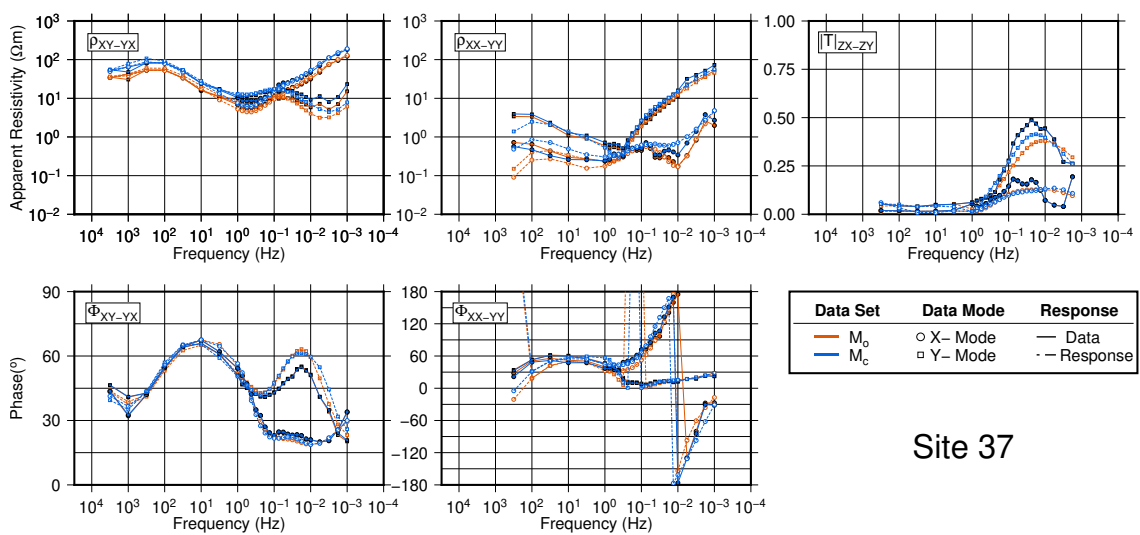


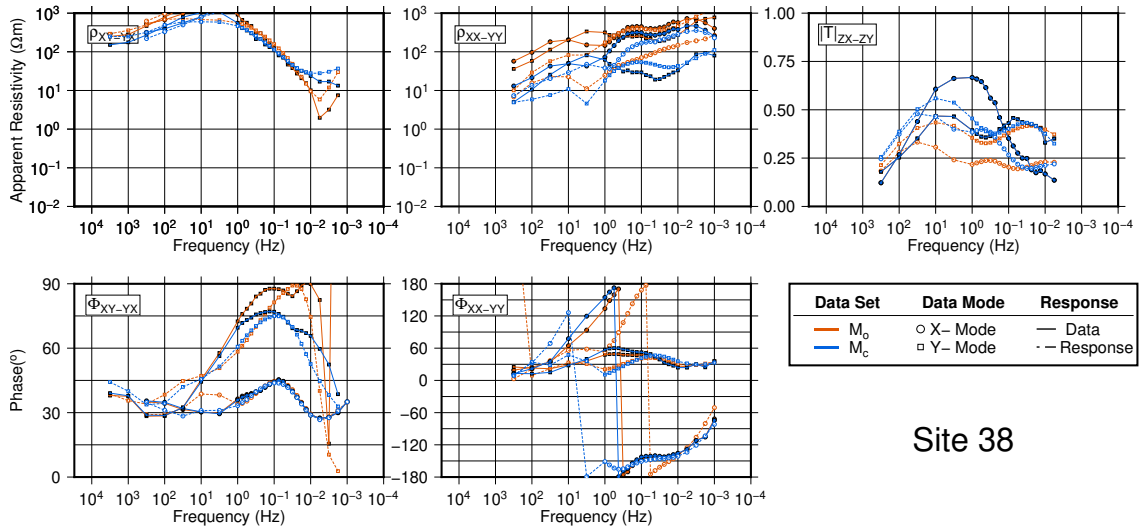


Site 35

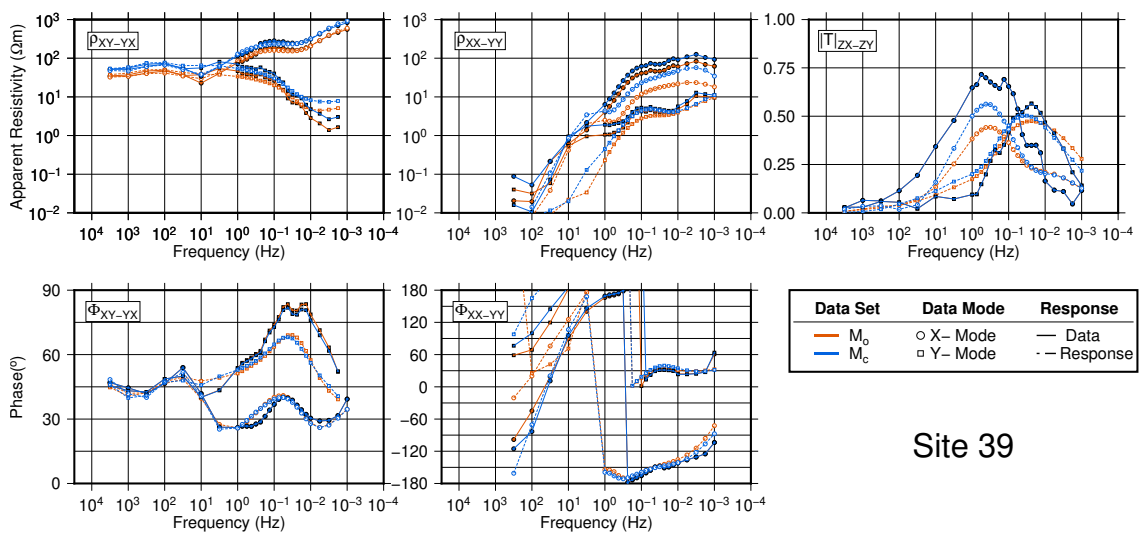


Site 36

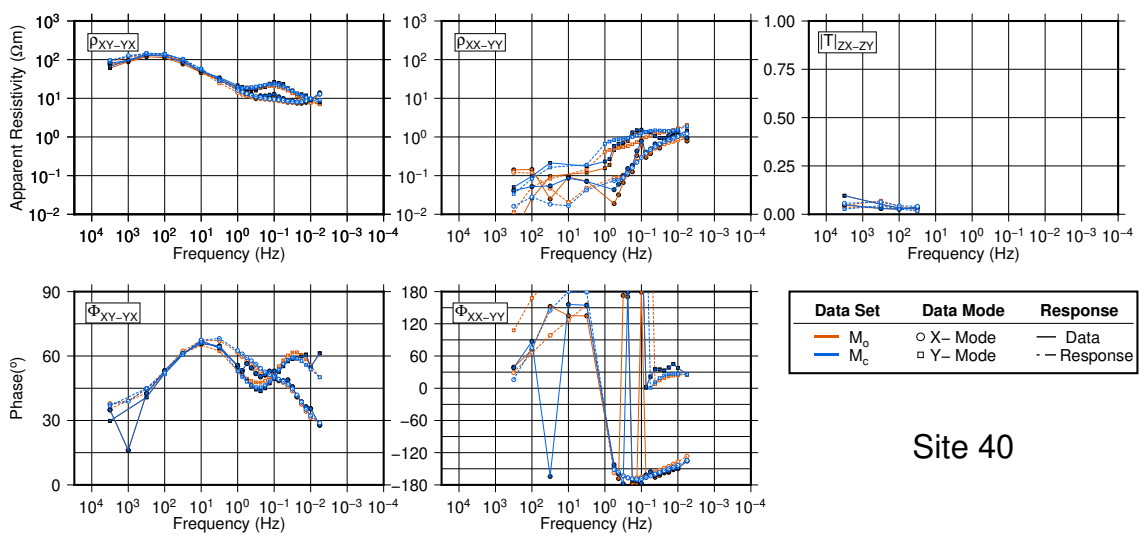


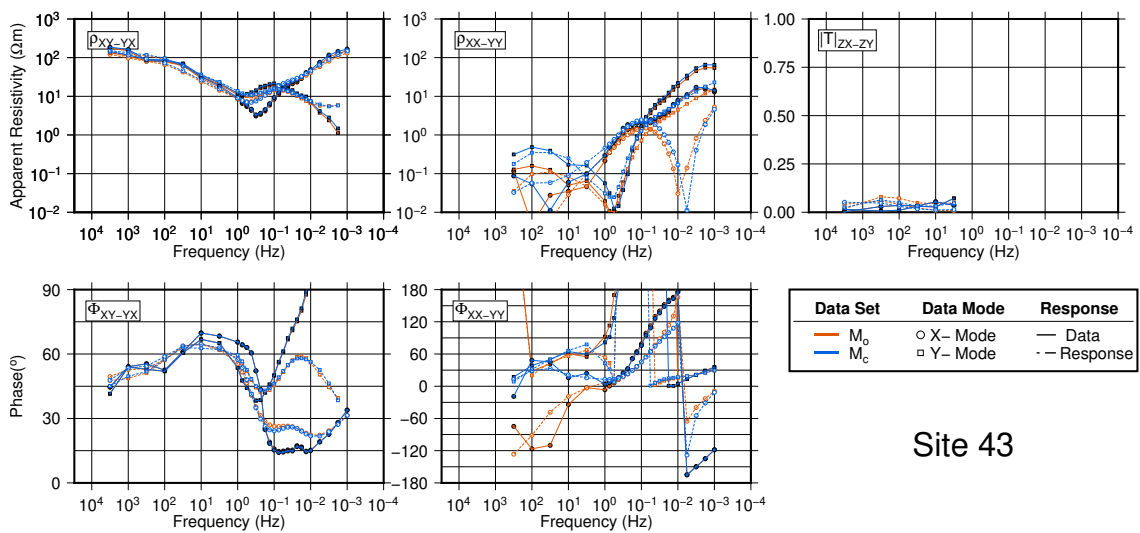
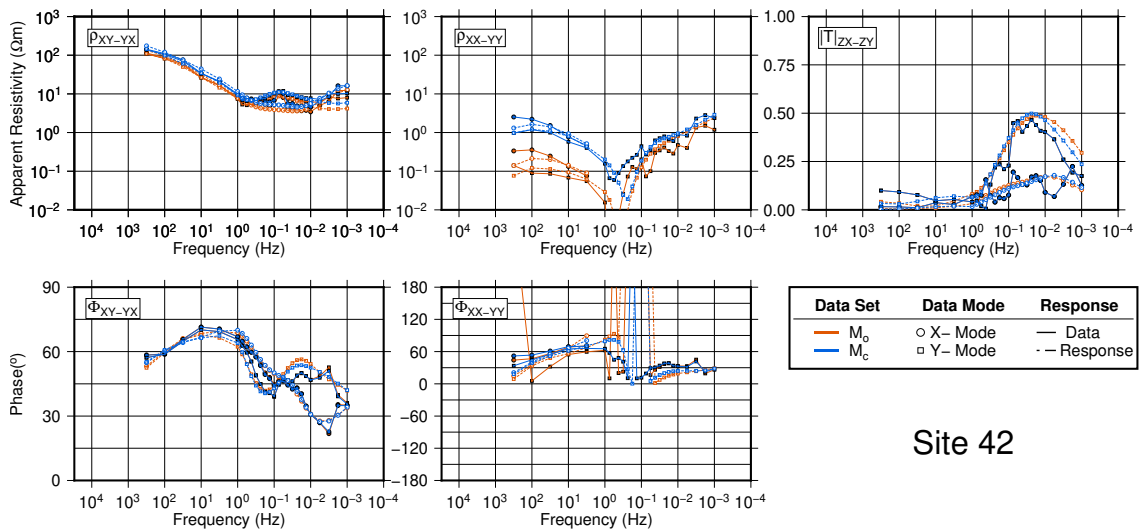
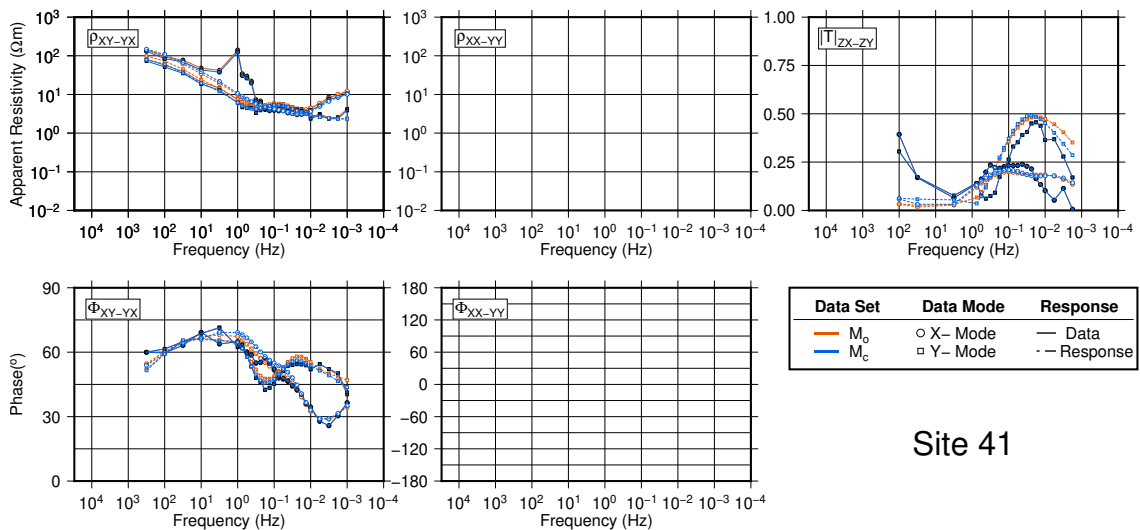


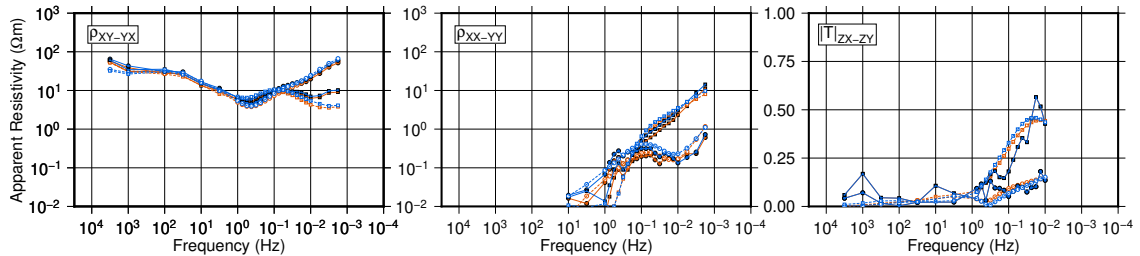
Site 38



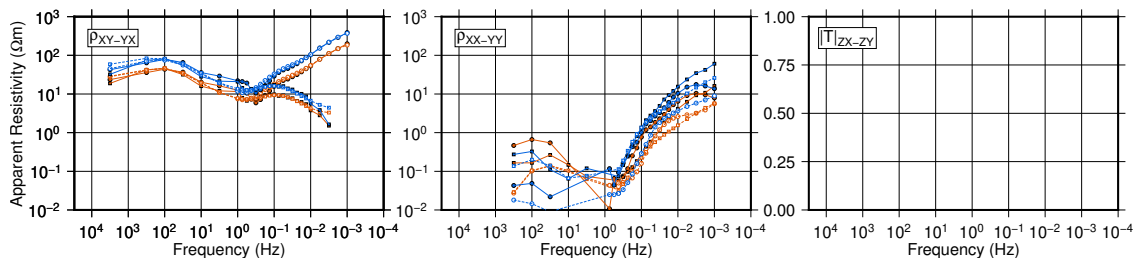
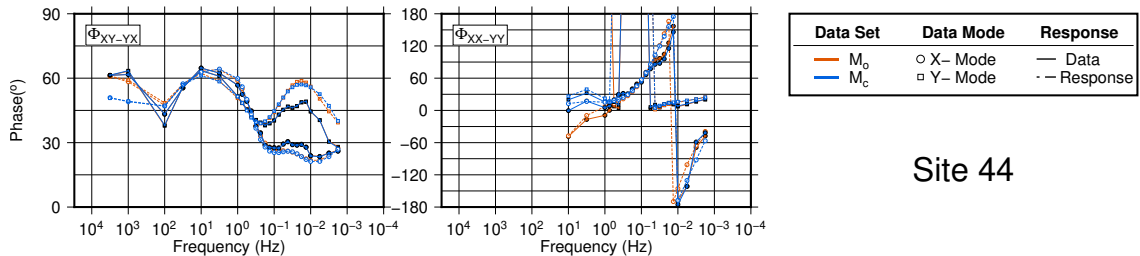
Site 39



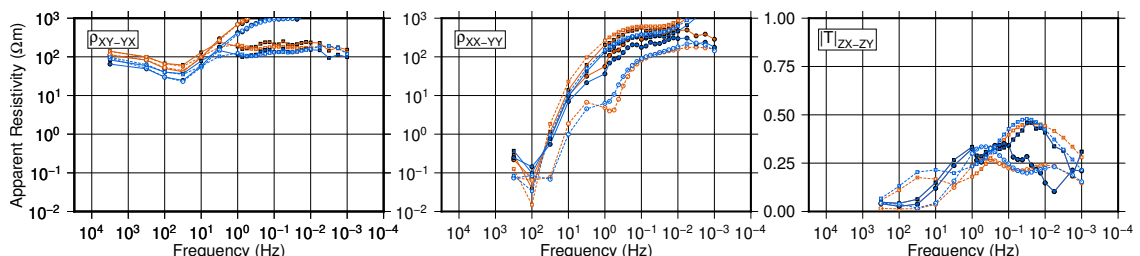
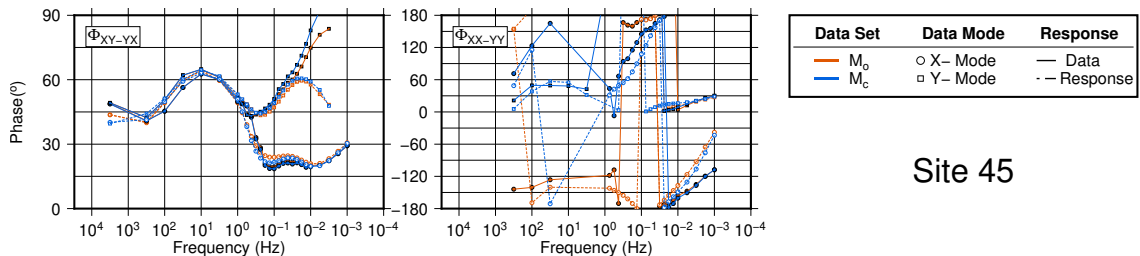




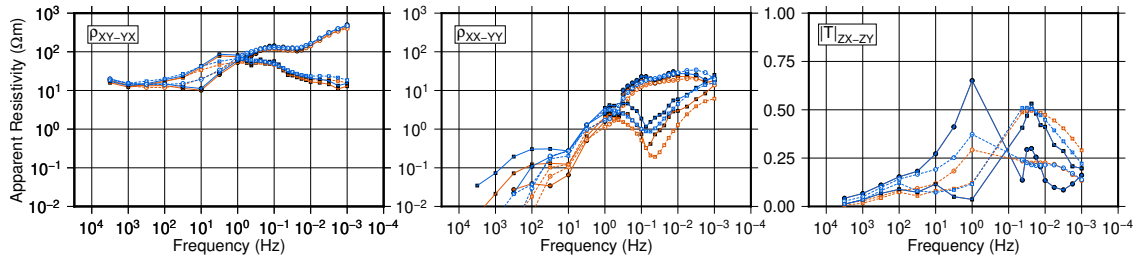
Site 44



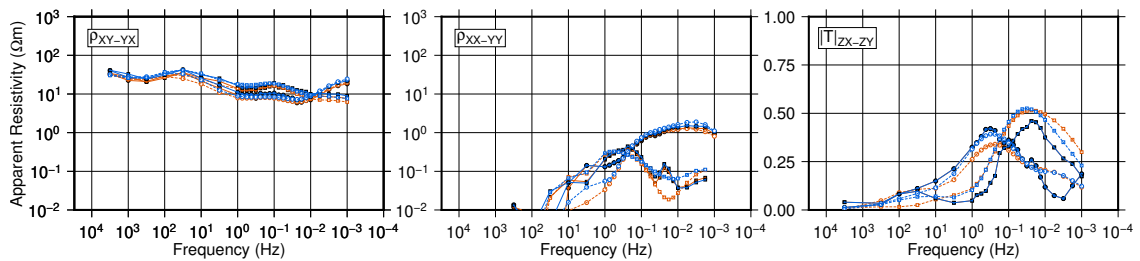
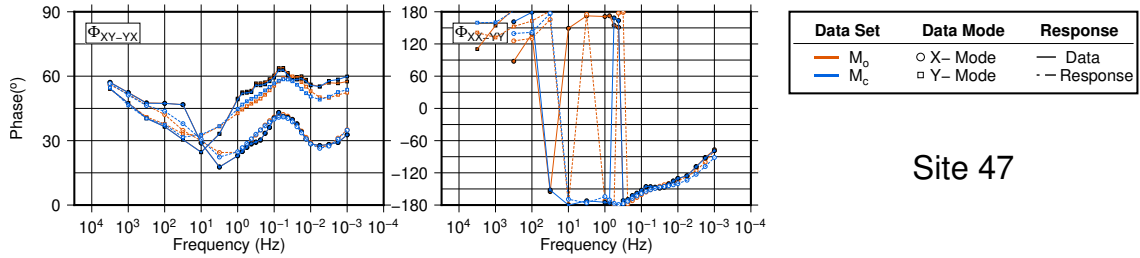
Site 45



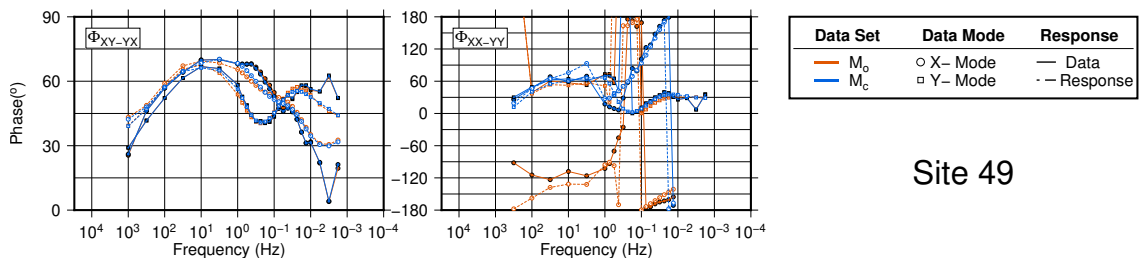
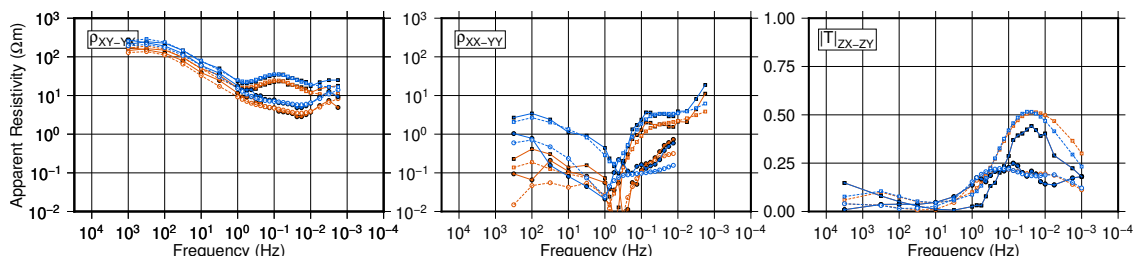
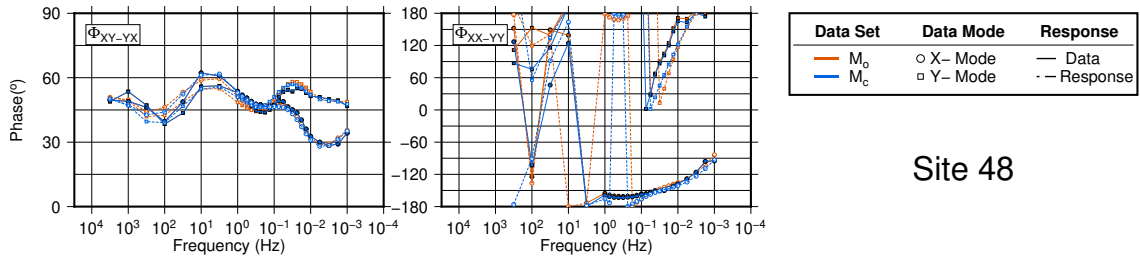
Site 46



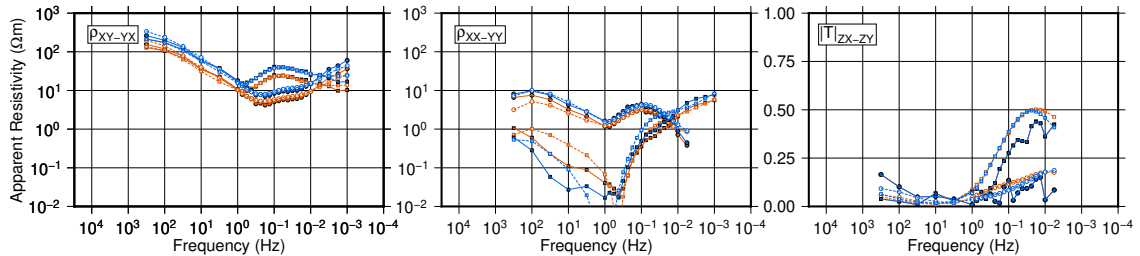
Site 47



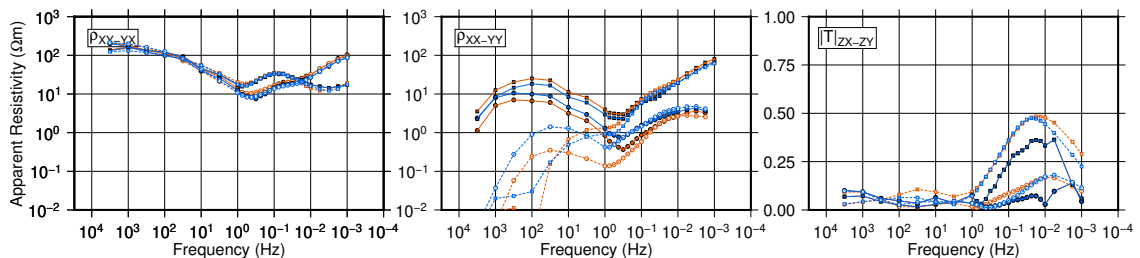
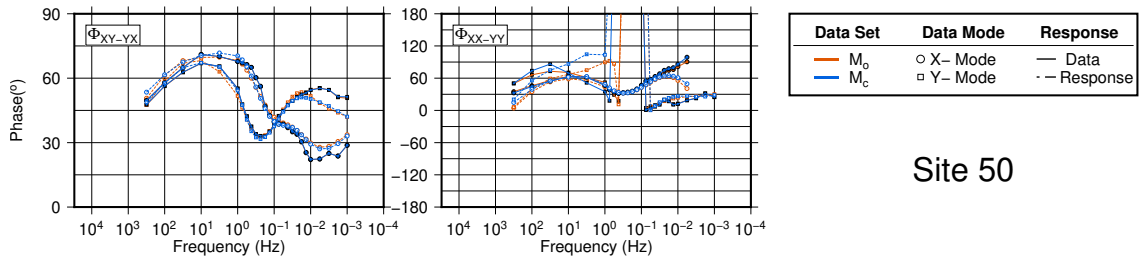
Site 48



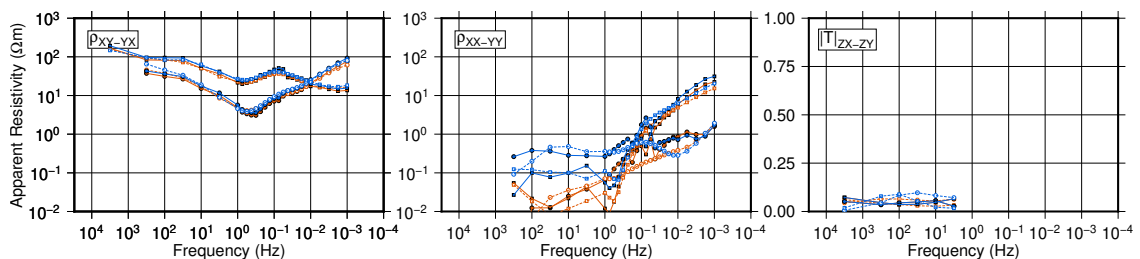
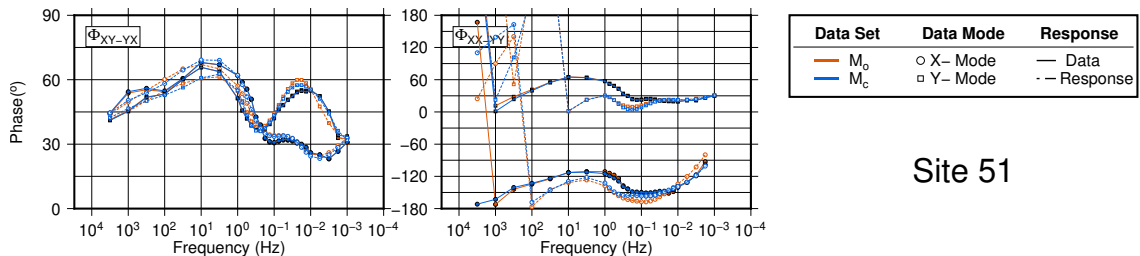
Site 49



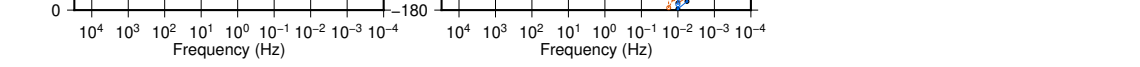
Site 50

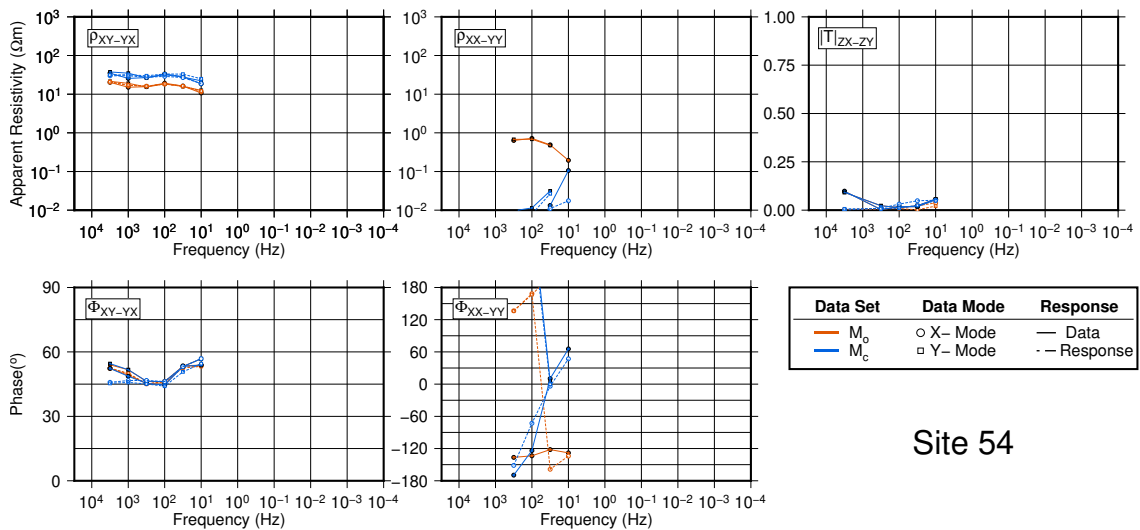
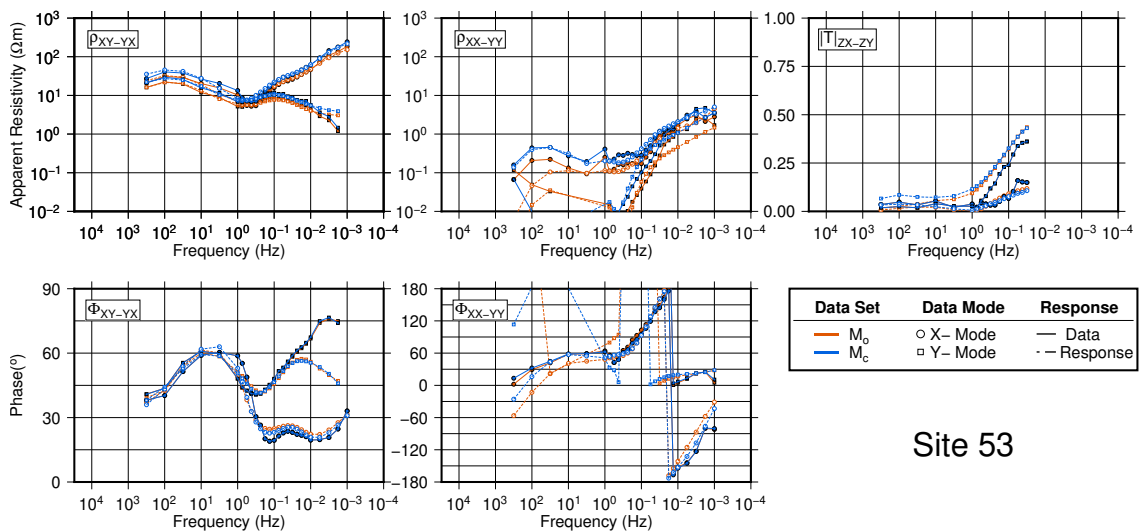


Site 51



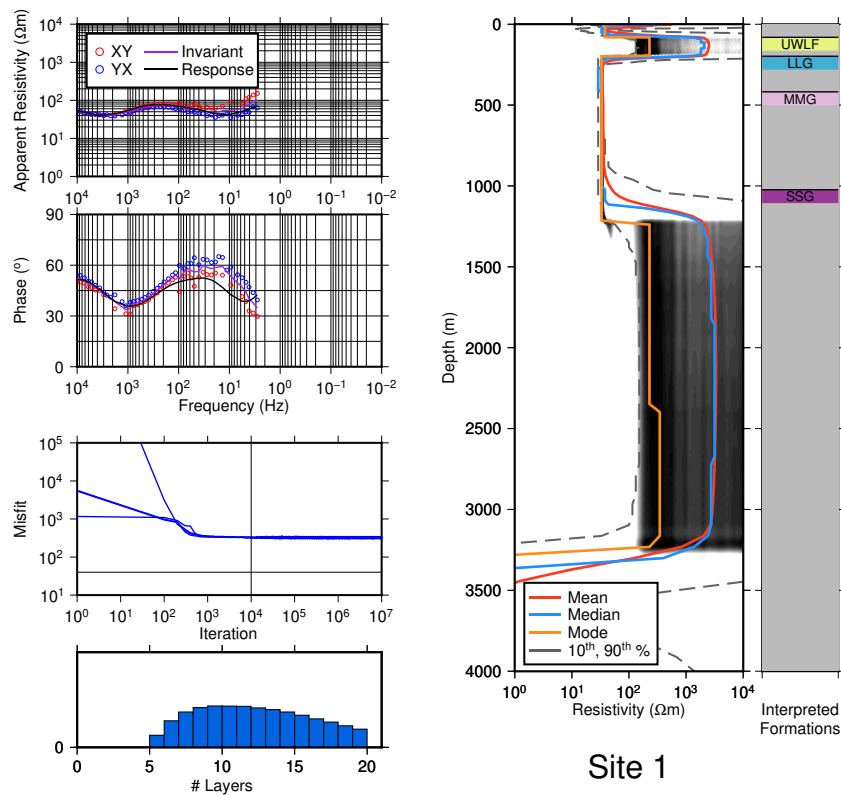
Site 52



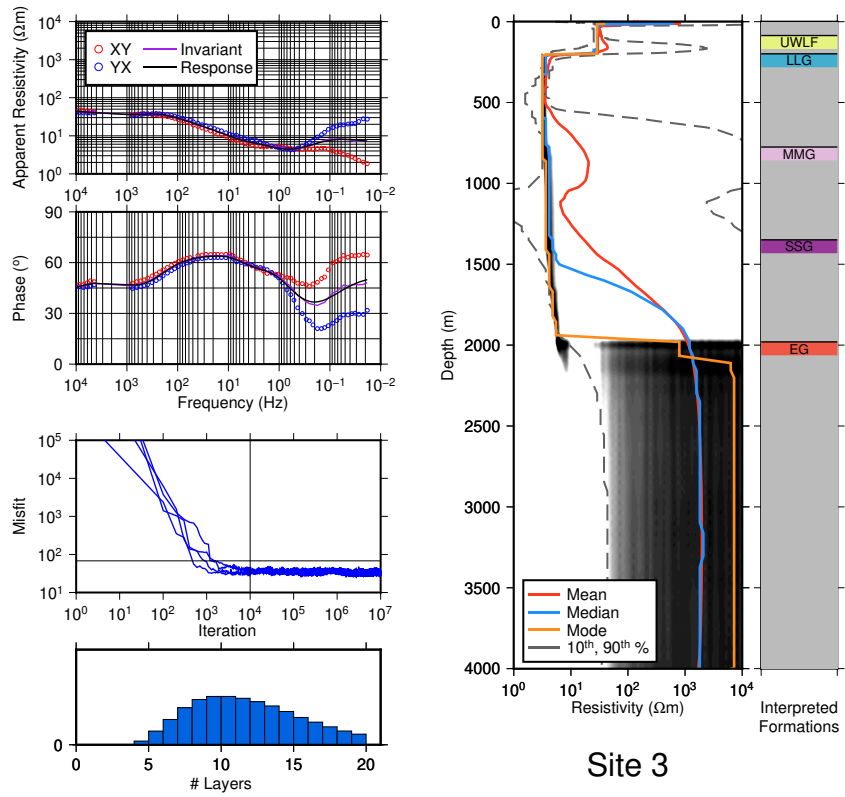
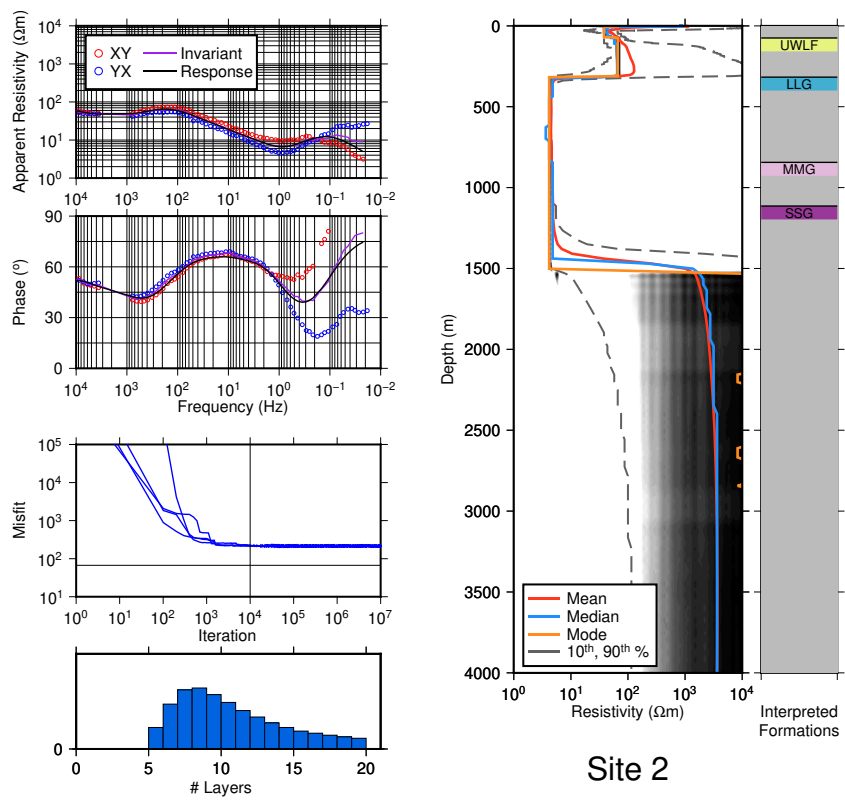


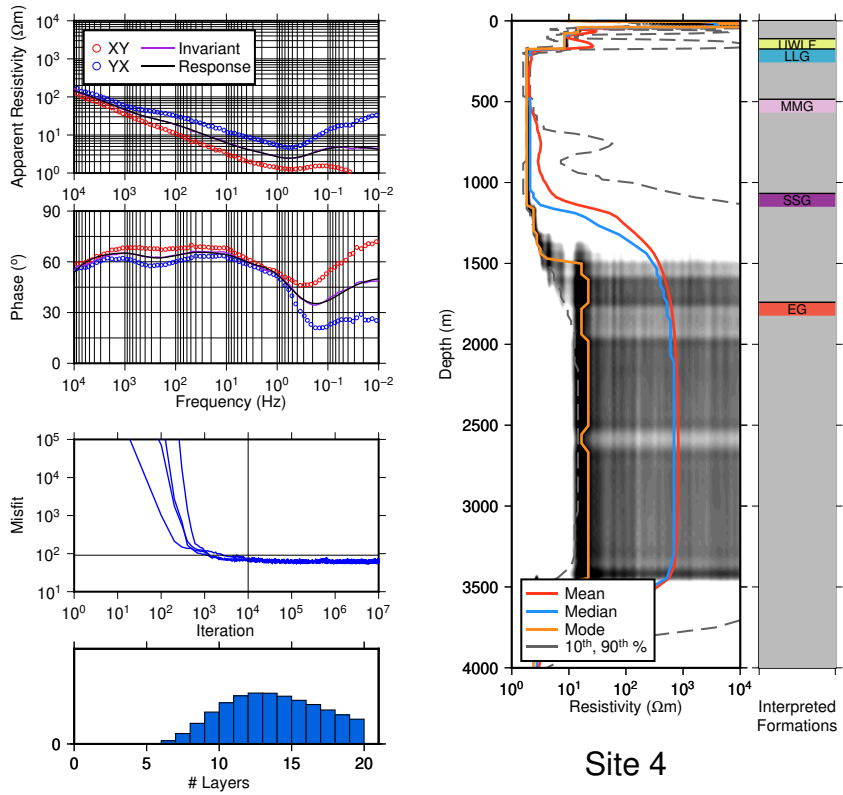
B

CHAPTER 3 DATA AND RESPONSES

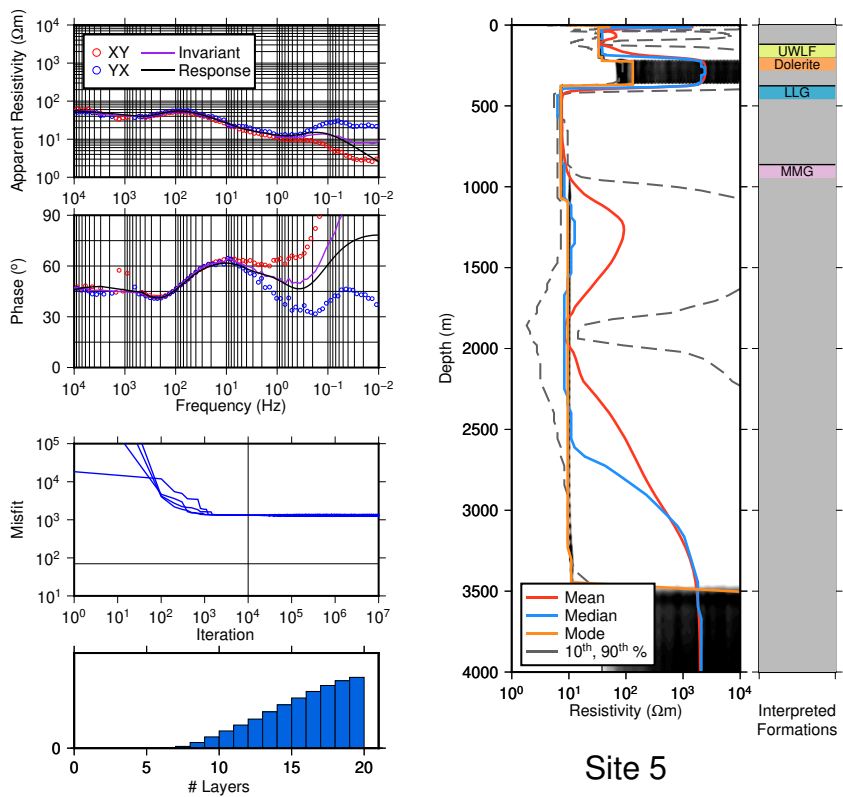


Site 1

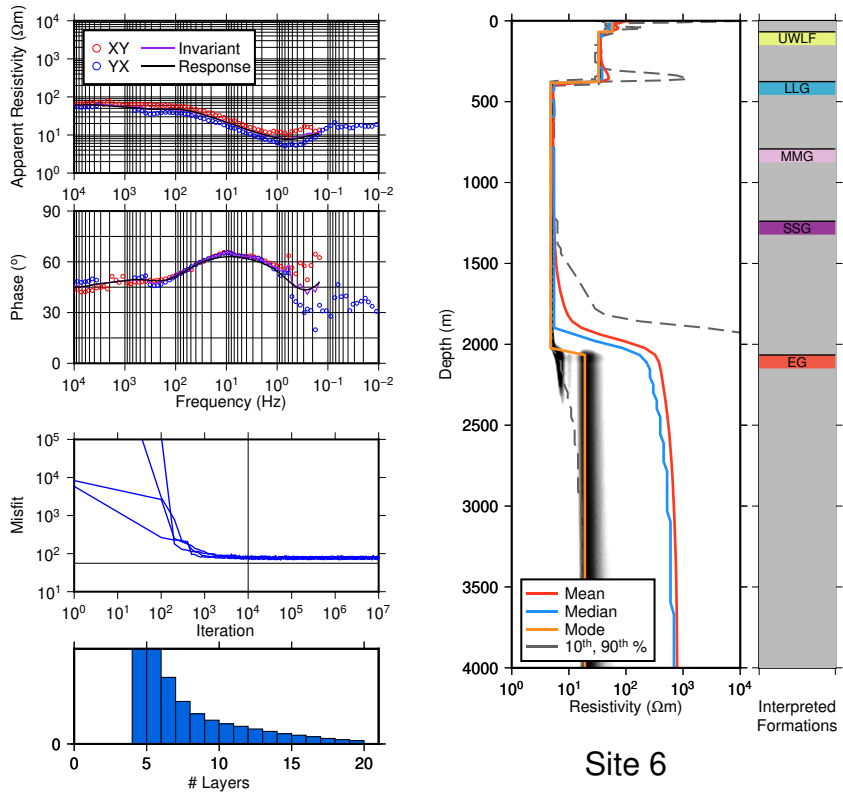




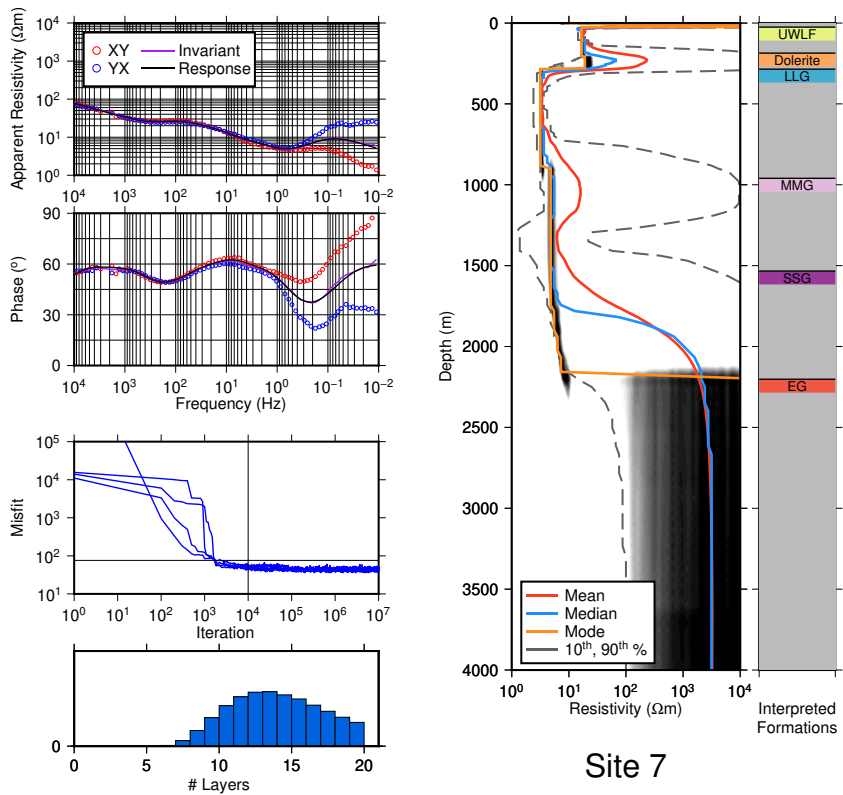
Site 4



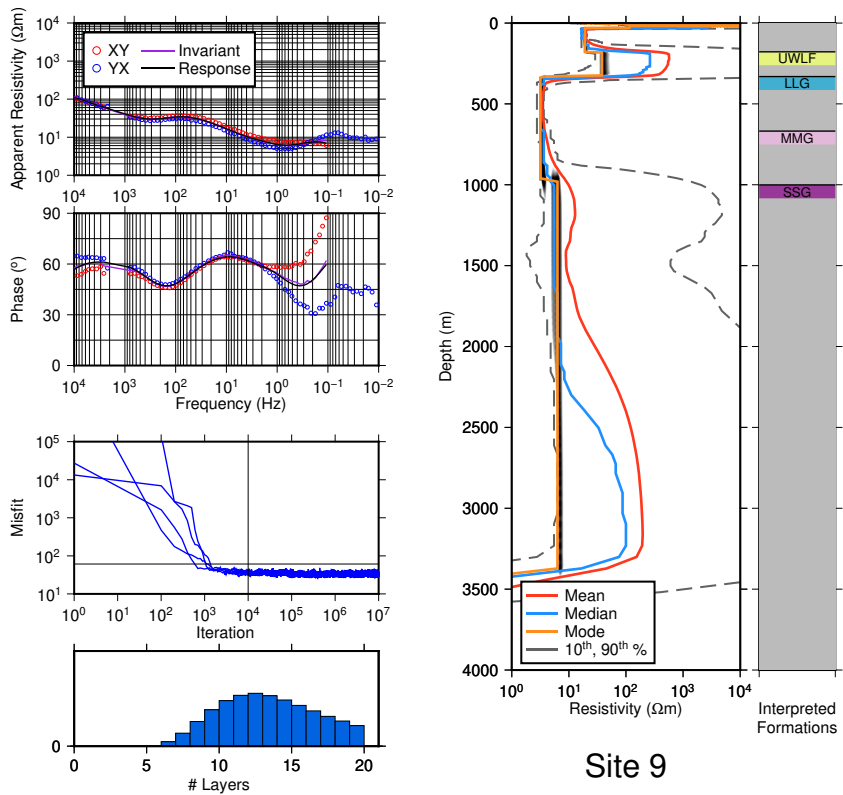
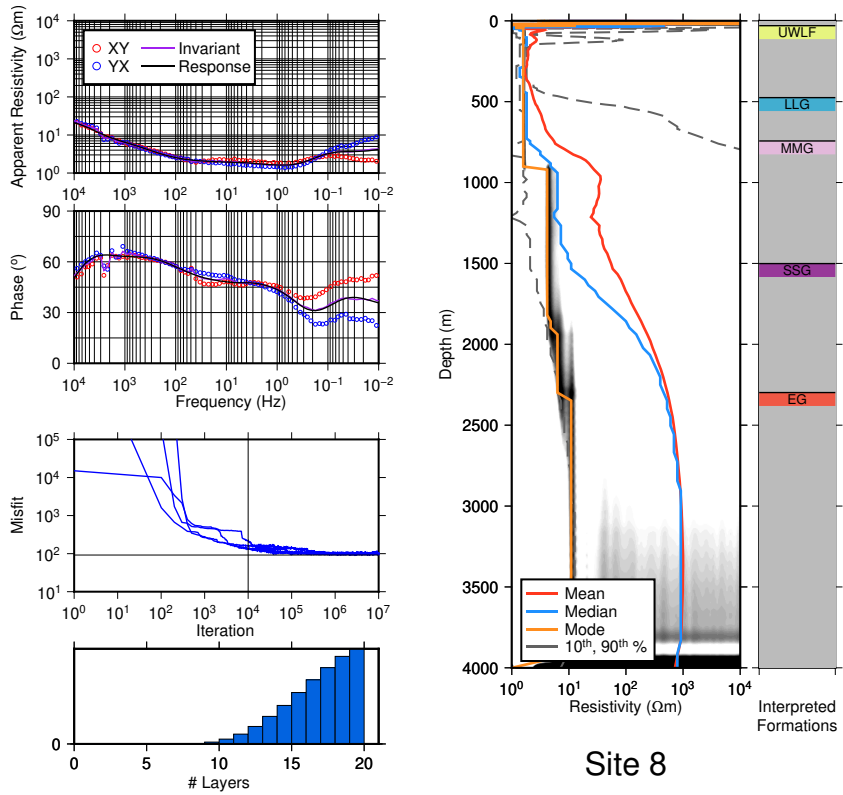
Site 5

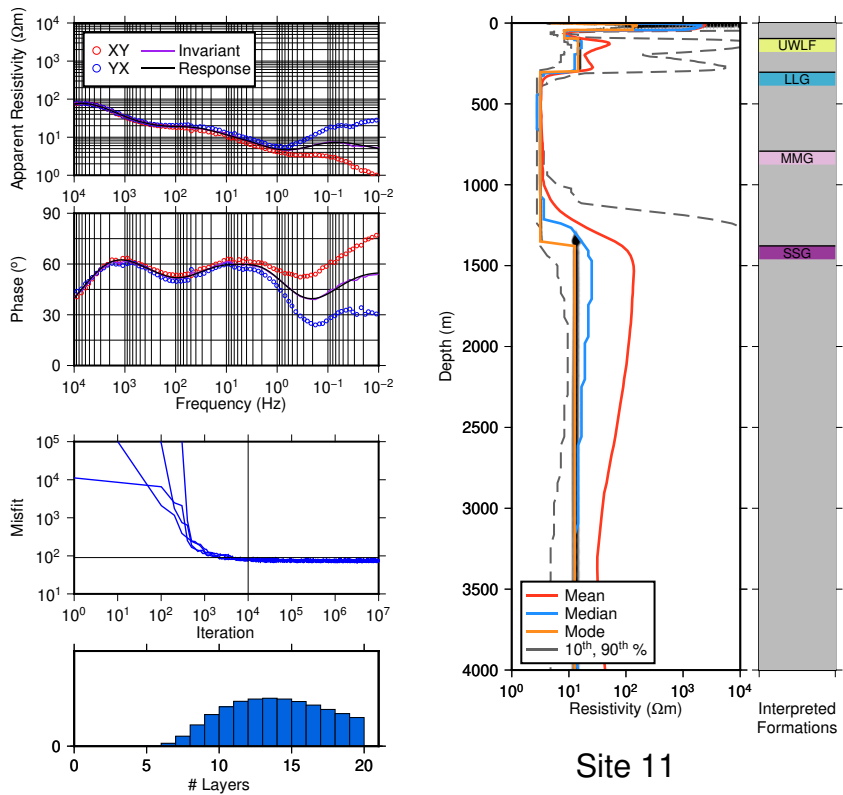
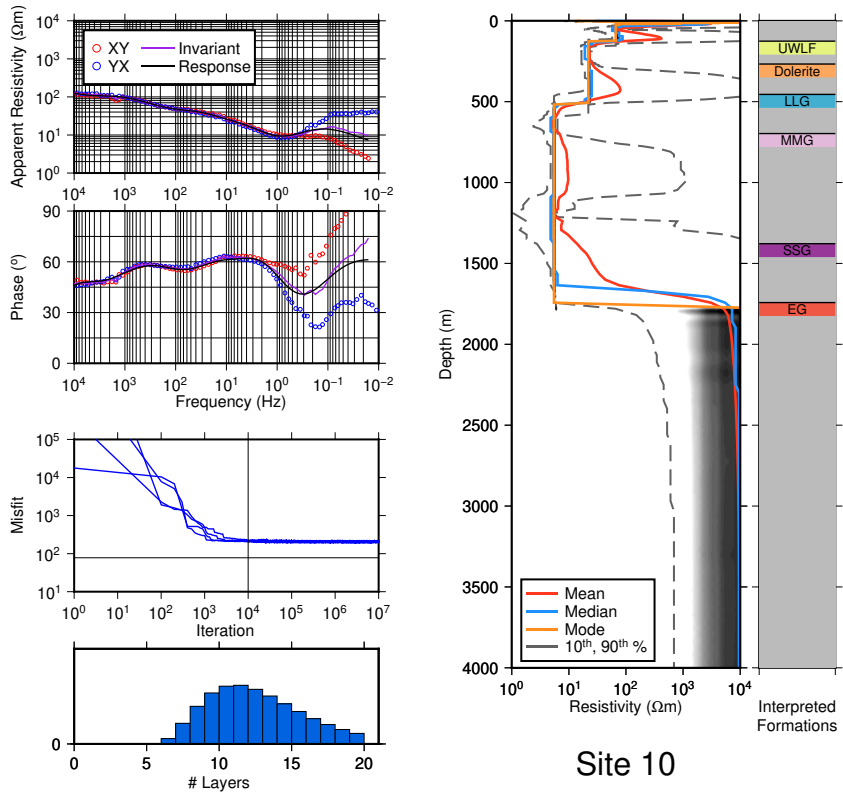


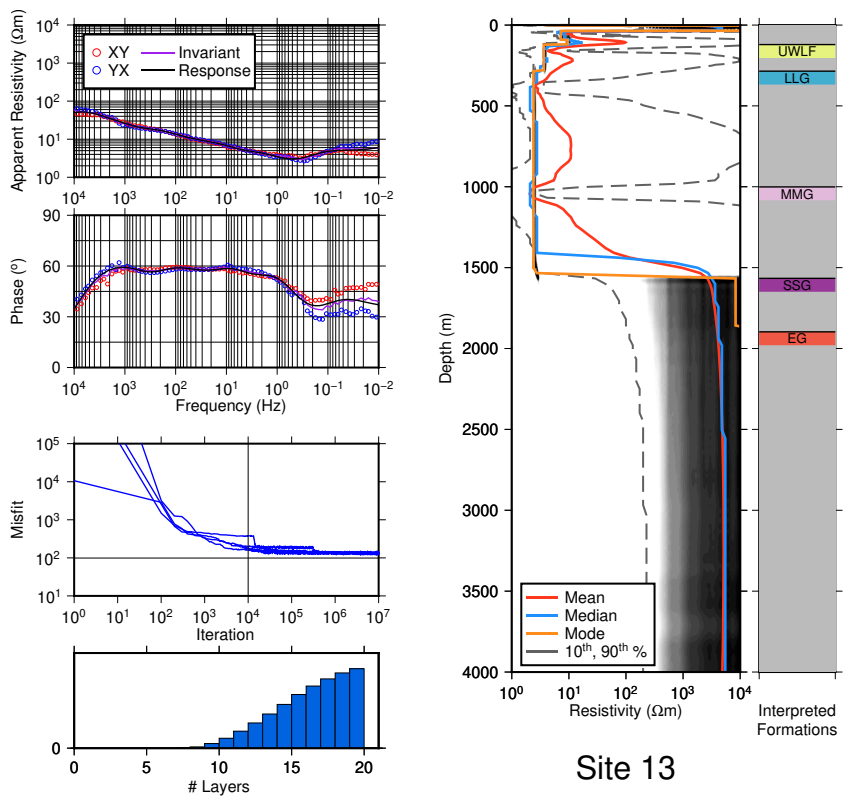
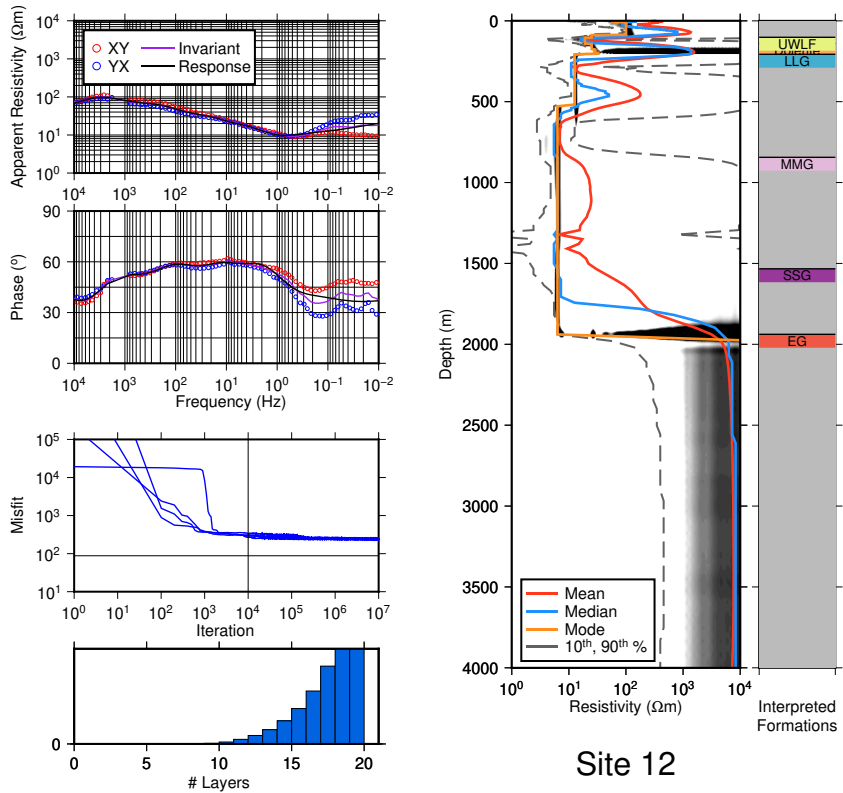
Site 6

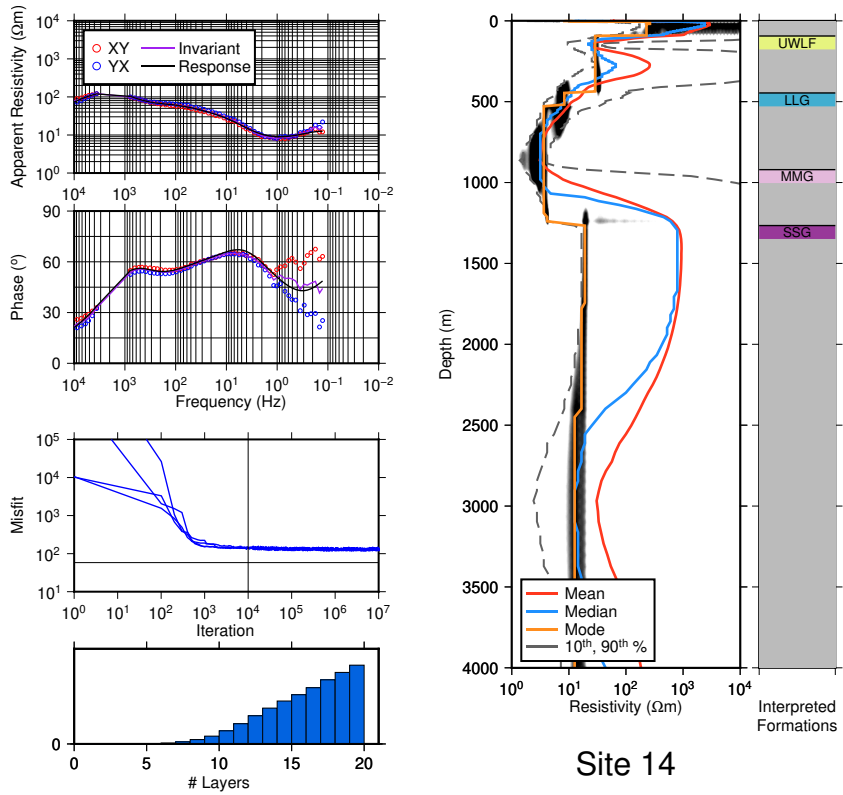


Site 7

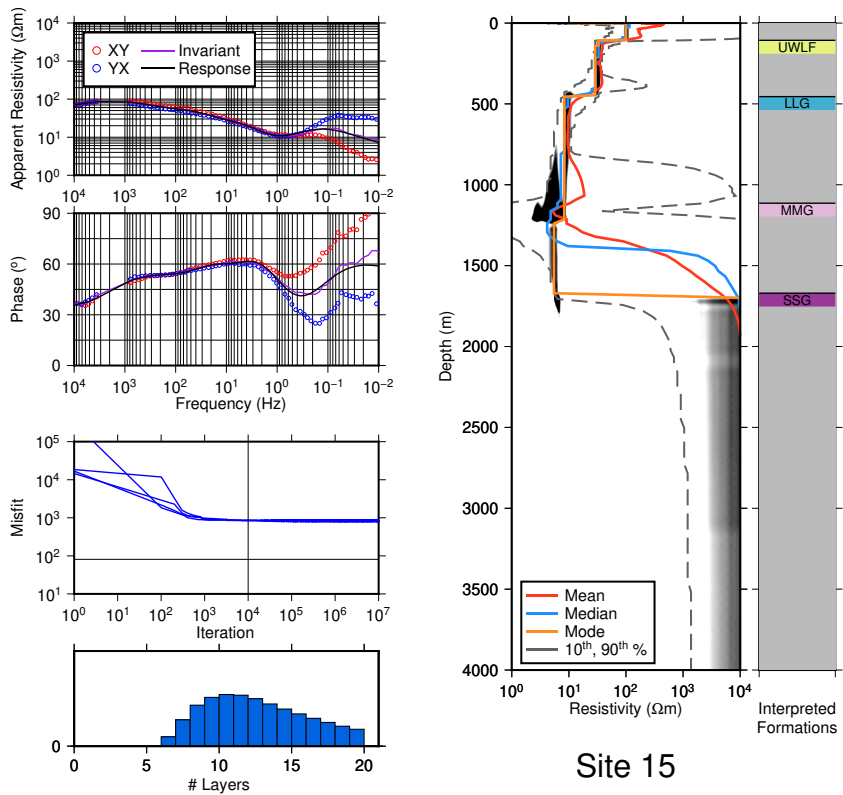




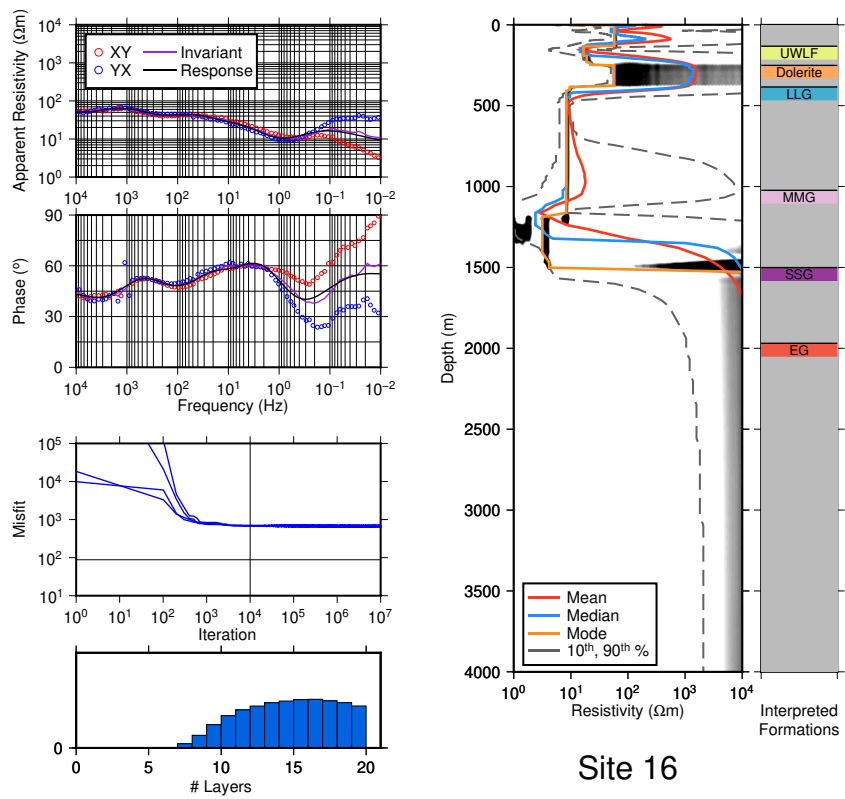




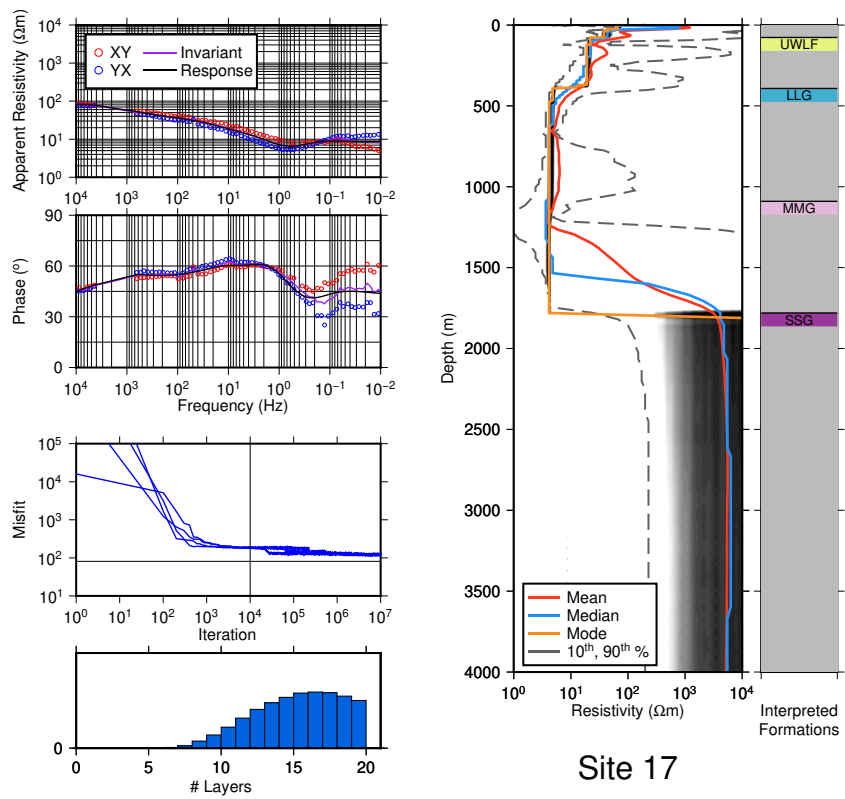
Site 14



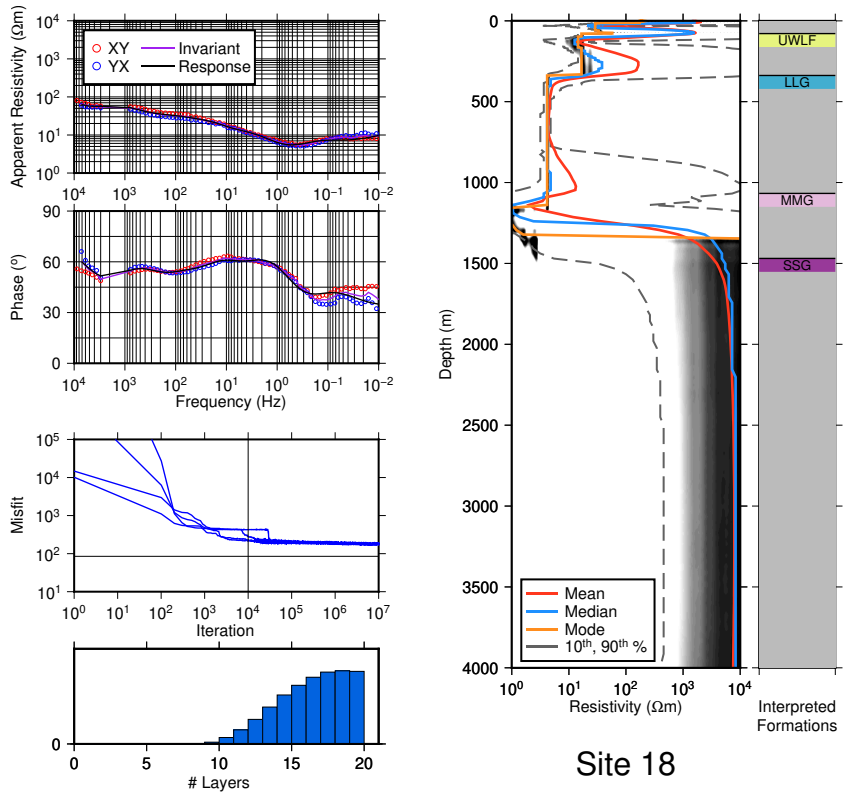
Site 15



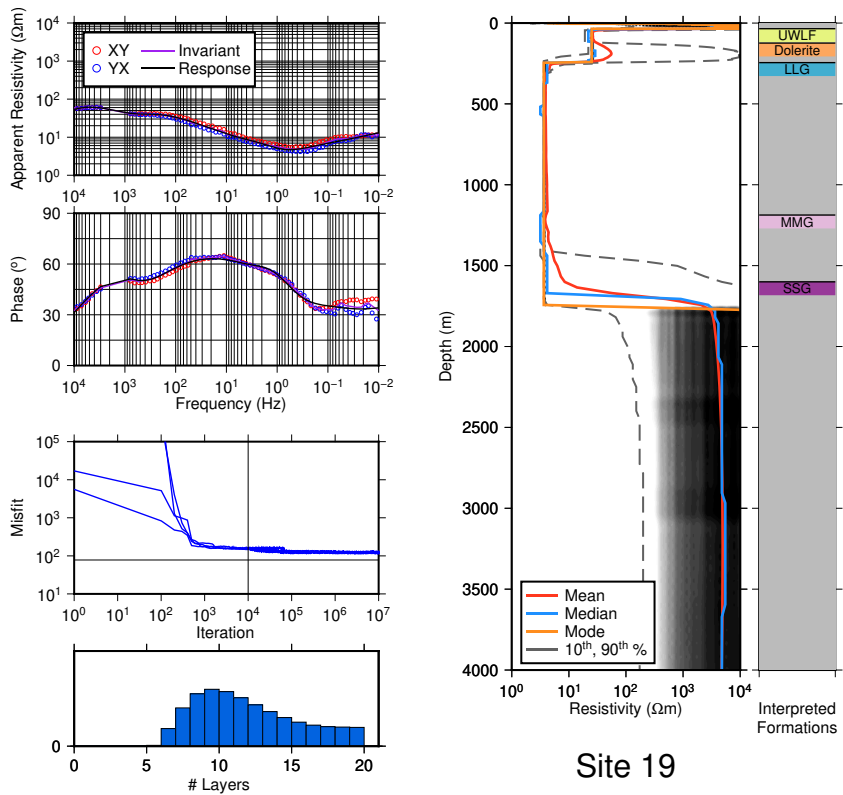
Site 16



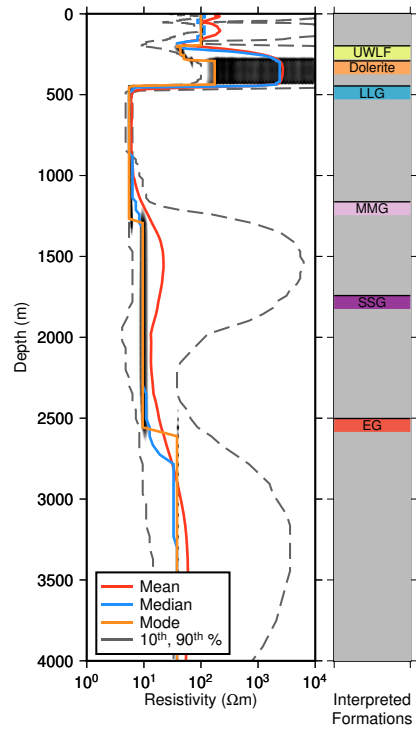
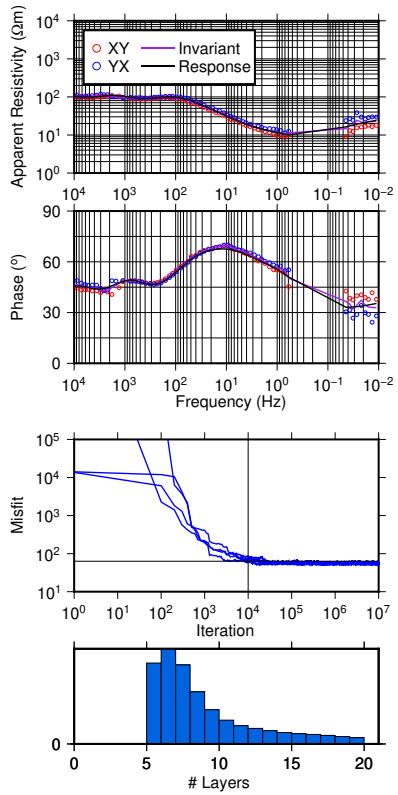
Site 17



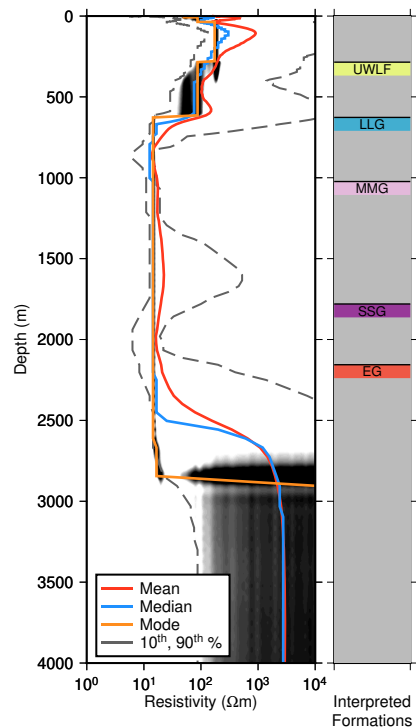
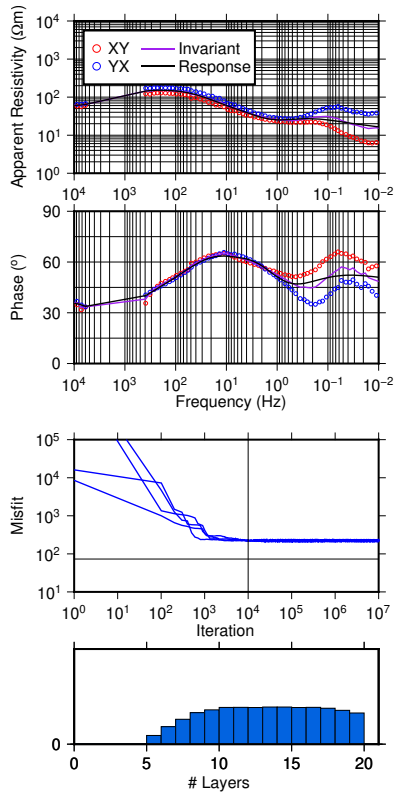
Site 18



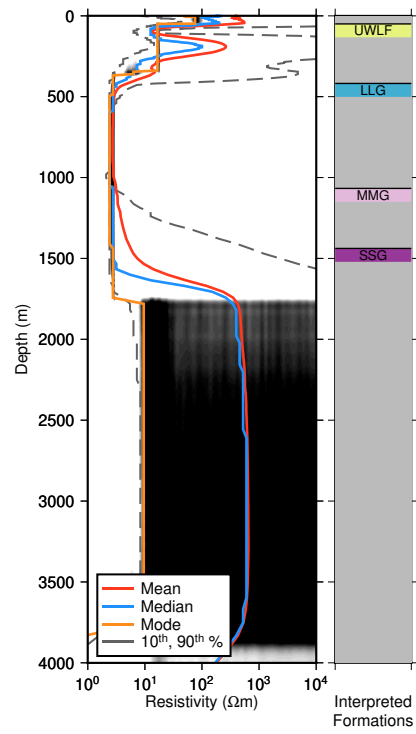
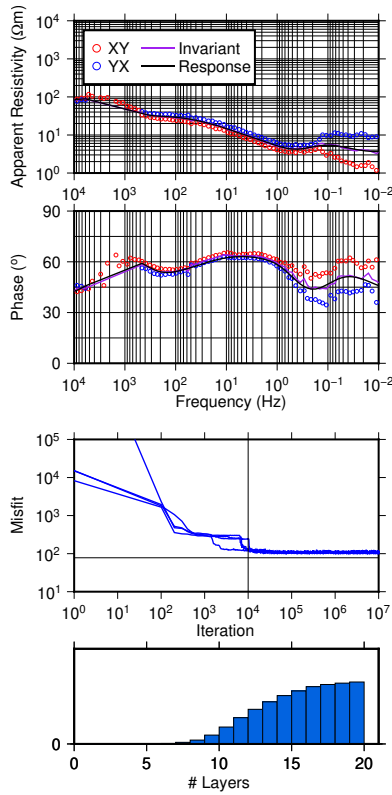
Site 19



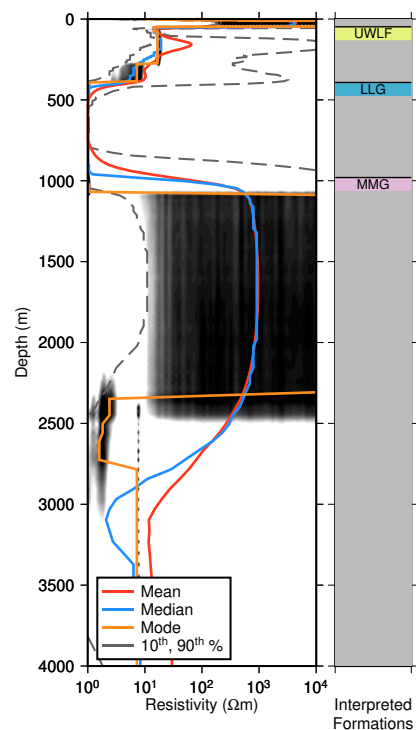
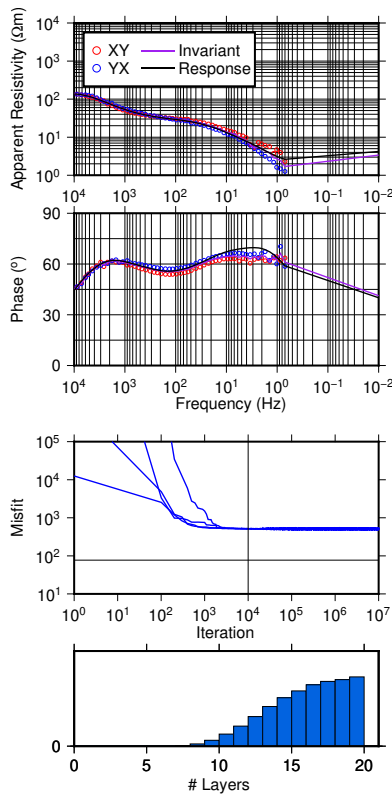
Site 20



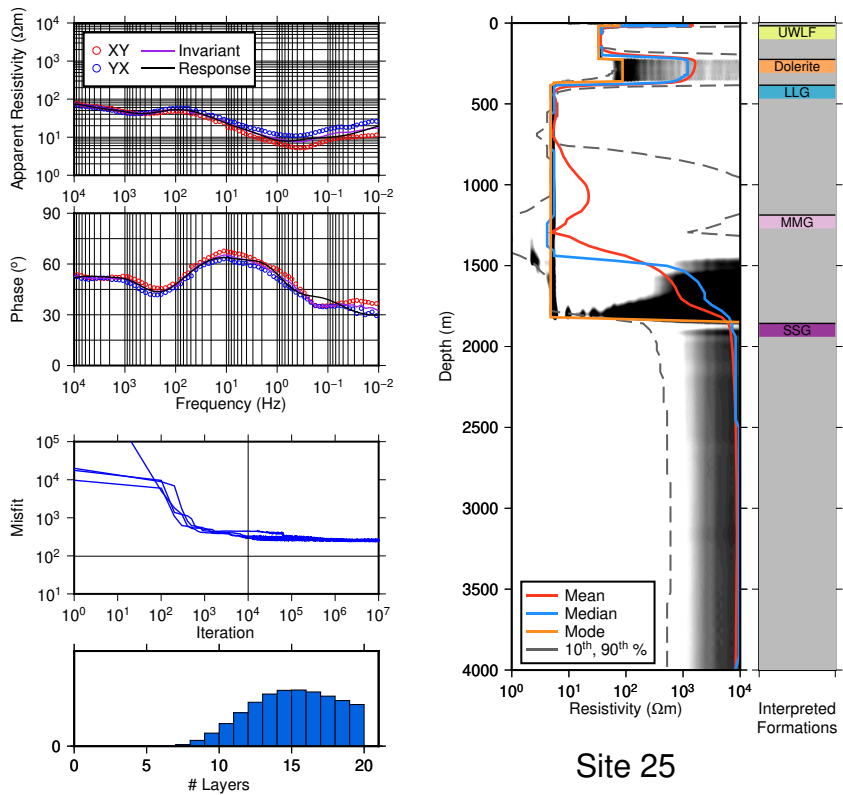
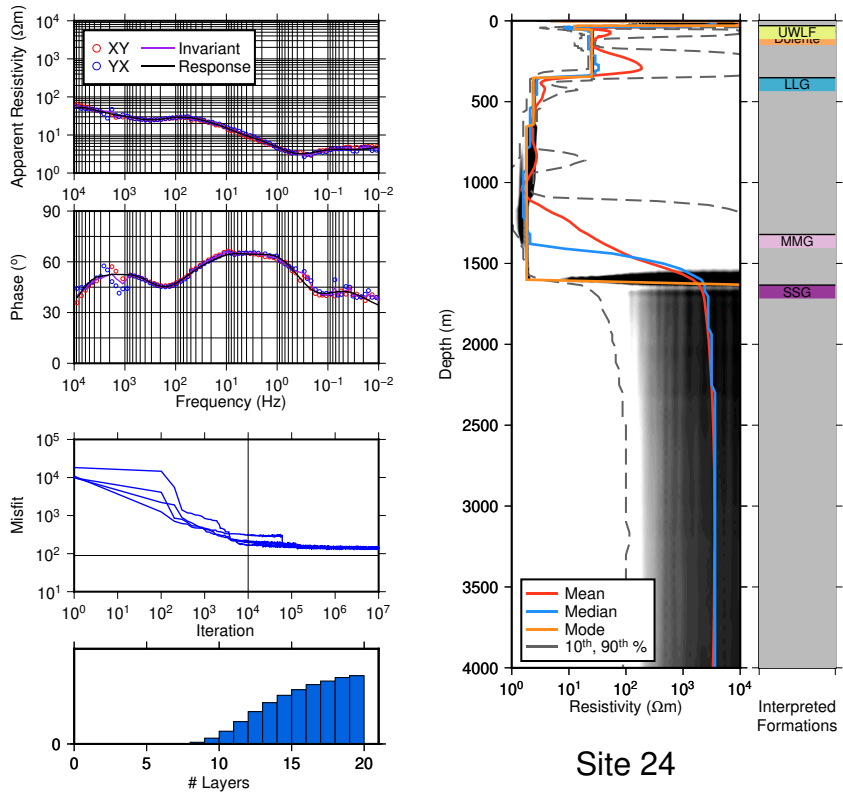
Site 21

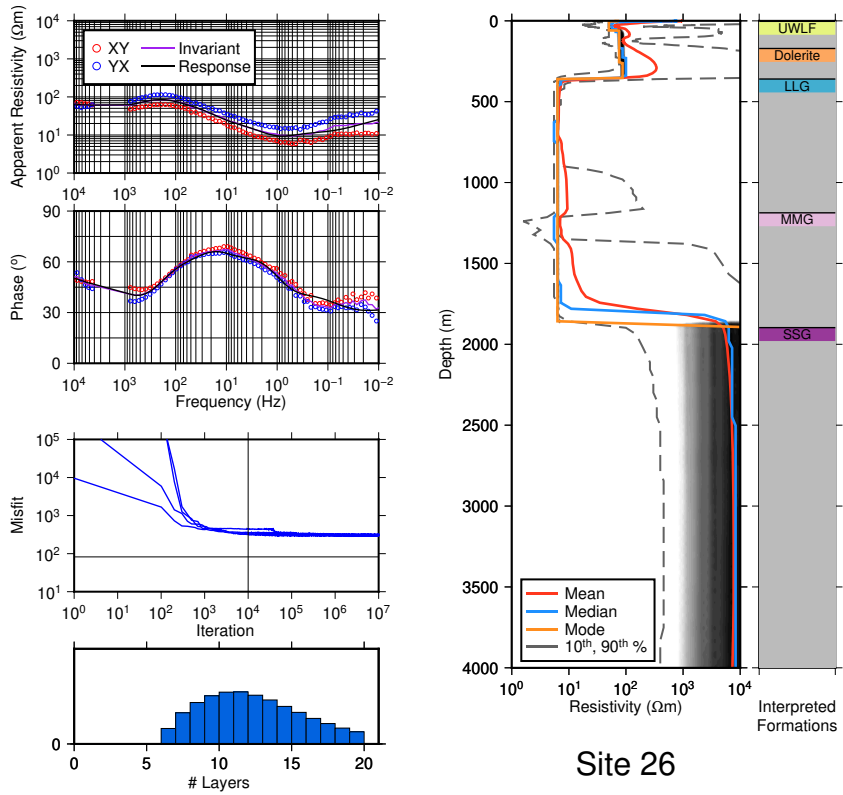


Site 22

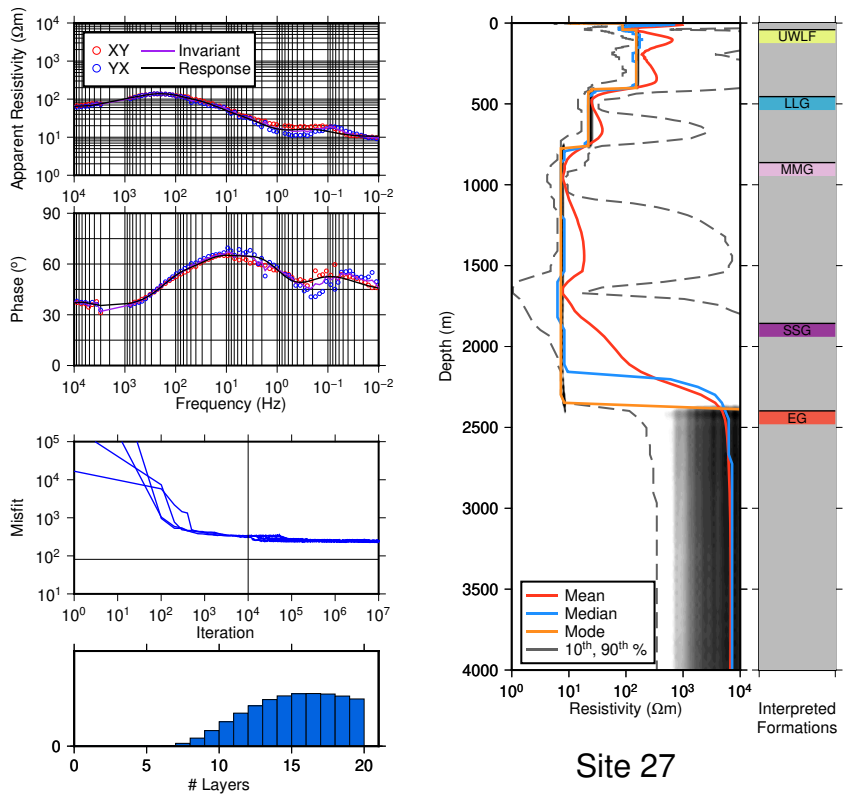


Site 23

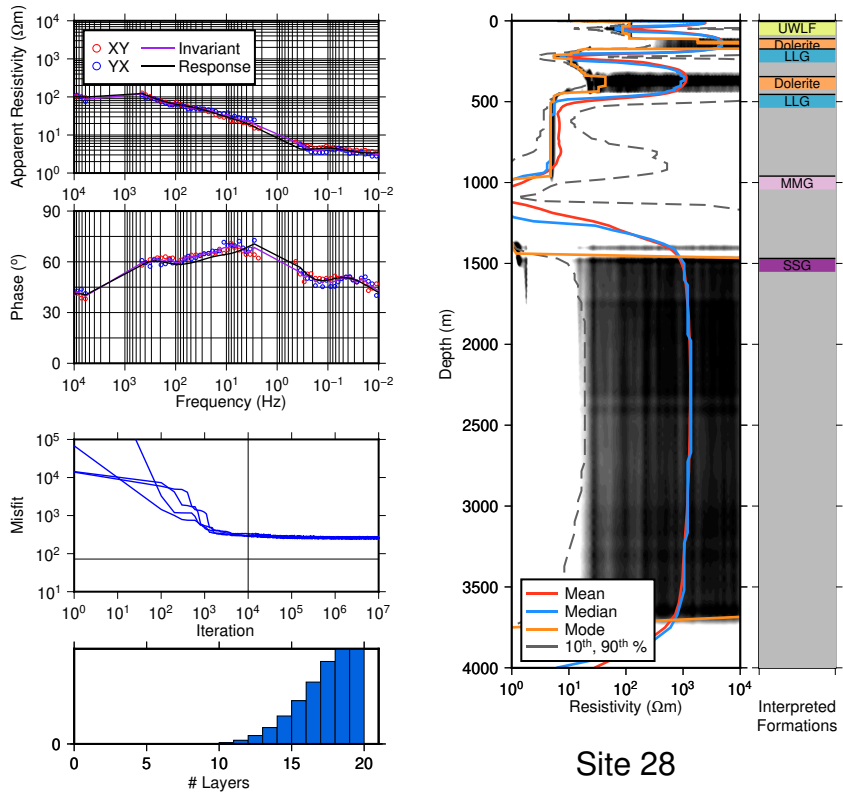




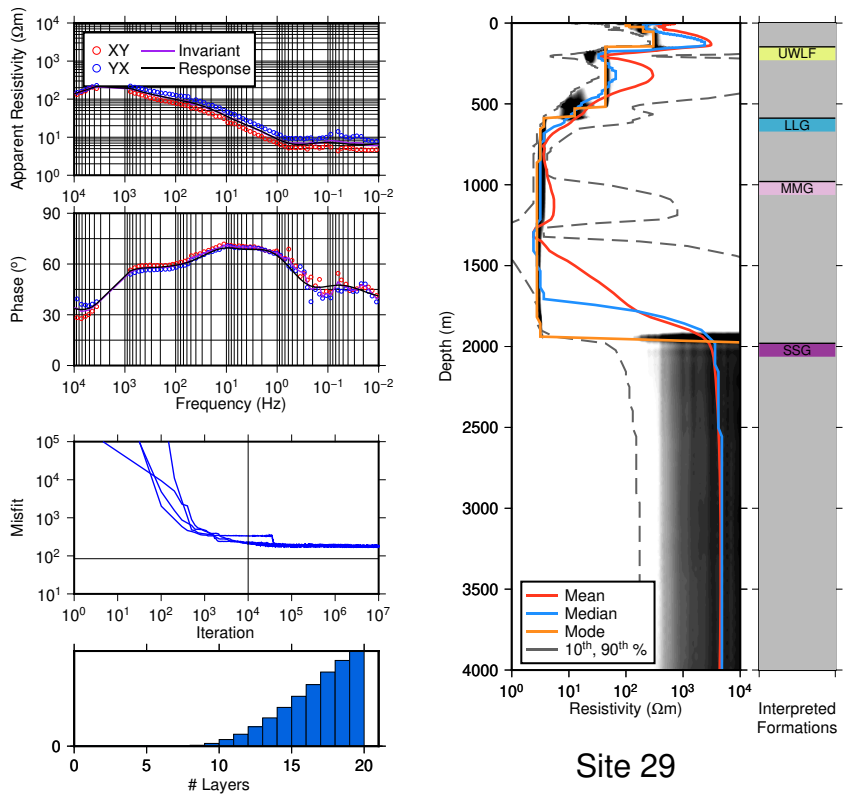
Site 26



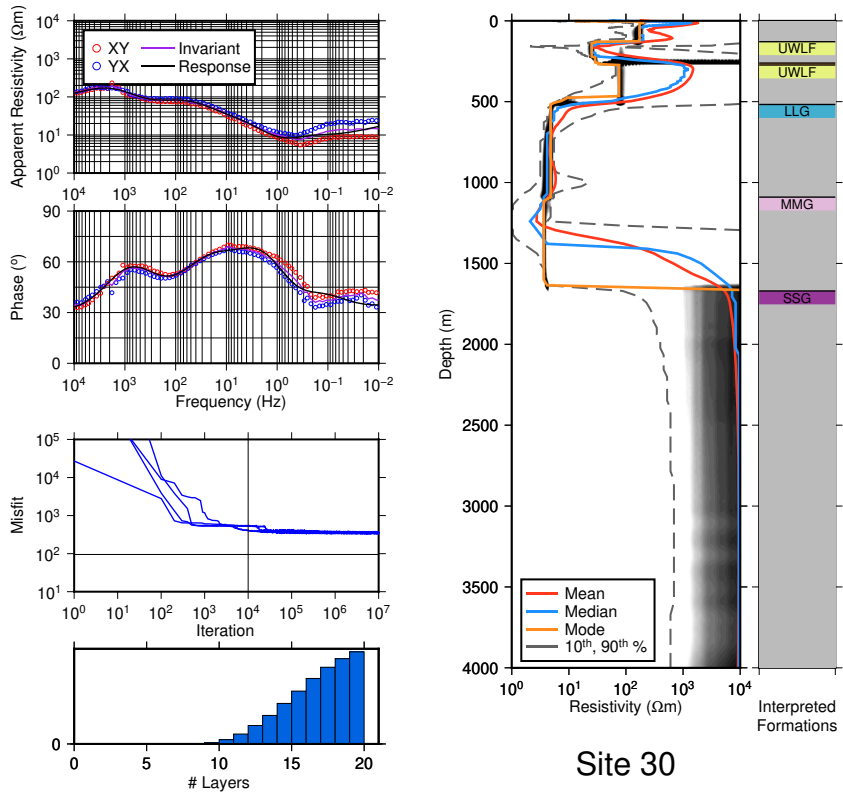
Site 27



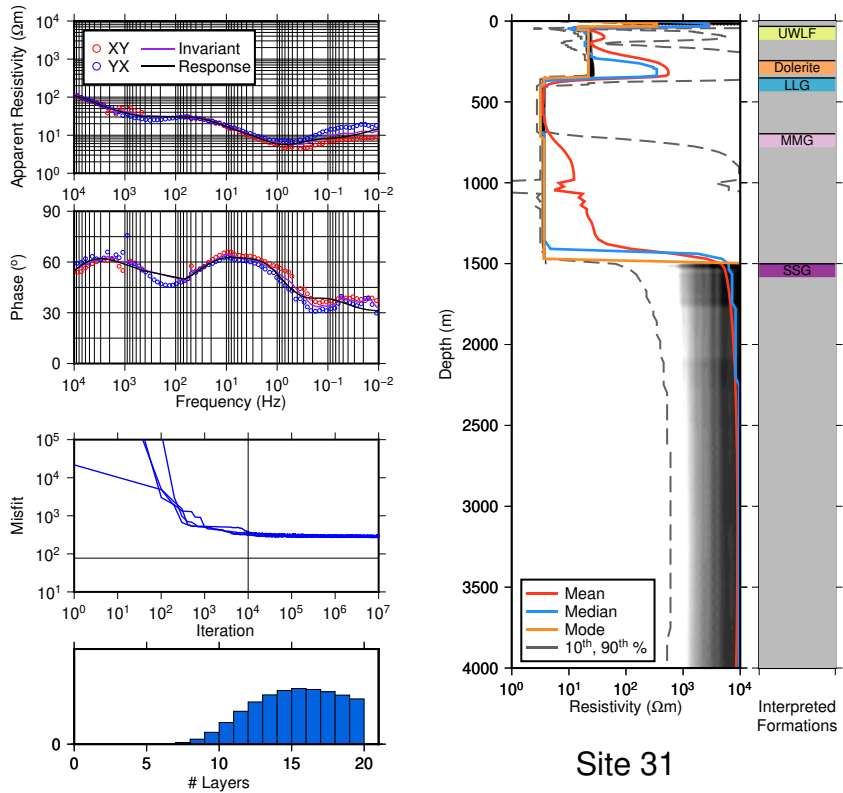
Site 28



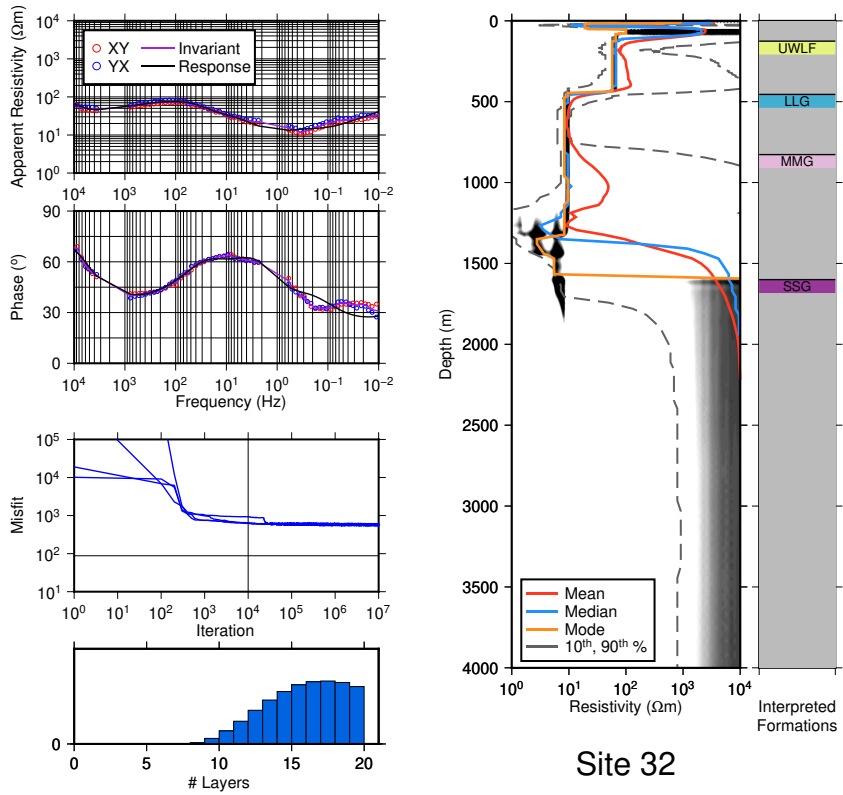
Site 29



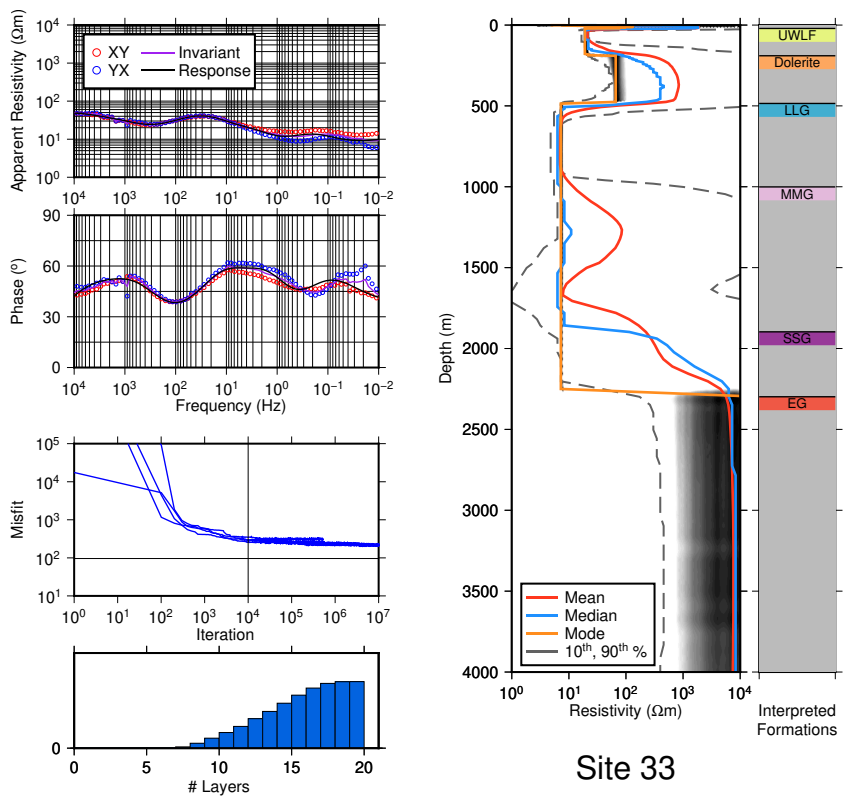
Site 30



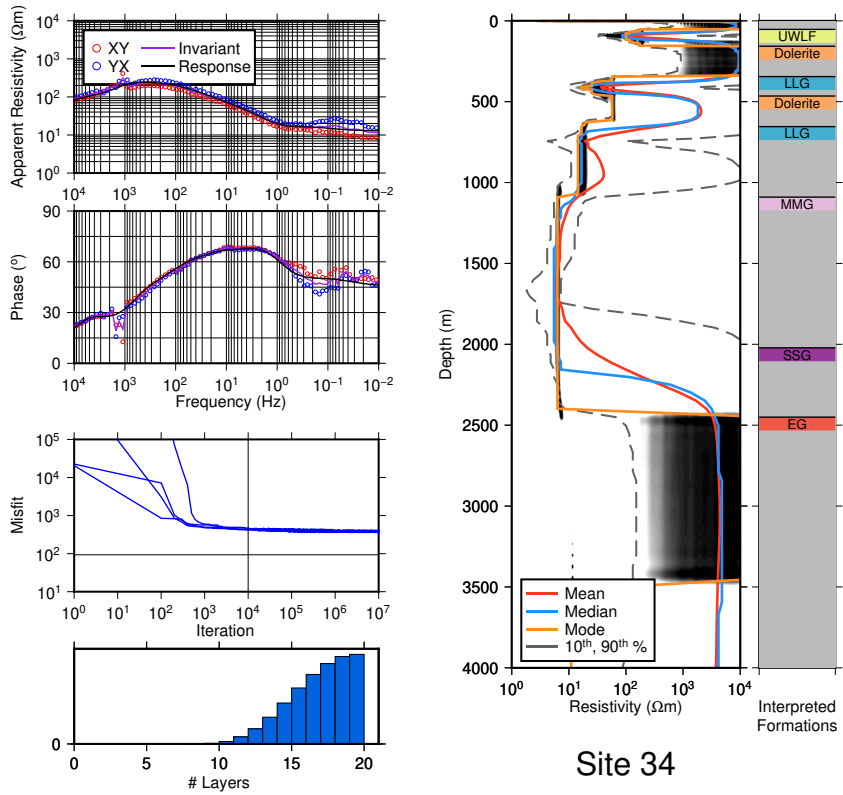
Site 31



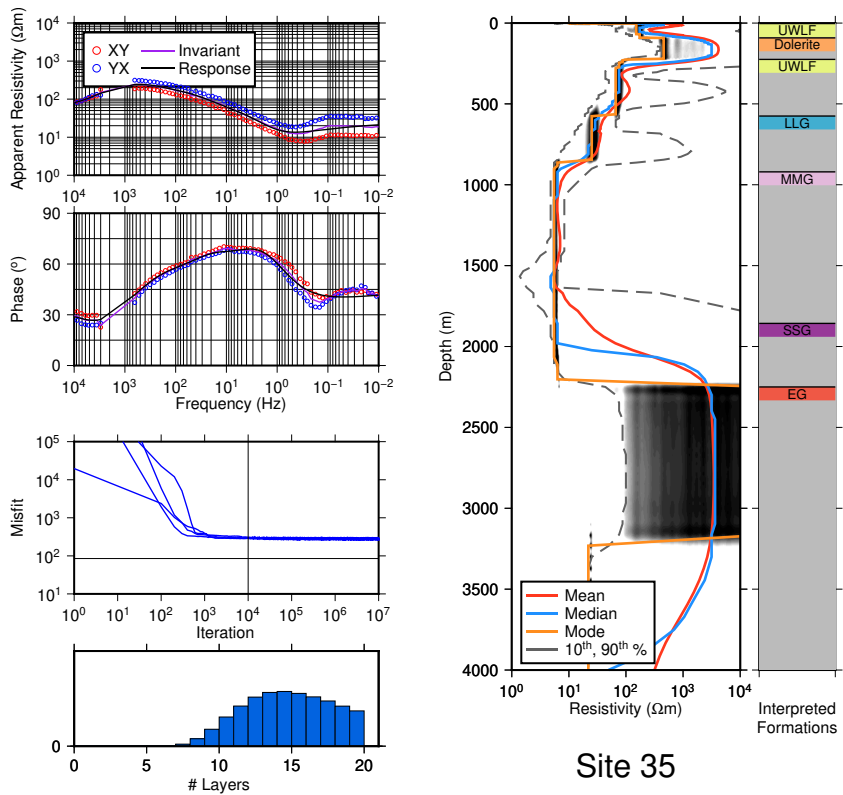
Site 32



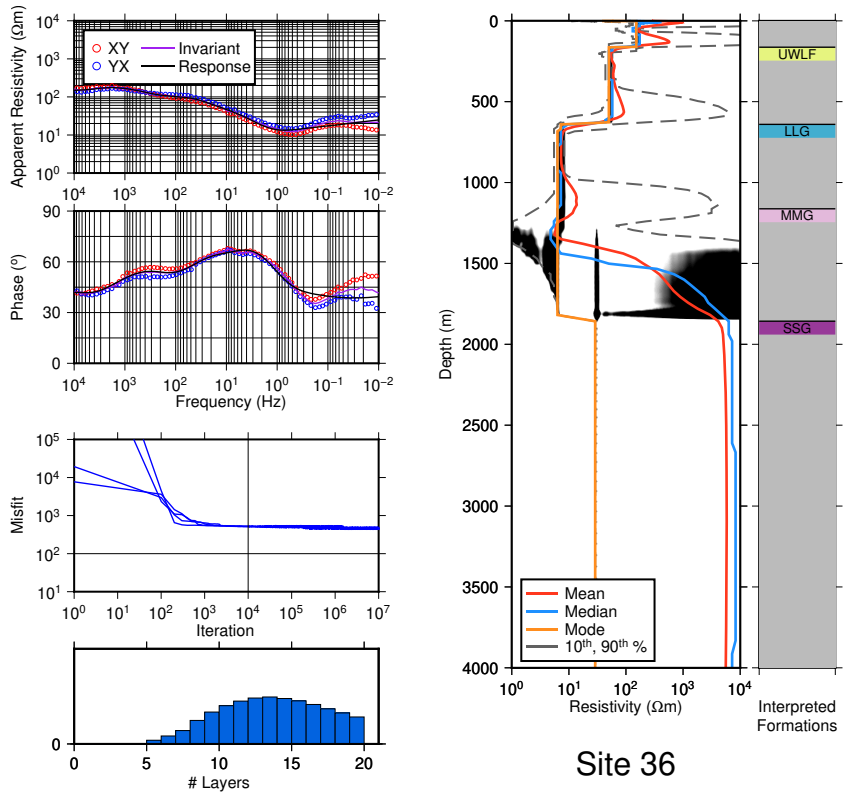
Site 33



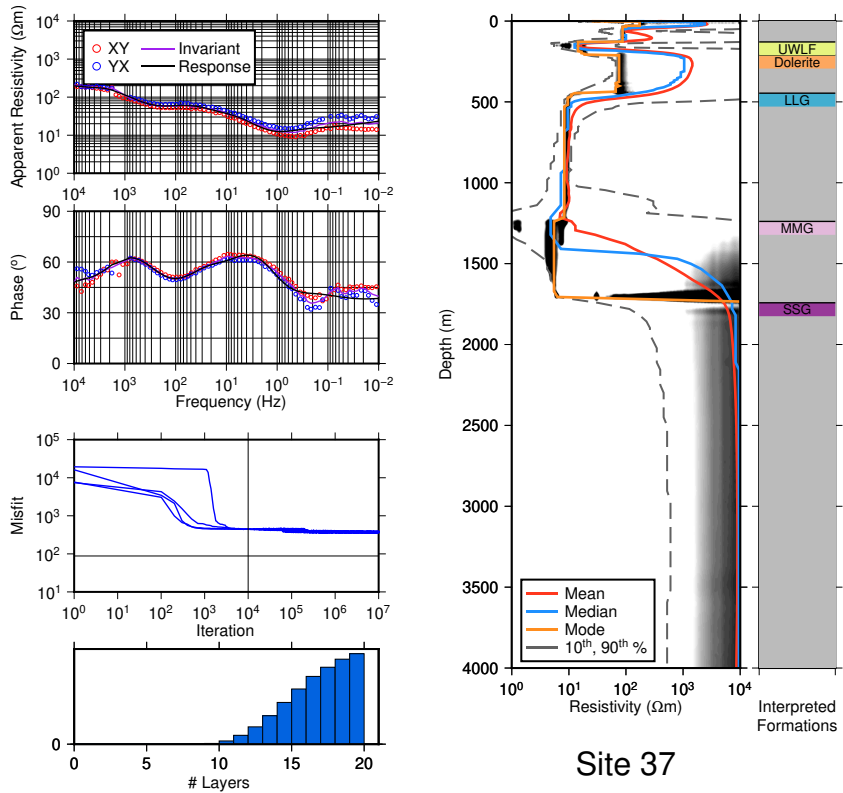
Site 34



Site 35



Site 36



Site 37

